

**CONTROLLING ELECTRONIC PROPERTIES AND MORPHOLOGY OF
ISOINDIGO-BASED POLYMERS FOR PHOTOVOLTAIC APPLICATIONS**

A Dissertation
Presented to
The Academic Faculty

by

Caroline Grand

In Partial Fulfillment
of the Requirements for the Degree of
Doctor of Philosophy in the
School of Chemistry & Biochemistry

Georgia Institute of Technology
May 2015

COPYRIGHT 2015 CAROLINE GRAND

**CONTROLLING ELECTRONIC PROPERTIES AND MORPHOLOGY OF
ISOINDIGO-BASED POLYMERS FOR PHOTOVOLTAIC APPLICATIONS**

Approved by:

Dr. John R. Reynolds, Advisor
School of Chemistry and Biochemistry
Georgia Institute of Technology

Dr. Seth R. Marder
School of Chemistry and Biochemistry
Georgia Institute of Technology

Dr. Jean-Luc Brédas
Physical Sciences and Engineering
Division
*King Abdullah University of Science and
Technology*

Dr. David G. Bucknall
School of Material Science and
Engineering
Georgia Institute of Technology

Dr. Elsa Reichmanis
School of Chemical and Biochemical
Engineering
Georgia Institute of Technology

Date Approved: December 15, 2014

To my family and in loving memory of my grandmothers

ACKNOWLEDGEMENTS

I would first like to acknowledge Prof. John R. Reynolds for his guidance throughout these five years of graduate school, not only for scientific input but also for leading a research group that promotes both creativity and progress. I have learned much more than I could have hoped for coming to graduate school, and for that I am very grateful. From the conception of a new project to writing a manuscript and presenting the research at conferences, Dr. Reynolds has always been dedicated to nurturing personal growth through scientific endeavors.

I would also like to thank the members of my committee at Georgia Institute of Technology, Prof. Seth Marder, Prof. Jean-Luc Brédas, Prof. David Bucknall and Prof. Elsa Reichmanis for their invaluable scientific input. The discussions that spurred from candidacy exams and six-month reviews, in addition to their individual expertise, have truly helped me grow as a scientist.

This work could not have come together if not for contributions from collaborators in a wide range of disciplines. The depth of understanding of device physics from Prof. Franky So, Dr. Jegadesan Subbiah, Sujin Baek, Tsung-Han Lai, Song Chen, Jesse Manders, Cephas Small, Dania Constantinou and other members of the So group in the Department of Material Science and Engineering at the University of Florida has been invaluable to the significance of my work in the field of organic photovoltaics. I would also like to thank Prof. Klaus Müllen, Prof. Wojtek Pisula and Wojtek Zajaczkowski at the Max Planck Institute for Polymer Research for their time and expertise on structural characterization of π -conjugated polymers and its correlation to organic field-effect

transistor devices. I would further like to thank Prof. David Bucknall and Nabankur Deb for sharing their expertise on scattering and reflectivity techniques, which have undoubtedly brought this work to a significantly higher level of characterization and insight on polymer morphology. Many thanks also go to the people that have helped me set up the SSDL at GT: Drs. Aubrey Dyer and Gaëlle Deshayes, Marcel Said, Nabil Kleinhenz and Boyi Fu.

I am very grateful to everyone in the Reynolds group who have contributed to making these five years so enjoyable, both at UF and GT. My first thanks go to Drs. Ken Graham and Romain Stalder, who have been tremendous mentors for both device fabrication and characterization and polymer synthesis and polymer characterization. I would not have been able to achieve this work without their initial guidance and breadth of knowledge. I would also like to thank Natasha Terán, Dr. Coralie Richard, Dr. Justin Kerszulis and Ray Bulloch for making graduate school an enjoyable experience both at UF and GT. I would further like to thank Drs. Leandro Estrada, Toan Pho, Eric Shen, and Anna Osterhölm for their combined knowledge in the field of organic electronics, and their willingness to share that knowledge. I would especially like to acknowledge Chi Kin Lo and Jeff Hernandez for their willingness to take over some of my responsibilities in the group and for their help in the last years, and Rylan Wolfe, Brian Schmatz and Ian Pelse for their contributions to the Reynolds' solid-state subgroup. I am convinced they will make significant contributions to the field of organic electronics.

I would also like to thank all the people who have helped me navigate through graduate school, Dr. Ben Smith and Lori Clark at UF and Drs. Cam Tyson and Kenyetta Johnson at GT. A lot of this work would not have been possible without the help of

Cheryl Googins, Sara Klossner, Aeryal Herrod and Venese Blake-Leggett who have made research convenient from behind the scenes. I would also like to thank GT's Center for Organic Photonics and Electronics for providing exciting opportunities for people in the field of organic electronics at GT through collaborations, talks, poster sessions, and the COPE Fellowship.

Last but certainly not least, I owe a tremendous thank you to my family. Without their support, who knows if I would even had taken the chance to pursue a degree on this side of the pond? Thank you to my parents, Jean-Pierre and Véronique, and sisters, Pauline and Margaux, who have supported me through the tough times and have been as excited as I was during the rewarding times. I could not have done it without you. Thank you to all of my family: Bernard, Christiane and Denise, Carole, Laure and Eryn, Edouard, Marie-Thérèse and Régis, Marie and Grégoire, Pierre, Cyrielle and Timéo, Christian and Chantal, Gaëlle, Pierre-Yves, Elise and Paul, Florence and William. I am very grateful for the emails/Skype/reunions, which have made up for the distance over these past five years.

TABLE OF CONTENTS

ACKNOWLEDGEMENTS	iv
LIST OF TABLES	x
LIST OF FIGURES	xi
LIST OF SCHEMES	xvii
LIST OF SYMBOLS AND ABBREVIATIONS	xviii
SUMMARY	xx
CHAPTER 1. INTRODUCTION	1
1.1. Organic Electronics Background	1
1.2. Electronic States in Polymer Semiconductors	3
1.3. Property Changes after Transition from Solutions to Thin Films	7
1.4. Comparison of Inorganic and Organic Semiconductors	12
1.5. Organic Electronics: Operating Principles	15
1.5.1. Organic Field Effect Transistors (OFET)	15
1.5.2. Organic Photovoltaics (OPVs) Background	19
1.5.3. OPV Device Operating Principles	20
1.5.4. The Bulk-Heterojunction (BHJ)	26
1.5.5. Space-Charge Limited-Current (SCLC) Mobility	27
1.6. Design of Conjugated Polymers for Frontier Orbital Energy and Morphology Control	29
1.6.1. The Donor-Acceptor Approach	30
1.6.2. The Isoindigo Unit: An Electron Deficient Synthron	32
1.7. From Molecules to Thin Film: Morphology in Solid State Organic Semiconductors	35
1.7.1. Solution Processing Techniques	36
1.7.2. Thermodynamics of Mixing and Solubility Parameters	38
1.7.3. Single Component Films: Morphological Considerations and Transport Properties in Polymer FETs	40
1.7.3.1. Polymer Structure and Crystallization Kinetics	41
1.7.3.2. Polymer Ordering in Thin Films	45
1.7.3.3. Post-Processing Treatments Effects on Polymer Arrangement	53
1.7.4. Polymer:Small Molecule Mixtures: Polymer:Fullerene Blends for OPVs	55
1.7.4.1. Fullerene Solubility and Selection of Fullerene Derivative	57
1.7.4.2. Liquid-liquid Demixing	57
1.7.4.3. Solid-liquid Demixing	59
1.7.4.4. Extended Control with Solvent Additives (or Tailing Solvents)	62
1.7.4.5. Solid-solid Demixing or Order-Disorder Transitions: Impact of Post-Processing Treatments on Phase Separation	65
1.7.5. All-Polymer Blends for OPVs	66
1.8. Overview of Dissertation	69
CHAPTER 2. CHARACTERIZATION TECHNIQUES AND EXPERIMENTAL METHODS	72
2.1. Density Functional Theory	72
2.2. Synthesis: Suzuki and Stille Polycondensations	75
2.3. Structural and Polymer Characterization	77

2.3.1.	General Structural Characterizations	77
2.3.2.	Thermal Characterizations	78
2.3.3.	Optical and Spectroscopic Techniques	80
2.3.4.	Electrochemical Methods	80
2.4.	Materials for Device Processing	81
2.5.	Device Fabrication	86
2.5.1.	Organic Field Effect Transistor Devices	86
2.5.2.	ITO Substrate Preparation	86
2.5.3.	Organic Photovoltaic Devices	88
2.5.4.	Space-Charge Limited Current Measurements	90
2.6.	Device Measurement Techniques	90
2.6.1.	Organic Field-Effect Transistor Testing	90
2.6.2.	SCLC Testing and Fitting	92
2.6.3.	Power Conversion Efficiency	94
2.6.4.	Incident Photon to Current Efficiency (IPCE)	97
2.6.5.	Charge Modulated Electroabsorption (CMEAS)	100
2.7.	Solubility Characterization	102
2.7.1.	Solubility Measurements	102
2.7.2.	Solution Scattering Studies	103
2.7.2.1.	Neutrons/X-rays and Matter	103
2.7.2.2.	Instrumentation	107
2.7.2.3.	Scattering Analysis	108
2.8.	Thin Film Morphology Characterization	110
2.8.1.	Profilometry	110
2.8.2.	Atomic Force Microscopy (AFM)	112
2.8.2.1.	Tapping Mode	113
2.8.2.2.	Phase Imaging in Tapping Mode	115
2.8.2.3.	Thickness Measurements	115
2.8.3.	Transmission Electron Microscopy	116
2.8.4.	Thin Film Structural Characterizations	118
2.8.4.1.	Synchrotron Grazing Incidence Wide Angle X-Ray Scattering	118
2.8.4.2.	X-Ray Photoelectron Spectroscopy	122
2.8.4.3.	Neutron Reflectivity	123
CHAPTER 3. ISOINDIGO IN N- AND P-TYPE POLYMERS FOR ORGANIC PHOTOVOLTAICS		127
3.1.	All-Acceptor Isoindigo-Based Conjugated Polymers	127
3.1.1.	Polymer Synthesis of P(iI), P(iI-BTD), P(iI-TPD), and P(iI-T-DPP-T)	127
3.1.2.	Optical Properties and Electrochemistry of P(iI), P(iI-BTD), P(iI-TPD) and P(iI-DPP)	130
3.1.3.	Polymer Modeling by DFT	133
3.1.4.	All-polymer Active Blend Solar Cells	134
3.1.4.1.	Device Characteristics	134
3.1.4.2.	Morphology of All-Polymer Blends	137
3.1.4.3.	Transport properties via SCLC Devices	137
3.2.	Donor-Acceptor Polymers for Blends with Fullerenes	139
3.2.1.	Polymer Synthesis of P(FI-iI), P(DTS-iI), and P(T ₂ DTS-iI)	139

3.2.2.	Optical Properties and Electrochemistry	141
3.2.3.	Polymer:Fullerene Active Blend Solar Cells	142
3.2.3.1.	Device Optimization and Characteristics	142
3.2.3.2.	Rationalizing low OPV performance of P(FI-iI) blends	144
3.2.3.3.	Effect of DIO in P(DTS-iI) and P(T ₂ DTS-iI) devices	145
3.3.	Principles Directing Transport and Charge Separation in Oligothiophene-Isoindigo Polymers	148
3.3.1.	Polymer Synthesis and Characterization	149
3.3.2.	Optoelectronic Characterization	151
3.3.3.	Polymer Packing	156
3.3.4.	Transport Characteristics in Organic Field-Effect Transistors	159
3.3.5.	Photovoltaic Devices	160
3.3.5.1.	Device Parameters	160
3.3.5.2.	Morphology of Blends of P[T-iI(HD)], P[T3(C6)-iI(HD)] or P[T3(C6)-iI(SiO)] with PC ₇₁ BM	162
3.3.5.3.	Photovoltage losses by CMEAS	165
3.3.5.4.	Inverted Devices and Roll-to-roll Processing	166
3.4.	Synthetic Details	168
CHAPTER 4. POLYMER PACKING TO CONTROL THIN-FILM MORPHOLOGY		175
4.1.	Synthesis of P[T3(R)-iI] Polymers	176
4.2.	Polymer Behavior in Solution - Quantification of Solubility	179
4.3.	Optoelectronic Properties of the P[T3(R)-iI(HD)] Family	179
4.4.	Molecular Interactions by GIWAXS	182
4.5.	Charge Transport in OFET devices	189
4.6.	Photovoltaic Devices	191
4.7.	Morphology Control via Polymer Structure	193
4.8.	Parameters Influencing Polymer:Fullerene Phase Separation	195
4.9.	Synthetic Details	196
CHAPTER 5. IMPACT OF POLYMER AND PROCESSING ADDITIVE STRUCTURES ON MORPHOLOGY IN POLYMER-BASED THIN-FILMS		202
5.1.	Choice of Polymers and Processing Additives	203
5.2.	Solution Properties of P1 by UV-vis-NIR and SANS	206
5.3.	Implications for OPV Devices	210
5.3.1.	OPV Device Characteristics	210
5.3.2.	Charge Mobility in SCLC Devices	212
5.4.	Thin Film Characterizations	213
5.4.1.	Effect on Phase Separation with PC ₇₁ BM	213
5.4.2.	Effect of Additives on Polymer Packing	215
5.5.	Mechanism of Action for Morphology Control using Additives	223
CHAPTER 6. CONCLUSIONS AND PERSPECTIVES		226
APPENDIX A. BEAMTIME PROPOSAL		230
REFERENCES		234
VITA		249

LIST OF TABLES

Table 1-1. Structure and OFET hole (μ_h) and electron (μ_e) mobility of solution-processed small-molecules and polymers as reported in the literature.....	18
Table 1-2. Isoindigo-based polymer in OFET and OPV devices.	34
Table 2-1. Characteristics of X-ray (values taken from SLAC beamline 11-3) and neutron sources (values taken from NIST Center for Neutron Research) for scattering studies.	104
Table 2-2. Main regimes of typical scattering curves and the corresponding information gained.....	109
Table 3-1. Summary of optoelectronic properties of P(iI), P(iI-BTD), P(iI-TPD) and P(iI-DPP), including SCLC electron mobilities.....	139
Table 3-2. Size exclusion chromatography (SEC) results and optoelectronic properties of P[T-iI(HD)], P[T3(C6)-iI(HD)] and P[T3(C6)-iI(SiO)].	156
Table 3-3. Thin film polymer microstructure determined by GIWAXS.	159
Table 3-4. Conventional OPV device characteristics.	161
Table 3-5. XPS data showing elemental composition and calculated material concentrations at the film surface as a function of processing conditions.....	164
Table 3-6. XPS analysis as a function of device area probed in P[T3(C6)-iI(HD)]:PC ₇₁ BM (1:1.5) blends spun cast from oDCB without DIO.	165
Table 3-7. Conventional and inverted device characteristics based on P[T-iI(HD)], P[T3(C6)-iI(HD)], and P[T3(C6)-iI(SiO)] polymer:PC ₇₁ BM blends processed with DIO.	167
Table 4-1. Purity, Molecular Weight, Solubility, Electrochemical, and Optical Properties of P[T3(R)-iI] polymers.....	182
Table 4-2. Backbone-to-backbone π and chain-to-chain d distances determined from polymer thin film GIWAXS and their corresponding coherence length, along with film crystallinity and HOF for the (100) peak.....	187
Table 4-3. π -stacking π and chain-to-chain d distances (left) estimated from line integration of equatorial peaks in the 2DWAXS data (right).	188
Table 4-4. Hole μ_h and electron μ_e OFET mobility, and OFET threshold voltage V_T after annealing at 120 °C.....	190
Table 4-5. OPV performance of P[T3(R)-iI] derivatives with PC ₇₁ BM spun-cast from oDCB.	192
Table 4-6. Chain-to-chain distances d and their corresponding coherence length determined from pristine polymer films and polymer:PC ₇₁ BM blends GIWAXS.....	195
Table 5-1. Boiling point (bp), Hansen solubility parameters (dispersive δ_D , polar δ_P , hydrogen bonding δ_H) and estimated component solubilities.....	206
Table 5-2. Shift in absorption maxima in polymer:PC ₇₁ BM chloroform solutions as a function of additive and temperature.	207
Table 5-3. Estimated SCLC hole mobility in the active layer blends, and corresponding film thickness.....	213
Table 5-4. π - π and lamellar (d) distances and coherence length of (100) peak ($L_{c,d}$) estimated from GIWAXS integration.	223

LIST OF FIGURES

Figure 1-1. Representative repeat unit structures of π -conjugated polymers.	2
Figure 1-2. Schematic representation of the ethylene orbital and the evolution of the highest occupied molecular orbital (HOMO), lowest unoccupied molecular orbital (LUMO) and energy gap with increasing conjugation.	3
Figure 1-3. Periodicity of the band energy as a function of wavevector (or location in direct space) and the reduction of the full description of the polymer chain in half of the Brillouin zone.....	4
Figure 1-4. (a) Density of states, (b) transition and (c) Jablonski diagram.	6
Figure 1-5. Ground and excited state energies, and how they relate to the bonding/anti-bonding pattern along the polymer backbone in the case of trans-polyacetylene and polythiophene.....	7
Figure 1-6. Transitions from molecular structure to macroscopic properties.....	8
Figure 1-7. (a) Overview of possible π - π geometric configurations of the benzene dimer, and (b) impact of interaction energy components on the energy of substituted benzene sandwiches relative to a benzene dimer.....	9
Figure 1-8. Self-organization of fluorene oligomers in flipped and shifted stacks, as well as side-chain organization into a Y-shape. The change in organization from solution to film leads to changes in the optoelectronic properties via UV-vis-NIR (solid line).	10
Figure 1-9. Impact of polymer packing on optoelectronic properties, in particular UV-vis-NIR absorption.....	11
Figure 1-10. Schematic DOS diagram of π -conjugated polymers (a) and its impact on charge carrier transport (b).....	12
Figure 1-11. Frenkel exciton formation after photoexcitation leading to the formation of an optical energy gap.	14
Figure 1-12. (A) (a) Example of the mode of operation of as OFET for (b,d) n- and (c, e) p-type transport, along with (B) charge carrier concentration in the semiconductor layer as a function of drain voltage (a) below the threshold voltage V_T , (b) in the linear regime, and (c) in the saturation regime.	16
Figure 1-13. Schematic illustration of the processes involved in current generation in an OPV device.	21
Figure 1-14. Molecular pictures of CT states obtained from quantum chemical calculations.	23
1-15. Processes involved in charge separation.	24
Figure 1-16. Representative J-V curve for a solar cell under illumination and the corresponding power density-voltage curve, which defines V_{oc} , J_{sc} , FF and P_{max}	25
Figure 1-17. Simulated domain boundaries for BHJ solar cell devices.....	27
Figure 1-18. State of the art polymer:fullerene or polymer:polymer BHJ devices.	27
Figure 1-19. Scheme of ohmic electron transport (a), trap-free space-charge limited transport when the number of injected carriers n_{inj} is higher than a threshold n_0 (b), and the corresponding J-V curve (c).....	28
Figure 1-20. General structure of conjugated polymers for solution processing.....	30
Figure 1-21. The donor-acceptor concept for energy gap control and examples of electron-rich and electron-deficient units.	31

Figure 1-22. Structures of the indigo, diketopyrrolopyrrole (DPP) and isoindigo (iI) dyes and structural similarities and differences.	32
Figure 1-23. (a) HOMO and LUMO levels computed at the B3LYP/6-31G(d) level on isoindigo model compounds describing electron density, and (b) crystal structures of (A) phenyl- and (B) thienyl-flanked 6,6'-(N,N'-dihexyl)isoindigo.	33
Figure 1-24. Morphological considerations ranging from the molecular scale to the micrometer scale.	36
Figure 1-25. Polymer structure and packing.	43
Figure 1-26. Influence of molecular weight (entangled chains on bottom) on (a) polymer packing in the solid state as seen in the phase images of polymer films, (b) schematic representation of polymer chains in the solid state, and (c) impact of the degree of polymerization on OFET hole carrier mobility.	47
Figure 1-27. Degree of ordering (GIWAXS) and schematic thin film morphology as a function of polymer structure.	48
Figure 1-28. Impact of siloxane-terminated side-chains on polymer solid state packing by GIWAXS.	49
Figure 1-29. Schematic representation of polymer interchain interactions.	50
Figure 1-30. Determination of polymer packing with NMR.	51
Figure 1-31. GIWAXS of thin films of (a) PDPPT-2T, (b) PDPPT-TT and (c) PDPPT-T before (left) and after (right) thermal annealing.	54
Figure 1-32. Schematic representation of processes that may occur in a ternary blend. ..	56
Figure 1-33. Ternary phase diagram, and the impact of film drying time.	59
Figure 1-34. Schematic representation of film formation in P3HT:PC ₆₁ BM blends.	60
Figure 1-35. Impact of polymer structure on film formation in blends with PC ₇₁ BM.	61
Figure 1-36. Schematic representation of film formation in 1:4 blends of polymer:PC ₇₁ BM, regardless of the polymer structure.	61
Figure 1-37. Scheme summarizing the various processes that can occur during film formation in BHJ devices.	62
Figure 1-38. (a) Structure of PBTD-DPP, and UV-vis-NIR absorbance in film and solution in the presence of DIO (b) and oDCB (c).	64
Figure 1-39. Binary phase diagram depicting polymer solubility as a function of the degree of polymerization N and of the Flory interaction parameter χ	66
Figure 1-40. Structures of P(NDI2OD-T2) and P3HT, and solvent selection to induce selective interaction of P(NDI2OD-T2) with xylene (XY) as a solvent rather than polymer:polymer interactions in chlorobenzene (CB) or oDCB.	67
Figure 2-1. Typical DSC thermogram for polymers reported in this dissertation showing a melting transition and crystallization transition.	79
Figure 2-2. (a) ITO etch pattern from Tinwell Technology, project # TI1678D, with dimensions in mm and a resistance of 15 ohm-square, and (b) shadow mask pattern for top electrode deposition.	87
Figure 2-3. Schematic description of charge flow in a p-type and n-type OFET.	91
Figure 2-4. Typical output and transfer characteristic measured on π -conjugated polymer thin films.	91
Figure 2-5. Logarithmic plot of the J-V curve showing the ohmic region, trap-filling region and SCLC region,	93

Figure 2-6. (a) Schematic representation of the three air mass conditions for measuring PV cells, and (b) the corresponding solar spectra.	94
Figure 2-7. (a, b) Relevance of statistical analysis to distinguish the actual improvement from method 2 versus method 1, and (c) illustration of Chauvenet's criterion.	97
Figure 2-8. Scheme of Newport IPCE setup.	100
Figure 2-9. Absorbance vs. concentration calibration curve measured for P[T3(C6)-iI] in oDCB.	103
Figure 2-10. Scheme of incident beam being diffracted by crystalline planes leading to beam interference.	104
Figure 2-11. Description of the scattering vector \mathbf{q} as a function of incoming beam \mathbf{k}_0 and outgoing diffraction vectors \mathbf{k}_s	105
Figure 2-12. Schematic relationship between a reciprocal lattice plane and real space diffraction planes.	105
Figure 2-13. NG7-30m beamline setup at NIST CNR.	108
Figure 2-14. Polymer chains in solution approximated by spheres at low q (dimensions \sim 50-100 nm) and stiff segments at high q (10-30 nm).	110
Figure 2-15. Feedback loop electronics involved in either the Veeco Innova or Bruker Icon AFM.	113
Figure 2-16. Schematic representation of the phase shift between the driving cantilever piezoelectric and the cantilever oscillation over a hard and soft region.	115
Figure 2-17. Schematic of GIWAXS setup and the information that can be extracted from GIWAXS patterns.	118
Figure 2-18. Typical GIWAXS image revealing information about π -stacking distances between (010) planes and lamellar packing between (100) planes.	119
Figure 2-19. Integration along q_{xy} and q_z axes highlighting scattering peaks.	120
Figure 2-20. Gaussian fits to scattering integrated over a 0° to 90° χ range.	121
Figure 2-21. Orientation of (100) peaks along χ , and the corresponding Herman orientation factors.	122
Figure 2-22. Emission process of core electrons in XPS with the kinetic energy of the photoelectron detected by the spectrophotometer.	122
Figure 2-23. Scheme of specular reflection of neutron beams and how the different layers normal to the surface are probed.	124
Figure 2-24. Influence of thin-film parameters (thickness, roughness and material/SLD) on composition depth profile and on the reflectivity measurement.	126
Figure 3-1. Normalized UV-Vis absorption spectra of P(iI), P(iI-BTD), P(iI-TPD), and P(iI-DPP) in thin films.	130
Figure 3-2. CV and DPV of (a) P(iI), (b) P(iI-BTD), (c) P(iI-TPD), and (d) P(iI-DPP) 132	
Figure 3-3. Lowest energy geometry (a) P(iI), (b) P(iI-BTD), and (c) P(iI-TPD) model tetramers as calculated by DFT.	133
Figure 3-4. Summary of electron affinities and ionization potentials for the four polymers, and their comparison to the energy levels in P3HT measured under the same conditions.	134
Figure 3-5. (a) Normalized thin-film absorbance of P(iI) and of P3HT:P(iI) active layers at different blend ratios (2:1, 1:1, and 1:2), and (b) J-V curves obtained at different P3HT:P(iI) blend ratios under AM1.5 illumination.	135

Figure 3-6. J-V curves of P3HT:P(iI-BTD) conventional devices under AM1.5 illumination fabricated from chloroform or chlorobenzene (CB) at varying blend ratios.	136
Figure 3-7. AFM height images of (a) P3HT:P(iI) blends and (b) P3HT:P(iI-BTD) blends spun-cast from chlorobenzene at varying ratios	137
Figure 3-8. SCLC region in electron-only (a) P(iI) and (b) P(iI-BTD) devices.	138
Figure 3-9. Thin film normalized UV-vis-NIR absorbance of P(FI-iI), P(DTS-iI) and P(T ₂ DTS-iI).....	141
Figure 3-10. J-V characteristics of (a) P(DTS-iI):PC ₇₁ BM and (b) P(T ₂ DTS-iI):PC ₇₁ BM under illumination and in the dark as a function of processing and device architecture.	143
Figure 3-11. AFM height image of (a) P(FI-iI):PC ₆₁ BM (1:2 ratio in CHCl ₃ , annealed at 100 °C) blend and (b) P(DTS-iI):PC ₇₁ BM (1:4 in CB) blend	144
Figure 3-12. AFM and TEM images of thin films of P(DTS-iI):PC ₇₁ BM at a 1:4 ratio without (a,b) and with 4% v DIO (c,d), and of thin films of P(DTS-iI):PC ₆₁ BM at a 1:4 ratio without (e,f) and with 2.5% v DIO (g,h).	145
Figure 3-13. AFM topology of P(T ₂ DTS-iI):PC ₆₁ BM (1:2) without (a) and with 2% v DIO (b), and P(T ₂ DTS-iI):PC ₇₁ BM (1:4) without (c) and with 2% v DIO (d).	148
Figure 3-14. Frontier molecular orbital energies for the T-iI and T3-iI model compounds at the B3LYP/6-31G(d) level of theory as a function of oligomer size.....	152
Figure 3-15. Model compounds and orbital localization in T-iI trimer and T3-iI dimer HOMO and LUMO levels.	152
Figure 3-16. (a) CV and DPV of thin films of P[T-iI(HD)] and (b) its corresponding scan rate dependence of the first reduction peak, and CV and DPV of thin films of (c) P[T3(C6)-iI(HD)] and (d) P[T3(C6)-iI(SiO)].....	153
Figure 3-17. Differential pulse voltammograms of P[T-iI(HD)], P[T3(C6)-iI(HD)] and P[T3(C6)-iI(SiO)]	154
Figure 3-18. Normalized UV-vis spectra of P[T-iI(HD)] (black), P[T3(C6)-iI(HD)] (red), and P[T3(C6)-iI(SiO)] (blue) in chloroform solution (top) and thin film (bottom).	155
Figure 3-19. GIWAXS images of pristine (a-c) and thermally annealed at 200°C (d-f) P[T-iI(HD)](a,d), P[T3(C6)-iI(HD)](b,e) and P[T3(C6)-iI(SiO)] (c,f) thin films prepared from oDCB. (g) Possible chain conformation in a unit cell illustrating an edge-on backbone orientation.	158
Figure 3-20. AFM images of blends of PC ₇₁ BM with (a,b) P[T-iI(HD)], (c,d) P[T3(C6)-iI(HD)], and (e,f) P[T3(C6)-iI(SiO)] without (top) and with 2.5% v DIO (bottom).	162
Figure 3-21. Neutron reflectivity data and fits (a) leading to scattering length density profiles of P[T3(C6)-iI(HD)] devices spun cast from oDCB without (b) and with 2.5% DIO (c).	163
Figure 3-22. Correlation between effective energy gap (molecular orbital picture, a) and CT states energy (electronic state view, b), and CMEAS results showing sub-energy gap absorption of P[T-iI(HD)] and P[T3(C6)-iI(HD)] blends with PC ₇₁ BM (c).	166
Figure 3-23. (a) Roll-to-roll processed P[T3(C6)-iI(HD)] cell based on PET/ITO/ZnO / P[T3(C6)-iI(HD)]:PC ₇₁ BM (1:1.5) + 2.5% v DIO in CB/MoO _x /Ag, and (b) J-V curves of slot-die coated cells with device parameters in inserted table.....	168
Figure 4-1. (a) TGA trace of the six polymers. (b) DSC analysis of C6 and 2EH at 10 °C/min (third DSC scan showed), and (c) DSC analysis of the second and third cycle of C6 at 20 °C/min	178

Figure 4-2. Calibration curves of absorbance at 659 nm versus the concentration of C6 (a) and at 634 nm versus the concentration of 2EH (b) in oDCB.	179
Figure 4-3. (a) Solution absorption spectra in oDCB, and (b) film absorption spectra of P[T3(R)-iI] polymers.	180
Figure 4-4. CV and DPV versus Fc/Fc^+ of (a) C6 and (b) 2EH	181
Figure 4-5. GIWAXS images in as-cast films of P[T3(R)-iI] from oDCB.	184
Figure 4-6. GIWAXS of P[T3(R)-iI] polymers annealed at 200 °C, and cooled to room temperature.	185
Figure 4-7. (a) q_{xy} and (b) q_z line integrations as a function of sample temperature.	186
Figure 4-8. (a) GIWAXS plot of C12 65k film focusing on (100) and (b) 2DWAXS equatorial integration plot of C12 high extruded fibers at RT and annealed at 120 °C and 200 °C.	189
Figure 4-9. (a) J-V curves of P[T3(R)-iI]:PC ₇₁ BM blends spun cast from oDCB, (b) the corresponding IPCE curves, and (c) device absorption spectra.	192
Figure 4-10. AFM height images of polymer:PC ₇₁ BM 1:1.5 blends spun cast from oDCB.	193
Figure 4-11. GIWAXS of P[T3(R)-iI]:PC ₇₁ BM blends spun cast from oDCB onto PEDOT:PSS-covered silicon wafers.	194
Figure 5-1. SANS of (a) P1 and (b) P2 in chloroform solutions without and with processing additives.	209
Figure 5-2. (a) Current density-voltage (J-V) curves of P1:PC ₇₁ BM (1:2) devices, and (b) the impact of processing additives on J_{sc} and PCE.	211
Figure 5-3. (a) Current density-voltage (J-V) curves of P2:PC ₇₁ BM (1:1) devices, and (b) the impact of processing additives on V_{oc}	212
Figure 5-4. SCLC devices based on (a) P1:PC ₇₁ BM and (b):P2:PC ₇₁ BM with field-dependent fits.	212
Figure 5-5. AFM height images of P1:P ₇₁ BM (1:2) devices spun-cast from CHCl ₃ as the main solvent without and with 2%v processing additive.	214
Figure 5-6. AFM height images of P2:P ₇₁ BM (1:1) devices spun-cast from CHCl ₃ as the main solvent without and with 2%v processing additive.	215
Figure 5-7. (a) Device absorbance through glass/ITO/PEDOT:PSS/P1:PC ₇₁ BM, and (b) focus on the 650 to 580 nm region looking at the aggregation peak.	216
Figure 5-8. GIWAXS images of P1 (top) and P1:PC ₇₁ BM (bottom) cast from chloroform without and with 2%v processing additive.	217
Figure 5-9. Line integration along the q_z axis of (a) P1 films and (b) P1:PC ₇₁ BM films, and integration along χ of the (100) scattering peak in (c) P1 films and (d) P1:PC ₇₁ BM films.	218
Figure 5-10. (a) Device absorbance through glass/ITO/PEDOT:PSS/P2:PC ₇₁ BM, and (b) focus on the 650 to 580 nm region looking at the aggregation peak.	219
Figure 5-11. GIWAXS images of P2 (top) and P2:PC ₇₁ BM (bottom) cast from chloroform without and with 2%v processing additive.	220
Figure 5-12. Line integration along the q_z axis of (a) P2 films and (b) P2:PC ₇₁ BM films, and integration along χ of the (100) scattering peak in (c) P2 films and (d) P2:PC ₇₁ BM films.	222
Figure 6-1. Suggested polymer and small molecule structures as novel acceptors for BHJ.	227

Figure 6-2. Illustration of previous work installing dipoles at the polymer:fullerene interface.....	228
--	-----

LIST OF SCHEMES

Scheme 2-1 Simplified mechanism of coupling reactions, involving (a) oxidative addition, (b) transmetallation, and (c) reductive elimination.....	75
Scheme 3-1. Synthesis of the dibromo- and diboron-isoindigo monomers.....	128
Scheme 3-2. Synthesis of three all-acceptor polymers based on iI.....	129
Scheme 3-3. Direct arylation polymerization yielding P(iI-DPP).	129
Scheme 3-4. Synthesis of P(FI-iI) via Suzuki coupling, and P(DTS-iI) and P(T ₂ DTS-iI) via Stille coupling.	140
Scheme 3-5. Synthesis of P[T-iI(HD)], P[T3(C6)-iI(HD)] and P[T3(C6)-iI(SiO)].	150
Scheme 4-1. Polymer structures reported in the literature and their processing conditions in blends with PC ₇₁ BM for OPVs. Conditions leading to small phase separation with fullerenes are written in green and those leading to large phase separation are in red...	175
Scheme 4-2. Synthesis of a family of terthiophene and isoindigo alternating polymers with varying side chains.....	177
Scheme 4-3. Synthesis of stannylated terthiophene monomers.....	196
Scheme 5-1. Structures of P1 and P2, along with the investigated processing additives.	204

LIST OF SYMBOLS AND ABBREVIATIONS

ACN	Acetonitrile
AFM	Atomic force microscopy
BHJ	Bulk heterojunction
BTD	2,1,3-Benzothiadiazole
CB	Chorobenzene
CN	1-Chloronaphthalene
CT	Charge transfer
CV	Cyclic voltammetry
D-A	Donor-Acceptor
oDCB	<i>o</i> -Dichlorobenzene
DCM	Dichloromethane
DIO	1,8-Diiodooctane
DMF	Dimethylformamide
DPP	Diketopyrrolopyrrole
dppf	1,1'-diphenylphosphino-ferrocene
DPV	Differential pulse voltammetry
Fc/Fc ⁺	Ferrocene/ferrocenium
FF	Fill factor
GPC	Gel permeation chromatography
iI	Isoindigo
IPCE	Incident photon-to-current efficiency
ITO	Indium tin oxide
J _{sc}	Short-circuit current density

ODT	1,8-Octanedithiol
OFET	Organic field-effect transistor
OPV	Organic photovoltaic
P3HT	Poly(3-hexylthiophene)
PC ₆₁ BM	[6,6]-phenyl-C ₆₁ -butyric acid methyl ester fullerene
PC ₇₁ BM	[6,6]-phenyl-C ₇₁ -butyric acid methyl ester fullerene
PCE	Power conversion efficiency
Pd ₂ (dba) ₃	Tris(dibenzylideneacetone)dipalladium(0)
PDI	Polydispersity index
PEDOT:PSS	Poly(3,4-ethylenedioxythiophene):poly(styrene sulfonate)
SCLC	Space-charge limited-current
TBAPF ₆	Tetrabutylammonium hexafluorophosphate
THF	Tetrahydrofuran
V _{oc}	Open-circuit voltage

SUMMARY

Novel organic conjugated materials have led to new technologies in the field of flexible electronics, with applications in the area of sensors, field effect transistors, or photovoltaic devices. Several material parameters and properties come into play in these devices, including energy of the frontier molecular orbitals, thin film morphology, and charge transport. These properties can be controlled by the chemistry of organic materials, and through processing conditions. In particular, this dissertation focuses on the isoindigo unit as an electron deficient unit to tune polymer light absorption, charge separation, charge transport in the first part of this dissertation, and morphology control in organic photovoltaic (OPV) devices in a subsequent section.

The first part of this dissertation introduces the synthesis and properties of isoindigo-containing polymers as n-type, p-type, or ambipolar semiconductors, and their application in all-polymer or polymer:fullerene blends OPV active layers. It is found that polymers with phenyl linkages along the backbone tend to have broader light absorption than polymers with alternating phenyl-thiophene rings; however, steric hindrance in the former leads to low charge mobilities, and poor device performance. In addition, this section highlights the importance of controlling phase separation in OPV devices by focusing on all-polymer blends, which show large phase separation, and polymer:fullerene blends, where the morphology can be controlled through processing additives generating a two-fold increase in device efficiency. Looking at poly(oligothiophene-isoindigo) polymers as model systems, emphasis is placed on photovoltage losses in these devices due to a decrease in effective energy gap between

the polymers and fullerene as the oligothiophene donating strength is increased, as well as explanation of the device parameters through description of morphology as solubility is varied.

The second portion of this dissertation focuses on solution properties of polymers and their correlation to thin film morphology. A first study investigates the influence of alkyl side chains on solubility, molecular packing, and phase separation in blends of poly(terthiophene-*alt*-isoindigo) with fullerenes. Specifically, as side chains are lengthened, solubility is increased, but with limited impact on the blends morphology. On the other hand increased backbone torsion leads to variations in energy levels, polymer packing and large phase separation in blends with fullerenes. These thermodynamic parameters are to put in perspective with the kinetic control of film formation during the coating process. This is discussed in a second study, which looks at the mechanism of thin film formation when processing additives are used. In particular, this study highlights the interactions that provide a driving force for polymer crystallite formation, depending on the mechanism followed when aliphatic and aromatic additives are used. These observations are then used to predict the morphology in spin-coated thin films.

.

CHAPTER 1. INTRODUCTION

1.1. Organic Electronics Background

Application of organic materials in electronic devices was only made possible through a series of breakthroughs in synthesis and characterization of electrical properties of various π -conjugated materials. Groundbreaking work on oxidation of aniline by Hofmann and Letheby, presumably the first reported syntheses of polyaniline,^{1,2} and on the conductivity of polypyrrole by Dall'Olio *et al.*³ led the field of π -conjugated polymers materials to the discovery of metallic conductivity in iodine-doped polypyrrole by Weiss *et al.*,⁴⁻⁶ and in polyaniline by Buvet *et al.*^{7,8} While the aforementioned polymers were synthesized by oxidative polymerization, the synthesis of low molecular weight linear polyacetylene by Job and Champetier⁹ and the development of coordination polymerization by Karl Ziegler and Giulio Natta, rewarded by a Nobel Prize in 1950, yielded high molecular weight polyacetylene,¹⁰ which was further studied by Berets and Smith. They found that doping polyacetylene by BF_3 enhanced the electrical conductivity of the material by three orders of magnitude.¹¹ Further work on polyacetylene by Ito *et al.*¹² demonstrated a successful synthetic procedure leading to free-standing films, which enabled recognition of conjugated polymers by the 2000 Chemistry Nobel Prize awarded to Alan Heeger, Alan MacDiarmid, and Hideki Shirakawa for their combined work on doped polyacetylene.^{13,14} Since then, focus has shifted towards synthesis of soluble π -conjugated polymers for device fabrication through solution processing. The development of palladium-catalyzed cross coupling reactions, in particular by Richard Heck, Ei-ichi Negishi and Akira Suzuki rewarded by a Nobel Prize in Chemistry in

2010,¹⁵ has enabled the synthesis of a variety of solution processable π -conjugated materials.

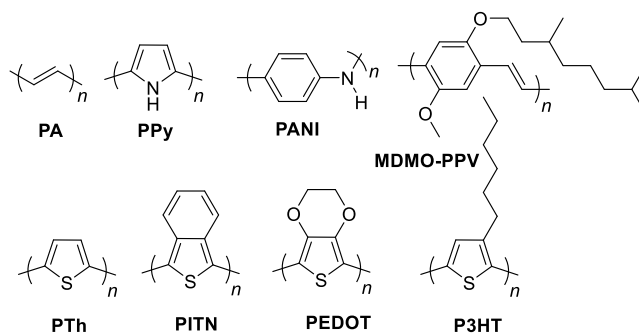


Figure 1-1. Representative repeat unit structures of π -conjugated polymers. PA: polyacetylene, PPy: polypyrrole, PANI: polyaniline, MDMO-PPV: poly[2-methoxy-5-(3',7'-dimethyloctyloxy)-*p*-phenylenevinylene], PTh: polythiophene, PITN: polyisothianaphthalene, PEDOT: poly(3,4-ethylenedioxythiophene), P3HT: poly(3-hexylthiophene).

These materials have primarily been studied as conductive (doped) materials, followed by research on integrating these semiconducting materials in light-weight, flexible organic electronic devices¹⁶⁻¹⁸ such as transistors,¹⁹⁻²³ electrochromic displays,²⁴ light emitting diodes,^{25,26} sensors,²⁷ and organic photovoltaic (OPV) devices.²⁸⁻³¹ In particular, the properties of organic materials in general depend on the molecular structure. As such, the synthesis of novel organic semiconductor structures can be tuned for specific properties and applications.³²⁻³⁴ In addition to molecular structure, the processing conditions can also be used to optimize device fabrication and performance.³⁵ Techniques include: spin coating,³⁶ blade coating,^{37,38} slot-die coating,³⁹ screen printing, ink-jet printing,⁴⁰ and spray coating,⁴¹ some of which are attractive for roll-to-roll processing over large areas.¹⁸ Throughout this dissertation the targeted applications make use of π -conjugated materials in the solid-state, and the following section will introduce

the fundamental concepts behind material design and properties to introduce new students to the field.

1.2. Electronic States in Polymer Semiconductors

The key feature of π -conjugated polymers is the repeat unit made up of alternating single and double bonds, creating a backbone of sp^2 hybridized orbitals with a remaining $2p_z$ orbital perpendicular to the sp^2 plane. The p_z orbitals overlap over consecutive atoms resulting in a manifold of bonding and antibonding π -orbitals. The electrons in the π orbitals are less bound to the nucleus compared to those in σ -orbitals, and give the resulting material its electronic properties. The simplest π -system is ethylene, and as the π -conjugation is extended from butadiene (first optical transition ~ 5.4 eV) to polyacetylene (first optical transition ~ 1.5 eV) energy bands start to form, and the energy gap between the occupied and unoccupied states decreases (Figure 1-2).

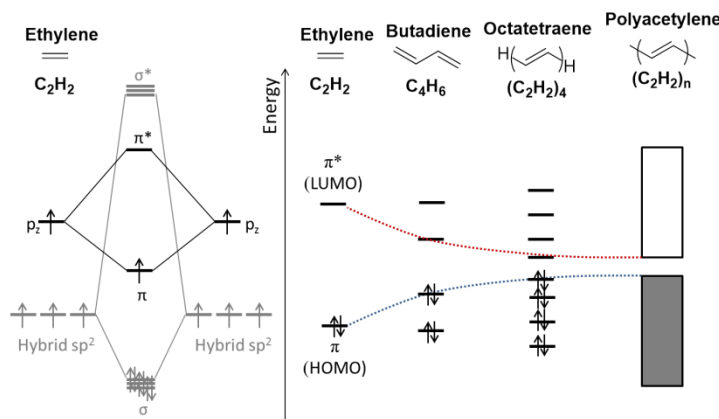


Figure 1-2. Schematic representation of the ethylene orbital and the evolution of the highest occupied molecular orbital (HOMO), lowest unoccupied molecular orbital (LUMO) and energy gap with increasing conjugation. (adapted from ⁴²) Here, electronic states are approximated by one molecular orbital configuration.

Polyacetylene chains can be described by Bloch's theorem, where the repeat unit (here considered to be the unit cell of characteristic length a) is used to describe the electronic structure of the whole polymer chain. Due to periodicity (translation

symmetry) along the chain, the electron density at a given point $\mathbf{r} + j\mathbf{a}$ in the j^{th} unit cell (j being an integer) is equal to the electron density at in point \mathbf{r} of the origin cell. Bloch's theorem leads to equation 1-1:

$$\psi(\mathbf{r} + j\mathbf{a}) = \exp(ikj\mathbf{a})\psi(\mathbf{r}) \quad (1-1)$$

where $\exp(ikj\mathbf{a})$ is the phase factor, and \mathbf{k} is the electron wavevector linked to the wavelength of the electron λ and defined by:

$$\mathbf{k} = \frac{2\pi}{\lambda} \quad (1-2)$$

$$\lambda = \frac{h}{mv} \quad (1-3)$$

where h is Planck's constant, m is the electron mass and v is the electron velocity. This shows that the wavevector \mathbf{k} is related to the electron momentum $\hbar\mathbf{k}$, which in turn is related to the electron energy. The band structure $E(\mathbf{k})$ (plot of energy E versus wavevector of the electron \mathbf{k}) of polyacetylene can then be derived from Bloch's theorem, and is shown in Figure 1-3.

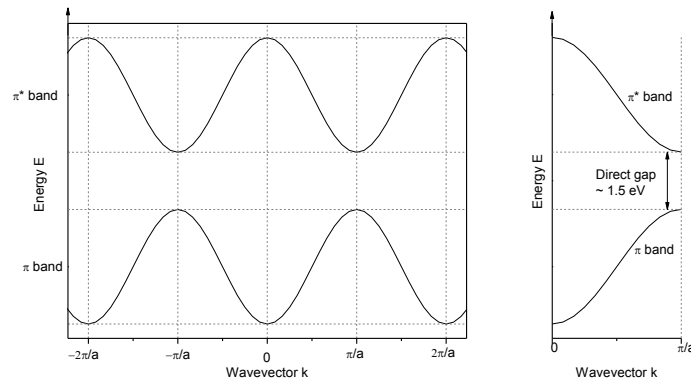


Figure 1-3. Periodicity of the band energy as a function of wavevector (or location in direct space) and the reduction of the full description of the polymer chain in half of the Brillouin zone.

The fact that the function $E(\mathbf{k})$ is periodic (of periodicity $2\pi/a$) and even leads to the electronic description of the full polymer chain by the first half of the Brillouin zone. In

polyacetylene, if all the bond lengths were equal (one-dimensional periodic lattice) the π and π^* bands would become degenerate leading to a zero-gap or metallic material. However, such a one-dimensional system is unstable, and the polymer backbone distorts to lower the system's energy, leading to bond length alternation between single and double bonds. This distortion, called Peierl's distortion, leads to the opening of the energy gap E_g between the occupied and unoccupied π -orbitals ($0 < E_g \leq 2\text{eV}$), and to the semiconducting properties of the π -conjugated polymer. This suggests that lowering the bond length alternation will increase the metallic character of the polymer by lowering the energy gap. The energy gap of π -conjugated polymers is the transition from the ground state to the lowest excited states. These states are defined as weighted linear combinations of electronic configurations (i.e. a set of molecular orbitals); however they are usually described by only one configuration as shown in Figure 1-3. The electronic structure of π -conjugated materials can then be described in terms of the density of states to illustrate the concepts of ionization potential (energy required to remove an electron from a species to the vacuum level: $A \rightarrow A^+ + e^-$, positive value), electron affinity (energy released when an species captures an electron from the vacuum level: $A + e^- \rightarrow A^-$, conventionally taken as a positive value) and energy gap, and understand some of the underlying fundamental principles that guide experimental determination of these parameters (Figure 1-4).

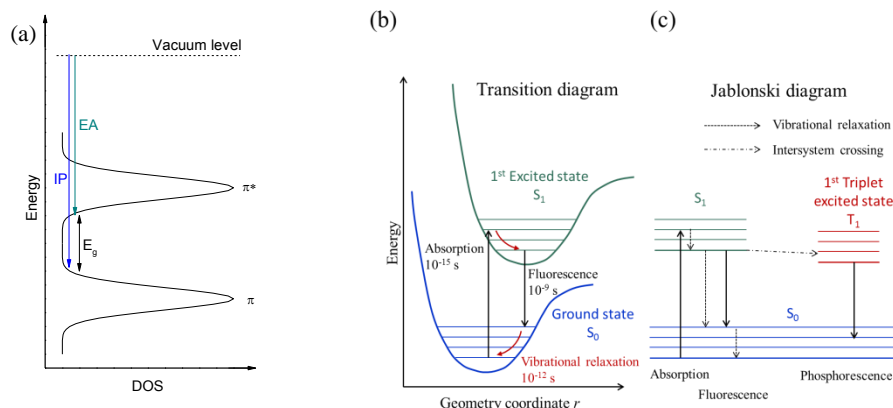


Figure 1-4. (a) Density of states, (b) transition and (c) Jablonski diagram. These define ionization potential (IP) linked to the ground state S_0 , electron affinity (EA), both defined against a vacuum energy level, and fundamental energy gap (E_g). Transitions between states can be further defined highlighting the photophysical processes that can occur involving ground S_0 and excited S_1 states, which further take into account exciton binding energy. (adapted from ⁴²)

While the concepts highlighted in this paragraph are common to all π -conjugated polymers, *trans*-polyacetylene holds a particular place due to its degenerate ground state (possibility to form solitons), which is not the case for any other π -conjugated polymer. In some other polymer systems, such as polyarylenes (poly(*para*-phenylene) PPP or poly(*para*-phenylenevinylene) PPV) and polyheterocycles in general, the backbone can take an aromatic form or a quinoidal form as described in Figure 1-5, which have different energy and geometry (possibility to form polarons and bipolarons, not solitons). In π -conjugated systems, the ground state can be approximated by the bonding-antibonding pattern of the aromatic structure, while the first excited state can be approximated by the quinoidal structure. The previously discussed strategy of tuning the energy gap by reducing bond-length alternation can then be described in terms of lowering the energy of the quinoidal form. This was highlighted by the work of Wudl *et al.*⁴³ with the design of poly(isothianaphthalene) (PITN), where the contribution of resonance forms led to a decrease of the bond length alternation compared to

polythiophene.⁴⁴ In summary, electronic transitions are a function of the structure of the π -conjugated material, which allows for material design and tunability of the resulting properties.

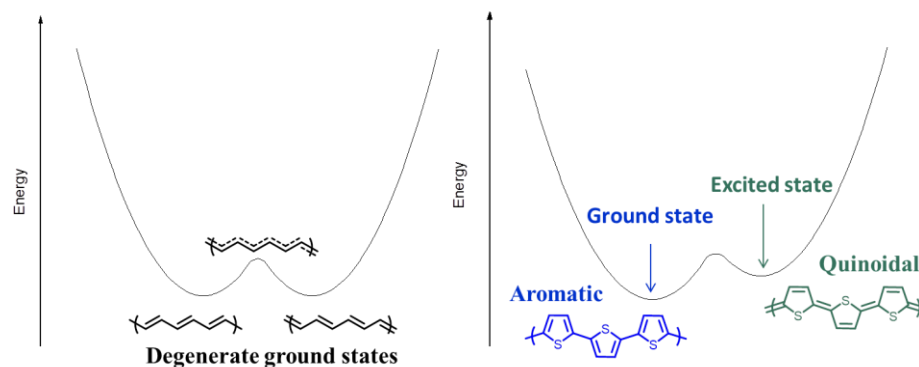


Figure 1-5. Ground and excited state energies, and how they relate to the bonding/anti-bonding pattern along the polymer backbone in the case of trans-polyacetylene and polythiophene. (adapted from ⁴⁵5)

1.3. Property Changes after Transition from Solutions to Thin Films

Original work on insoluble, infusible materials such as polyacetylene, poly(*p*-phenylenevinylene) and polythiophene⁴⁶ has driven interest for solution processable polymers. Indeed, the rigidity and polar/ π -interactions⁴⁷ (which are Van der Waals dipole-induced dipole London interactions, often simplified to π - π interactions or π -stacking⁴⁸) of the aromatic rings along the backbone hinders solubility of these materials. To increase conformational disorder, flexible alkyl chains were appended to the conjugated backbone and induced solubility of high molecular polymers in chlorinated and aromatic solvents, as demonstrated in poly(3-alkylthiophenes).⁴⁹⁻⁵³ The Yokozawa⁵⁴ and McCullough⁵⁵⁻⁵⁷ groups demonstrated this concept independently through the development of what may be the best known π -conjugated polymer to-date, regioregular poly(3-hexylthiophene) P3HT.

In this work, applications of π -conjugated polymers in devices involve transition of the same polymeric material from solution state to solid state (Figure 1-6), as opposed to electrochemical polymerization for instance. Molecular building blocks and solubilizing side chains are first selected to form extended conjugated systems, based on previously reported structure-property relationships. However, the transition from isolated molecular systems to supramolecular arrangements leads to complex systems, where the behavior of the resulting materials and devices cannot be easily predicted.^{58,59} In particular, as molecules transition from the liquid phase to the solid phase, they undergo supramolecular arrangements driven by intermolecular interactions, such as π /polar interactions, which can lead to local defects. These defects can be controlled through processing, which influences the domain sizes, orientation, and grain boundaries.

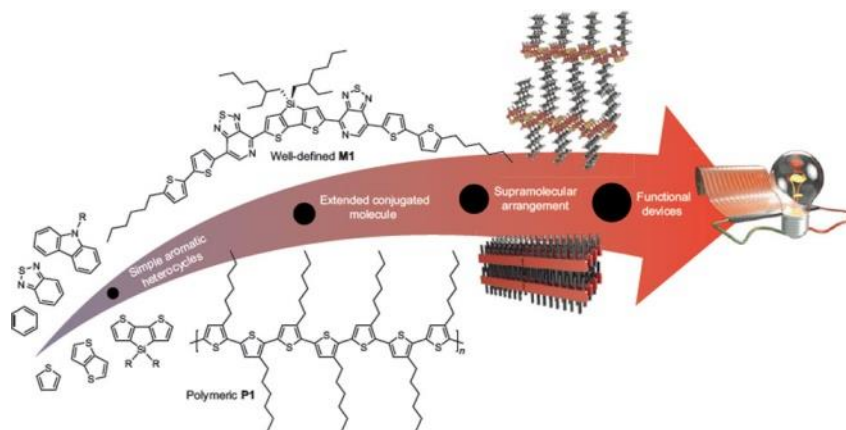


Figure 1-6. Transitions from molecular structure to macroscopic properties. (adapted from ⁶⁰)

In films of π -conjugated small molecules, pentacene or rubrene for instance, intermolecular interactions dictating packing in thin films is governed by polar/ π -interactions, first explained by Hunter and Sanders through electronic density considerations alone.⁴⁷ Intermolecular interactions lead to either parallel-displaced π -stacks (which could lead to J-aggregates with a bathochromic or red shifted absorption

compared to the monomer) or edge-to-face stacks, and face-to-face π -stacks (or H-aggregates with a hypsochromic or blue shifted absorption compared to the monomer) in certain cases (Figure 1-7a).^{48,61} Sherrill further included London dispersion forces to model π -interactions,⁶² and Figure 1-7b illustrates the influence of both electrostatic interactions (electronic density) and dispersion interactions on overall attraction of substituted benzene dimers relative to unsubstituted dimers. By modifying the molecular structure, via donor-acceptor effects for examples, various aggregate structures can be formed, with subsequent differences in their properties.^{63,64}

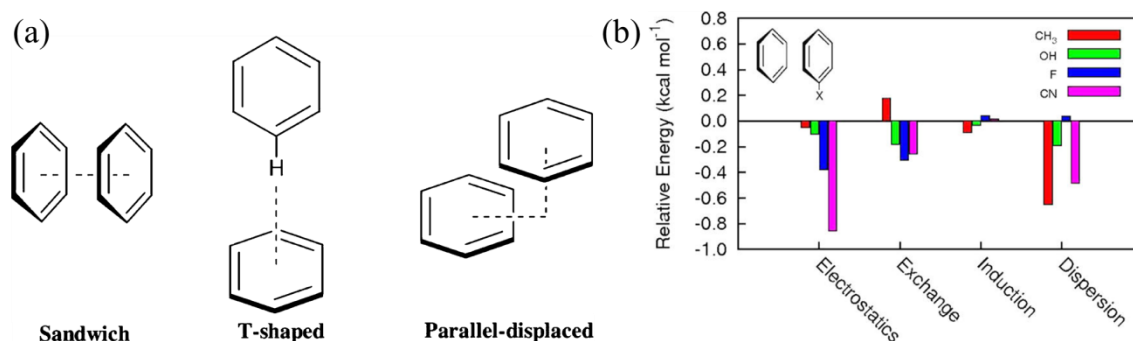


Figure 1-7. (a) Overview of possible π - π geometric configurations of the benzene dimer, and (b) impact of interaction energy components on the energy of substituted benzene sandwiches relative to a benzene dimer. (adapted from ⁶²)

This view can be extended to polymeric systems, where crystalline and amorphous domains also need to be taken into account. Using poly(fluorene) as a model system, the background on π -conjugated polymer films will be explained based on the work of Beljonne *et al.*⁶⁵ On the molecular level, modeling of fluorene oligomers substituted with methyl groups shows similar trends in interchain interactions to the small molecule systems, with a compromise between steric hindrance and attractive quadrupolar interactions. Oligofluorenes can form flipped stacks (fluorene rings are superimposed but the methyl groups point in opposite directions) or shifted stacks (fluorene rings are

shifted by a half period relative to one another). In these two-layer stacks, the interchain distance is 0.37 nm and the torsion angle between fluorene rings is 40° . As the number of polymer chains in the stack is increased, the polymer chains planarize (torsion angle around 30°) but the polymer chains move further away from one another (intermolecular distance around 0.45 nm). To further describe the behavior of *n*-octyl substituted poly(fluorene), octyl groups were appended to the model oligomers and are shown to orient in two different ways: roughly parallel (Y-shaped) or perpendicular (T-shaped) to the oligofluorene backbone. Calculations conducted on both structures indicate that the octyl groups reorient to a Y-shaped arrangement, regardless of their initial conformation. The choice of side-chains has been showed to have a direct effect on polymer interactions and packing, and, furthermore, the effect of polymer packing on macroscopic properties is clearly observed in the photoluminescence spectra of the thin film versus solution (Figure 1-8).

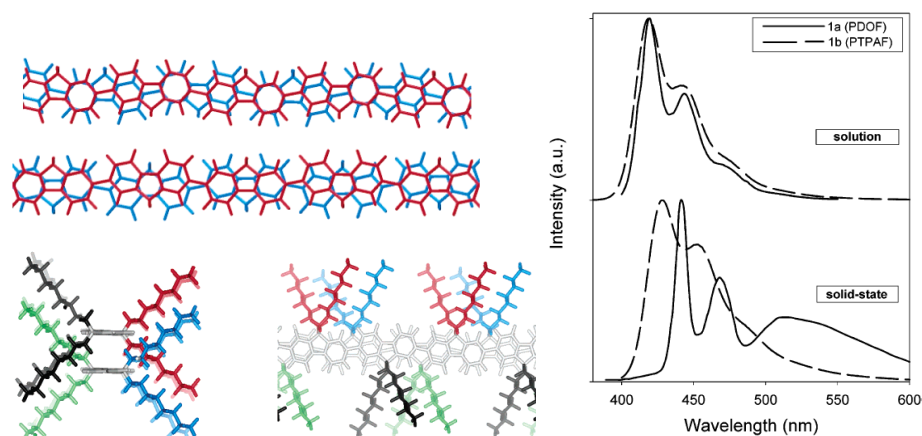


Figure 1-8. Self-organization of fluorene oligomers in flipped and shifted stacks, as well as side-chain organization into a Y-shape. The change in organization from solution to film leads to changes in the optoelectronic properties via UV-vis-NIR (solid line). (adapted from ⁶⁶)

Planarization of the polymer chains in the solid state leads to a red-shift (lower energy) of the absorption, and the formation of π -aggregated species in the solid state leads to the appearance of a new aggregation band in the UV-vis-NIR spectra. These two effects were demonstrated by Kim and Swager by using compression on Langmuir films of amphiphilic polymers illustrated in Figure 1-9. In particular, polymer 2 shows a blue shift in absorption as the layer is compressed, most likely due to decreased π -conjugation length as the film is forced to occupy a decreasing area. This illustrates the principle of absorption red-shift with backbone planarity, i.e. increased orbital overlap or π -conjugation length. Furthermore, polymer 4 in a Langmuir film has a distinct new absorption band compared to the solution absorption spectrum, which is due to π - π interactions promoted in the Langmuir films compared to solutions.

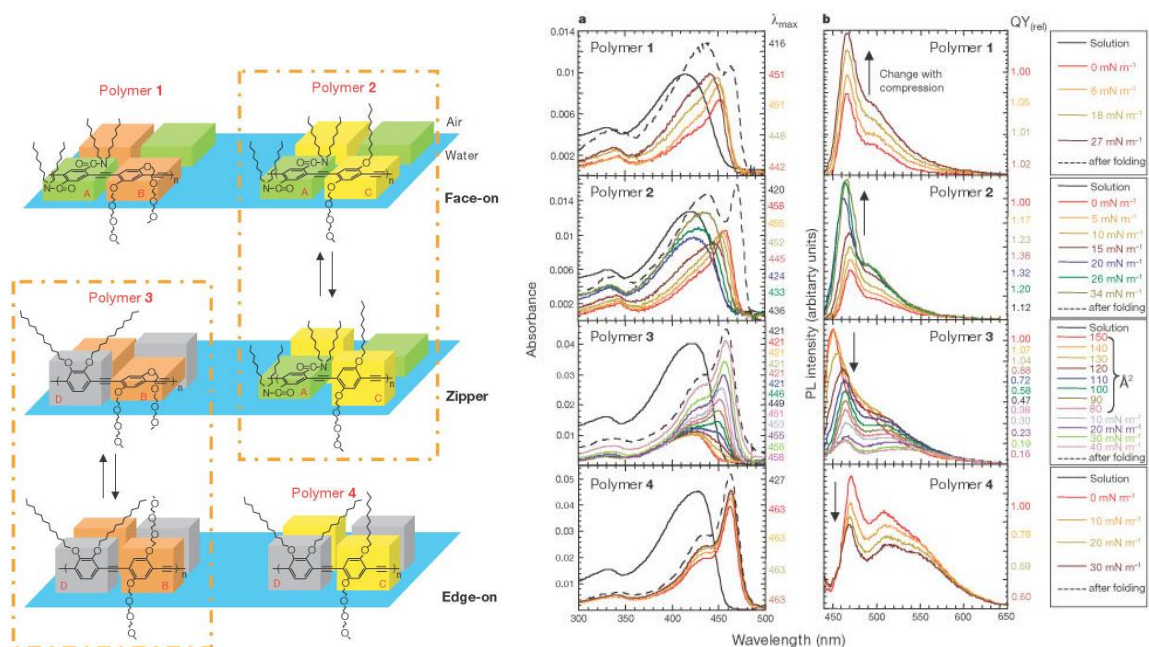


Figure 1-9. Impact of polymer packing on optoelectronic properties, in particular UV-vis-NIR absorption. (adapted from ⁶⁷)

Beyond packing at the nanoscopic scale, the high molecular weights of polymers lead to an intrinsic degree of disorder in these semicrystalline systems, with the presence of

crystalline and amorphous domains. The degree of disorder in thin films of π -conjugated polymers can be translated to traps in the density of states (DOS) diagram and contributes to energetic disorder in these materials. For instance, the crystalline domains of a polymer film present less structural defects than the amorphous regions, which increase energetic disorder and the number of shallow energy traps as shown schematically in the DOS diagram in Figure 1-10. This leads to the formation of an energy landscape through which charge carriers can be transported under an electric field.

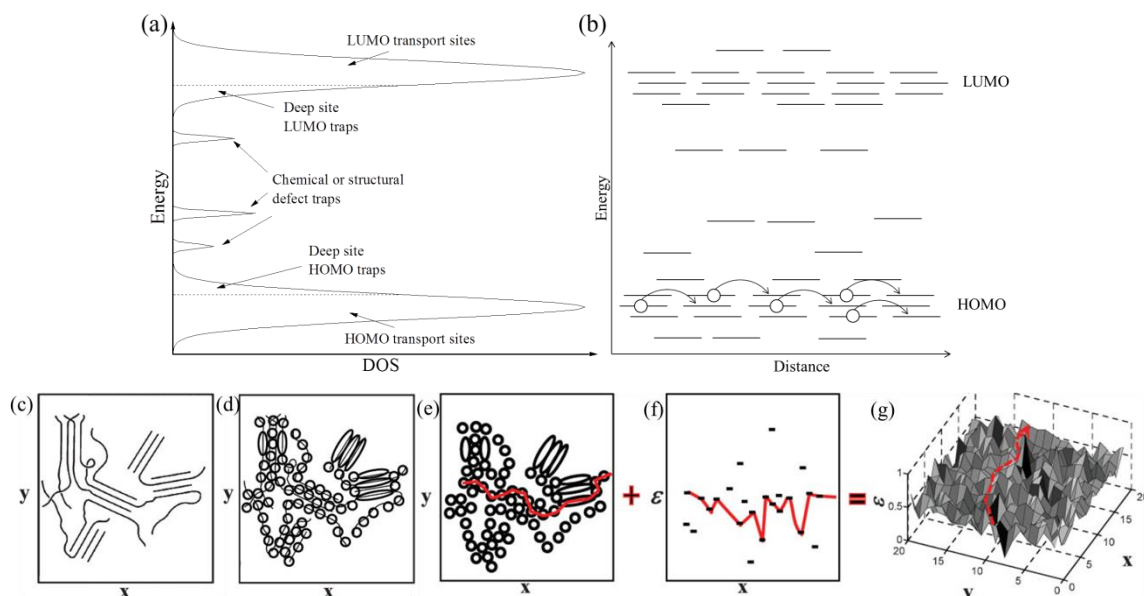


Figure 1-10. Schematic DOS diagram of π -conjugated polymers (a) and its impact on charge carrier transport (b). Structural illustration of energetic disorder in polymer films (c), where conjugation lengths can be described with varying units (d) and the position (e) and energetic (f) disorder leading to the energy landscape for charge carrier transport (g). (adapted from ⁶⁸)

1.4. Comparison of Inorganic and Organic Semiconductors

Several material parameters lead to large variations of properties when comparing organic and inorganic semiconductors: processability, nature of the energy gap, low dielectric constant and large charge-geometry coupling, and high degree of disorder. The parameters are discussed in the context of photovoltaic devices in this paragraph.

First of all, inorganic materials need to be highly ordered in order to achieve their potential in electronic devices, which leads to high production costs and strict substrate requirements (typically require lattice matching of the semiconductor with the substrate and are typically not compatible with flexible substrates).⁶⁹ By comparison, organic semiconductors are typically polycrystalline or even amorphous and can be processed using less expensive methods compared to epitaxial growth of silicon crystals for instance.

Furthermore, when considering materials for solar harvesting for example, light absorption is a function of the nature of the energy gap. As discussed in section 1.2.1., organic semiconductors exhibit a direct energy gap, which sets them apart from silicon-based semiconductors, which have an indirect band gap. This has a direct impact on the material's absorption coefficient and the device thickness. For instance, crystalline silicon has an absorption coefficient of 10^5 cm^{-1} at around 2 eV above its band edge leading to photovoltaic devices based on silicon to require 100 μm thick active layers⁷⁰ while organic materials, with an absorption coefficient of 10^5 cm^{-1} at 0.25 eV above the band edge for MDMO-PPV (Figure 1-1) for instance, typically rely on 100 nm thick films to balance light absorption and resistance within the active layer.⁷¹ However, inorganic semiconductors do not always have indirect band gaps. For instance GaAs or InSb (group III-V compounds) also have a direct band gap,⁷² which enables the use of thin-film light absorbing layers and leads to flexible solar cells.⁶⁹

Following absorption of a photon, free charges need to be created in order to generate photocurrent in solar cells, which is a function of the dielectric constant of the materials with inorganic materials typically exhibiting higher dielectric constants ϵ_r than their

organic counterparts. For instance, the bulk averaged dielectric constant in crystalline silicon is around 12 (at 1 kHz) versus 3-4 (at 100 kHz)^{73,74} in π -conjugated polymers. In both materials, optical excitation will lead to the formation of excitons (coulombically bound electron-hole pairs, i.e. charge-less particles that can diffuse). However the difference in dielectric constant implies that excitation of crystalline silicon leads to the formation of Wannier excitons, which are only weakly bound (~ 10 meV) with an average radius (~ 100 Å) larger than the lattice spacing. By comparison, excitation of organic materials leads to formation of Frenkel excitons, which have binding energies on the order of 500 meV with an average radius of 10 Å.^{75,76} The low dielectric constant in organic materials, combined with the correlation between electrons and geometrical rearrangements, means that absorption of a photon at room temperature by π -conjugated materials does not lead to free charge carriers, contrary to inorganic materials. This defines two energy gaps in π -conjugated materials: the fundamental energy gap (linked to the IP and EA) and the optical energy gap (linked to exciton formation after photoexcitation) as described in Figure 1-11.

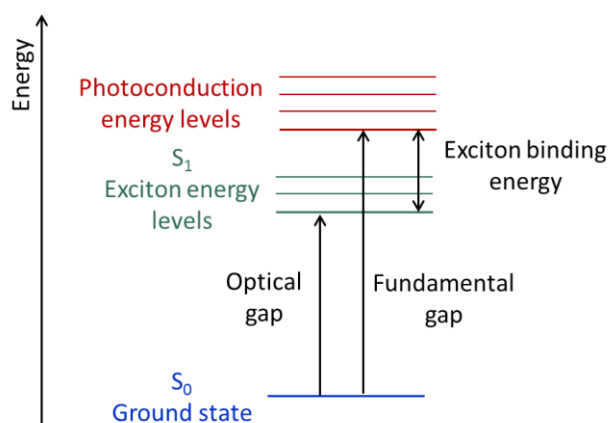


Figure 1-11. Frenkel exciton formation after photoexcitation leading to the formation of an optical energy gap. (adapted from ⁷⁷)

The coupling between electronic structure and geometric relaxation also impacts charge transport, where transport in inorganic materials can be typically modelled using band transport whereas transport in disordered organic materials, containing defects and traps, is typically described by hopping transport. By comparison with crystalline silicon, organic materials are highly disordered leading to the formation of shallow charge traps as discussed in the previous section. The rotational degrees of freedom leading to static disorder and dynamic disorder in loosely assembled supramolecular structures can be structurally influenced (ladder-type structures, regioregularity, secondary interactions, etc.) in order to reduce energetic disorder in the semiconducting film. These fundamental factors explain the difference in device physics involved in organic electronics compared to the well-known physics in inorganic silicon-based devices.

1.5. Organic Electronics: Operating Principles

1.5.1. Organic Field Effect Transistors (OFET)

Field effect transistors (FETs) use an electric field to modulate the flow of charge carriers in a semiconductor material, and are employed in logic circuits. Light-weight organic FETs (OFETs) have the potential to be used in flexible displays based on electrophoretic ink,⁷⁸ in organic light emitting diode (OLED) displays,⁷⁹ or in bioelectronics for sensing, delivery, and stimulation.⁸⁰ OFETs also have an opportunity to impact transistor fabrication throughput thanks to solution, roll-to-roll processability of π -conjugated materials.

Figure 1-13 shows the operating processes in OFETs, and highlights the analogy to water faucets: the current (charge flow) between the source and the drain is modulated by a gate (which determines the charge carrier concentration), just like water flow is

modulated by a valve. The OFET device can be viewed as a capacitor with one plate being the gate electrode and the other plate is the conducting channel, which sandwich a dielectric layer.

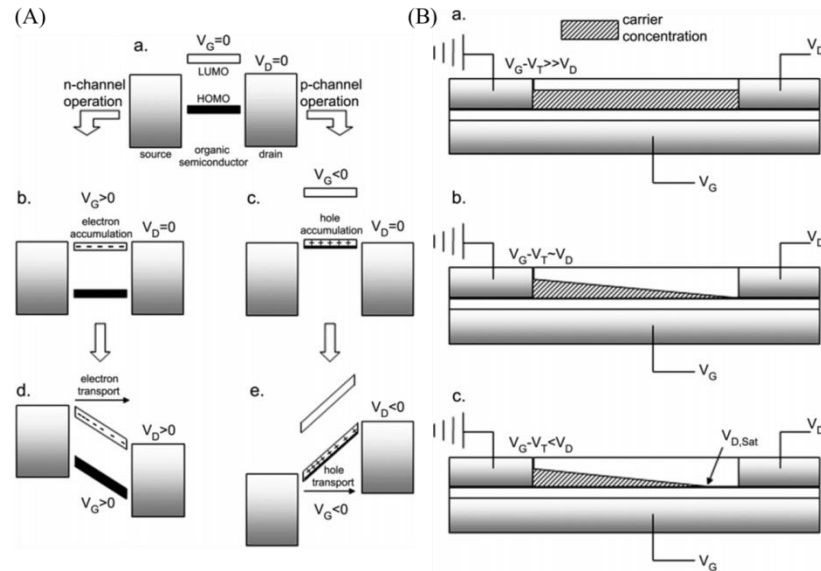


Figure 1-12. (A) (a) Example of the mode of operation of an OFET for (b,d) n- and (c, e) p-type transport, along with (B) charge carrier concentration in the semiconductor layer as a function of drain voltage (a) below the threshold voltage V_T , (b) in the linear regime, and (c) in the saturation regime. (adapted from ⁸¹)

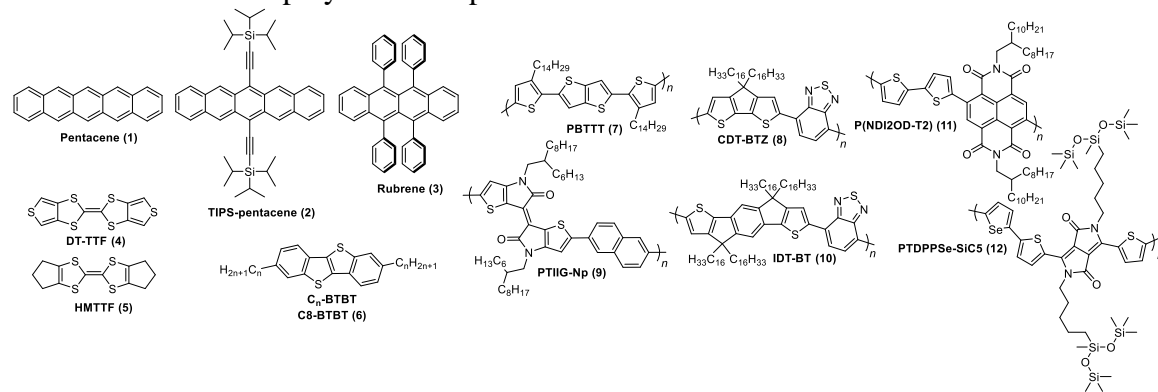
The nature of charge carriers (hole or electron) in the device is a function of the gate voltage, and the example of hole carriers will be used to illustrate OFET operating principles. If a negative bias is applied between the gate and the source (V_G), two inversion layers grow within the dielectric film, and lead to accumulation of hole carriers in the semiconductor layer. If a potential is then applied between the drain and the source (V_{SD} or V_D), the charges are then able to flow through the semiconductor. While keeping V_G constant, at low V_D , the hole carrier concentration is uniform in the semiconductor and the current between the source and drain (I_{SD} or I_D) is linear with V_D . As V_D is increased a linear gradient of hole carrier concentration forms in the semiconductor, and reaches a saturation regime when the region near the drain electrode is depleted of hole

carriers. When this regime is reached, further increase to V_D does not lead to additional current.

The figure of merit for FETs is the charge carrier mobility μ , which is measured to be around $1 \text{ cm}^2 \text{ V}^{-1} \text{ s}^{-1}$ for amorphous silicon and above $20 \text{ cm}^2 \text{ V}^{-1} \text{ s}^{-1}$ in the case of polycrystalline silicon.⁷⁸ In comparison, mobility in organic FETs (OFETs) based on solution processed π -conjugated materials now reach $25 \text{ cm}^2 \text{ V}^{-1} \text{ s}^{-1}$ using a benzotheno[3,2-b][1]benzothiophene small molecule,³⁶ and $10 \text{ cm}^2 \text{ V}^{-1} \text{ s}^{-1}$ in polymer-based thin films.^{23,82,83} The reported mobility values should be taken with a grain of salt, as the structure factor of the device (channel length and width) and the measurement parameters (device hysteresis, regime chosen to extract mobility value) may have an impact on the mobility values calculated based on current-voltage measurements.^{78,81} As shown in Table 1-1, state of the art OFET devices have traditional relied on small molecule semiconductors, which tend to exhibit higher charge carrier mobilities. Some examples of π -conjugated small molecule-based materials that have performed well in OFET devices are acene-based materials such as rubrene or triisopropyl-silylethynyl substituted pentacene (TIPS-pentacene), fused thiophene-based small molecules such as benzothenobenzothiophene (BTBT), or dithiophene- tetrathiafulvalene (DT-TTF) and hexamethylene-TTF (HMTTF). The design of small molecules for OFETs relies on the molecular structure and the intermolecular packing in order to control the reorganization energy (structural relaxation) and the transfer integral (electronic coupling). For more detail on charge transfer and the hopping regime, the reader is directed to Beljonne *et al.*⁶⁵ However, these concepts are not as straight-forward in polymer-based OFETs. Some of the state-of-the art polymer OFETs are based on polythiophenes such as P3HT,

poly(3,3'-dialkyl-quaterthiophene) (PQT) or n poly(2,5-bis(3-alkylthiophen-2-yl)thieno(3,2-b)thiophene) (PBTtT), and alternating polymer structures such as copolymers of naphthalenediimide and bithiophene (PNDI2OD-T2) and copolymers of cyclopentadithiophene or indacenodithiophene and benzothiadiazole (CDT-BTZ or IDT-BT).

Table 1-1. Structure and OFET hole (μ_h) and electron (μ_e) mobility of solution-processed small-molecules and polymers as reported in the literature.



Small molecules			Hole transporting polymer			Electron/hole transporting polymer			
	μ_h ($\text{cm}^2 \text{V}^{-1} \text{s}^{-1}$)			μ_h ($\text{cm}^2 \text{V}^{-1} \text{s}^{-1}$)			μ_h ($\text{cm}^2 \text{V}^{-1} \text{s}^{-1}$)	μ_e ($\text{cm}^2 \text{V}^{-1} \text{s}^{-1}$)	
2	11	37	7	1.1	84,85	11		0.8	86
4	3.6	87	8	5.5	88	12	5.7	1.8	89
5	10	90	9	12	82				
6	16-25	21,36	10	3.6	91				

The semicrystallinity of the polymer films makes the determination of structure-property relationships in these systems more difficult, but some guidelines have been uncovered as described in a review by Sirringhaus.⁷⁸ The first factor in polymer design for high mobility OFETs appears to be a coplanar backbone to reduce the contribution of backbone torsion to the reorganization energy for charge transfer. Secondly, a high degree of chain alignment with the long axis of the polymer backbone being orthogonal

to the source-drain contacts (regardless of the orientation of the backbone, edge-on or face-on, versus the substrate) seems to be a required condition for high charge carrier transport, as illustrated by increasing molecular weight and investigating polymer packing via grazing-incidence wide-angle X-rays scattering (GIWAXS). Finally, the choice of the solubilizing side-chain is crucial to dictate the arrangement of the conjugated backbone, hence controlling the transfer integral for charge transfer. Some questions remain unanswered, in particular regarding the importance of interchain interactions at the molecular level and as to the necessity for the polymer backbones to be mainly edge-on or face-on relative to the dielectric layer. It is also crucial to keep in mind differences in charge carrier transport in polymer aggregates versus amorphous regions^{91,92} and at the dielectric/semiconductor interface versus in the bulk of the semiconductor layer.⁹³

1.5.2. Organic Photovoltaics (OPVs) Background

Crystalline silicon-based inorganic cells make up 85% of the market for solar energy thanks to efficiencies ranging from 14 to 25%.⁹⁴ However, due to their high manufacturing costs and limited modularity,⁷⁰ crystalline silicon-based cells do not yet provide an alternative to fossil fuels for electricity production. One strategy to reduce the cost of electricity produced by photovoltaic devices is the use of organic semiconductors that can be vacuum deposited at low-temperatures (small molecules) or solution-processed (molecules and polymers) over large areas. In particular, organic photovoltaics (OPVs) can lead to applications where low-cost, light-weight, and flexible devices are required. In this work, the focus will be on polymer-based solar cells, as opposed to small

molecule solar cells, as they allow for continuous solution processing on an industrial scale, using roll-to-roll fabrication for example.⁹⁵

OPVs had their first breakthrough with the seminal work of Tang who introduced the concept of using two different organic materials in a bilayer organic solar cell and reported a power conversion efficiency (PCE) of 1% in 1986.⁹⁶ Since then, interest has sparked for OPVs and although efficiencies in large area modules still do not allow for commercial applications, significant research on organic materials and device engineering has led to a jump in efficiencies from 1% to 12% for solid-state solar cells in both single-junction and tandem devices.^{97,98}

While the physics involved in inorganic cells rely on the intensively studied p-n junction, the understanding of fundamental processes in organic cells requires further research. For instance, a key difference in the processes taking place in organic compared to inorganic solar cells is the nature of the optically excited states,⁹⁹ as previously discussed. In inorganic photovoltaic devices, free carriers are generated when light hits the inorganic semiconductor; in OPVs, coulombically bound excitons are generated, which require a blend of two materials to separate them into free charges. This led to the second breakthrough in OPV research, which involved the discovery of photoinduced ultra-fast charge transfer from poly(3-octylthiophene) to C60 fullerene.^{28,100} This difference in generated charge species between inorganic and organic PV devices leads to changes in the device operating principles as highlighted in the following paragraphs.

1.5.3. OPV Device Operating Principles

As light hits the donor:acceptor active layer, photons are absorbed and the photon energy promotes electrons from the ground state to the excited state of the donor (or the

acceptor) as illustrated in Figure 1-14 (i). This creates a coulombically bound electron-hole pair, or exciton, with binding energies on the order of 500 meV because of the material's low dielectric constant,⁷⁵ to be compared to a few meV in the case of inorganic materials. As free carriers cannot be generated solely based on thermal energy at room temperature (25 meV), the exciton needs a thermodynamic driving force for dissociation at the donor-acceptor interface (ii), and once at the interface the exciton goes through a charge transfer state (iii) before the charges can be fully separated into free carriers thanks to the energy offset (iv). These free carriers then drift to their respective electrodes as a result of the built-in voltage, and electrons and holes are collected at the cathode and anode respectively generating photocurrent (v). It is important to note that around 2/3 of free charges are created within 100 fs in mixed domains of donor and acceptor materials, followed by charge separation of excitons after diffusion to a donor:acceptor mixed phase.^{101,102}

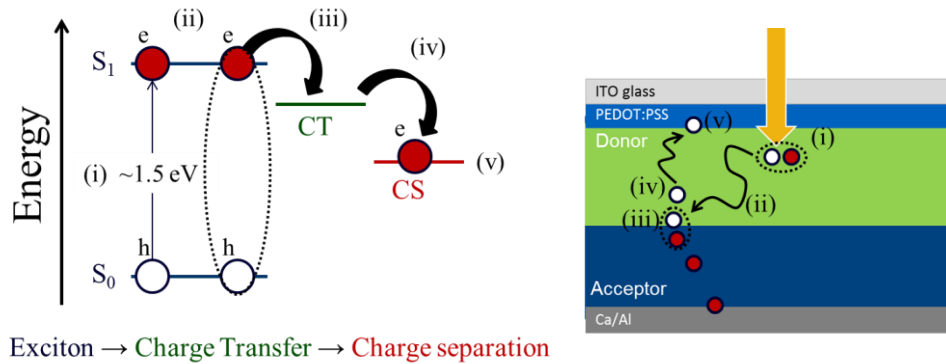


Figure 1-13. Schematic illustration of the processes involved in current generation in an OPV device. (i) Exciton creation following photon absorption, (ii) exciton diffusion, (iii) charge transfer at donor:acceptor interface, (iv) charge separation and transport, and (v) charge collection.

From these five processes some material design guidelines can be outlined based on structure-property relationships in terms of electronic and geometric parameters. The

processes relying on the energy levels of the materials are photon absorption, charge transfer and separation, and charge injection. Charge carrier diffusion to a donor/acceptor interface and charge carrier transport to the electrodes are closely linked to the geometry of the material and the active layer morphology. However, these electronic and structural factors are closely linked in organic materials and it can be challenging to separate their effects on the various processes.

In terms of photon absorption, the energy difference between the ground and excited state for the donor should be around 1.5 eV to absorb low energy photons, and maintain high orbital overlap to increase oscillator strength (increases extinction coefficient). The acceptor's absorption should also complement that of the donor to take advantage of the width of the solar spectrum. In early OPV devices, light absorption relied on P3HT and a fullerene derivative (PC₆₁BM) that only absorbed photons between 350 nm and 650 nm, with PC₆₁BM contributing only weakly to the total absorbance.¹⁰³ Several approaches have been developed to increase the breadth of light absorption in OPV blends: decreasing the energy gap of the polymer donor and decreasing the energy gap in fullerene derivatives by lower their symmetry,¹⁰⁴ or by using non-fullerene acceptors.¹⁰⁵

However, a balance needs to be struck between light absorption by lowering the energy gap through lowering of the excited state energy and charge separation at a donor/acceptor interface. Indeed, in donor (polymer)/acceptor junctions, photo-induced charge separation is usually assumed to proceed via formation of a columbically-bound, localized excited state (Frenkel exciton) on the conjugated polymer, which requires a driving force for exciton dissociation into free charges. The energy offset between the excited states of the donor and acceptor provides a thermodynamic driving force for this

charge dissociation.¹⁰⁶ However, the transition between Frenkel exciton and charge separated states is still under debate but all models involve manifold of charge transfer (CT) states, arising from various configurations of CT excitons.¹⁰⁶⁻¹¹⁴ At the molecular level, CT excitons can be thought of as intermediates between Wannier excitons and Frenkel excitons as shown in Figure 1-15a. At a polymer:fullerene interface, a Frenkel exciton (EX) can lead to the formation of inter-donor excitons (DD) along with interfacial excitons with electron density on the neighboring fullerene cages (CT). Figure 1-15b further highlights differences at polymer:polymer interfaces compared to polymer:fullerene interfaces, where charges in CT states at the polymer:fullerene interface (A, B) appear to be more separated (~ 10 Å) compared to polymer:polymer interfaces (~ 7 Å) (C, D).

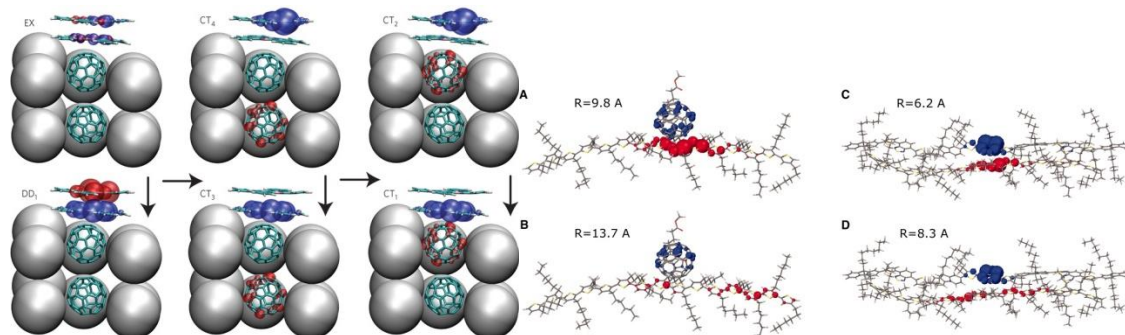
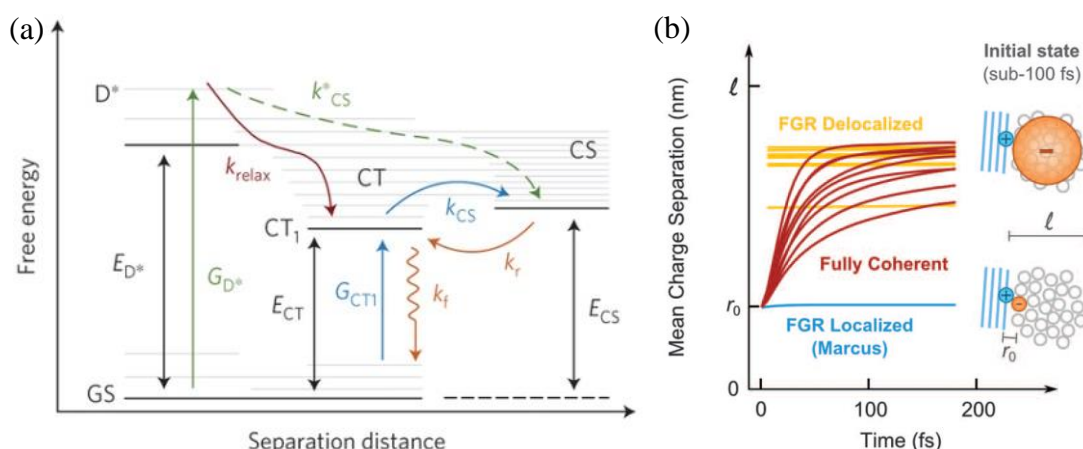


Figure 1-14. Molecular pictures of CT states obtained from quantum chemical calculations. (adapted from^{108,109})

Figure 1-16a gives an overview of a possible model for charge dissociation at the donor/acceptor interface. Photoexcitation leads to the formation of a donor excited state D^* from the ground state GS. This excited state can then directly go to a charge separated state CS or relax into the CT manifold to CT_1 before the charges can separate. Previous results seemed to indicate that generation of free charge carriers had to originate from higher energy, more delocalized CT states rather than “relaxed” CT states (comparable to

CT₁ in Figure 1-16a). However, work by Gélinas *et al.*¹¹³ and Vandewal *et al.*¹¹⁴ points to the fact that the CT states are all at thermal equilibrium and that no excess energy contributed by “hot” CT states is required for efficient charge separation. Rather than excess energy, delocalized, band-like states are cited as being a requirement for charge separation. Figure 1-15b illustrates the need for charge delocalization within fullerene aggregates at times scales on the order of a couple 100 fs for charge separation (yellow and red lines). By comparison, localized acceptor sites (blue line) lead to tightly bound CT states, which do not dissociate at 100 fs time scales.



1-15. Processes involved in charge separation. (a) absorption from the ground state (GS) to the donor excited state (D*) followed by either direct charge separation with a rate of k_{CS}^* or relax to the lowest energy charge transfer state (CT₁) then charge separate; (b) Driving force for charge separation through delocalization into large fullerene aggregates (yellow and red) and hindered charge separation in the absence of delocalization (blue). (adapted from ^{113,114})

Eventually, charge collection at the electrodes relies on Ohmic contact between the active layer and the electrodes by tuning the electrode work function to allow charge injection with limited carrier recombination at the interface.^{115,116} Furthermore, light reflection at the back contact also enables further light absorption within the active layer.

In addition to this paragraph, further information on OPV device operating principles can also be found in recent reviews by Heeger¹⁰¹ and Dou *et al.*¹¹⁷

These processes then dictate the photocurrent generation in OPV devices and can be correlated to device parameters as described in current density-voltage (J-V) curves shown in Figure 1-17. The performance of the solar cell is described by extracting the open circuit voltage (V_{oc}), short circuit current (J_{sc}) and fill factor (FF) from the J-V curve to calculate the power conversion efficiency (PCE) of the device. These parameters are interrelated through the power density, given by the product of the current density and voltage. Indeed, the PCE is the ratio of maximum power output to power input as given by Equation 1-5, and as such OPV devices operate at their maximum efficiency when the circuit resistivity is such that P_{max} is reached.

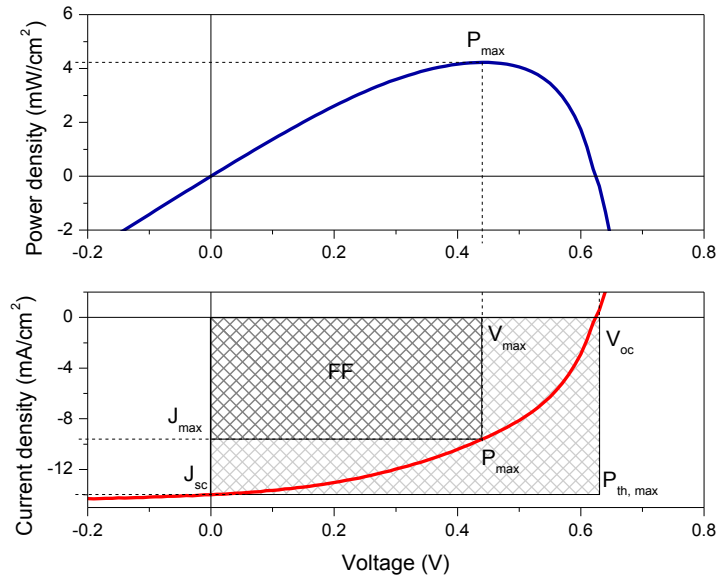


Figure 1-16. Representative J-V curve for a solar cell under illumination and the corresponding power density-voltage curve, which defines V_{oc} , J_{sc} , FF and P_{max} .

The FF is a way to characterize the “ideality” of the device by taking into account the series and shunt resistances. The fill factor is the ratio of the maximum power density

output by the device over the theoretical maximum power density if the device followed an ideal diode behavior:

$$FF = \frac{V_{max}J_{max}}{V_{oc}J_{sc}} \quad (1-4)$$

By replacing the expression of the output power density P_{out} into the power conversion efficiency, equation 1-5 is obtained:

$$PCE = \frac{P_{out}}{P_{in}} = \frac{V_{max}J_{max}}{P_{in}} = \frac{V_{oc}J_{sc}FF}{P_{in}} \quad (1-5)$$

1.5.4. The Bulk-Heterojunction (BHJ)

After photoexcitation, the formed exciton needs to diffuse to a donor:acceptor interface to dissociate into free-charges. The diffusion length L is a function of the diffusion coefficient D ($\text{cm}^2 \text{s}^{-1}$) and the exciton lifetime τ (s):

$$L = \sqrt{D\tau} \quad (1-6)$$

Based on previous work in donor/acceptor bilayers, the diffusion length was determined to be around 5-10 nm in these disordered organic semiconductors. In order to promote free charge generation, the bulk-heterojunction (BHJ) concept was introduced, which allowed more intimate mixing of the donor and acceptor components and increased interfacial area.¹¹⁸⁻¹²⁰ However, the interface between donor/acceptor should not be viewed as a sharp boundary but rather as a mixed phase of donor and acceptor molecules as illustrated in Figure 1-18.¹²¹ Moreover, it is currently accepted that BHJ layers are made up of at least 3 phases: a donor-rich phase, an acceptor-rich phase and a mixed phase, which also provide an energetic drive for charge separation as modeled by Burke *et al.*¹⁰²



Figure 1-17. Simulated domain boundaries for BHJ solar cell devices. (adapted from ¹²¹)

State of the art BHJ devices rely on polymer:fullerene systems, but small molecule:fullerene blends or even polymer:polymer blends are now reaching similar efficiencies. Ternary blends and tandem devices are also researched in order to increase the maximum power of the device.¹²²⁻¹²⁴ From Figure 1-19, no obvious structure-relationship can be outlined, although some trends stand out. First of all, all polymer structures are composed of phenyl-thienyl or thienyl-thienyl linkages, no phenyl-phenyl linkages, and secondly, most structures contain rigid, fused heterocycles.

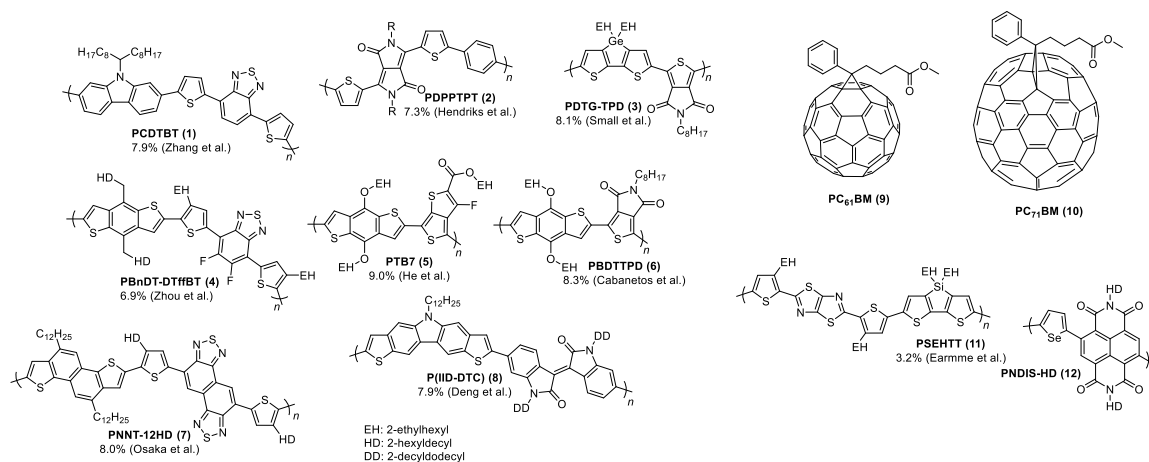


Figure 1-18. State of the art polymer:fullerene or polymer:polymer BHJ devices.

1.5.5. Space-Charge Limited-Current (SCLC) Mobility

Space-charge limited-current (SCLC) modeling is a useful tool to quantify charge carrier mobility in the vertical direction, across the film thickness, as an alternative to OFETs, which measure charge carrier mobility in the horizontal direction. As shown in Figure 1-20, in diode-like devices for SCLC modeling, one type of charge carrier is

probed and the type of charges in the device is dictated by the work function of the charge injecting (which needs to be an Ohmic contact, i.e. not injection-limited) and collecting electrodes. At low voltage bias (Figure 1-20a), the number of charge carriers in the devices does not impact the internal field, and the current follows Ohm's law. As the voltage bias is increased (Figure 1-20b), the density of charge carriers in the device increases, leading to the formation of a space-charge region, which impacts the internal electric fields and limits the current out of the device (SCLC regime).¹²⁵

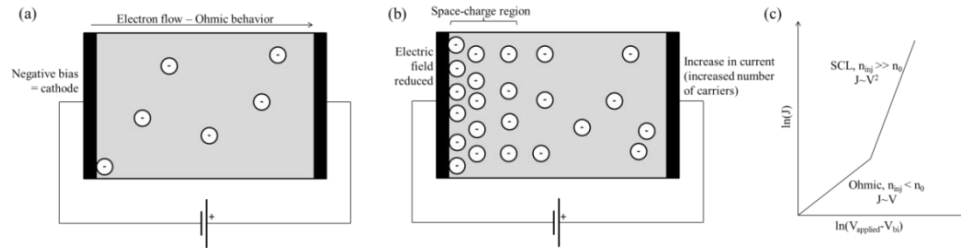


Figure 1-19. Scheme of ohmic electron transport (a), trap-free space-charge limited transport when the number of injected carriers n_{inj} is higher than a threshold n_0 (b), and the corresponding J-V curve (c). Charge balance in this example of electron-only devices is accomplished by stationary positive charges, which are not collected by the electrodes.

The current density J in the trap-free space-charge limited-current region is described by Child's law:

$$J = \frac{9}{8} \epsilon_r \epsilon_0 \mu \frac{V^2}{L^3} \quad (1-7)$$

where ϵ_r is the relative permittivity of the material, ϵ_0 is the permittivity of free space, μ is the charge carrier mobility, V is the effective voltage (i.e. applied voltage V_{applied} minus the built-in voltage V_{bi}) and L is the semiconductor layer thickness.¹²⁶

When shallow traps are present, which is generally the case in disordered organic materials, the charge carrier mobility and current density become field-dependent (strong

electric fields lower the trap barrier height, also known as the Poole-Frenkel effect)¹²⁷ and the Mott-Gurney equation takes into account this field-dependence:

$$\mu = \mu_0 \exp(\gamma \sqrt{E}) \quad (1-8)$$

$$J = \frac{9}{8} \epsilon_r \epsilon_0 \mu_0 \exp(0.891 \gamma \sqrt{E}) \frac{V^2}{L^3} \quad (1-9)$$

where μ_0 is the zero-field mobility, γ represents the field dependence parameter and E is the electric field through the semiconductor (also described by voltage over thickness).¹²⁸

For hole carrier mobility, high work function materials such as molybdenum trioxide (MoO_3) or gold have been used as hole injecting and electron blocking layers respectively;¹²⁹ whereas calcium or lithium fluoride and aluminum have been used as electron injecting and hole blocking layers respectively.¹³⁰

Based on the highlighted material and morphology requirements for optimal device operation, several paths to understand material design to match the desired electronic properties and morphology are described in the following sections.

1.6. Design of Conjugated Polymers for Frontier Orbital Energy and Morphology Control

As shown in the previous paragraph, organic semiconductors can be structurally tuned in order to achieve the targeted properties, which is one of their benefits over inorganic materials. Control of the electron density along with structural rigidity and functionalization for solubility (Figure 1-21) are extremely valuable handles on the structure-property relationships in order to achieve the desired macroscopic effect, may it be for energy harvesting or logic circuits. The design of polymer structures for organic electronics is described in this section.

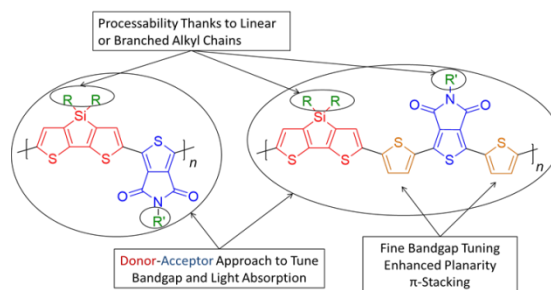


Figure 1-20. General structure of conjugated polymers for solution processing. (adapted from ¹³¹)

1.6.1. The Donor-Acceptor Approach

Originally, energy gap engineering involved stabilization of the quinoidal structure in order to reduce bond length alternation and the energy gap in π -conjugated polymers. This approach to reduce the energy gap in conjugated materials has been extended using the donor-acceptor (D-A) concept, first introduced by Havinga *et al.* in 1993, which led to 0.5-1.4 eV energy gaps in polysquaraines and polycroconaines depending on the electron richness of the donor unit.¹³² When considering that the first optical transition occurs from the ground to the excited state and can be approximated by a HOMO-LUMO transition, which ties into the geometric difference between the aromatic and quinoidal structures, the D-A approach relies on the fact that the HOMO of the donor moiety and the LUMO of the acceptor moiety largely dictate the HOMO and LUMO in the resulting D-A alternating copolymer (Figure 1-22). The strength of the D-A concept resides in the ease of control over frontier energy levels and energy gap, along with the endless library of electron-rich and electron-poor conjugated units, which enable the design of numerous polymers of targeted properties to fit a particular device application.

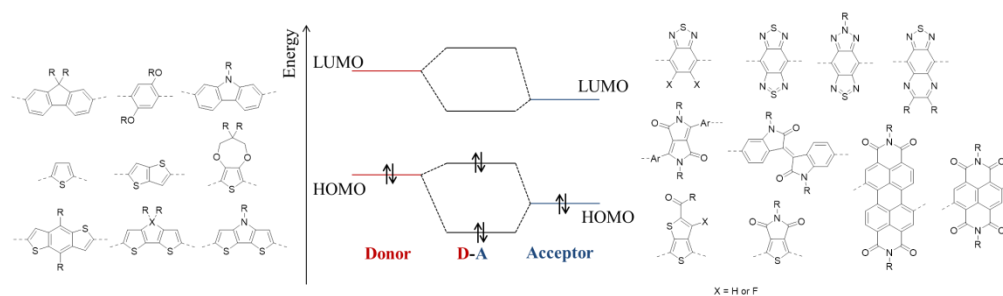


Figure 1-21. The donor-acceptor concept for energy gap control and examples of electron-rich and electron-deficient units. (adapted from ⁴²)

Electron-rich units are typically based on benzene, thiophene, furan and pyrrole rings, which can be further fused with other ring to yield rigidity and possibility for further functionalization. For instance, dioxothiophenes have added electron-richness compared to thiophenes due to the electron-donating oxygens on the ring and provide a handle for functionalization away from the polymer backbone, which can prevent twisting and lead to increased interchain interactions. Electron-deficient units are based on thiadiazole rings,¹³³ amide/imide functionalities¹³⁴⁻¹³⁶, which can be further functionalized using fluorine,^{137,138} as π - or σ - electron-withdrawing groups in a wide range of structures. Material design in D-A polymers hence needs to take into account aromaticity and bond length alternation, rigidity and planarity, functionalization, and interchain interactions. In particular, the rigidity of the polymer backbone can be used to maximize π -conjugation and reduce the energy gap by constructing ladder-type polymers.^{139,140} The D-A concept has led to the synthesis of a conjugated polymer with an optical energy gap of 0.5 V by alternating a strong donor dithieno[3,2-b:2',3'-d]pyrrole with a strong acceptor benzo[1,2-c;4,5-c']bis[1,2,5]thiadiazole.¹⁴¹ For a thorough review of energy gap engineering via D-A concepts, the reader is directed to the work of van Mullekom *et al.*¹⁴²

Of particular interest for OPV devices, the light absorption properties of these D-A polymers are broadened compared to homopolymers, due to dual band absorption in D-A

polymers.³² The dual band absorption in D-A polymers is thought to arise from contributions to light absorption from an intramolecular charge transfer state and a π - π^* transition at higher energies.³² Reviews by Zhou *et al.*³⁴ and Li¹⁴³ provide extensive insight into polymer design as donor materials for BHJ solar cells, and a latter portion of this introduction will describe material design as it pertains to BHJ morphology.

1.6.2. The Isoindigo Unit: An Electron Deficient Synthon

As seen in the previous section, organic dyes with amide/imide functionalities have been used as building blocks and incorporated into π -conjugated backbones to tune optoelectronic properties and processability of the resulting polymers.¹³⁴ Structures such as 3,6-diaryl-2,5-dihydro-pyrrolo[3,4-c]pyrrole-1,4-dione, or diketopyrrolopyrrole (DPP)¹⁴⁴ were used as pigments in paints (pigment red 254 or Ferrari red produced by Ciba),¹⁴⁵ before being applied to materials for organic electronics.¹⁴⁶ Isoindigo is another one of these dye-based building blocks (Figure 1-23). Isoindigo can be synthesized from isatin, which can be found in many plants, such as *Isatis tinctoria*, *Calanthe discolor*, and *Couroupita guianensis*, and oxindole,¹⁴⁷ which is derived from isatin. The use of this isomer of the indigo dye in materials for organic electronics was first reported in a patent by Ciba¹⁴⁸ before being introduced to the open literature by Mei *et al.*¹⁴⁹

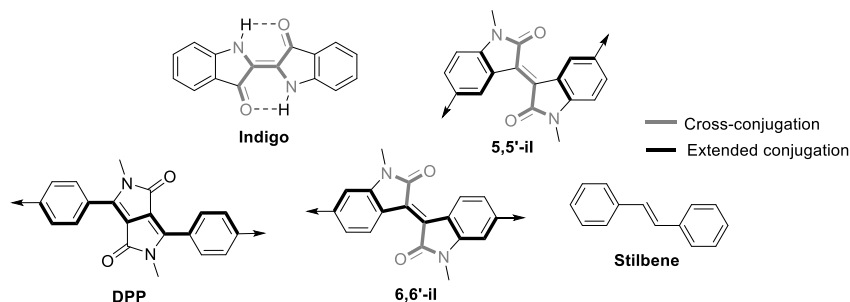


Figure 1-22. Structures of the indigo, diketopyrrolopyrrole (DPP) and isoindigo (il) dyes and structural similarities and differences.

In the indigo molecule, the chromophore has been identified to be the carbon-carbon double bond substituted with two electron-withdrawing carbonyl groups and two electron-donating amine groups in a cross-conjugated, H-chromophore arrangement.¹⁵⁰ While the structure of indigo prevents long-range conjugation through the central double bond, substitution along the 6,6'-axis of isoindigo allows for extended conjugation while the bis-amide functionality in isoindigo also leads to cross-conjugation. As shown in Figure 1-24, isoindigo is electronically similar to stilbene in its HOMO level with extended conjugation on the phenyl ring and (E)-1,1'-dimethyl-[3,3'-bipyrrolylidene]-2,2'-(1H,1'H)-dione (BPD) in its LUMO level.¹⁵¹

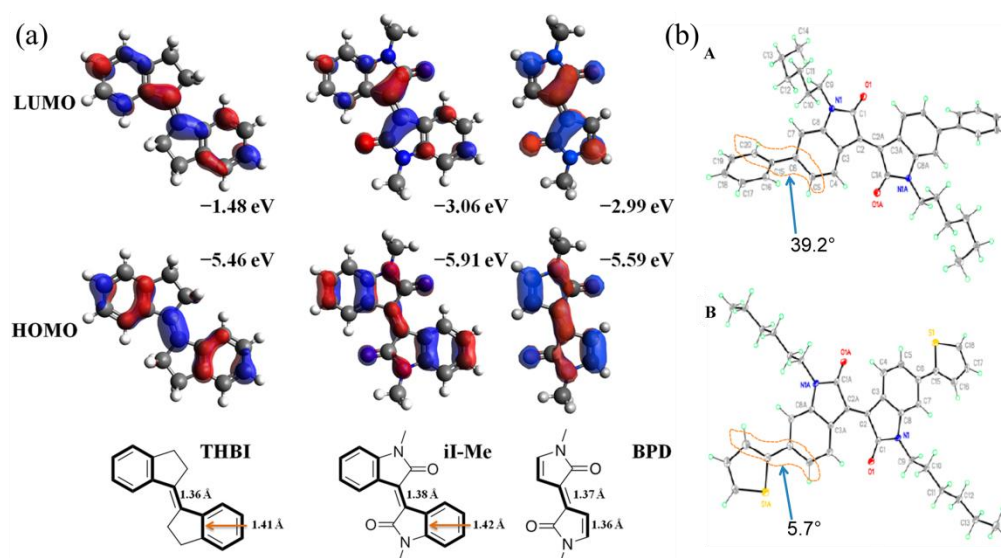
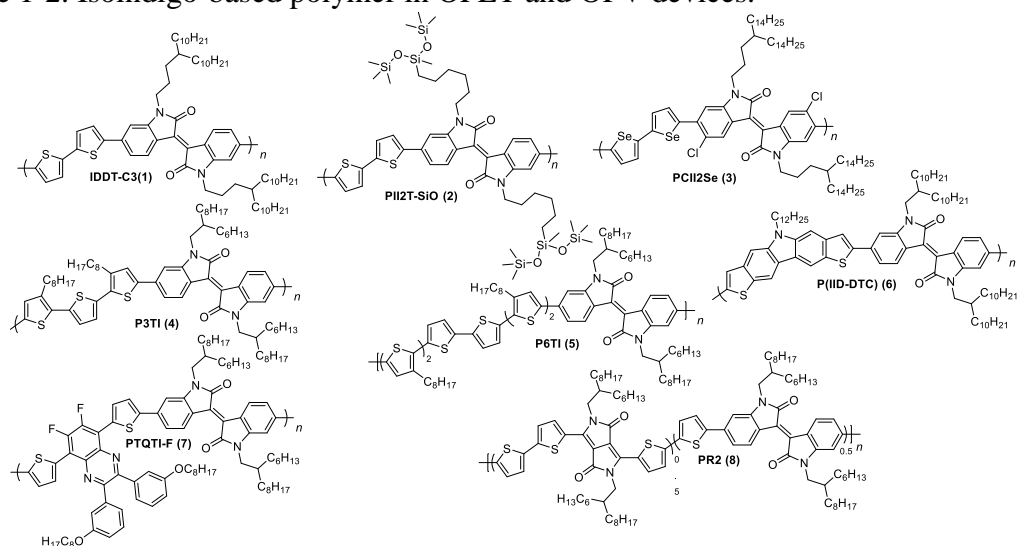


Figure 1-23. (a) HOMO and LUMO levels computed at the B3LYP/6-31G(d) level on isoindigo model compounds describing electron density, and (b) crystal structures of (A) phenyl- and (B) thienyl-flanked 6,6'-(N,N'-dihexyl)isoindigo. (adapted from ¹⁵¹)

Structurally, the hydrogens on the phenyl rings of isoindigo give rise to steric hindrance with neighboring rings, where crystal structures have shown that the dihedral angle between phenyl groups and isoindigo is around 40° (similar to PFO) and 6° between thienyl groups and isoindigo. These parameters have guided the design of

isoindigo-based materials for organic electronics, with examples of high performing materials given in Figure 1-25. The isoindigo electron-deficient unit has been widely used in organic electronics as covered in reviews by Stalder *et al.*,¹⁵² Wang *et al.*,¹⁵³ Lei *et al.*,¹⁵⁴ and Peng *et al.*,¹⁵⁵ and the reader is referred to these publications for a more thorough review of isoindigo-based materials.

Table 1-2. Isoindigo-based polymer in OFET and OPV devices.



OFET	μ_h ($\text{cm}^2 \text{V}^{-1} \text{s}^{-1}$)	V_T (V)	μ_e ($\text{cm}^2 \text{V}^{-1} \text{s}^{-1}$)	V_T (V)	I_{on}/I_{off}	Ref.
1	3.0	-2			$>10^6$	156
2	2.0	-3			$>10^6$	157
3	0.9	-68	0.6	27	10^5 - 10^6	158

OPV	Solvent	V_{oc} (V)	J_{sc} (mAcm^{-2})	FF	PCE (%)	Ref.
4:PC ₇₁ BM	<i>o</i> DCB/DIO	0.70	13.1	0.69	6.3	159,160
5:PC ₇₁ BM	<i>o</i> DCB/CN	0.72	15.7	0.64	7.1	161
6:PC ₇₁ BM	<i>o</i> DCB	0.79	14.6	0.62	6.9	162
7:PC ₆₁ BM	<i>o</i> DCB/DIO	0.93	12.6	0.54	6.3	163
8:PC ₇₁ BM	CB/DIO	0.77	13.5	0.58	6.0	164

Recent work on isoindigo derivatives involves modifying the functionality of the phenyl rings with pyridine, furan¹⁶⁵ or thiophene rings (thienoisindigo), which has proven successful in the design of polymers for OFETs,^{82,166,167} or by extending the

isoindigo structure¹⁶⁸ and investigating bay-annulated isoindigo.¹⁶⁹ Further work could look into extending the rigidity of isoindigo through fused rings to the phenyl rings.

1.7. From Molecules to Thin Film: Morphology in Solid State Organic Semiconductors

The previous paragraph discussed material properties based on their molecular formula alone without taking into account material interactions in the solid state, which makes molecular design a challenging task. This was touched on in section 1.2.2., and the following section describes the transition from solution to thin film, along with post-processing treatments, in order to control solid state morphology and understand its influence on the final material properties.

As described in the previous paragraphs, π -conjugated polymers have the distinct possibility to be solution processed to form the active film in organic electronic devices, while maintaining mechanical integrity for flexible devices^{170,171} (although this can also be achieved using π -conjugated small molecules,¹⁷² inorganic semiconductors such as amorphous silicon, or conducting composites).^{16,17,173,174} Their tunable structure thus allows more control over the processing conditions, by modifying the chemistry of the side-chains for example,¹⁷⁵ and the resulting thin film morphology. The device performance and properties at the macroscopic scale are due to structural effects over a range of length scales, extending from the molecular scale to the microscopic scale as shown in Figure 1-25.

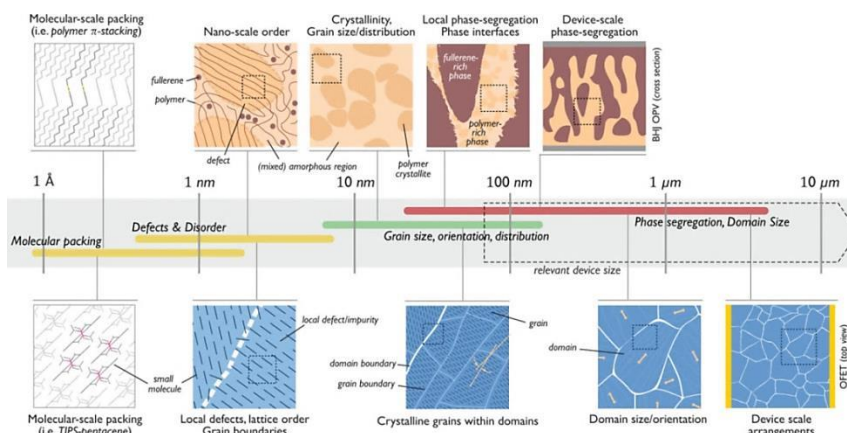


Figure 1-24. Morphological considerations ranging from the molecular scale to the micrometer scale. (adapted from ¹⁷⁶)

The morphology over the various length scales is a result of both thermodynamic (material interactions) and kinetic (film drying time: solvent vapor pressure, deposition conditions) parameters, as most of the solution processing conditions lead to metastable morphologies due to relatively fast drying times (10-300 s depending on solvent system and processing method).^{177,178}

1.7.1. Solution Processing Techniques

The work in this dissertation only makes use of drop coating or spin coating to cast the active layer. However, prior to reviewing the fundamental thermodynamic aspects behind film formation from solution, a brief overview of possible solution processing techniques is given. The choice of the processing technique is crucial from the standpoint of technology development for organic electronics as it will define the throughput and thus the cost of the manufactured devices. Historically, the goal for solution processed organic electronic devices was for roll-to-roll, continuous manufacturing using shearing processes, such as slot-die coating.¹⁷⁹ Other continuous printing processes include spray-coating, and inkjet printing. On the research scale, efforts are focused on spin coating as the processing method for the active layer in organic electronics, as is the case for the

work in this thesis. While spin coating provides uniform films, it is not amenable to continuous processing and more than 90% of the coating solution is wasted. Furthermore even at the research scale, large area spin coating presents some technological challenges.¹⁸⁰ For these reasons, the drive is now to translate the guidelines established using spin coating to other processing techniques, which could also provide control of polymer chain alignment to promote crystalline regions, reduce grain boundaries between neighboring crystalline domains, and dictate orientation alignment and improve intermolecular orbital overlap.¹⁸¹ Blade coating stands out as a processing technique bridging laboratory scale devices and roll-to-roll manufacturing.^{38,182} Ultimately, slot-die coating appears as the targeted solution processing technique as it provide continuous processing with little material waste and control of the film homogeneity.^{39,183}

Other types of solution processing techniques include spray deposition,¹⁸⁴ and inkjet printing.⁴⁰ The main advantage of inkjet printing is the capability for patterning with micrometer resolution, which makes it ideal for multicolor patterning for displays, and for screening device fabrication conditions. However, the resulting films have low thickness uniformity and solvent evaporation may clog the nozzle, which limits the solvent options accessible for this technique.

Compared to vacuum deposition or physical vapor deposition of small molecule thin films, solution-based processing presents challenges for multiple layer deposition, which can be solved by using orthogonal solvents or by solubility modification of the underlying layer.¹⁸⁵

1.7.2. Thermodynamics of Mixing and Solubility Parameters

Solution processed materials rely on mixed solvent:polymer systems, and even ternary phase systems. In order to understand the driving forces behind morphology control, thermodynamic principles relevant to understanding the processes involved in film formation will be recalled. The basis for these principles can also be found in the dissertation of Dr. Kenneth Graham.¹³⁰ The free energy change for a physical process such as mixing involves both an enthalpic (through the internal energy of the system U) and entropic term S :

$$\Delta F = \Delta U - T\Delta S \quad (1-10)$$

$$S = k\ln(\Omega) \quad (1-11)$$

The entropic term is related to the probability of molecular configurations (Ω), which is in turn a function of volume occupied a given molecule (number of lattice sites times the volume fraction of the compound). Entropy of mixing per lattice site ($\Delta\bar{S}_{mix}$) is always positive (i.e. negative contribution to the total free energy), which means that mixing is always favored by entropy:

$$\Delta\bar{S}_{mix} = -k\left(\frac{\phi_A}{N_A}\ln(\phi_A) + \frac{\phi_B}{N_B}\ln(\phi_B)\right) \quad (1-12)$$

where $\phi_{A/B}$ is the fraction composition of A/B and $N_{A/B}$ is the number of sites occupied by A/B. The change in internal energy of the system is a function of the Flory-Huggins interaction parameter χ , which describes the interactions between the two components A and B:

$$\Delta\bar{U}_{mix} = \chi\phi_A\phi_B kT \quad (1-13)$$

Overall the free energy change (per lattice site) in the system will thus be:

$$\Delta\bar{F}_{mix} = kT\left(\frac{\phi_A}{N_A}\ln(\phi_A) + \frac{\phi_B}{N_B}\ln(\phi_B) + \chi\phi_A\phi_B\right) \quad (1-14)$$

The sign of the change in free energy then depends on the magnitude on the magnitude of the Flory interaction parameter. This brings up a discussion on Flory-Huggins interaction parameter. As suggested by the name, the χ parameter depends on the interaction energy between the two components as defined in equation 1-15 in the case of non-polar compounds:

$$\chi = \frac{V_{ref}}{kT} (\delta_A - \delta_B)^2 \quad (1-15)$$

where $\delta_{A/B}$ are the Hildebrand solubility parameters for A/B and V_{ref} is a reference volume (often 100 cm³). The Hildebrand parameters can be calculated from surface energy γ (determination using contact angle measurements) using equation 1-16:

$$\delta_i = K\sqrt{\gamma_i} \quad (1-16)$$

where K is a proportionality constant, which has been reported to be $116 \times 10^3 \text{ m}^{-1/2}$ for a DPP-based conjugated polymer and PC₇₁BM.¹⁸⁶ As such, if the two components have similar solubility parameters (decreasing χ), the blend miscibility increases. According to equation 1-15, χ is positive, but the interaction parameter can become negative when specific interactions such as dipole-dipole or hydrogen bonding interactions are present (not included in the Hildebrand solubility parameter), and thus results in fully miscible systems. The next question then is what dictates the solubility parameter? Very generally, the chemical structure of the compounds will determine the solubility parameters, leading back to the fact that structural similarity favors mixing. This was further proposed by Hansen through the Hansen solubility parameters, which translate the chemical structure into a set of separate values for dispersion, dipolar and hydrogen bonding interactions based on physical properties, as described by Dr. Kenneth Graham.¹³⁰ These values can then be used to predict miscibility of two components¹⁸⁷ and to define new solvent

systems in order to replace the typically used chlorinated solvents for processing of organic semiconductors.¹⁸⁸

Particular mention must be made on the thermodynamics of (amorphous) polymer mixing as in this case the entropy increase is small (large values for the number of occupied sites $N_{A/B}$, which is linked to the degree of polymerization) and the enthalpic term is crucial in determining the thermodynamic result of the mixing process. Furthermore, in the case of polymer solutions, the polymer-solvent interaction parameter is the sum of an enthalpic component and an entropic component, leading to equation 1-17:

$$\chi = \frac{V_s}{kT} (\delta_p - \delta_s)^2 + 0.34 \quad (1-17)$$

where V_s is the molar volume of the solvent, δ_p and δ_s are the Hildebrand parameters for the polymer and solvent, and 0.34 is an empirical factor.^{189,190} This factor is most likely an entropic parameter to take into account the difference in free volume (or density) between a low molecular weight solvent (with a higher free volume) and a polymer.¹⁹¹ In the case of highly crystalline polymers, the heat of fusion needs to be included; however this will not be considered here as most of the donor-acceptor systems are only weakly crystalline (semi-crystalline with low degree of order).

1.7.3. Single Component Films: Morphological Considerations and Transport Properties in Polymer FETs

Noriega et al. have highlighted interconnected paracrystalline domains in polymer-based FETs as a key factor to high charge carrier mobility (rather than long range order seen in semi-crystalline polymers like P3HT),⁹² in addition to backbone rigidity and planarity leading to decreased reorganization energy and increase in the transfer integral

at the molecular level.⁷⁸ Structurally, backbone rigidity and planarity also tend to lead to low polymer solubilities due to increased polymer-polymer interactions relative to polymer-solvent interactions. The following paragraph discusses the design of polymer structures to balance solubility and ordering in thin film, along with kinetic factors leading to order in polymer thin films.

1.7.3.1. Polymer Structure and Crystallization Kinetics

Conjugated polymers are typically thought of as rigid-rod polymers compared to coil polymers like polystyrene. However, solution studies have shown that the persistence length of P3HT is around 3 nm in *ortho*-dichlorobenzene (*o*DCB) (around 10 repeat units),¹⁹² which is only 2-3 times the persistence length of polystyrene or poly(methylmethacrylate) (persistence length over 4-5 repeat units). The polymer conformation (rod-like or coil-like) in both solution and thin film can be tuned through chemical structure or processing.

Solubility of π -conjugated polymers is enhanced when solvent-polymer interactions become favored over polymer-polymer interactions (enthalpic effect), as is the case with any dissolution process. Structurally, chain interactions can be limited through decreasing the rigidity of the polymer backbone, increasing the conformational degree of freedom and steric hindrance induced by the side-chains. Polymer solubility can be further increased by lower the polymer molecular weight. However, polymer molecular weight is typically one of the harder structural parameters to control due to polymer synthesis via step-growth polymerizations. While high molecular weight hinders polymer solubility, it is a key requirement for the formation of interconnected ordered domains that appear to be crucial to charge carrier transport in polymer FETs.^{92,193} Since high molecular weights

are targeted for organic electronic applications, this paragraph will omit discussion on polymer molecular weights and solubility to focus further on the impact of the chemical structure on solubility by using examples from extensively studied diketopyrrolopyrrole (DPP)-based polymers.

First of all, the polymer backbone chemistry, especially thinking about rigidity and side-chain density, has a large impact on solubility. As seen in Figure 1-26, Li *et al.*¹⁹⁴ have qualitatively investigated six DPP-based polymers with varying donor units. They find that polymers with fused rings or lower side-chain density have lower solubility than DPP-based polymers with a terthiophene unit. Furthermore, the alternating copolymer of terthiophene and DPP requires branched alkyl side-chain to promote solubility in the casting solvent. These bulky side-groups are thought to induce a decrease in thin film ordering of the polymer and thus reduce effective charge carrier transport, although this is not always true. In order to increase polymer solubility without resorting to branched side-chains or sacrificing the molecular weight, the DPP-containing polymer backbone was modified to include furan units (Figure 1-26f).¹⁹⁵ By doing so, linear chains could replace branched chains leading to increased thin film ordering while the polymer maintained its solubility.

solvent boiling point and evaporation time is not straightforward as shown by Yang *et al.*¹⁹⁹

In addition to longer drying times, one pathway to increase polymer ordering in a thin film relies on tuning polymer behavior in solution by inducing polymer aggregation in the casting solution.²⁰⁰ The impact of polymer pre-aggregation in solution on photoluminescence has previously been studied by Nguyen *et al.*^{58,59} in the context of organic light emitting diodes. Further work on the impact of solution aggregation on film formation was studied *in situ* during spin coating of P3HT from toluene. The increased solubility with increased temperature (equation 1-16) can be visualized in P3HT solutions with toluene solutions of P3HT being yellow (limited interchain interactions) at 65 °C and brown/red at room temperature (interchain interactions leading to new absorption bands). Abdelsamie *et al.*¹⁷⁸ discussed the combination of kinetic effects (initial presence of polymer aggregates to act as nuclei and slower drying time in the pre-aggregated solution) and their impact on interconnected polymer fibrils for charge carrier transport in OFETs (1×10^{-3} versus $1 \times 10^{-2} \text{ cm}^2 \text{ V}^{-1} \text{ s}^{-1}$ in fully dissolved and pre-aggregated P3HT respectively).

Investigating beyond P3HT to D-A polymers, Chen *et al.*¹⁹⁶ added methanol to chloroform solutions as a poor solvent for the polymer to induce aggregation in the solution, and monitored any shift in energy levels via UV-vis-NIR. Interestingly, the UV-vis-NIR spectrum of PDPP3F-C16 (see repeat unit structure in Figure 1-26f) (already exhibiting higher degrees of ordering from chloroform alone) was slightly red shifted in the presence of methanol and the OFET device performance showed little effect of the addition of a poor solvent. However, PDPP3F-BO (Figure 1-26f) showed a significant

red-shift in its solutions absorption peak and peak broadening indicating the formation of aggregates within the solution. Addition of methanol in the casting solution also led to decreased π - π distances and favored orientation of the polymer backbones edge-on to the substrate in the resulting thin film, as well as increase charge carrier transport in OFETs. As such, the formation of pre-aggregates in polymer solutions, where aggregation would otherwise be slower or even thermodynamically prevented, leads to the formation of ordered domains that would otherwise not be observed. Other routes to crystalline polymer thin films from solution include crystallization at elevated temperatures from dilute polymer solutions, crystallization under elevated pressures or influencing crystallization and orientation through a solid substrate (epitaxy).¹⁹³

1.7.3.2. Polymer Ordering in Thin Films

At the microscopic scale, polymer thin films exhibit both ordered and amorphous areas as illustrated in Figure 1-29. The degree of ordering in these semi-crystalline films will depend on several parameters: molecular weight, steric arrangement of the side-chain, nature of the polymer backbone, branching and defects, chain ends, and interchain interactions, in addition to factors controlled by processing (polymer solubility, film drying time, etc.).

A prominent factor is the molecular weight of the polymer, which impacts both solubility and thin film morphology. As the molecular weight increases, highly ordered polymers in an extended chain conformation transition to entangled chains exhibiting both crystalline and amorphous domains, and as such polymer thin films should be considered as a two phase system.²⁰¹ Kline *et al.*²⁰² have demonstrated the effect of P3HT molecular weight on morphology and charge carrier transport in OFETs (Goh *et al.*²⁰³

have shown similar trends in SCLC charge carrier mobility). Using atomic force microscopy (AFM), some structure-property relationships have been highlighted and are summarized in Figure 1-27. The top AFM image is of low molecular weight P3HT films, which shows rod-like crystals whereas no distinct crystalline features can be seen in the bottom AFM image of high molecular weight P3HT. This observation was further supported by X-ray diffraction (XRD), which also showed a broad distribution of crystal orientation in the case of low molecular weight P3HT and a narrower distribution in the case of higher molecular weight P3HT. As such, it is hypothesized that low molecular weight P3HT, although more crystalline, presents more grain boundaries that can hinder charge transport, compared to interconnected, although smaller, crystalline domains in high molecular weight P3HT due to entanglements shown in the bottom AFM image and schemes of Figure 1-27a. As seen in Figure 1-27b, this translates into an increase in charge carrier mobility in OFETs as P3HT molecular weight increases (increasing the size of the crystalline domains, thus decreasing the number of grain boundaries) until a critical molecular weight is reached, where entanglements begin to form. Past this critical molecular, the charge carrier mobility saturates at a maximum value.

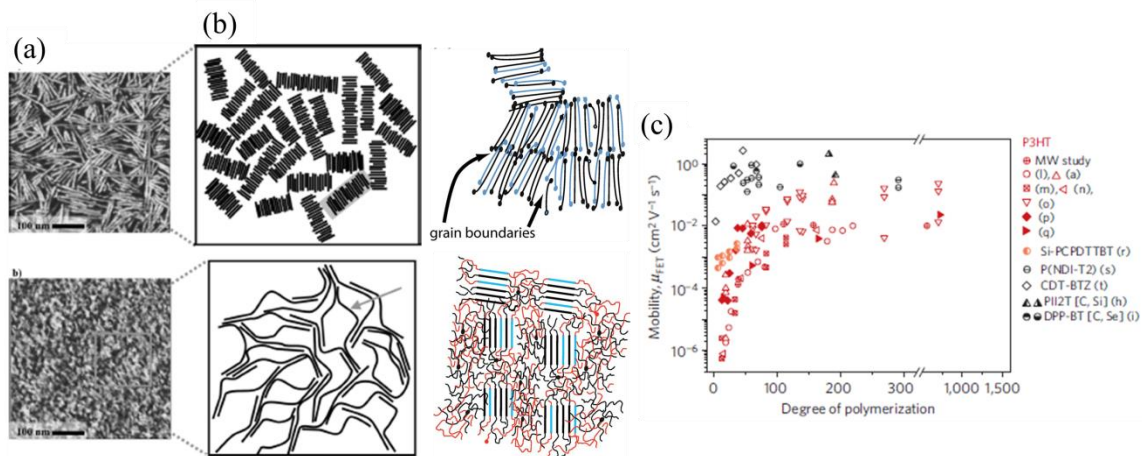


Figure 1-26. Influence of molecular weight (entangled chains on bottom) on (a) polymer packing in the solid state as seen in the phase images of polymer films, (b) schematic representation of polymer chains in the solid state, and (c) impact of the degree of polymerization on OFET hole carrier mobility. (adapted from ^{92,193,201,204})

At the molecular level, the degree of ordering and the size of the ordered domains in thin films can be tuned through polymer structure, as demonstrated by polytriarylamine-type (PTAA) materials which exhibit high torsion due to steric effects, hence preventing close interactions leading to improved solubility and decreased ordering in the solid state (Figure 1-28a) as discussed by Noriega *et al.*⁹² As discussed earlier, this work highlighted that polymer packing in thin films for OFET devices requires a threshold degree of ordered domains (representative GIWAXS image shown in Figure 1-28b) interconnected through amorphous chains to promote charge carrier transport, as is the case in most donor-acceptor polymers like PCDTBT, not necessarily long range order as in P3HT for example (representative GIWAXS image shown in Figure 1-28c).

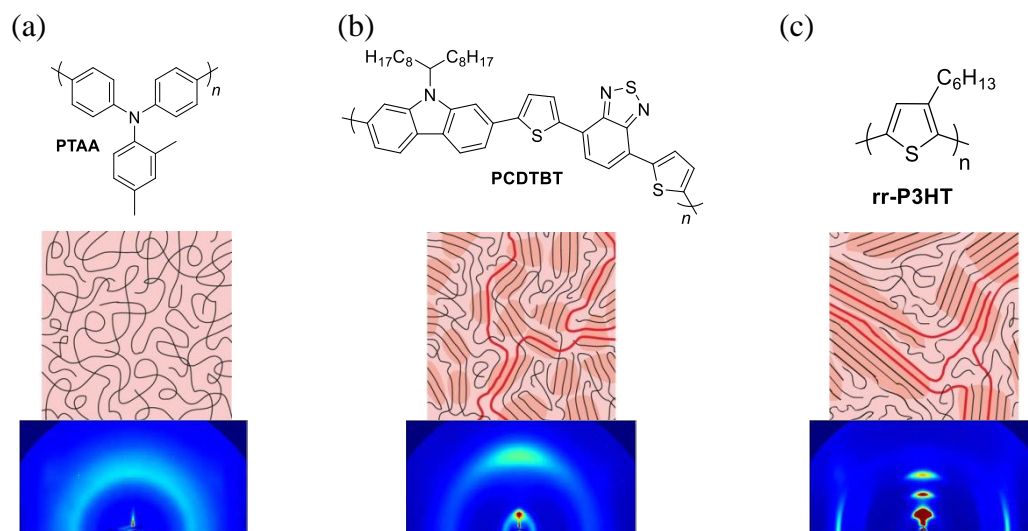


Figure 1-27. Degree of ordering (GIWAXS) and schematic thin film morphology as a function of polymer structure. (adapted from ⁹²)

The importance, not only of ordered domains, but also of amorphous domains has also been described by Zhang *et al.*⁹¹ In this study, the authors demonstrate that an extended coplanarity of the backbone combined with an exceptionally uniform orientation of the conjugated molecular units with respect to the substrate plane not only in the crystalline, but also in the amorphous regions of the films in this polymer can explain the order of magnitude higher hole carrier mobility in indacenodithiophene–benzothiadiazole copolymers compared to P3HT or PDPPT-T.

In terms of polymer structure, the design of side chains to maintain solubility but improve interchain interactions has recently been explored by moving the branching point of the side-chains further away from the conjugated backbone. An example of this has been demonstrated by Mei *et al.*¹⁵⁷ by replacing 2-octyldodecyl side-chains by siloxane-terminated side-chains on poly(bithiophene-*alt*-isoindigo) (P[T2-iI]) (Figure 1-29). This strategy led to reduced π – π stacking distances from 3.75 Å with 2-octyldodecyl side chains to 3.58 Å with the siloxane chains, and induced a change in the orientation of

ordered domains as measured by GIWAXS. Indeed, Figure 1-29A shows scattering from the (010) π -stack planes along the q_{xy} axis (i.e. in-plane, polymer backbones are edge-on to the substrate) in films of P[T2-iI(HD)], while Figure 1-29B shows (010) peaks both along q_z and q_{xy} , indicating backbone orientation edge-on and face-on in films of P[T2-iI(SiO)]. Both of these observations were used to explain the increase in charge carrier mobility from to in the alkyl-substituted and siloxane-substituted polymers respectively, and this strategy of moving the side-chain branching point away from the conjugated backbone is now widely used to yield polymers with high mobilities in OFETs.²⁰⁵

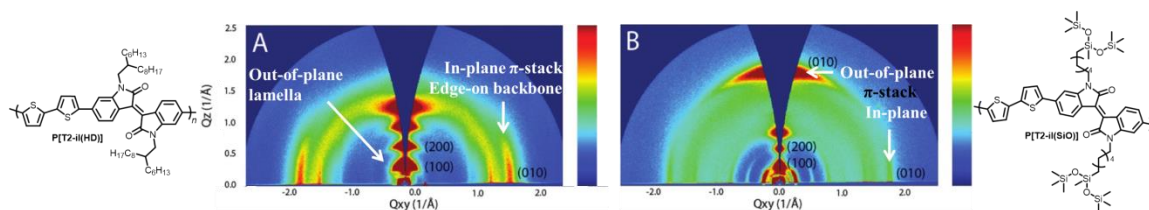


Figure 1-28. Impact of siloxane-terminated side-chains on polymer solid state packing by GIWAXS. (adapted from ¹⁵⁷)

Alkyl chains with increasing distance between branching point and polymer backbone have also been developed to study this same concept using 3-decyltridecyl (C2), 4-decyltetradecyl (C3), and 5-decylpentadecyl (C4) side-chains instead of 2-octyldecyl (C1) side-chains on P[T2-iI(R)].¹⁵⁶ The π - π distances were found to be 3.75, 3.61, 3.57, and 3.57 Å for C1, C2, C3, and C4 respectively. However no direct correlation can be made between the distance and hole carrier mobility measured to be 0.66, 0.28, 2.98, and 1.44 cm² V⁻¹ s⁻¹ in C1, C2, C3 and C4 respectively. These observations again prove that the amorphous polymer domains also need to be taken into account when explaining trends in charge carrier mobility by investigating polymer packing.

In addition to side-chain design, the quadrupolar and symmetry effects of the donor-acceptor backbone have also been used to rationalize polymer packing as it relates to

charge transport. These effects are illustrated in Figure 1-30. First of all, the concept of “molecular docking”, seen in Figure 1-30b and c, where smaller, non-sterically hindered monomer units can “dock into” a large aromatic core yielding increased order in the thin film, has been used to explain the GIWAXS measurements.²⁰⁶ This notion recalls the slipped stack arrangement of polyfluorene described earlier.^{65,66} Furthermore, the arrangement of the polymer backbones dictated by axisymmetry versus centrosymmetric monomer units (Figure 1-30d and e) has been widely used in the literature to explain polymer packing observed using GIWAXS.^{161,206} Axisymmetric units are thought to induce “waviness” of the polymer backbone, leading to decreased interchain interactions, whereas centrosymmetric units yield more linear chains.

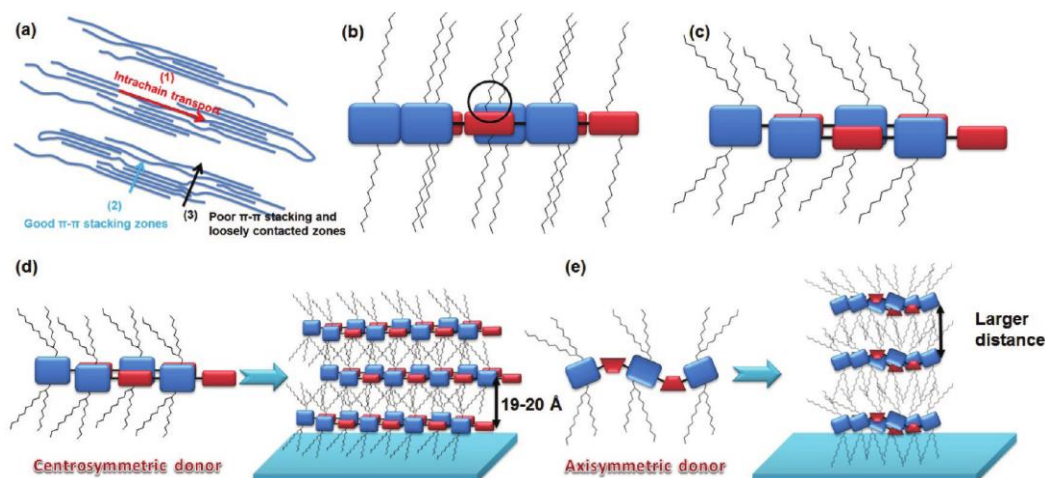


Figure 1-29. Schematic representation of polymer interchain interactions. (a) Scheme of different charge carrier transport pathways within a semicrystalline polymer film. (b, c) Steric effects of the side-chains on D-A interactions across neighboring backbones, highlighting the “molecular docking” concept in (c). (d, e) Impact of monomer symmetry on lamellar stack distances. (adapted from ²⁰⁶)

However few studies actually probe the nature of interchain interactions using techniques such as 2D solid state NMR in order to prove the existence of interchain donor-acceptor interactions as they are depicted in Figure 1-31. The group of Klaus Müllen has studied dithienocyclopentadiene- and dithienolsilole-benzodithiazole

(CPDT-BTD and DTS-BTD respectively) polymers, and found that the repeat units are indeed π -stacked, but also showed that the BTD acceptor units are heterogeneously packed throughout the sample (the acceptor groups are not always located at the exact same position with respect to the neighboring polymer chains).²⁰⁷ These solid-state NMR results are supported by molecular modeling where donor-on-donor/acceptor-on-acceptor stacking with a small shift along the polymer backbone was determined to be the most likely intermolecular packing geometry.²⁰⁸ In the case of copolymers of fused dithienyl units and BTD units, it appears that the flipped stacking dictates interchain interactions rather than slipped stack donor-acceptor interactions as would be assumed based on the “molecular docking” scheme, possibly due to the arrangement of side-chain on one side of the monomer unit (rather than on either side as is the case with isoindigo for example).

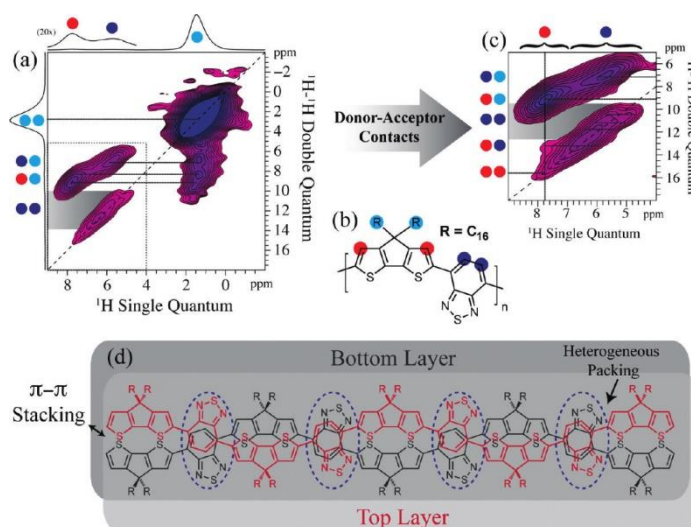


Figure 1-30. Determination of polymer packing with NMR. (a) ^1H - ^1H solid-state NMR correlation of CPDT-BTD with the H atoms color coded (b). (c) Expansion of the region showing the H on the polymer backbone highlighting interchain D-A interactions. (d) Schematic representation of the interaction between neighboring polymer chains. (adapted from ⁸⁸)

The combination of backbone and side-chain design for control of polymer packing in thin films has been studied further by Guilbert *et al.*²⁰⁹ The authors find that both CPDT-

BTD and DTS-BTD are able to form two polymorphs thermodynamically, and that the kinetics of the chosen processing conditions determines the contribution of both polymorphs to the polymer packing in the solid state. Furthermore, the softer silicon-carbon bond in DTS-BTD was shown to impact the flexibility of the side-chain around the bridging silicon atom compared to CPDT-BTD, which is thought to influence both the thermodynamics and kinetics of crystallization. This would explain the differences in crystallinity and polymer packing observed when both polymers are processed in similar ways. Using longer or less bulky side-chains (increasing side-chain flexibility) suppresses the thermodynamic formation of one polymorph in CPDT-BTD, leading to favorable thermodynamic formation of the polymorph with shorter π - π distances.

As such, beyond polymer structure, the effects of processing will largely dictate polymer packing. First of all, there are some preliminary observations about the conformation of polymer chains in solution as a function of the aliphatic or aromatic nature of the solvent. Indeed it has been suggested that aromatic solvents may lead to the formation of aggregates or microgels^{210,211} while aliphatic solvents lead to more negligible polymer segmental association.²¹² Increased π - π interactions between solvent molecules and polymer segments are hypothesized to stabilize the formation of polymer aggregates in aromatic solvents. In addition to solvent effects, the effect of processing was also shown by Himmelberger *et al.*²¹³ In this study, the film thickness of poly-(2,5-bis(3-tetradecylthiophene-2-yl)thieno[3,2-b]thiophene) (PBTtT) was varied and showed that thinner films led to a more narrow distribution of crystallite orientation, which lead to a dependence of the charge carrier mobility on the crystallinity of the films as a function of polymer orientation. In thicker films, crystallite orientation is the first barrier

to overcome for high charge carrier mobility value rather than degree of ordering. Morphology variation at interfaces versus in the bulk has previously been demonstrated in P3HT, where highly oriented crystals were observed at the buried dielectric/semiconductor interface.²¹⁴ Lee *et al.*²¹⁵ further discussed the impact of both solvent choice and processing technique on polymer morphology and charge mobility in OFETs thin films based on a donor-acceptor fused thiophene-diketopyrrolopyrrole polymer. In this study, the use of small amounts of *p*-xylene in a polymer solution in tetrahydronaphthalene (THN) led to the formation of crystalline nanofibers which could be further aligned through solution shearing leading to average mobilities of $3 \text{ cm}^2 \text{ V}^{-1} \text{ s}^{-1}$ (compared to $2 \text{ cm}^2 \text{ V}^{-1} \text{ s}^{-1}$ in spun cast devices).

1.7.3.3. Post-Processing Treatments Effects on Polymer Arrangement

The impact of processing on morphology and charge transport is discussed further with the use of post-processing treatments. Thermal annealing has been a predominant technique to reach a more thermodynamically stable morphology as it provides increased energy to the system to induce reorganization. At the molecular level, thermal annealing promotes molecular motion of the alkyl side-chains and reorganization of the polymer backbone, leading to improved local order (seen in solid state NMR).²⁰⁷ At the nanoscopic level, this translates into more defined scattering peaks (Figure 1-32)⁹³ as well as shorter π - π distances in some systems. Thermal annealing can also induce a change in orientation of the polymer crystallites, also seen in Figure 1-32. In DPP-based polymer films containing a small fraction of polymer backbones orientated face-on to the substrate, thermal annealing leads to the majority of the crystallites with polymer backbones edge-on ((010) peak along q_{xy} and (h00) peaks along q_z), with negligible face-

on orientation (Figure 1-32a and b). In PDPPT-T films (Figure 1-32c), where a preferentially face-on orientation is observed in the as-cast films, thermal annealing enhances the population of edge-on domains, leading to a bimodal orientation distribution. Rivnay *et al.*²¹⁶ have taken this concept further by melt annealing poly[N,N-9-bis(2-octyldodecyl)naphthalene-1,4,5,8-bis(dicarboximide)-2,6-diyl]-alt-5,5'-bithiophene) P(NDI2OD-T2) (structure in Figure 1-41) followed by slow cooling to ambient temperature. Prior to annealing, a majority of the polymer backbones in the crystallites are face-on with respect to the substrate; after melt annealing, a majority of the chains are edge-on and the films exhibit a two-fold increase in crystallinity. The combination of these results suggests that orientation of polymer backbones edge-on versus the octadecyltrichlorosilane (OTS)-modified substrate is thermodynamically favored.

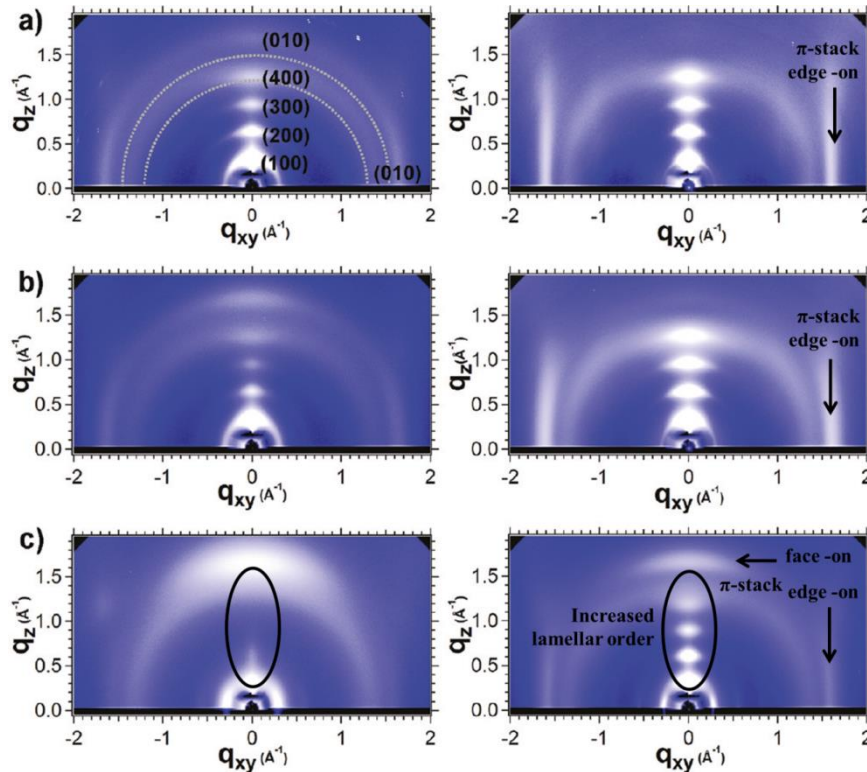


Figure 1-31. GIWAXS of thin films of (a) PDPPT-2T, (b) PDPPT-TT and (c) PDPPT-T before (left) and after (right) thermal annealing. (adapted from⁹³)

Solvent annealing is also a technique used to promote polymer motion to increase ordering by giving the polymer chains longer times to reorganize. In this case, the solvent vapors act as plasticizers to induce reptation of the polymer chains (motion of polymer chains against one another) and the longer drying times allow the chains to reach thermodynamic equilibrium.¹⁸¹ Taking solvent annealing to an extreme, Wang *et al.*²¹⁷ were able to form fibers of CPDT-BTD (structure in Figure 1-31) with widths around 0.5 μm , thicknesses around 120 nm and lengths between 5 μm and 20 μm by drop casting a polymer solution and letting the solvent evaporate under a saturated solvent vapor atmosphere. These fibers were then used in OFETs and showed average hole carrier mobilities of $4 \text{ cm}^2 \text{ V}^{-1} \text{ s}^{-1}$.

1.7.4. Polymer:Small Molecule Mixtures: Polymer:Fullerene Blends for OPVs

Physical mixing of the two blend components followed by solution processing allows for little control over the final phase separation. However, several processing parameters can be tuned in order to reach optimized active layer morphology for enhanced device performance. The development of novel in-situ characterization techniques of thin films as they dry has shed some light on film formation mechanisms.^{177,182,218,219}

One of the first questions is the mechanisms that drive phase separation during solution deposition. Once the mechanisms are highlighted, the factors that impact the outcome can be outlined. Kouijzer *et al.*¹⁸⁶ have described the ternary phase diagram made up of solvent, polymer and small molecule, and have simplified the mechanism for phase separation into three main categories as illustrated in Figure 1-33: liquid-liquid (L-L) or liquid-solid (L-S) demixing or no phase separation. The contribution of each

category depends on the structure of the compounds (interactions that have the possibility to lead to aggregation versus steric bulk that decreases that probability) and on the kinetics of film formation (quenching of liquid-liquid demixing versus allowing for aggregates to form and grow). Typically, blends cast from chloroform will follow liquid-liquid demixing due to the fast drying time, which prevents aggregation of either two components. Other single solvent systems will follow liquid-liquid demixing if liquid-solid demixing is not thermodynamically or kinetically accessible.

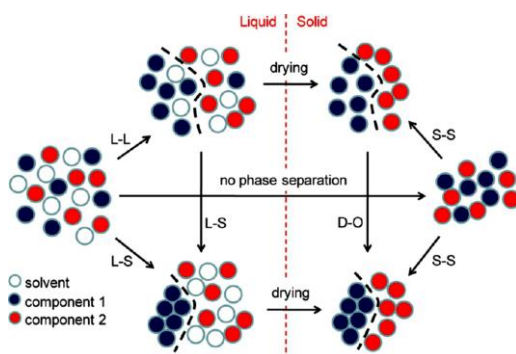


Figure 1-32. Schematic representation of processes that may occur in a ternary blend. L-L: liquid-liquid demixing, L-S: liquid-solid demixing, S-S: solid-solid phase separation and D-O: disorder-order transition. (adapted from ¹⁸⁶)

It is important to note that crystallization of polymer chains will be different than what was discussed in the previous section. Indeed, small molecules (solvents, additives, or fullerenes) that interact with the polymer chains through van der Waals interactions for example can cause depression of the melting temperature of the polymer solid, and thus influence crystallization. Since the phase separation is quenched by solvent evaporation in most cases, the thermodynamically favored morphology is not obtained directly after coating. As illustrated in Figure 1-33, once the film is solidified, further solid-solid (S-S) phase separation as well as disorder-order (D-O) transitions can occur during post-deposition treatments, such as thermal or solvent annealing.

1.7.4.1. Fullerene Solubility and Selection of Fullerene Derivative

Current research groups mostly focus their efforts on blends of polymer with either [6,6]-phenyl-C₆₁-butyric acid methyl ester (PC₆₁BM) or [6,6]-phenyl-C₇₁-butyric acid methyl ester (PC₇₁BM). The extinction coefficient at 400 nm for PC₆₁BM and PC₇₁BM are 4,900 and 19,000 mol⁻¹ cm⁻¹ respectively, which is why PC₇₁BM tends to give higher light absorption and better performance in OPV blends. However, their difference in solubility and miscibility with the polymer domains also impacts phase separation in the BHJ. There have been some conflicting reports on the solubility of PC₆₁BM relative to PC₇₁BM; however, Kronholm *et al.*²²⁰ and Troshin *et al.*²²¹ have demonstrated that PC₇₁BM is more soluble than PC₆₁BM in chloroform, chlorobenzene and *o*DCB, which is in agreement with previous reports of the higher solubility of C₇₀ compared to C₆₀ due to the increased polarizability of C₇₀ compared to C₆₀.²²² In terms of polymer-fullerene miscibility, Collins *et al.*^{223,224} have measured the miscibility of PC₆₁BM and PC₇₁BM in three different polymer systems and found that PC₇₁BM tends to be more miscible (40 %_w in a poly(dithienosilole-*alt*-benzodiathiazole) polymer) than PC₆₁BM (26 %_w in the same polymer) in polymer domains, regardless of the polymer's order pointing to the fact that BHJ morphology needs to be thought of as a (at least) three-phase system. Beyond miscibility, the formation of bimolecular crystals of polymer and fullerene derivative with intercalation of fullerenes in between alkyl side chains has been shown to occur in PBTTT and has been extensively described in the literature.²²⁵

1.7.4.2. Liquid-liquid Demixing

Liquid-liquid demixing is seen in a wide variety of BHJ blends, and is impacted mainly by both kinetic factors. First of all, in most systems, even those where ordering is

favored, fast solidification times (using chloroform as the casting solvent for example) will lead to liquid-liquid demixing. Kouijzer *et al.*¹⁸⁶ have studied the effect of liquid-liquid demixing in PDPPT-3T:PC₇₁BM blends spun-cast from chloroform (Figure 1-34b). In order to determine the pathway for phase separation and the composition of the domains in the thin film, the authors calculated the liquid-phase ternary phase diagram using equation 1-14 (extended to a three-component system) after determining the χ interaction parameters using equations 1-16 and 1-17. The ternary phase diagram distinguishes between three domains as illustrated in Figure 1-34a: i) the coexistence domain (single-phase), ii) the binodal domain (biphasic, stable to small composition fluctuations), and iii) the spinodal domain (two-phase region unstable to small composition fluctuations). The composition of each phase can be determined by the coordinates of the points at the extremities of the tie lines (points A and B in Figure 1-34a). Based on the ternary phase diagram, the authors find that the large, rather pure PC₇₁BM domains formed in these blends result from a liquid droplet phase that mainly contains solvent and PC₇₁BM (A). This liquid droplet phase has separated via spinodal demixing from the second continuous phase that contains solvent, PDPPT-3T and PC₇₁BM (B). If the film is allowed to dry over longer times, modeled in this work by thicker films, the large droplets grow at the expense of smaller droplets via Ostwald ripening, and the amount of PC₇₁BM in the continuous phase decreases. By adding a small volume percent of a higher boiling point solvent such as oDCB (Figure 1-34c), liquid-liquid demixing is suppressed and solid-liquid mixing then dictates the phase separation.

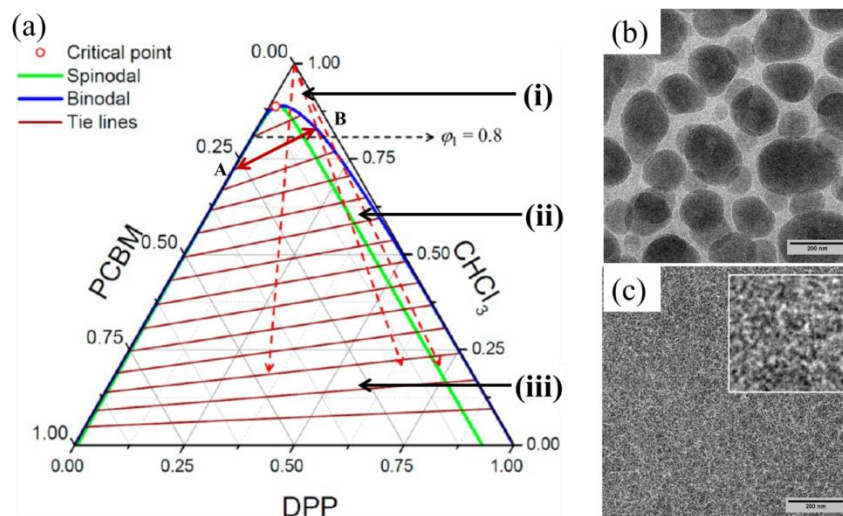


Figure 1-33. Ternary phase diagram, and the impact of film drying time. Ternary phase diagram at constant temperature, pressure conditions calculated from the Flory-Huggins model. (b) Spinodal (liquid-liquid demixing) transition in chloroform leading to large phase segregation shown by transmission electron microscopy, and (c) impact of adding *o*DCB to the solution on phase separation. (adapted from ¹⁸⁶)

1.7.4.3. Solid-liquid Demixing

Solid-liquid demixing will depend on the relative crystallinity of each material, their relative composition in solution and the casting solvent used. The intentional pre-aggregation of either polymer or fullerene in solution will also have a significant influence on the kinetics of film formation. Typically, if sufficient time is given to the drying film either polymer or fullerene crystallization will induce solid-liquid demixing. This is a crucial step in BHJ formation that needs to be understood and controlled for optimal device performance. Furthermore, the choice of the main casting solvent will influence not only the conformation of the polymer chains and the size of fullerene aggregates in solution, but it will also control the film drying kinetics. Polymer solubility as a function of solvent parameters was discussed in section 1.5.3.1., as such the focus in this paragraph is the impact of polymer and fullerene solubility and film drying on phase separation. In a first paragraph, polymer crystallization and morphology control will be

described followed by fullerene crystallization as a driving factor for phase separation in a second paragraph.

In the case of P3HT:PC₆₁BM blends, in situ studies of spun-cast films from warm chlorobenzene has shown that polymer crystallization dominates film formation at PC₆₁BM contents <50% (Figure 1-35). At higher PC₆₁BM content, fullerenes hinder P3HT crystallization, and as P3HT crystallites form towards the end of the spinning process, their growth is quenched by solvent evaporation, leading to a glassy solid. The balance between P3HT crystallization (leading to reduced mixing of PC₆₁BM into amorphous phases) and phase separation in blends containing around 40% PC₆₁BM leads to the highest PCE.²¹⁹ Further support of this film forming mechanism has been provided by in situ studies on blade-coated P3HT:PC₆₁BM films from *o*DCB or chlorobenzene.^{177,226} Troshin *et al.*²²¹ have further hypothesized that in P3HT:fullerene derivative blends, optimal phase separation for BHJ is achieved when the polymer and fullerene have comparable solubility in the casting solvent.

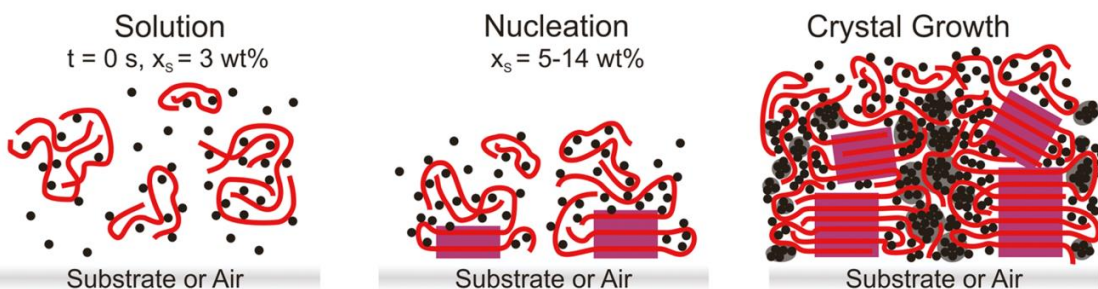


Figure 1-34. Schematic representation of film formation in P3HT:PC₆₁BM blends. (adapted from²²⁶)

In D-A polymers the thermodynamic tendency for crystallite formation will lead to different pathways for film formation in semicrystalline relative to amorphous polymers. For instance, Guo *et al.*²²⁷ and Osaka *et al.*²²⁸ have showed that, when the same processing conditions are used, similar polymer structures follow different pathways to

phase separation (Figure 1-36). Of course, the ability of polymer crystallites to form will depend on the polymer solubility and on the solvent evaporation time.

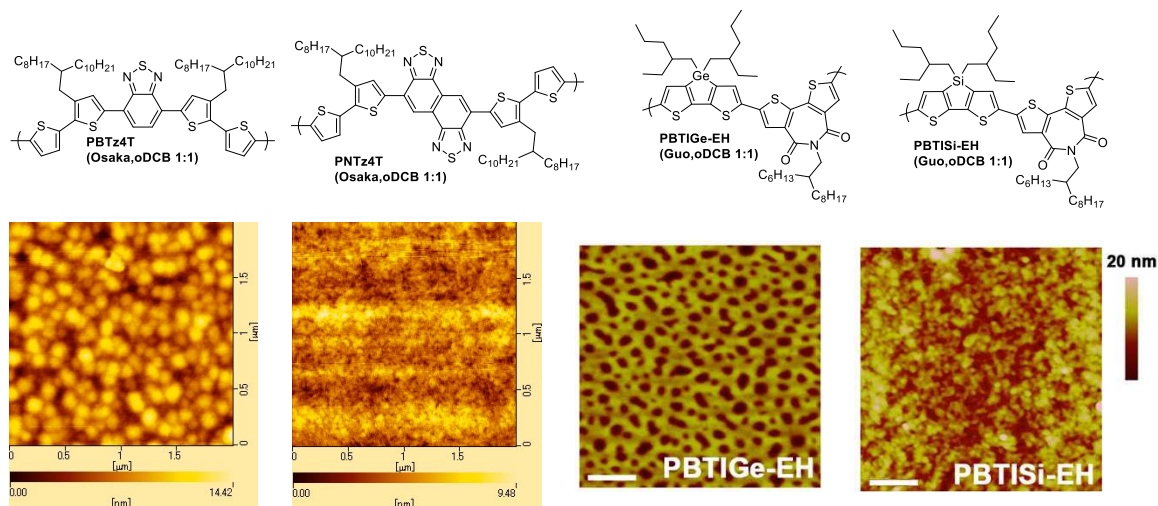


Figure 1-35. Impact of polymer structure on film formation in blends with PC₇₁BM. (polymer:fullerene ratio and solvent indicated under structures) (adapted from^{227,228})

If the onset for polymer aggregation is lower than the onset of aggregation for fullerenes, polymer-liquid demixing will typically occur. However, the kinetics of crystallization of fullerenes can also be dictated by the polymer:fullerene ratio as shown by Pearson *et al.*²²⁹ In the case where the polymer:PC₇₁BM ratio is close to 1:4 in *o*DCB, fullerene aggregation dictates the final morphology with polymer ordering (Figure 1-37), even though the formation of the fullerene aggregates depends on the polymer:fullerene interactions. On the other hand, at polymer:fullerene ratios around 1:1 to 1:2, polymer aggregation seems to dictate the final morphology.

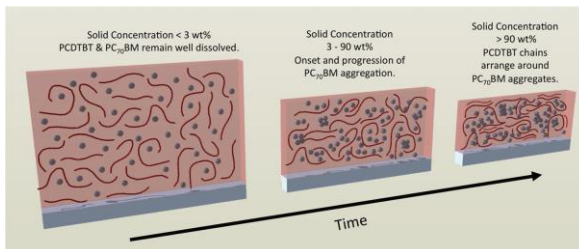


Figure 1-36. Schematic representation of film formation in 1:4 blends of polymer:PC₇₁BM, regardless of the polymer structure. (adapted from²²⁹)

Schematically, film formation in polymer:fullerene blends can be summarized by Figure 1-38. When low boiling point, good solvents for both the polymer and fullerene (such as chloroform) are used, liquid-liquid demixing occurs, leading to large phase separation in the BHJ layer. When higher boiling point solvents are used, the polymer versus fullerene solubility, as well as the ratio of polymer:fullerene, will dictate the thermodynamics and kinetics of solid-liquid demixing.

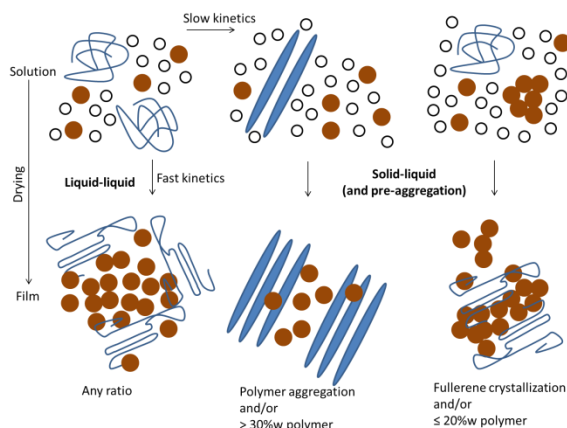


Figure 1-37. Scheme summarizing the various processes that can occur during film formation in BHJ devices. Solvent molecules: white circles; polymer chains: blue lines; fullerene molecules: brown circles.

1.7.4.4. Extended Control with Solvent Additives (or Tailing Solvents)

Addition of a high boiling point solvent additive to the casting solution has been shown to have a drastic impact on phase separation in polymer:fullerene blends.²³⁰ This method of using a main solvent with a high vapor pressure for fast evaporation, leaving behind a lower vapor pressure “tailing” solvent to further shape the thin film morphology has been extensively used in the coating industry. In the field of OPV, Peet *et al.*²³¹ introduced octanedithiol (ODT) as a solvent additive and showed increased OPV device performance. Since then, research efforts have focused on understanding the mechanisms involved in morphology control when solvent additives are used. As of today, it appears

that the aliphatic versus aromatic structure of the additive is the main factor behind the differences in thin film formation. This is linked to the fact that the thin film morphology is set in two stages: at the solution stage with pre-aggregation and at the drying stage, which has been shown to last over 40 min in some cases.²³² In particular, solvent additives can be separated into two categories: good solvent for both polymer and fullerene or poor solvent for polymer/good solvent for fullerene.

Using grazing-incidence small-angle X-ray scattering (GISAXS) on solutions with and without solvent additive, Schmidt. *et al.*²³³ and Lou *et al.*²³⁴ point out differences in the polymer and fullerene derivative behavior in solution. Schmidt *et al.* show that DPP-based polymer chains in chlorobenzene are aggregated and that addition of 5%_v 1-chloronaphthalene (CN) in the solution induces more ordered aggregates (presence of a swelled lamellar-type peak). The hypothesis is that CN leads to ordered aggregates that then act as nucleating sites for polymer ordering, and increasing the number of nucleating sites decreases the polymer domain size. On the other hand, work by Lou *et al.* indicates that fullerene aggregates in chlorobenzene decrease in size when DIO is added to the solution, leading to increased miscibility between the polymer domain and fullerene domain and smaller domain sizes overall.

Bridging these two studies, the work by Shin *et al.*,¹⁸² Richter *et al.*¹⁷⁷ and Gao *et al.*²³⁵ have compared effects stemming from aliphatic and aromatic additives in blade-coated or spun cast blends. In blade-coated P3HT:PC₆₁BM blends, P3HT crystals are formed as chlorobenzene evaporates. Furthermore, addition of 1-chloronaphthalene to a chlorobenzene solution leads to an increased growth of P3HT crystals from a solid P3HT/P3HT:PC₆₁BM solution mixture, whereas addition of octanedithiol to the

chlorobenzene solution leads to the formation a solid P3HT/PC₆₁BM liquid/P3HT:PC₆₁BM liquid mixture resulting in a slight increase in the growth of P3HT crystals as ODT evaporates. In PBDTP-DPP:PC₇₁BM blends (Figure 1-39), Gao *et al.*²³⁵ observed a slight 1 nm red-shift in the absorption maximum of the polymer solution with 1%_v DIO and a 11 nm red-shift when 3%_v *o*DCB is added. The authors thus concluded that addition of 1-8-diiodooctane (DIO) to a polymer solution in chloroform leads to the formation of amorphous aggregates in the chloroform solution whereas addition of *o*DCB forms more ordered aggregates, on par with the findings of Schmidt *et al.*²³³ with CN as an aromatic additive. Overall, both mechanisms led to solid-liquid demixing and increased PCEs in OPV devices.

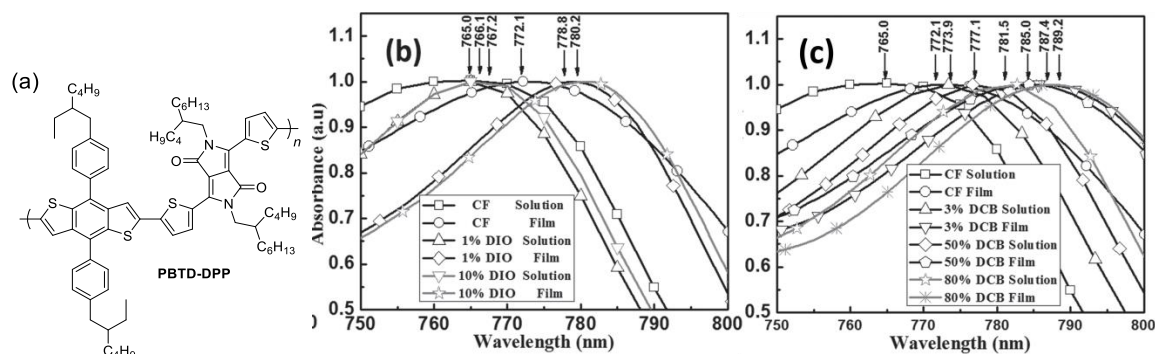


Figure 1-38. (a) Structure of PBTD-DPP, and UV-vis-NIR absorbance in film and solution in the presence of DIO (b) and *o*DCB (c). (adapted from²³⁵)

These results can help understand the observations from Li *et al.*¹⁹⁴ and Yang *et al.*,²³⁶ where optimal processing conditions made use of DIO as an additive in blends with more soluble polymers, and *o*DCB led to optimized conditions in the less soluble polymer blends. Indeed, *o*DCB can increase order within polymer aggregates and can act as a compatibilizer for amorphous polymer and fullerene mixed domains. On the other hand, DIO acts as a poor solvent for more soluble polymers, which can induce nucleation and growth of both polymer-rich phases and fullerene aggregates. It is important to note that

solvent additives can be viewed as plasticizers swelling the polymer-rich domains to enable further chain motion.

1.7.4.5. Solid-solid Demixing or Order-Disorder Transitions: Impact of Post-Processing Treatments on Phase Separation

In polymer:fullerene blend films subject to thermal annealing or solvent vapor annealing, further reorganization and crystallization can be induced. Phase separation in initially well-mixed films can also be initiated by the crystallization of either polymer or fullerene thanks to thermal or solvent annealing.

In particular for P3HT:PC₆₁BM blends, thermal annealing is reported to increase P3HT crystallinity prior to increasing the size of PC₆₁BM-rich domains by allowing PC₆₁BM molecules to diffuse out of disordered P3HT regions.^{237,238} This effect of thermal annealing seen in P3HT:PC₆₁BM blends can be generalized to donor-acceptor polymer:fullerene blends as shown by Huang *et al.*²²⁸ and Kim *et al.*,²²⁹ where thermal annealing leads to growth of both polymer ordering and fullerene-rich phases.

Solvent annealing slows the solidification rate by keeping the active layer under saturated solvent atmosphere. During solvent annealing, the solvent swells the thin film and allows for the blends components to remain mobile and diffuse, forming a thermodynamically favored phase separation. The slow evaporation time leads to increased phase separation and crystallization of the P3HT domains in P3HT:PC₆₁BM blends, which can be further controlled by the choice of solvent vapor and annealing time.²³⁹

1.7.5. All-Polymer Blends for OPVs

Polymer:fullerene blends have dominated OPV research due to efficient charge transfer to fullerene aggregates followed by charge separation. Close laying fullerene excited states appear to increase the charge transfer rate and seem to be a key design parameter for novel (universal) acceptors.^{105,240} One drive to replace fullerene derivatives is to increase light absorption from the acceptor to complement that of the donor polymer. The tunability of polymer structures for increased light absorption and electron transport has led to the development of polymer:polymer blends for OPVs.

One hurdle to overcome for all-polymer blends is the control of phase separation. As seen in equation 1-14 of Section 1.5.2., polymer mixing is not entropically favored and relies on specific interactions between different polymer chains. In the case of polymers with equal degrees of polymerization N , equation 1-14 can be rewritten as:

$$\Delta\bar{F}_{mix} = \frac{kT}{N} (\phi_A \ln(\phi_A) + \phi_B \ln(\phi_B) + \chi N \phi_A \phi_B) \quad (1-18)$$

highlighting the importance of the product of the interaction parameter χ with the degree of polymerization N . χN gives an indication of the miscibility of the two polymers as described in Figure 1-40, where phase separation is thermodynamically favored for χ greater than $2/N$.

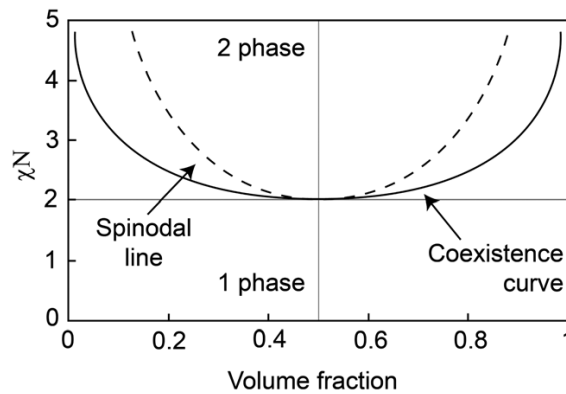
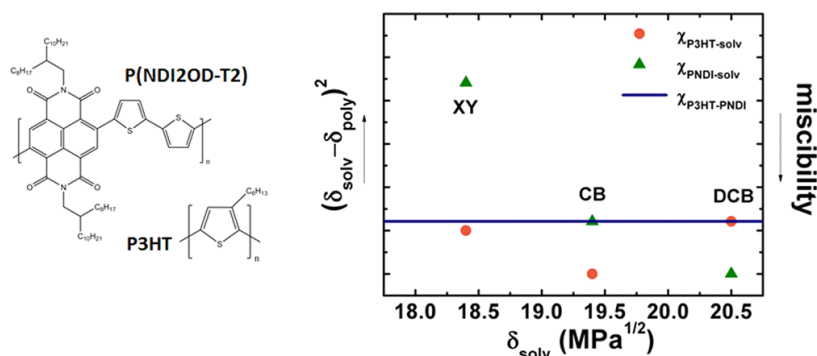


Figure 1-39. Binary phase diagram depicting polymer solubility as a function of the degree of polymerization N and of the Flory interaction parameter χ . (adapted from ²⁴¹)

In all-polymer blends for OPVs, a balance needs to be struck between fully miscible polymer systems and large phase separation that is driven by entropy. Since all-polymer blends are cast from solution, this becomes a three-phase problem. Beyond control of large phase separation, low electron carrier mobility and inefficient charge separation in polymer blends compared to fullerenes have also limited the impact of all-polymer active layers on OPV research compared to polymer:fullerene blends. However, some headway has been made on these challenges.



Another strategy to promote smaller phase separation in polymer:polymer blends is the use of similar structures to promote polymer-polymer interactions. This concept was also demonstrated in ternary blends of two polymers and a fullerene derivative,²⁴³ with the polymers being intimately mixed to form an “alloy”.¹²² Li *et al.*²⁴⁴ designed a thiazole-flanked DPP polymer, which has similar electron mobility to PC₆₁BM in OFETs (0.13 vs. 0.2 cm² V⁻¹ s⁻¹) but lower hole carrier mobility compared to other DPP-containing ambipolar polymers (6×10⁻³ cm² V⁻¹ s⁻¹). In 1:0.8 blends with a oligothiophene-*alt*-DPP polymer donor, the polymers are so intimately mixed after spin coating from chloroform that bimolecular recombination is promoted as shown by the low FF. The authors then induced different polymer-solvent interactions by using DIO, oDCB and CN to create a solubility difference between the two polymers, thought to lead to an increase in phase separation. Increasing domain size can also be achieved using thermal annealing as shown in poly(9,9'-dioctylfluorene-co-bis(N,N'-(4, butylphenyl))bis(N,N'-phenyl-1,4-phenylene)diamine) PFB:F8BT, as polymer domains grow after first becoming purer. However, the domain growth in these all-polymer blends is still higher than the exciton dissociation length, and highlight the challenge in designing all-polymer blends that could compete with polymer:fullerene blends.²⁴⁵

Based on this discussion, what are the determining factors in the design of all-polymer blends? As of today, there are no clear cut answers. Mori *et al.*²⁴⁶ have achieved PCEs of 2.6 % (average) in blends of P3HT and poly[2,7-(9,9-didodecylfluorene)-*alt*-5,5-(4',7'-bis(2-thienyl)-2',1',3'-benzothiadiazole)] thanks to large V_{oc} of 1.3 V, however the J_{sc} and FF remain low at 3.9 mA cm⁻² and 55 % respectively. Increased charge carrier

transport with increased molecular weight of the acceptor polymer and thermal annealing is cited as the rationale for the high PCE, however no measure of mobility is given in the study. Earmme *et al.*²⁴⁷ have reported at 3.2% average PCE PSEHTT:PNDIS-HD (equal to the PCE of PSEHTT:PC₆₁BM, mostly thanks to a V_{oc} of 0.75 V compared to 0.64 V in the case of PC₆₁BM). This record efficiency for all-polymer BHJ devices was rationalized by balanced charge carrier transport on the order of $10^{-4} \text{ cm}^2 \text{ V}^{-1} \text{ s}^{-1}$ for both hole carrier and electron carrier mobility measured through the blend with SCLC devices. In this case however, the phase separation was on the order of 200 nm but did not hinder charge generation. As such, the design of acceptor polymers with high excited states to increase V_{oc} (while still enabling efficient charge separation) and with high electron carrier mobility through the bulk should be targeted, with the possibility of tuning phase separation through solvent interactions.

1.8. Overview of Dissertation

This dissertation focuses on the design, synthesis, characterization, and structure-processing-property relationships of isoindigo-based π -conjugated polymers for application in organic photovoltaic devices. Particular to this work is the discussion of polymer structure as it impacts optoelectronic properties as well as polymer packing and phase separation in the solid state. The thesis behind this work is that design of new materials for organic electronics should stress the impact not only of the polymer backbone, but also the need for rational selection of the polymer side-chains and processing conditions to control morphology.

Chapter 3 of this dissertation discusses the synthesis and characterization of acceptor and donor polymers for OPVs, demonstrating the versatility of the isoindigo synthon as a

building block for organic electronics. Of particular importance for acceptor polymers is the fabrication of all-polymer cells in blends with P3HT with PCEs of 0.5%, where strategies for improvement are clearly highlighted in terms of balance of charge carrier mobilities. Design principles learned from the design of these n-type polymers were also proven useful in defining structure-property relationships in donor isoindigo-based polymers, where alternating structures of isoindigo with three different fused donor units gave further insight on design principles to tune frontier energy levels and charge carrier transport. These polymer systems are then used in blends with fullerene derivatives, and clearly demonstrate the influence of the blend components on phase separation and OPV device characteristics. In order to investigate these observations at a deeper level, three new polymers based on oligothiophenes and isoindigo were synthesized, and the impact of polymer structure on charge separation and thin film morphology is discussed in the last section of this chapter.

Beyond the molecular formula, polymer packing and processing conditions have been shown to further impact the resulting properties, such as absorption or charge carrier mobility, in the solid state. The thesis behind Chapters 4 and 5 is that design of these polymer structures not only needs to target properties based on the frontier energy levels, but the morphology of the polymer in the solid state. Chapter 4 in particular discusses the impact of backbone torsion and polymer solubility on energy levels, polymer packing and phase separation in blends with fullerenes in a family of six poly(terthiophene-*alt*-isoindigo). These thermodynamic parameters are to put in perspective with the kinetic control of film formation during the coating process. Chapter 5 focuses on both kinetic and thermodynamic impacts of the use of solvent additives in terms of their influence on

the film drying time, and in terms of both their structure and functionality by investigating differences between aliphatic and aromatic additives.

CHAPTER 2. CHARACTERIZATION TECHNIQUES AND EXPERIMENTAL METHODS

2.1. Density Functional Theory

The frontier orbital energy levels were computed on model oligomers using density functional theory (DFT) calculations in order to gauge trends in the energy levels of the respective polymers, and determine their use for a particular application prior to synthesis or explain trends seen in their characterization.²⁴⁸ Out of the four types of methods generally used for computations (molecular mechanics, semi-empirical, density functional, and ab initio), DFT was chosen to balance accuracy and computation time for small to medium molecules (around 10 to 150 atoms). An overview of calculation methods and uses can be found in “A Guide to Molecular Mechanics and Quantum Chemical Calculations” by Warren J. Hehre.²⁴⁹

Starting from the time-independent Shrödinger equation, where:

$$\hat{H}\psi(r_1, \dots, r_n; r_A, \dots, r_N) = E\psi(r_1, \dots, r_n; r_A, \dots, r_N) \quad (2-1)$$

with \hat{H} the Hamiltonian describing the system, ψ the wavefunction of the system of particles, and E the total energy of the system. In a many-body problem, the time-independent Shrödinger equation cannot be solved exactly, and the Born-Oppenheimer approximation is made that the electron, because of its relatively light weight compared to the nucleus, is able to adjust its position instantly as the nuclei move, i.e. the nuclei are put at rest while the electrons move in a field of fixed nuclei. Furthermore, in the Hartree-Fock theory the interaction between different electrons is replaced by an average interaction between one electron and the mean field due to the other electrons, leading to a set of coupled one-electron equations. In Hartree-Fock models, the motion of electrons

is treated independent of one another, which leads to an overestimation of the electron-electron repulsion energy and the total energy found by Hartree-Fock models will always be higher than the exact energy. To take into account the correlation of electron motions, the correlation energy is defined as the difference between the experimental energy and the Hartree-Fock energy.

DFT models explicitly introduce a correlation term in the calculation of the total energy. DFT is based on theorems by Hohenberg and Kohn, where there is a unique relationship between the electronic density ρ (rather than wavefunction ψ) and the external potential v in a system with a non-degenerate ground state. DFT calculations yield Kohn-Sham orbitals for a system of non-interacting particles, which generate the same density as a system of interacting particles. In DFT,

$$E_v[\rho] = V_{en}[\rho] + T[\rho] + V_{ee}[\rho] \quad (2-2)$$

$$V_{en}[\rho] = \int \rho(\vec{r})v(\vec{r})d\vec{r} \quad (2-3)$$

with V_{en} the electron-nuclear interaction potential, T the kinetic energy and V_{ee} the coulomb potential. This leads to the Kohn-Sham equation:

$$E_v[\rho] = V_{en}[\rho] + T_{unc}[\rho] + V_{ee-unc}[\rho] + E_{xc}[\rho] \quad (2-4)$$

where the first three terms describe nuclear attraction, kinetic energy and uncorrelated electron-electron interactions, and the exchange-correlation E_{xc} describes electron-electron interactions and kinetic energy. This is where hybrid functionals like B3LYP (Becke, three parameter, Lee-Yang Parr) come in to approximate the exchange-correlation energy functional by introducing exchange contributions from Hartree-Fock theory and correlation energy from empirical or ab initio sources.

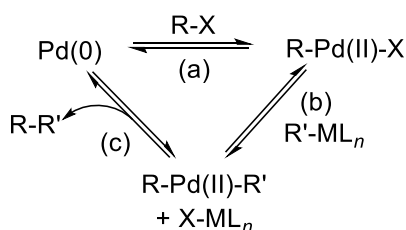
The accuracy of calculations will depend on the choice of the hybrid functional for a particular system, as well as on the basis set used. Basis sets were introduced to solve Hartree-Fock equations analytically by using linear combinations of a basis set (i.e. atomic orbitals) to describe wavefunctions. The basis set takes the form of Gaussian functions to describe exponential wavefunctions and render calculations easier as the product of two Gaussians remains a Gaussian. The basis functions used in these calculations involve a split-valence basis set: two basis functions per valence atomic orbital and one basis function per core atomic orbital, with the possibility to add polarization functions to allow electron distribution away from the nucleus. For example, a 6-31G basis set is constructed using six Gaussians to describe the core orbitals, and valence orbitals are split into three and one Gaussian functions representing its inner and outer components respectively. In the case of a 6-31G* (or 6-31G(d)) basis set, a d-type polarization is added as a single Gaussian for all atoms, except for hydrogen.

The following paragraph describes the practical approach to computations used for this work. Estrada *et al.*¹⁵¹ and Salvatori *et al.*²⁵⁰ have previously demonstrated good correlation between density functional theory (DFT) calculations at the B3LYP/6-31G(d) level and electrochemically estimated frontier orbitals energy levels for isoindigo-containing systems. As such, DFT calculations at the B3LYP/6-31G(d) level were carried out on model structures of the polymers studied to investigate the energy of the frontier molecular orbitals. In these systems side chains have been replaced by methyl groups in order to reduce computation time. The oligomers were built from monomers to dimers, trimers, and tetramers to outline trends and simplify geometry optimization. The calculations were conducted using the Gaussian09 program package provided by the

Partnership for an Advanced Computing Environment (PACE) center at the Georgia Institute of Technology. The orbitals were represented using the Chemcraft 1.6 software,²⁵¹ with 0.03 e/bohr^3 as the isodensity value.

2.2. Synthesis: Suzuki and Stille Polycondensations

Carbon-carbon bond formation is a central tool in the synthesis of pi-conjugated materials, and the outline of a general mechanism involved in these late transition metal catalyzed reactions is given in Scheme 2-1.



Scheme 2-1 Simplified mechanism of coupling reactions, involving (a) oxidative addition, (b) transmetalation, and (c) reductive elimination.

In this dissertation, Suzuki¹⁵ and Stille²⁵² coupling reactions were used, and the synthetic procedures followed are described here.

- Suzuki coupling:
$$\text{R-X} + \text{R}''\text{B(OR}'')_2 \xrightarrow[\text{Base (aq.)}]{\text{Pd(0)}} \text{R-R}' + \text{XB(OR}'')_2$$
- Stille coupling:
$$\text{R-X} + \text{R}''_3\text{SnR}' \xrightarrow{\text{Pd(0)}} \text{R-R}' + \text{R}''_3\text{SnX}$$

It is of particular importance to note the possibility for homocoupling defects as highlighted by Hendriks *et al.*²⁵³ in Stille polymerizations, as well as in Suzuki couplings,²⁵⁴ and as such attention needs to be paid to the ratio of ligand to catalyst.²⁵²

The general procedure followed for Suzuki polymerizations is as follows: In a 100 mL flame-dried Schlenk flask, the dibrominated monomer (0.5 mmol, 1 equiv.), the bis(pinacolato)diboron comonomer (0.5 mmol, 1 equiv.), Pd₂(dba)₃ (15 mg, 4%) and P(*o*-

tol)₃ (10 mg, 6.6 %) were subjected to three cycles of evacuation/argon purging, and then dissolved with 5 mL of degassed toluene after which 1.5 mL (1 M) of degassed aqueous solution of Et₄NOH was added. The reaction mixture was stirred at 85 °C for 60 hours under argon, after which 2-(tributylstannyl)thiophene (0.2 mmol) was added and allowed to react for 3 h followed by addition of 2-bromothiophene (0.2 mmol), which was allowed to react for another 3 hours. The reaction mixture was then cooled to room temperature, and a spatula tip of diethylammonium diethyldithiocarbamate was added to act as a palladium scavenger. The reaction mixture was left stirring with the scavenger at room temperature for 3 hours, and was then precipitated in 100 mL of methanol and filtered through a 0.45 µm nylon filter. The dark solids were purified using a Soxhlet apparatus with methanol until the extracts appeared colorless. The polymers were then fractionated in the Soxhlet apparatus using acetone, hexanes, dichloromethane, and chloroform fractions yielding varying amounts of oligomers and polymer after complete extraction depending on the nature of the comonomer used. Separate concentration and reprecipitation of the hexanes, dichloromethane or chloroform fractions (depending on solubility of the final polymer) in methanol allowed filtering the solids through a 0.45 µm nylon filter to afford the targeted polymer after complete drying in vacuo.

The general procedure for Stille polymerization is as follows: The dibrominated monomer (0.5 mmol, 1 equiv.), Pd₂(dba)₃ (15 mg) and P(*o*-tol)₃ (10 mg) were added to a flame-dried Schlenk flask which was then evacuated and backfilled with argon three times to dry the powders. The bis(trimethylstannyl) comonomer (0.5 mmol, 1 equiv.) was dissolved in a dried separate vial in 5 mL of toluene, then subsequently degassed with argon for one hour. The solution was then added to a Schlenk flask and the reaction

mixture was stirred at 95 °C for 60 hours under argon, after which 2-(tributylstannyl)thiophene (0.2 mmol) was added and allowed to react for 3h followed by addition of 2-bromothiophene (0.2 mmol), which was allowed to react for another 3 hours. The reaction mixture was then cooled to room temperature, and a spatula tip of diethylammonium diethyldithiocarbamate was added to act as a palladium scavenger. The reaction mixture was left stirring with the scavenger at room temperature for 3 hours, and then the mixture was precipitated in 100 mL of methanol and filtered through a 0.45 μ m nylon filter. Fractionation and isolation of the targeted polymer solids followed the same procedure as Suzuki polymerizations.

While in this dissertation conventional Suzuki and Stille polymerizations used, reaction times can be reduced by using microwave couplings or polymerizations,^{255,256} and a reduction in the number of steps can be achieved by using direct arylation (as shown in Chapter 3), also called carbon-hydrogen bond activation, in some cases.²⁵⁷⁻²⁶⁰

2.3. Structural and Polymer Characterization

2.3.1. General Structural Characterizations

All ^1H NMR (300 MHz) and ^{13}C NMR (75 MHz) spectra were recorded on a Varian Mercury 300 spectrometer. Chemical shifts for ^1H and ^{13}C NMR were referenced to residual signals from CDCl_3 (^1H NMR δ =7.26 ppm and ^{13}C NMR δ =77.23 ppm). For future work, it is suggested that NMR analysis be conducted on a 500 MHz NMR in order to increase peak sharpness, and improve chemical characterization of polymers in particular. Elemental analyses were carried out by Atlantic Microlab, Inc. The molecular weight estimations reported in Chapter 3 were obtained using gel permeation chromatography (GPC) performed at 40 °C using a Waters Associates GPCV2000 liquid

chromatography system with an internal differential refractive index detector and two Waters Styragel HR-5E columns (10 μ m PD, 7.8 mm ID, 300 mm length) using HPLC grade THF as the mobile phase at a flow rate of 1.0 mL/min. Injections were made at 0.05-0.07 %w/v sample concentration using a 220.5 μ L injection volume. In chapter 4, GPC was performed in 1,2,4-trichlorobenzene at 135 $^{\circ}$ C with a flow rate of 1.0 mL/min at the Max Planck Institute for Polymer Research (MPIP) in Mainz, using a PSS-WinGPC (pump: Alliance GPC 2000) with an internal differential refractive index detector and a PL-Guard column followed by a PL-MIXED-B column (particle size: 10 mm, dimension: 0.8x30 cm). Injections were made at sample concentration using a 200.0 μ L injection volume. In all cases, retention times were calibrated against narrow molecular weight polystyrene standards (Polymer Laboratories; Amherst, MA were used at UF).

2.3.2. Thermal Characterizations

The thermal stability of the synthesized polymers was determined using thermogravimetric analysis (TGA). TGA was performed on 3 to 5 mg of sample in a Pt pan, using a heating rate of 10 $^{\circ}$ C/min from 50 $^{\circ}$ C to 900 $^{\circ}$ C while maintaining the chamber under nitrogen. Differential scanning calorimetry (DSC) was then conducted by loading 3 to 5 mg of sample into an aluminum pan, and sealing it hermetically with an aluminum lid to determine thermal transitions between -60 $^{\circ}$ C and 350 $^{\circ}$ C. The samples were scanned for three cycles at a rate of 10 $^{\circ}$ C/min or 20 $^{\circ}$ C/min (to increase sensitivity to the glass transition), as the first two cycles were used to erase the thermal history of the sample to remove inconsistencies between samples. The DSC cycles reported in this dissertation include the cycle number that is studied.

DSC measures specific heat by comparing the heat supplied to the sample relative to a known standard (here, an empty aluminum pan) as a function of heating rate, and yields thermograms highlighting glass transition temperature (T_g) and melting (T_m) or crystallization (T_c) transition temperatures when present (Figure 2-1).¹⁸⁹

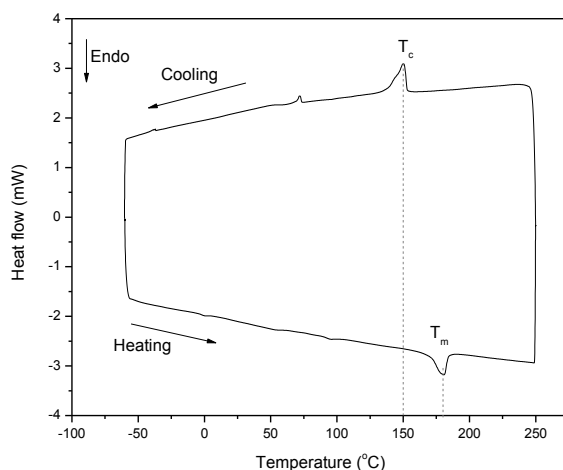


Figure 2-1. Typical DSC thermogram for polymers reported in this dissertation showing a melting transition and crystallization transition. The glass transition is not visible in this thermogram of P[T3(2EH)-iI(HD)], reported in Chapter 4.

The glass transition is a second order transition, where the volume exhibits an abrupt change in slope versus temperature. T_g is related to the change in the range of motion of the polymer chains, and can be explained by the free volume theory. Melting and crystallization are first order transitions, associated with an abrupt change (or discontinuity) in volume at the transition temperature. Semicrystalline polymers form partially crystalline folded chain lamellas, which melt over a temperature range, rather than at a sharp melting point as is the case for small molecule crystals. Melting is an endothermic process, and the T_m range is related to the size of the crystalline lamellae and their degree of order. In particular, strong intermolecular interactions induce a higher T_m , all other parameters being equal. Polymer crystallization is an exothermic process,

which only occurs at significant undercooling (15 °C to 50 °C) because the nucleus has to be stable for further crystal growth.

2.3.3. Optical and Spectroscopic Techniques

In order to quantify light absorption, energy gap, and aggregation in films, solution and film absorption spectra were measured with a Varian Cary 5000 Scan UV-vis-NIR spectrophotometer. Solution absorption was measured in quartz crystal cells using HPLC grade solvents when available or solvents filtered through a 0.45 µm PFTE filter, with the optical density at the maximum of absorbance kept below 0.2. Film absorption was measured on spin coated 1"×1" glass slides using 1 to 5 mg/mL solutions either in chloroform or *o*-dichlorobenzene.

2.3.4. Electrochemical Methods

Electrochemistry was employed to experimentally estimate the ionization potential and electron affinity of the materials synthesized in this dissertation. Cyclic voltammetry (CV) and differential pulse voltammetry (DPV) experiments were performed using an EG&G Princeton Applied Research model 273A potentiostat-galvanostat in an argon filled glovebox. The electrochemical cell was setup using a Ag/Ag⁺ electrode as the reference, a platinum flag or coil as the counter electrode, and a 0.1 M solution of tetra *n*-butylammonium hexafluorophosphate (TBAPF₆, 98 % Acros, recrystallized from ethanol) in acetonitrile (ACN, dispensed from a Vacuum Atmospheres solvent purification system into the glovebox) as the electrolyte. The working electrode consisted of a thin film of polymer drop-casted from a 1 mg/mL chloroform solution onto a platinum disk electrode (0.02 cm²). The calibration of the scans was done by measuring the oxidation potential of the ferrocene/ferrocenium (Fc/Fc⁺) couple dissolved in the electrolyte solution versus the

Ag/Ag⁺ reference. Based on measurements of the formal potential for Fc/Fc⁺ at 0.4 V versus saturated calomel electrode (SCE) in acetonitrile,²⁶¹ and of -4.5 eV being equivalent to 0.0 V versus normal hydrogen electrode (NHE)²⁶²⁻²⁶⁴ (with SCE at +0.2 V versus NHE), the formal potential of Fc/ Fc⁺ is taken to be -5.1 eV versus vacuum, as discussed in Barry Thompson's dissertation²⁶⁵ and highlighted by Cardona et al.²⁶⁶

The background current was recorded from -2.0 V to +1.5 V vs. Fc/Fc⁺ before each set of experiments using a clean platinum disk electrode as the working electrode in the electrochemical cell, and different working electrodes were used for oxidation and reduction studies of the polymers (i.e. the polymer film on the Pt working electrode was only p-doped or n-doped in one given experiment, for the complimentary study, the electrode was replaced with a new polymer film on another Pt electrode). The stability of the polymers was determined by cycling through the corresponding range of potentials in CV experiments at a scan rate of 50 mV s⁻¹ until stabilization of the current response is reached. In some cases, a decrease in the peak current with the number of cycles was observed due to delamination of the polymer film from the electrode. In the case of stable films, the scan rate dependence in CV was measured and the onset of oxidation or reduction was determined by DPV.

2.4. Materials for Device Processing

Solvent Purification: Solvents (chloroform, chlorobenzene, *o*-dichlorobenzene) were purchased anhydrous when available and were deoxygenated through three freeze-pump-thaw cycles. The glassware required is a clean Schlenk flask, thoroughly rinsed with toluene, acetone, and isopropanol followed by flame drying under vacuum or drying overnight in a high temperature oven. Once the flask cooled, the solvent is transferred

into the Schlenk flask using a cannula needle cleaned in the same fashion with a positive pressure of argon in the solvent container, and the flask under static vacuum to induce solvent flow. During the freeze-pump-thaw cycle, the solvent is frozen throughout by submerging the flask in liquid nitrogen for an appropriate amount of time for the particular quantity of solvent (freeze). Once the solvent is frozen, the flask is put under dynamic vacuum for about 3 minutes while remaining in liquid nitrogen (pump), then the vacuum is closed and the solvent is allowed to thaw under static vacuum during which time the dissolved oxygen could be clearly observed bubbling out of solution (thaw). This procedure is repeated 3-5 times until very little, if any, bubbling is observed. The solvent is then taken into the argon atmosphere glovebox (generally <0.1 ppm H₂O and O₂) and stored in cleaned and dried amber glass bottles with PTFE lined caps. During solvent preparation all ground glass joints should be sealed with Teflon tape; Teflon sleeves can also be used to prevent any type of joint grease to leak into the solvents. In particular, no silicone grease should be used in any part of this procedure as if this contacts your solvent it will contaminate the solvent and potentially alter device results.^{267,268} Chloroform was purchased anhydrous from Sigma Aldrich (≤ 1 % water, with 0.5-1.0 % ethanol as stabilizer, product # 288306-1L), and chlorobenzene and *o*-dichlorobenzene were purchased in 1 L Sure/Seal™ bottles (product # 284513-1L and 240664-1L respectively).

Processing additives were used as received since it is unlikely that the amounts of water and oxygen contained in 2-5 %v of the non-anhydrous and non-deoxygenated solvents would impact device performance. 1,8-diiodooctane (DIO) was purchased from Sigma Aldrich (product # 250295-5g) with 98 % purity and stabilized over copper.

Previously Ken Graham described purifying DIO via Kugelrohr vacuum distillation then transferring the purified DIO back into the original container with copper shavings,¹³⁰ but this was not followed for the work described here in order to have similar materials to our collaborators. Diethylene glycol dibutyl ether (DEG-DBE) was purchased from Sigma Aldrich (product # 205621-100ML, ≥ 99 % purity), and used as received. *o*-Dichlorobenzene and 1,2,4-trichlorobenzene were used anhydrous and deoxygenated as described in the previous paragraph. Other processing additives including: hexadecane, 1-iodooctane, 1,6-diiodohexane, 1,8-octanedithiol, triethylene glycol, nitrobenzene, 1-methylnaphthalene, and 1-chloronaphthalene were obtained from previously purchased containers, and checked via ^1H NMR. For further details on purification of processing additives, see Ken Graham's dissertation¹³⁰ and Purification of Laboratory Chemicals by Wilfred L.F. Armarego and Christina L.L. Chai.²⁶⁹

Materials for Active Layer: The fullerene acceptor, [6,6]-phenyl-C61-butyric acid methyl ester was purchased from nano-C, cat. # Nano-CPCBM-BF, >99.5 % purity, and was stored in the glovebox and used as received. Nano-C determined material purity using a 250 x 4.6 mm Cosmosil Buckyprep column and toluene as with a flow rate of 1 mL/min with detection at 360 nm. The Buckyprep column is made up of pyrene-functionalized silica that will provide the best resolution for fullerene purification. The C70 derivative, [6,6]-phenyl-C71-butyric acid methyl ester, was purchased from American Dye Source, Inc., cat. # ADS71BFA, >99 % purity. The purity of the fullerenes was not investigated further, although purification and purity evaluation can be conducted on fullerene derivatives using column chromatography on silica gel using toluene, chlorobenzene, or a mixture of the two.²⁷⁰ Thin layer chromatography (TLC) in toluene

will show if there is any unreacted C60 or C70 in the corresponding PCBM derivative. However, it will be difficult to tell via TLC if there is any PC₇₁BM contaminating PC₆₁BM (or vice versa). For a quantitative analysis of fullerene purity analytical HPLC using a reverse stationary phase can be used to distinguish between C60, C70, PC₆₁BM, PC₇₁BM and other compounds such as PC₈₄BM, which can act as charge carrier traps. Previous work by Cowan *et al.* has shown that the presence of 0.1 % PC₈₄BM in polymer:PC₆₁BM blends leads to a decrease in OPV device performance due to its lower LUMO level (0.35 eV below that of PC₆₁BM); however lower amounts of PC₈₄BM in the blend (0.01%) do not lead to variations in OPV device characteristics.²⁷¹ This enforces that fullerene with lower purities than 99 % should not be purchased for OPV device fabrication. All other materials used were synthesized by Romain Stalder or Chi Kin Lo, and their synthesis and purification are described in this dissertation.

Interlayer Materials: Poly(3,4-ethylenedioxythiophene):poly(styrene sulfonate) (PEDOT:PSS) was purchased from Heraeus (product # Clevios™ P VP AI 4083) and used within six months of purchase. Aluminum oxide coated tungsten boats purchased from R.D. Mathis (catalog # S35BAO-W) were used for all depositions. The aluminum oxide layer around the edges of the boat helps to confine the molten metal to the center region of the boat. Aluminum slugs (99.99%, product # 40417) and calcium shots (99.5%, product # 10127) were purchased from Alfa Aesar. MoO₃ was purchased as a powder from Sigma Aldrich (99.99%, product #: 203815-5G). Lithium fluoride (LiF) was purchased as a powder from Acros Organics (97%, product # 200013). Gold was used from Canadian Maple Leaf coins (99.99% purity) purchased from a local supplier (National Coins, 2007 NW 43rd St, Gainesville, FL 32605, 352-378-3983). The gold

coins were cut into small pieces (2-3 mm in all dimensions) by the machine shop at UF. The pieces were thoroughly cleaned by sonicating in hexanes, toluene, acetone and isopropanol before being brought into the glovebox for use. All materials were used as received unless otherwise noted.

Items for Device Preparation: The materials used for device processing are particularly important as even extremely small quantities of contaminants present in devices can have a significant effect on device performance (hence the use of only PTFE lined lids). It is strongly advised that ANY changes to ANY materials used in device processing first be tested with a control device set before being applied to general device fabrication. The materials commonly used in device fabrication are as follows:

- Vials - Amber, PTFE lined caps. For instance, screw top with solid green Melamine cap with PTFE liner from Sigma Aldrich (item # 27001-U)
- Syringes for active layer - Glass, Popper and Sons (thoroughly cleaned following use by sonicating in chloroform, toluene, and isopropanol for 15 minutes each).
- Stir bars - PTFE coated (thoroughly cleaned following use by heating to 50°C in chloroform overnight).
- Hydrophilic filters for PEDOT:PSS - Whatman puradisc 0.45 μm pore size, nylon, 13mm diameter.
- Hydrophobic filters for active layer solution - Whatman puradisc 0.45 μm pore size PTFE, 13 or 4mm diameter, or EMD Millipore Millex 0.45 μm Fluoropore PTFE, 4mm diameter (product # SLFHR04NL).
- ITO - Pre-patterned from Tinwell Technology, 15 Ω/\square .

2.5. Device Fabrication

2.5.1. Organic Field Effect Transistor Devices

To gain insight into the charge carrier transport parallel to the substrate, bottom gate-bottom contact thin film organic field effect transistor (OFET) devices were fabricated by Wojciech Zajackowski (Max Planck Institute, Mainz, Germany) using substrates with a 300 nm thick SiO₂ dielectric covering highly p-doped Si (p-doping with boron) acting as the gate electrode. The substrates were cleaned by sonication in acetone followed by isopropanol for 20 min each for remove contaminating particles/organic impurities. This was followed by 60 min under UV-ozone to remove trace organic impurities. The SiO₂ surface was functionalized by drop-casting hexamethyldisilazane (HMDS) and heating the substrates to 150 °C for 6 h in a closed vessel. The HMDS layer minimizes interfacial trapping sites. The substrates are then cooled to room temperature, and stored in a glove-box before thermal deposition of the source and drain. The source and drain electrodes are made of 50 nm thick gold contacts. The channel lengths and widths are 10 μm and 700 μm, respectively. The polymer films were prepared under glovebox conditions by drop casting from 4.4 mg/mL oDCB solution at 120 °C on HMDS-functionalized SiO₂ substrate kept at 120 °C and subsequently annealed at 120 °C for 1 h. All the electrical measurements are performed using Keithley 4200 SCS in a glovebox under nitrogen atmosphere.

2.5.2. ITO Substrate Preparation

Pre-patterned films of Indium Tin Oxide (ITO) on glass were received from Tinwell Technology (tinwell@incnets.com , project # TI1678D), and were cleaned following the procedure described below for both space-charge limited current (SCLC) devices and

organic photovoltaic devices. The ITO pattern used throughout this thesis is shown in Figure 2-2, and the active area of the device (0.07 cm^2) is considered to be the overlapping area between the conducting ITO and top electrode layers.

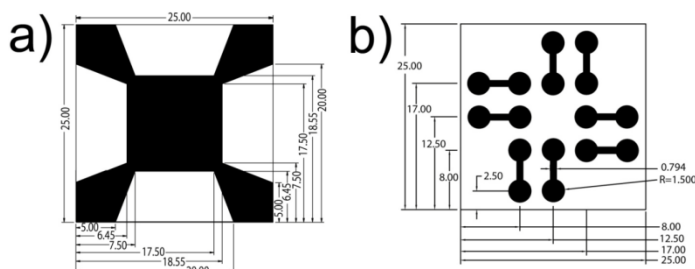


Figure 2-2. (a) ITO etch pattern from Tinwell Technology, project # TI1678D, with dimensions in mm and a resistance of 15 ohm-square, and (b) shadow mask pattern for top electrode deposition. The black regions indicate ITO in (a) and holes in the mask in (b).

When received, the ITO patterned glass shows traces of dust and grime, which are removed by scrubbing the surface with a kimwipe soaked by a sodium dodecyl sulfate solution, followed by sonication in that same solution for 15 min. The remaining aqueous and organic impurities are removed by sequential sonication in deionized water (18 MΩ at 25 °C) for 5 min, then acetone and isopropanol for 15 min each. After sonication, the substrates were removed from the isopropanol solution individually with clean tweezers, blown dry with ultra-high purity argon, and transferred immediately into a Novascan PSDP-UV6T UV-ozone cleaner in a laminar flow hood. Acetone is used to remove organic impurities while removing some of the water, while isopropanol is used because of its higher boiling point in order to blow-dry the substrates to leave fewer residues behind prior to setting the substrates in the UV-ozone cleaner. The substrates were then exposed to UV-ozone plasma for 15 min. Immediately following UV-ozone cleaning, the appropriate interlayer was put down.

For OPV devices and some SCLC devices, PEDOT:PSS (Clevios P VP Al 4083) was spun cast on top of clean ITO-patterned substrates at 5000 RPM for 40 s with a 3 s initial ramp using the Laurell WS-650Mz-23NPP spin coater in a laminar flow hood. The PEDOT:PSS solution was processed from a 5 mL plastic BD syringe and filtered with a 0.45 μm nylon syringe filter (Whatman Puradisc, 13 mm diameter) directly onto the substrate for spin coating. The 5000 RPM spin rate yielded films that were approximately 30 nm thick for OPV devices. The substrates were then set in plastic cases (Althor Product, item #H-1), and were brought into the argon filled glovebox where they were dried at 130 $^{\circ}\text{C}$ for 20 min. The substrates were then cooled on a metal block before being transferred back to their plastic cases for storage in the dry side the glovebox until use. PEDOT:PSS covered ITO substrates were used within a week due to possible variations in the conductivity of the PEDOT:PSS layer with solvent vapors.²⁷²

2.5.3. Organic Photovoltaic Devices

In order to get comparable device results from set to set, care should be taken to repeat the fabrication process as similarly as possible, and a control device should be fabricated within each set. Separate solutions of the donor material and acceptor material were prepared; in the case when the acceptor material was a fullerene derivative, the solution was stirred for at least one hour before being added to the polymer donor solution to form the desired ratio, and in the case of polymer:polymer blends, the polymer solutions were stirred for at least four hours before being combined. If solvent additives were used, the parent solution was left to stir for at least four hours then separated into different vials, and the desired volume of solvent additive was added. The mixed solutions were then stirred overnight to ensure homogeneity and repeatability. It is

important to note the possible impact of solution aging on polymer aggregation in solution and its influence on polymer packing and phase separation in thin films. Furthermore, experiments by Dania Constantinou in the So group have highlighted differences in OPV device performance depending on the mixing time with processing additives. As such, all time scales for solution and film preparation should be recorded.

The solutions were filtered from glass syringes through a 0.45 μm PTFE filter onto the PEDOT:PSS covered substrate, and the active layer was spun as specified. Plastic syringes should not be used to process the active layer as the active layer morphology can be altered. Indeed, Graham *et al.*²⁶⁷ and Carr *et al.*²⁶⁸ separately showed that polydimethylsiloxane (PDMS) present in plastic syringes to lubricate the syringe plunger is incorporated into the active layer solution and leads to changes in the thin film morphology and device performance. Some films were thermally annealed on a hotplate in the glovebox prior to the deposition of the top electrode (the temperature used is detailed in the specific chapters). The devices were then transferred into a holder with the mask shown in Figure 2-2b in order to define the top electrode areas, and the holder was placed inside the thermal evaporator and exposed to 2×10^{-6} torr vacuum for at least four hours for devices reported in chapters 3, and for at least 1.5 h for devices reported in chapters 4 and 5. The overlap between the shadow mask and the ITO pattern resulted in 8 independent cells with an area of 0.07 cm^2 (circle of 3 mm diameter) on one substrate. The top electrode consisted of 10 nm of calcium evaporated with a rate of 1 $\text{\AA}/\text{s}$ and 80 nm aluminum evaporated at a rate of 2 $\text{\AA}/\text{s}$.

2.5.4. Space-Charge Limited Current Measurements

Electron-only and hole-only diode devices were fabricated and tested to extract charge carrier mobilities in pure polymer films as well as donor:acceptor blends, in a similar fabrication process to organic photovoltaic devices. For both types of space-charge limited current (SCLC) devices, ITO substrates were cleaned as described previously, and were immediately placed into the thermal evaporator inside the argon filled glovebox after UV-ozone cleaning. For reasons discussed in Chapter 1, the architecture of electron-only devices was: ITO/Al(100 nm)/organic layer/LiF(1 nm)/Al(100 nm) and the architecture for hole-only devices was: ITO/MoOx(7 nm)/organic layer/Au(80 nm). The organic layer was deposited by spin-coating using a similar process to OPV device fabrication immediately after bottom electrode deposition to prevent shifts in work function.¹²⁹ The fabrication conditions specific to each device are detailed in the subsequent chapters.

2.6. Device Measurement Techniques

2.6.1. Organic Field-Effect Transistor Testing

In an OFET device the source electrode is grounded, thus the gate (V_G) and drain (V_{DS}) voltages can be described relative to the source. For example, with application of a negative gate voltage, an electric field is generated perpendicular to the device layers and produces a buildup of positive charges at the dielectric-semiconductor interface when the semiconductor is p-type (Figure 2-3). Applying a drain voltage simultaneously can cause the charge carriers to travel from the source towards the drain, hence setting the device at its “on” state, as opposed to the “off” state when $V_G = 0$ V. Furthermore, a threshold voltage (V_T) characterizes the gate voltage at which the charge carriers start flowing

between source and drain, and gives an estimate of the concentration of traps in the semiconductor that need to be filled before charge carriers can flow through the device.

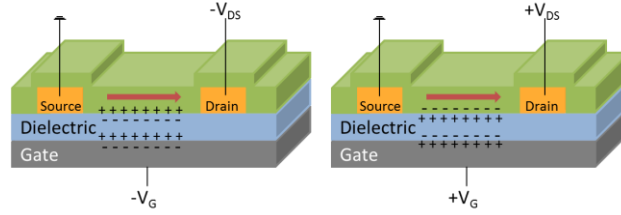


Figure 2-3. Schematic description of charge flow in a p-type and n-type OFET.

The performance of an OFET is commonly illustrated by its output and transfer characteristic curves representing the plot of the source-drain current I_{DS} as a function of the drain voltage V_{DS} for various gate voltages applied, and as a function of the gate voltage V_G (see Figure 2-4). In the output characteristics, at low V_{DS} values I_{DS} increases in a near-linear fashion, and then saturates at higher V_{DS} .^{78,273}

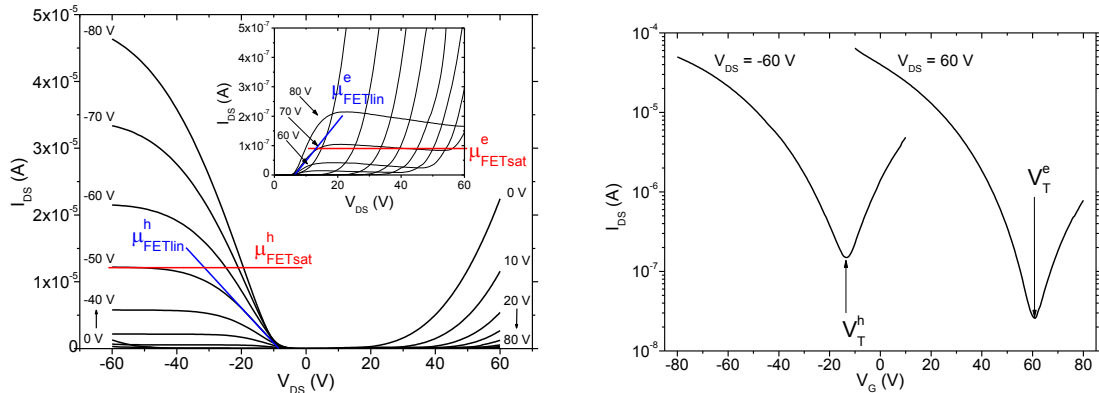


Figure 2-4. Typical output and transfer characteristic measured on π -conjugated polymer thin films. Devices characterized here are bottom-gate/bottom-contact devices fabricated following the procedure described in section 2.5.1. using P[T3(C6)-iI] as the semiconductor as discussed in Chapter 4.

The near-linear regime of the drain current I_{DS} is described by equation 2-5 where L is the channel length, W the channel width, C_i the capacitance of the dielectric per unit area and $\mu_{FET,lin}$ the charge-carrier mobility in the linear regime. Hence, plotting I_{DS} as a

function of V_G at constant V_{DS} allows the determination of $\mu_{FET,lin}$ with the slope of the resulting transfer characteristic curve being given by Equation 2-6 (when $V_{DS} \ll V_G - V_T$).

$$I_{DS} = \frac{WC_i}{L} \mu_{FET,lin} [(V_G - V_T)V_{DS} - \frac{V_{DS}^2}{2}] \quad (2-5)$$

$$\frac{\partial I_{DS}}{\partial V_G} = \frac{WC_i}{L} \mu_{FET,lin} V_{DS} \quad (2-6)$$

In the saturation regime (where $V_{DS} > V_G - V_T$), the charge-carrier mobility at saturation $\mu_{FET,sat}$ can be calculated from the slope of $I_{DS}^{1/2}$ as a function of V_G at constant V_{DS} (using Equation 2-7).

$$I_{SD} = \frac{WC_i \mu_{FET,sat}}{2L} (V_G - V_T)^2 \quad (2-7)$$

All OFET electrical measurements (using a Keithley 4200 unit) were performed inside a nitrogen-filled glovebox at room temperature. The output characteristics were recorded by sweeping V_G from +10 V to -80 V with -10 V steps and V_{DS} from +10 V to -80 V with -0.5 V steps to determine the hole transport, and V_G from -10 V to +80 V with +10 V and V_{DS} from -10 V to +80 V with +0.5 V steps for the electron transport. Transfer curves were obtained by sweeping V_{DS} from +10 V to -80 V with -0.5 V steps with fixed gate voltage at -80 V for hole transport, and V_{DS} from -10 V to +80 V with +0.5 V steps for electrons.

2.6.2. SCLC Testing and Fitting

The current-voltage curves of the devices were measured under dark conditions (i.e. charges are not generated in the active layer through photoexcitation) in the glovebox, scanning a -10 V to +10 V range on one to two cells per device. Because of the asymmetry of the device, electron injection from the LiF/Al electrode (i.e. negative bias at this electrode) and hole injection from the MoOx coated ITO (i.e. positive bias at the

ITO/MoOx electrode) showed better fits to the SCLC model, and the rest of the pixels were scanned from 0 V to +10 V with the positive bias to the bottom Al electrode and the negative bias to the top LiF/Al electrode or positive bias to ITO/MoOx and negative bias to Au for electron and hole-only devices respectively. After converting the current to current density J in A m^{-2} and subtracting the built-in voltage from the applied voltage, the J-V data was plotted on a log-log scale for each pixel. As a first approximation, in the J-V log-log plot, the region where a slope of two is observed is the SCLC region (Figure 2-5). The film thickness L was measured through atomic force microscopy (AFM) or profilometry, and the average thickness was used in the field-dependent SCLC equation 2-8 to determine the zero-field charge carrier mobility (μ_0):

$$J = \frac{9}{8} \mu_0 \epsilon_r \epsilon_0 \exp(0.891 \gamma \sqrt{E}) \frac{V^2}{L^3} \quad (2-8)$$

where ϵ_r is the relative permittivity of the material, ϵ_0 is the permittivity of free space, γ is the field dependent parameter, and E is the electric field (or voltage V over film thickness L) in V m^{-1} .

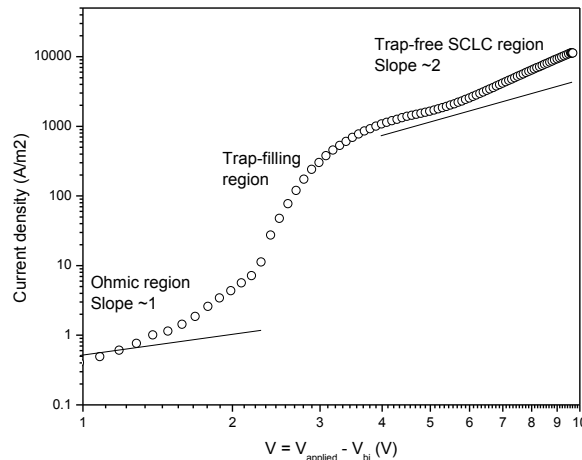


Figure 2-5. Logarithmic plot of the J-V curve showing the ohmic region, trap-filling region and SCLC region, where the slope in log-log plots is usually >2 . In some case, no trap-filling-region is observed and the SCLC region is observed directly after the ohmic region.

For future work, it is encouraged to run SCLC mobility measurements on at least three films with different thickness to verify the dependence of the current density on $1/L^3$ in the SCLC region. The field-dependent SCLC equation was fit to the J-V data in the SCLC region over a minimum of 2 V range. The field-dependent SCLC equation was entered into Origin Pro along with the active layer thickness L and the dielectric constant ϵ_r , which was set to 3.0 based on other conjugated materials reported in the literature.^{272,274}

2.6.3. Power Conversion Efficiency

The performance of a photovoltaic (PV) cell is highly dependent on the intensity and the emission spectrum of the light source. In order to standardize testing of these cells, three main conditions of air mass (AM) have been defined regarding incoming light intensity and irradiance spectrum. These are AM0 (solar spectrum prior to reaching the Earth's atmosphere), AM1.0 (solar spectrum after penetrating through one Earth atmosphere normal to the Earth), and AM1.5G (solar spectrum after penetrating through 1.5 Earth atmospheres, i.e. at an incident angle of 48.2° versus the vertical; the G stands for global and includes both direct and diffuse radiation) as illustrated in Figure 2-6.²⁷⁵

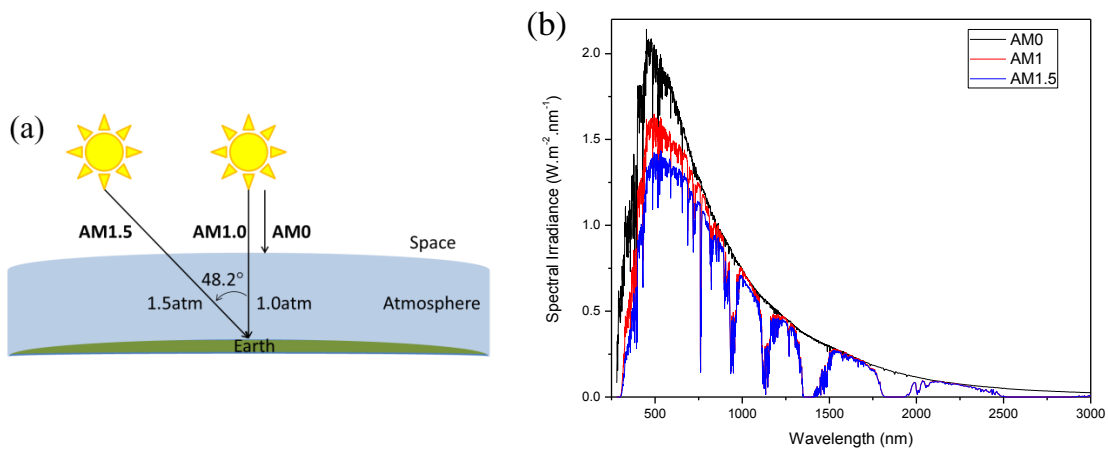


Figure 2-6. (a) Schematic representation of the three air mass conditions for measuring PV cells, and (b) the corresponding solar spectra.

AM0 conditions are used to characterize photovoltaic cells for space applications, while AM1.5 conditions are representative of the solar spectrum in the continental United States over a year. The sum of the total irradiance from the AM1.5G condition is approximately 890 W m^{-2} (89 mW cm^{-2}), although an irradiance of 100 mW cm^{-2} is typically used for characterization. At the University of Florida, AM1.5G illumination was simulated by a 150W xenon arc lamp (Newport 66902 lamp housing and Newport 66907 power supply) fitted with a collimating lens and an AM1.5 filter to generate a relatively uniform column of AM1.5 solar simulated light. To ensure that the irradiance at the surface of the cell was of 100 mW cm^{-2} , the radiant power was measured with a calibrated thermopile detector (Newport 70260) masked with a $5 \text{ mm} \times 5 \text{ mm}$ square aperture (25 mm^2 opening). The location of the aperture and the cell under testing was kept the same with regards to the light source in order to prevent shifts in light intensity. The aperture area was slightly bigger than the PV cells (7 mm^2 circles). For all AM1.5 measurements the irradiance over the 0.25 cm^2 aperture was $25 \pm 0.25 \text{ mW}$, resulting in an irradiance of $100 \pm 1 \text{ mW cm}^{-2}$. At Georgia Institute of Technology, the AM1.5G solar simulator uses a Newport Oriel 69907 power supply connected to a 150 W xenon arc lamp (Newport 6255) with collimating lenses in a Newport Oriel 94021A simulator lamp housing. The collimating lens of the lamp housing modifies the output of the lamp to produce a beam of nearly uniform energy distribution, however perfect collimation is not possible and care should still be taken to properly align solar cells so that they are positioned in the same location as the reference cell. The spectral mismatch of the lamp Xe arc lamp is corrected by use of an AM1.5G filter (Newport 81088A). The solar simulated light passes through a quartz window, into the glovebox where the incoming

light intensity is measured with a reference silicon cell of $2 \times 2 \text{ cm}^2$ (Newport 91150V). The measured light intensity is measured to be $100 \pm 3 \text{ mW cm}^{-2}$.

The cells under AM1.5 illumination are tested by applying a voltage bias and measuring the resulting current with a Keithley 2410 source-measurement unit (SMU). This yields a current-voltage curve that can be converted to a current density-voltage curve if the active area is known in order to remove any active area size dependence. From these curves, the solar cell device characteristics, open-circuit voltage (V_{oc}), short-circuit current (J_{sc}), and fill factor (FF), can be measured and the power conversion efficiency (PCE) of the device can be calculated.

If the field of organic photovoltaics is to become comparable to that of inorganic devices, care has to be taken in the measurement and reporting of the power conversion efficiency as the figure of merit. Statistical analysis of the device characteristics should be conducted and reported. In this work, averages and standard deviations are reported over at least 16 active areas (with 8 active areas on one substrate). The work in this dissertation has attempted to describe discrepancies between the measurement of short-circuit currents in OPVs by comparing the integration of under-filled IPCE measurements to the short-circuit current (J_{sc}) measured through AM1.5 to correct for any cross-talk between active area pixels and to correct for errors on the determination of the active area,²⁷⁶ generally assumed to be 0.07 cm^2 in this work. It is understood that due to the nature of the work conducted in the Reynolds group (focus on the development of novel materials rather than on the development of new electrodes or processes) establishing a standard cell for each material becomes limited by the quantity of material. However, as discussed by Lubner and Buriak,²⁷⁷ further insight on statistical characterization of OPV

characteristics should be gained by reporting the number of different devices tested (active area pixels on one given substrate along with the number of different substrates fabricated and tested), and by establishing the Chauvenet criterion for data rejection (Figure 2-7). Indeed, human tendencies would be to discard data obtained on lower performing cells while retaining data obtained on the highest performing cells (data picking). To limit these tendencies, all the data points N should be recorded (with only bad data points that can be explained by mistake in experimental technique or compared to a known standard with outlying performance being discarded) and averaged, and the standard deviation should be recorded. The Chauvenet criterion then states that data points can be considered for rejection only if the probability (determined based on a Gaussian, or normal, distribution) of obtaining their deviation from the mean is less than $1/(2N)$.

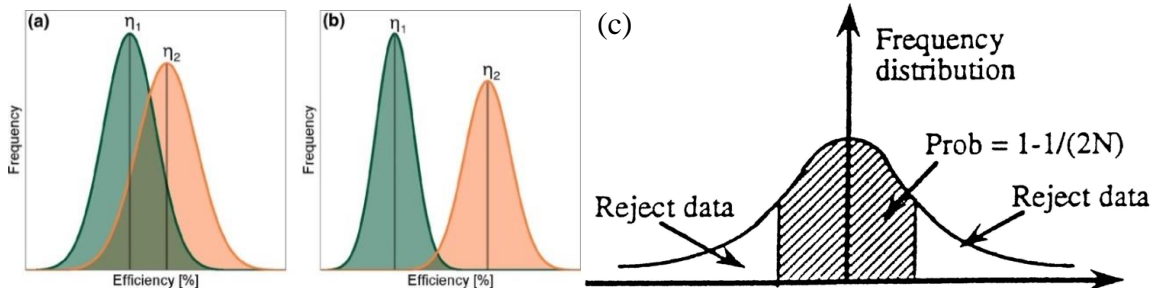


Figure 2-7. (a, b) Relevance of statistical analysis to distinguish the actual improvement from method 2 versus method 1, and (c) illustration of Chauvenet's criterion. (adapted from ^{277,278})

2.6.4. Incident Photon to Current Efficiency (IPCE)

The efficiency of a solar cell determined under AM1.5 illumination conditions represents the overall PCE, and more information can be gathered by measuring the efficiency of current generation as a function of the illumination wavelength λ . This is done in an incident photon to current efficiency (IPCE) measurement, also called external

quantum efficiency (EQE) measurement, where the current is measured as a function of incident light wavelength in short circuit conditions. An IPCE curve is most often expressed as the percentage of incident photons that are absorbed and reflected through the various layers of the devices and are converted into electrons by the solar cell as a function of wavelength. This can be expressed as:

$$IPCE(\%)|_{\lambda} = \frac{\#electrons}{\#incident\ photons} \times 100 |_{\lambda} \quad (2-9)$$

where the number of incident photons can be calculated by measuring the incident power P (in Watts) at a given wavelength λ (in meters):

$$\frac{\# incident\ photons}{s} = \frac{Power}{Photon\ energy} = \frac{P\lambda}{hc} \quad (2-10)$$

with h being Plank's constant ($6.626068 \times 10^{-34} \text{ m}^2 \text{ kg s}^{-1}$), and c the speed of light in vacuum ($299\,792\,458 \text{ m s}^{-1}$). The number of generated electrons when the device is under illumination can be calculated by measuring the output current I of the cell under short circuit conditions (no applied bias) following:

$$\frac{\# generated\ electrons}{s} = \frac{I}{e} \quad (2-11)$$

with e being the charge of an electron ($1.602 \times 10^{-19} \text{ C}$). Combining equations 2-9, 2-10 and 2-11, the IPCE as a function of λ can be expressed by equation 2-12:

$$IPCE(\%)|_{\lambda} = \frac{hcI}{eP\lambda} \times 100 \quad (2-12)$$

IPCE characterization at the University of Florida was performed with a Newport 70612 Illuminator equipped with a Cornerstone 130 1/8M monochromator. The radiant power incident on the cell was determined through the use of the same calibrated Si photodiode coupled with a UDT optometer. Similar to AM1.5 calibration, the photodiode was masked with a $5 \times 5 \text{ mm}^2$ square aperture positioned in the same location as the cell.

The calibration was originally performed in 10 nm increments with smaller increments where large intensity variations were observed. At wavelengths longer than 680 nm, a 665 nm longpass (LP) filter was placed between the monochromator and the photodiode or PV cell to eliminate the second harmonic radiation from interfering with the measurement at wavelengths above 700 nm.

At Georgia Institute of Technology, the IPCE setup was composed of a collimated 600 W Xe lamp (Newport #66485) passing through the appropriate filters to remove second harmonic radiation and a 30 Hz light chopper before being sent to a Cornerstone 260 1/4M monochromator to generate monochromatic light (Figure 2-8). The beam path is focused on a calibrated silicon photodetector masked to have the same area as the active solar cell device, and a radiometric measurement is made to gather the total optical power incident on the detector. The solar device under test is then placed in the exact position where the detector was to maintain the same incident power, and the current is measured as a function of wavelength by a dual channel Merlin digital lock-in radiometry system (RS-232 Newport #70104). Both the detector and the cell under test are connected to an Oriel Merlin digital lock-in amplifier to increase the signal to noise ratio. The TracQ Basic 6.0 software records the data obtained from the Merlin digital lock-in radiometry system, and compares the reference data from the detector scan to the solar cell data to calculate IPCE as a function of wavelength.

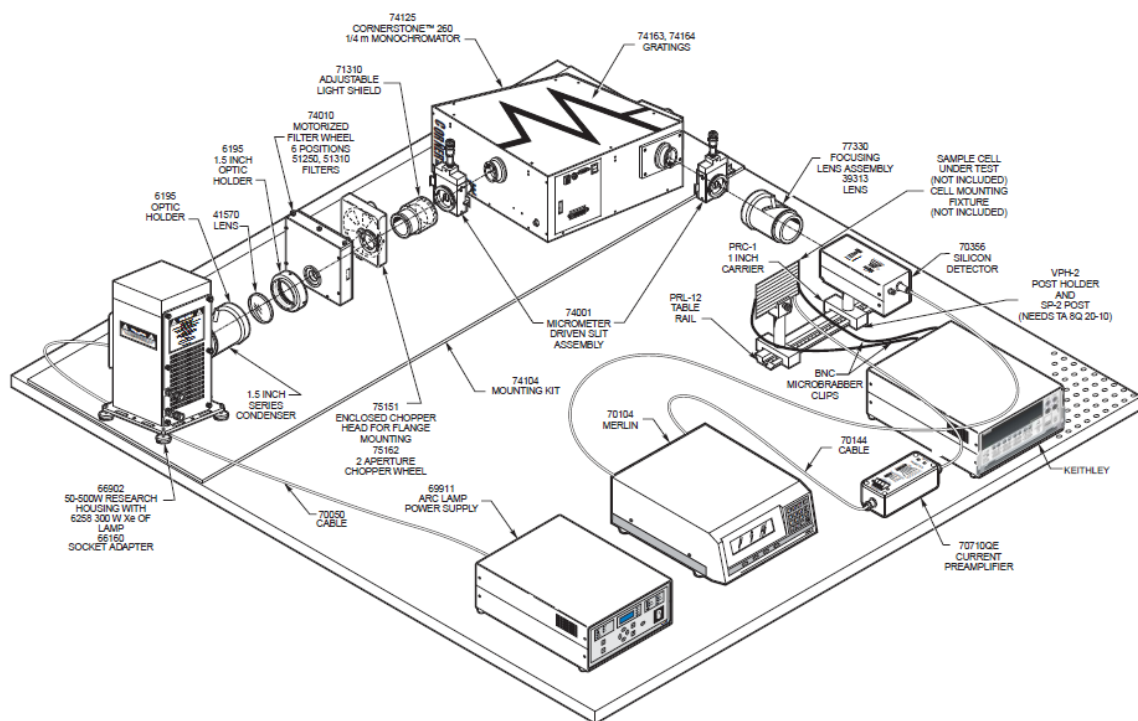


Figure 2-8. Scheme of Newport IPCE setup. (taken from Newport QE system manual)

2.6.5. Charge Modulated Electroabsorption (CMEAS)

In this work, charge modulated electroabsorption spectroscopy (CMEAS) is used to understand the charge transfer (CT) state energy within the active layer of an OPV device, which has been regarded as the effective bandgap in the OPV active layer blend. CMEAS is a technique that detects changes in optical absorption by modulating the electric field to directly measure the effective band gap.^{74,279} More details can be found in the work of Brown *et al.*²⁸⁰ and Tsang *et al.*²⁷⁹ and a brief summary of the measurement principles are summarized here. A monochromatic beam is shined on the active layer and photoexcites charges directly into the charge transfer manifold for incident beam energies that are above a threshold energy, but still below the excited state energies for the individual blend component. Upon photo-excitation at sub-energy gap energies into the CT manifold, charge separation can occur at the blend interfaces and the photo-generated

carriers couple with a modulating electric field to induce changes in the optical absorption of the active layer in the sub-energy gap region. The onset of change in film transmittance ($\Delta T/T$) is then used to determine the effective energy gap in the blend. This novel technique allows detecting the CT states, which have been correlated with open circuit voltage, with a higher signal-to-noise resolution compared to linear optical absorption techniques, and takes into account interfacial effects between the two compounds in contrast to electrochemical measurements.

The OPV devices were probed using an incident monochromatic beam onto the sample through ITO with an incident angle of 45° , which is reflected by the back Al electrode and captured by a calibrated silicon and germanium photo-detector. The sample's internal electric field is modulated by a DC bias superimposed with a small AC voltage at modulation frequency of 1 kHz. A current amplifier and a lock-in amplifier were connected to the detector to increase the signal-to-noise ratio. The samples were kept in a cryostat with a pressure of 10^{-3} torr. The measurements were carried out at room temperature. The OPV devices were probed using an incident monochromatic beam onto the sample through ITO with an incident angle of 45° , which is reflected by the back Al electrode and thus passes through the active layer twice before being captured by a calibrated silicon and germanium photo-detector. The sample's internal electric field is modulated by a DC bias superimposed with a small AC voltage at modulation frequency of 1 kHz. The final signal $-\Delta T/T$ was the ratio of the signals with and without AC field modulation, and is plotted versus the incident beam energy.

2.7. Solubility Characterization

2.7.1. Solubility Measurements

Polymer solubility was measured in *o*-dichlorobenzene (oDCB) by using UV-vis absorbance spectroscopy on a saturated solution and comparing the absorbance to a calibration curve, following the Beer-Lambert law. The calibration curves were constructed for each polymer in oDCB by preparing a mother solution at 1 mg/mL in oDCB, and diluting this initial solution in 3000 μ L oDCB in 2 μ L increments while measuring the absorbance while it remains below 0.5 in order to stay within the linear Beer-Lambert regime. The absorbance at the peak wavelengths were recorded and plotted vs. concentration to make up the calibration curve as seen in Figure 2-9.

The solubilities were measured by adding a sufficient amount of polymer to the filtered HPLC grade oDCB solvent to saturate the solutions. Because of the opaque, dark color of the solutions, no precipitates could be visualized, and solutions with concentrations of 30 mg/mL were targeted. The solutions were stirred using a PTFE coated stir bar and heated to 60 °C overnight, before removing the stir bars and letting the solutions cool down to room temperature for one hour. The solutions were then centrifuged at 4000 RPM for 45 min to separate the non-dissolved material from solution. The precipitated polymers formed a crust on top of the separated solution due to the density of oDCB being 1.3 g cm⁻³ versus being around 1.1 g cm⁻³ for π -conjugated polymers. A pipette was used to remove the solution, and known volumes were added to 3000 μ L oDCB in a quartz cuvette. Absorbance measurements were taken at 3 to 5 different dilution values while remaining in the 0 to 0.5 absorbance domain. The

absorbance was then compared to the calibration curve to determine the amount of polymer dissolved in the original solution.

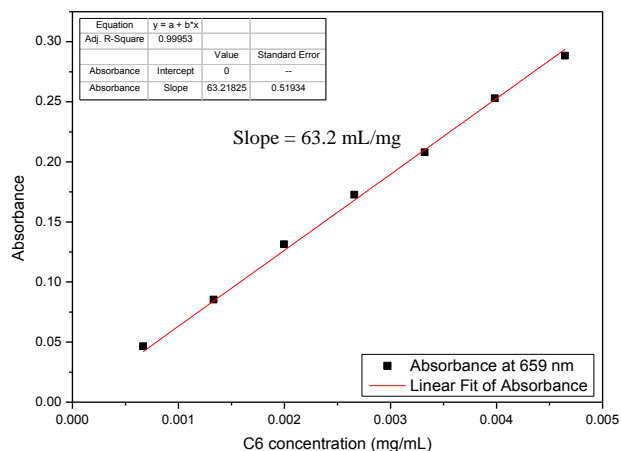


Figure 2-9. Absorbance vs. concentration calibration curve measured for P[T3(C6)-iI] in oDCB.

2.7.2. Solution Scattering Studies

To examine the structural details within polymer aggregates in solution (amorphous aggregates versus ordered aggregates exhibiting lamellas), solution scattering experiments were conducted. Radiation scattering is a non-destructive method giving accurate structural information on averaged particle systems. The following paragraph will give background in X-ray and neutron scattering as they are used in transmission measurements, may it be small-angle X-ray scattering (SAXS) or small-angle neutron scattering (SANS).²⁸¹

2.7.2.1. Neutrons/X-rays and Matter

Any technique using interactions between radiation and matter relies on scattering and absorption processes, which indicates the importance of contrast in the sample in order to gather information.²⁸² For example, contrast in small-angle X-ray scattering (SAXS) is established by the difference in electron density between the particles and their

matrix, while contrast in neutron scattering arises from interactions with the nuclei and is more sensitive to the atomic number (Table 2-1).²⁸³ X-ray diffraction (XRD) and neutron diffraction are non-destructive techniques used to characterize scattering centers, such as crystallites within semi-crystalline polymers.²⁸⁴ Diffraction techniques can answer questions relative to crystallinity, conformation of polymer chains and interchain stacking, shape of crystals, and orientation versus a substrate.

Table 2-1. Characteristics of X-ray (values taken from SLAC beamline 11-3) and neutron sources (values taken from NIST Center for Neutron Research) for scattering studies.

	X-Ray Source	Thermal Neutron Source
Wavelength	0.97 Å (12.735 keV)	1.8 Å (25 meV)
Particle Mass	0.00054858 amu = 9.10940×10^{-31} kg	1.008665 amu = 1.67495×10^{-27} kg
Interactions	Electron cloud (electromagnetic wave)	Atomic nucleus (particle wave)
Contrast	Stronger absorption, but light elements hard to detect High brilliance of source	Lower absorption, but light elements can be seen Low source intensity

In either case, the scattering theory is the same whether the radiation source is X-rays or neutrons, and it is based on the coherent scattering of radiation beams from ordered planes. In order for constructive interference between diffracted waves to occur, their phase has to be the same. This condition can be described in terms of the path length difference being equal to an integer number of wavelength, and can be expressed by Bragg's law (Figure 2-10).

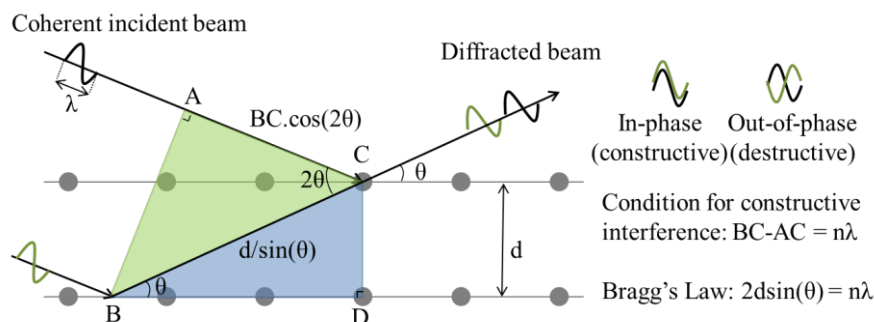


Figure 2-10. Scheme of incident beam being diffracted by crystalline planes leading to beam interference.

Spacings between planes of a crystal d can be obtained when constructive interference is detected at Bragg's angle θ_B for a given wavelength of the incident beam λ . This can also be described in terms of the scattering vector \mathbf{q} (or momentum transfer), which is the difference between the incoming beam \mathbf{k}_0 and outgoing diffraction vectors \mathbf{k}_s (with $|\mathbf{k}_0| = 2\pi/\lambda$) as shown in Figure 2-11. In SAXS or SANS, there is no energy transfer, and as such these are elastic scattering techniques, which give information on structures.

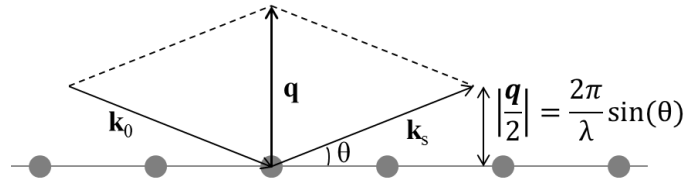


Figure 2-11. Description of the scattering vector \mathbf{q} as a function of incoming beam \mathbf{k}_0 and outgoing diffraction vectors \mathbf{k}_s .

The crystal spacings d can be further defined by Miller indices (hkl) , which represent of series of parallel planes in a crystal with a spacing d_{hkl} . The diffraction spots of various (hkl) planes form a three dimensional array that makes up the reciprocal lattice of a crystal. In this reciprocal space, \mathbf{d}_{hkl}^* is a reciprocal lattice vector with a magnitude being $1/d_{hkl}$ (Figure 2-12).

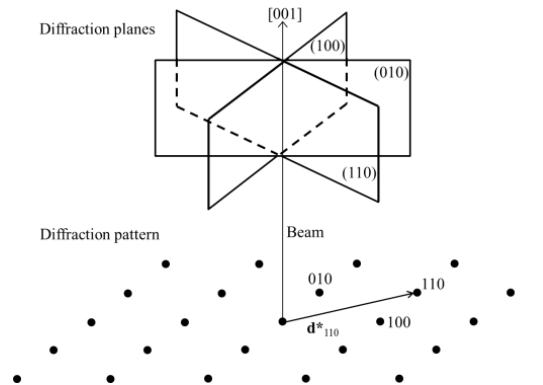


Figure 2-12. Schematic relationship between a reciprocal lattice plane and real space diffraction planes. The reciprocal lattice plane is composed of diffraction spots from crystal planes $(hk0)$ that can be described by the reciprocal lattice vectors \mathbf{d}_{hk0}^* . The zone axis $[001]$ is perpendicular to the reciprocal lattice plane. (adapted from reference ²⁸⁵)

In the reciprocal space, the requirement for constructive interference becomes $e^{i\mathbf{q} \cdot \mathbf{d}_{hkl}^*} = 1$, or $\mathbf{q} = \mathbf{d}_{hkl}^*$, i.e. the Bragg condition is satisfied when the scattering vector \mathbf{q} intersects a reciprocal lattice point defined by \mathbf{d}_{hkl}^* . Following geometric considerations from Figure 2-10, the magnitude of the scattering vector \mathbf{q} that satisfies the Bragg condition (\mathbf{q}_B) is defined by:

$$|\mathbf{q}_B| = \frac{4\pi}{\lambda} \sin(\theta_B) = 2\pi |\mathbf{d}_{hkl}^*| \quad (2-13)$$

Therefore, Bragg's law can be rewritten by:

$$|\mathbf{q}_B| = \frac{2\pi}{d_{hkl}} \quad (2-14)$$

The intensity of the diffraction peak is a function of the structure factor F , which at the Bragg condition is defined by:

$$F_{hkl} = F(\mathbf{q}_B) = \sum_n^{N_B} f_n e^{i2\pi \cdot \mathbf{d}_{hkl}^* \cdot \mathbf{r}_n} \quad (2-15)$$

where f_n is the atomic scattering factor, N_B is the number of atoms in a unit cell, and \mathbf{r}_n is the vector defining the position of an atom within the unit cell. The structure factor gives information about the arrangement of electron distribution within the unit cell. Thus depending on the technique and scattering vector range, WAXS (higher q values) can be used to determine crystal size, orientation and extent of crystallinity, while SAXS (lower q values), can be used to determine particle domain sizes, shape and distribution.

In SANS experiments, the differential scattering cross-section $\frac{\partial \Sigma}{\partial \Omega}(\mathbf{q})$ is measured, and can be confused with the intensity of scattering $I(\mathbf{q})$.²⁸⁶ Contrast in neutron scattering or reflectivity experiments arises from difference in the scattering length density (SLD) of the materials present. The nuclear SLD is to neutron scattering what refractive index is to light scattering, and determines the feasibility of a neutron scattering experiment. As

described by the basic scattering equation 2-16, the differential scattering cross-section of coherently, elastically scattered radiation is a function of the scattering vector q :

$$\frac{\partial \Sigma}{\partial \Omega}(q) = N(\Delta \bar{\rho} V)^2 P(q) S(q) + B \quad (2-16)$$

where N is the number of molecules per unit volume, V is the molecular volume, $\Delta \bar{\rho}$ is the scattering density difference between the scattering particle and solvent, $P(q)$ is the form factor (information on particle size and shape), $S(q)$ is the structure factor (information on inter-particle correlation distances, and degree of local order) and B is the background signal. Thus, a higher difference in SLD between the solvent and particle leads to a higher scattering intensity. The SLD can be calculated from the bulk density of the molecule and the empirical formula of the molecule, and the calculations can be carried out using the NIST Neutron Activation Calculator.²⁸⁷

2.7.2.2. Instrumentation

To get access to neutron sources and high-energy X-ray synchrotron sources, proposals for beamtime need to be submitted to the relevant center. A list of neutron and photon sources and can be found on the National Institute of Standards and Technology (NIST) Center for Neutron Research (CNR) webpage, and examples of proposals can be found in Appendix 1.²⁸⁸

The samples were prepared to be similar to the solutions of polymer in chloroform used for device fabrication and, due to the heavy chlorine atoms in the solvent, neutron scattering was used (as opposed to X-ray scattering) in order to optimize contrast between the polymer system and the deuterated CDCl_3 solvent. The setup for a SANS experiments is described in Figure 2-13.

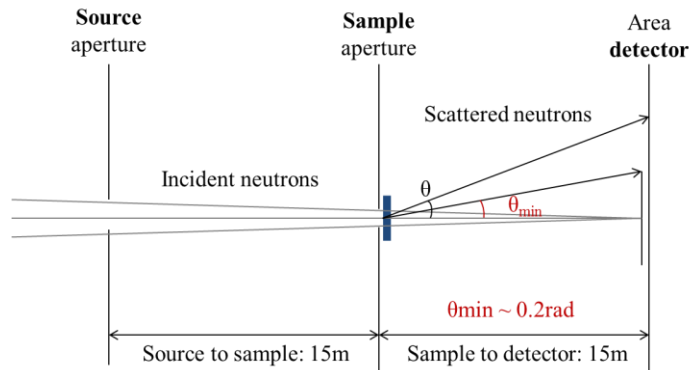


Figure 2-13. NG7-30m beamline setup at NIST CNR.

In this work, two neutron beams were used: LOQ at ISIS and NG7-30m at NIST. The main difference between the two beamlines is the type of source – at ISIS, LOQ uses a pulsed source where the whole q -range is measured over a set time interval; while at NIST, NG7-30m uses a continuous source, where the detector scans the q -range over time.²⁸³ More resources on neutron scattering can be found at the NIST CNR webpage.²⁸⁸

2.7.2.3. Scattering Analysis

The raw scattering intensity of the sample versus scattering vector needs to be corrected by removing scattering from the background (cuvette plus solvent in this case). SANS data reduction was conducted following equation 2-17 to correct for the empty cell and the blocked beam scattering:

$$I(q) = \frac{[I_{sample} - I_{blocked\ beam}]}{T_{sample}} - \frac{[I_{cell} - I_{blocked\ beam}]}{T_{cell}} \quad (2-17)$$

where I is the scattering intensity and T is the transmitted beam.

Plots of the differential scattering cross-section as a function of the scattering vector give structural information about the sample, and three scattering regimes can be distinguished in log-log plots as described in Table 2-2.²⁸⁶

Table 2-2. Main regimes of typical scattering curves and the corresponding information gained. Models used in this dissertation are highlighted in bold.

	Low q ($q < R_g^{-1}$)	Intermediate q ($R_g^{-1} < q < l^{-1}$)	High q ($l^{-1} < q$)
$0 < c < c^*$	Overall dimensions, molecular weight	Excluded volume	Chain flexibility
Examples of fitting models	<ul style="list-style-type: none"> • Guinier 	<ul style="list-style-type: none"> • Gaussian coil • Swollen coil 	<ul style="list-style-type: none"> • Porod • Kratky-Porod wormlike chain
$c^* < c < c^{**}$	Concentration dependent correlation length		

R_g : Radius of gyration, l : persistence length, c^* : overlap concentration

In particular, previous SANS studies on π -conjugated polymers in solution have focused on a handful of fitting models: Debye (i.e. Gaussian coil) or worm-like chain fit to model behavior of P3HT in deuterated *o*-dichlorobenzene or deuterated toluene,¹⁹² worm-like model to fit PTB7 polymers in deuterated chlorobenzene,²⁸⁹ or fractal model for donor-acceptor polymers in deuterated chloroform.²³⁵ The parameters involved in these models, and how they relate to the polymer structure, are described in Figure 2-14 below. In the low- q regime, polymer chains close to theta conditions can be approximated by a spherical form factor in the Guinier approximation, which defines the radius of gyration R_g of the sphere (which can be related to the statistical (Kuhn) length l and the number of repeat units N). Intermediate- q regimes also lead to information on dimension of polymer chains in solution through the Debye model. In the high- q regime, lengths scales probed are on the order of a single polymer chain, which is more adequately represented by a thin cylinder of length l (persistence length) in the Kratky-Porod worm-like chain model.

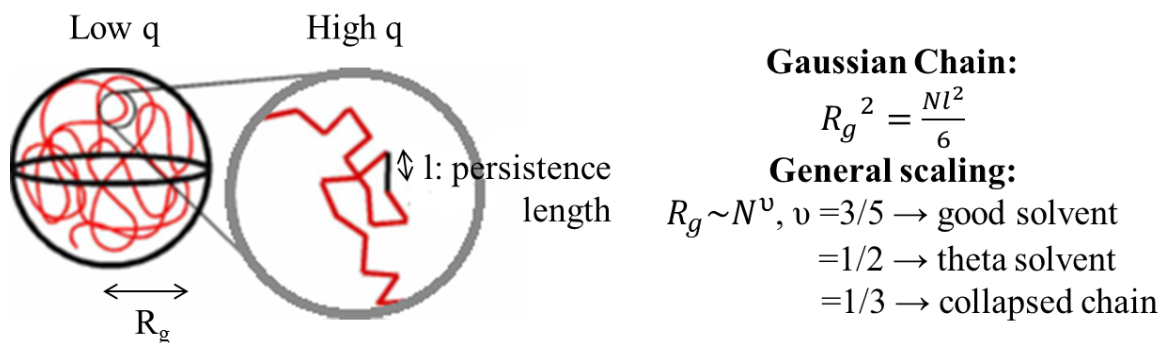


Figure 2-14. Polymer chains in solution approximated by spheres at low q (dimensions ~ 50 - 100 nm) and stiff segments at high q (10 - 30 nm). (adapted from reference ²⁹⁰)

2.8. Thin Film Morphology Characterization

Morphology characterization of thin-films requires the use of complementary techniques to gain a thorough understanding from the molecular to the macroscopic scale. Working our way down from the device scale to the molecular scale, different techniques give surface information whether it is topologic (profilometry and atomic force microscopy (AFM)) or chemical (X-ray photoelectron spectroscopy (XPS)), and bulk information at the microscopic scale (transmission electron microscopy (TEM) or neutron reflectivity) or nanoscopic scale (grazing incidence wide angle X-ray scattering, GIWAXS).

2.8.1. Profilometry

A profilometer is used to scan a surface's profile, in order to measure thickness and quantify roughness of a surface. There are two ways to conduct this measurement: contact or non-contact profilometry. The Bruker DektakXT used for this work is a contact profilometer, which uses a diamond stylus moved vertically in contact with a sample, and then moved laterally across the sample for a specified distance and specified contact force. Contact profilometers use a stylus, which touches its tip to the surface to be

measured. When the surface is displaced relative to the stylus in a horizontal direction, the stylus follows the height changes of the surface in the vertical direction. As the probe is moved across the surface of the sample, the vertical movement of the stylus is captured, and a two dimensional trace of the sample surface is made. In this manner, step heights and surface roughness can be measured, while film stress can be calculated by measuring the curvature of the film. A typical profilometer can measure small vertical features ranging in height from 50 nm to 1 mm. The height position of the diamond stylus generates an analog signal that is converted into a digital signal, which can then be analyzed. The radius of diamond stylus ranges from 20 nm to 50 μm , and the horizontal resolution is controlled by the scan speed and data signal sampling rate. The stylus tracking force can range from less than 1mg to 50 mg.

In this dissertation, the Bruker Dektak XT profilometer was used for measuring thin-film thickness via step height, but it can also be used for 3D mapping of rough surfaces (i.e. surfaces with a Z range on the order of micrometers). It is controlled via the Vision 64 software installed on the computer. Thickness measurements were conducted using a 12.5 μm radius stylus with a 3 mg force on the sample. The force can be varied in order to reproduce the surface more accurately as it is increased but care has to be taken so that the sample (generally a polymer film with a thickness on the order of 100 nm) is not damaged by too great of a force. Little influence has been seen on the height measurement of the active layer when the force is changed from 3mg to 10mg. The height range was set to 6.5 μm to reduce error on the height measurement, but can be increased to 65 μm if the line trace comes out of range due to the substrate not being fully horizontal. Line traces were recorded with a resolution of less than 1 μm /point, and with

at least a third of the trace being the bare substrate, exposed by scratching part of the film with a razor blade. This was used to flatten the trace and then measure the height difference between the substrate and active layer. Generally, at least five measurements were taken next to the pixels of the device that are on each side or closer to the center in order to calculate an average and standard deviation.

2.8.2. Atomic Force Microscopy (AFM)

Atomic force microscopy (AFM) is a form of scanning probe microscopy (SPM), which consists of a family of microscopy methods where a sharp tip is scanned across a surface and probe/sample interactions are monitored. In AFM, a tip with a radius around 10nm is attached to the end of a cantilever and interacts with the surface, experiencing either attractive or repulsive forces that cause the cantilever to bend. The bending of the cantilever is monitored by a laser reflection on a photodiode, and is used to generate various images as the tip scans lines back and forth across a defined area (Figure 2-15). These images reveal surface topology, but can also give information through phase images. Two different AFMs were used for this work: a Veeco Innova (UF) and a Bruker Icon (GT), with the main difference being the location of the piezoelectric scanner. In the Veeco Innova AFM, the scanner head and tip do not move across the sample, but the piezoelectric scanner moves the sample based on the feedback loop in order to keep the tip oscillation amplitude constant, whereas in the Bruker Icon AFM, the sample is maintained in the same location and the scanner head moves according to the feedback loop.

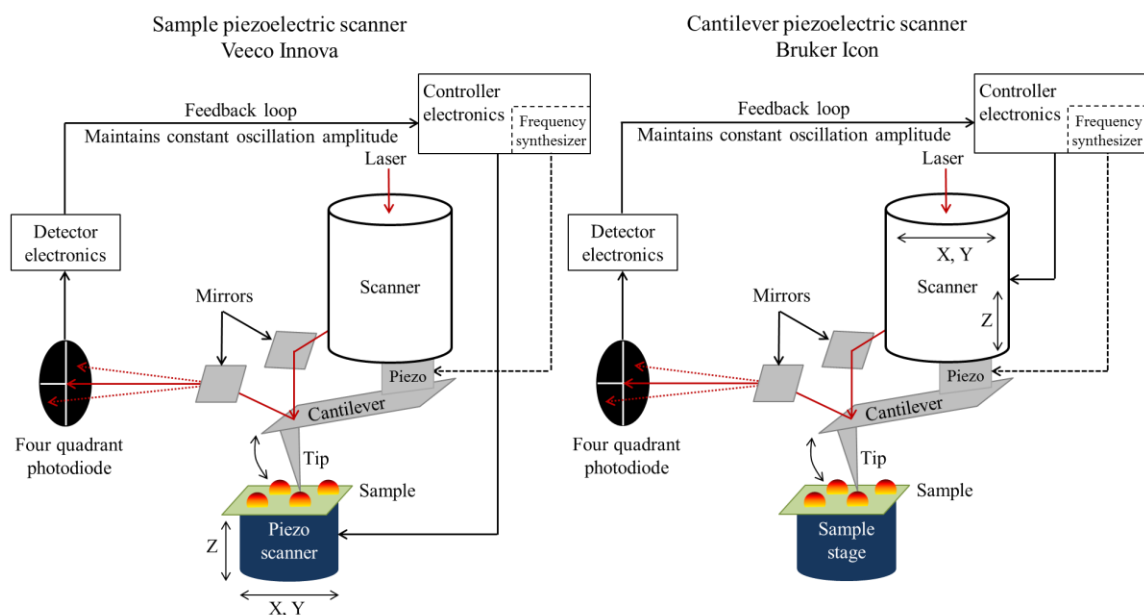


Figure 2-15. Feedback loop electronics involved in either the Veeco Innova or Bruker Icon AFM.

2.8.2.1. Tapping Mode

Tapping mode AFM operates by scanning the sample surface with a tip attached to the end of an oscillating cantilever. The cantilever is oscillated at, or just below, its resonance frequency (either 150 kHz or 300 kHz) by a piezoelectric crystal present in the tip holder with an amplitude around 500 nm (called the drive amplitude). This causes the tip to lightly “tap” the surface and contact the sample at the bottom of its oscillation as it is scanning along the XY direction. By contrast, in contact mode AFM the tip does not oscillate and is maintained in constant contact with the sample throughout the scan. This can cause damage to the sample surface, especially in soft materials where tapping mode is thus commonly used.

Topology images are generated from oscillation amplitude changes as the tip interacts with the sample surface. The tip oscillation amplitude is set and can be dampened when a protrusion above the surface is encountered. This is recorded by the photodiode detector,

which feeds into the controller, which in turn adjusts the height of the sample (in the case of the Innova) or of the scanner head (in the case of the Icon) to maintain the set oscillation amplitude. The change in sample or scanner height Z is recorded for each (X,Y) point and generates an image of the surface topology.

One advantage of having the piezoelectric scanner in the scanner head is that the scans can take place in both ambient and liquid environments, and the temperature of the sample can be adjusted to visualize melting and crystallization transitions.

Several parameters must be adjusted for proper imaging. The AFM is set to scan over the same line in the forward and backward direction, and these two line traces should be compared to distinguish real features from instrument noise (ideally, the two traces should overlap). The scan parameters that can be modified to include: oscillation amplitude setpoint, data collection frequency, and the PID (proportional, integral, and derivative) parameters of the feedback loop. Increasing the value of the P and I (larger impact) terms leads to an increased instrument response time (the D term was rarely adjusted), and a sweet-spot between response time, noise, and resolution can be found. To generate an optimal image the P and I parameters were increased just below the point where noise started occurring.

In particular, the work described in this thesis was conducted by using either 300 kHz tips with a 40 N/m spring constant (Bruker, model: RTESP, part: MPP-11100-10) or 160 kHz tips with a 5 N/m spring constant (μ masch, model: HQ:NSC14/No Al). Active layer blends were scanned over a $2 \times 2 \mu\text{m}^2$ area with a scan rate of 0.7 Hz and adjusting the amplitude setpoint after tip engage and scan initialization in order to reduce noise and increase overlap between the forward and backward scans. The Z range was decreased

from 14.5 μm to 1.0 μm as surface height differences did not reach over a couple hundred nanometers, leading to decreased error in the height measurement. The PID parameters were typically set at $P = 0.8$ and $I = 0.4$ and adjusted by 0.05 increments to decrease height error.

2.8.2.2. Phase Imaging in Tapping Mode

Phase imaging generates an image from the phase difference between the drive oscillation of the tip piezoelectric and the oscillation of the tip as illustrated in Figure 2-16. This type of imaging provides qualitative information on the nature of the material probed, but needs to be analyzed with caution. For example, the tip may penetrate and stick to a soft, amorphous part of the film resulting in a large phase difference, and it can also bounce off of a hard, crystalline region. However, surface effects can cause artifacts in the phase image, interacting differently with the surface on slopes or on different phases of the same material (crystalline and amorphous regions) for example.

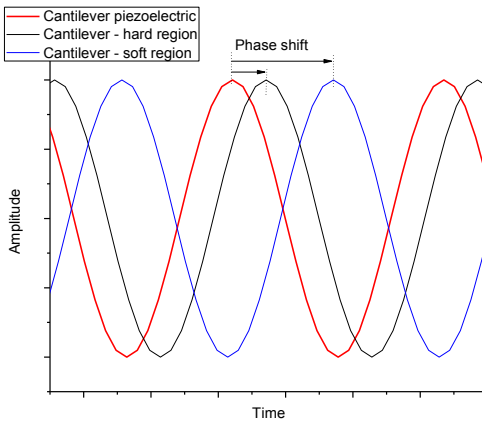


Figure 2-16. Schematic representation of the phase shift between the driving cantilever piezoelectric and the cantilever oscillation over a hard and soft region.

2.8.2.3. Thickness Measurements

When profilometry was not available for thickness measurements, AFM was used. The thickness of the polymer films was measured by removing part of the polymer film

using a razor blade to introduce a height difference between the substrate and the top of the film (step height). The AFM tip was positioned over the scratch and scanned such that part of each line trace was over the film (half to a third of the scan) and part over the area where the film was removed (half to two thirds of the scan). The image was then flattened using the substrate as reference and the height difference between the substrate and polymer film measured. Generally three measurements were taken per device and averaged to get the representative thickness of the device.

2.8.3. Transmission Electron Microscopy

Transmission electron microscopy (TEM) is complementary to AFM as it gives information on the phase composition of the active layer,²⁸¹ and not only the surface topology. TEM operates on the same principles as optical microscopy but uses electron as the source for contrast in order to get resolution on the order of a few angstroms. In bright-field TEM, contrast between materials comes from interactions between the beam of high energy (100-300 keV) electrons and the electron density in a 10 to 200 nm thin film.²⁸⁵ Areas with higher electron density scatter electrons more than lighter elements and less dense materials, which results in the more dense areas appearing darker (crystalline domains will appear darker than amorphous domains for example). Contrast in polymer:fullerene blends is a result of the difference in density between fullerene clusters and polymer fibrils.²⁹¹ However, in samples where contrast is poor, staining one phase or material with a heavy atom is one way to increase contrast. Since the electrons are being transmitted through the film the resulting image is a two dimensional projection of the bulk morphology, which also influences contrast.

Samples for top-down TEM are prepared directly from a solar cell device as the active layer thickness is usually on the order of 100 nm. Top-down samples refer to the fact that the TEM images through the top of the film to the bottom, as opposed to cross-section TEM where the sample is imaged from the side. To prepare TEM samples, the OPV device is broken (using a diamond cutter on the glass side of the device and applying pressure) into smaller pieces near an active area in order to image the morphology that resembles most what is between the electrodes in the active device. After a small piece of sample was broken off, the active layer film was cut by a razor blade to form small squares with areas less than $1 \times 1 \text{ mm}^2$. The broken piece was then placed on the surface of deionized 18 M Ω water in a shallow petri dish, with the glass substrate facing upwards. As the PEDOT:PSS layer dissolved away, the active layer was left floating on the water surface and could be deposited on a holey carbon coated copper TEM grid (Electron Microscopy Sciences #HC200-Cu-100) by approaching the TEM grid over the floating active layer and gently making contact. The use of holey carbon rather than continuous carbon allows for easier correction of aberrations in the TEM and for better contrast. Excess water was removed by applying the edge of a Kimwipe to the bottom of the grid, which also helped with adhesion of the film to the grid, and letting the sample dry in air for several hours before being observed by TEM. This lift-off method to preparing TEM samples has been previously reported in peer-reviewed literature.^{239,291}

All TEM images reported in this dissertation were collected by Ken Graham with the JEOL 200CX TEM at the Major Analytical Instrumentation Center (MAIC), in the Department of Material Science and Engineering at the University of Florida. For more

details on the setup of the TEM and the use of under-focus to increase contrast, the reader is directed to Ken Graham's dissertation.¹³⁰

2.8.4. Thin Film Structural Characterizations

2.8.4.1. Synchrotron Grazing Incidence Wide Angle X-Ray Scattering

Grazing incidence wide angle X-ray scattering (GIWAXS) gives information about order at high scattering vectors q (i.e. low distances) in thin films. It is particularly useful for pi-conjugated polymer thin films to determine pi-stacking and lamellar distances, the extent of crystalline order, and backbone orientation versus the substrate (if a two dimensional detector is used) as shown in Figure 2-17.

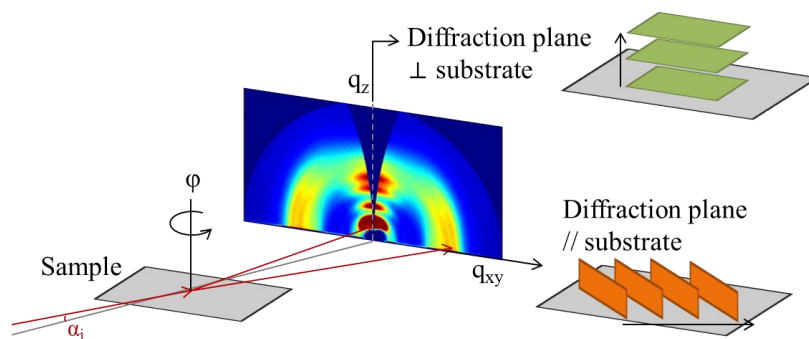


Figure 2-17. Schematic of GIWAXS setup and the information that can be extracted from GIWAXS patterns. (adapted from reference²⁹²)

GIWAXS was performed at Stanford Synchrotron Radiation Lightsource (SSRL) on beamline 11-3. Beamline 11-3 is equipped with a MAR345 image plate detector and operates at an energy of 12.7 keV, corresponding to a photon wavelength of 0.0978 nm. The distance between the sample and the detector was kept at 400mm and the incident angle α_i was maintained at 0.12° in order to achieve the highest scattering intensity from the sample (polymer critical angle $\sim 0.08^\circ$) without interference from the substrate (critical angle for silicon substrate $\sim 0.14^\circ$). The scattering images were calibrated using a

LaB₆ standard. Samples were loaded into a chamber purged with helium to reduce beam damage to the sample and reduce the air scattering background.

The scattered vector can be projected onto the horizontal q_{xy} and vertical q_z axes, with in-plane scattering showing up as peaks along the q_{xy} axis, and out of-plane scattering along the q_z axis (Figure 2-18). The interplane distances can be calculated from the GIWAXS images, as well as degree of crystallinity, coherence length, and the Hermann orientation factor. The data analysis was conducted using the WxDiff software developed by Dr. Stefan Mannsfeld.²⁹³

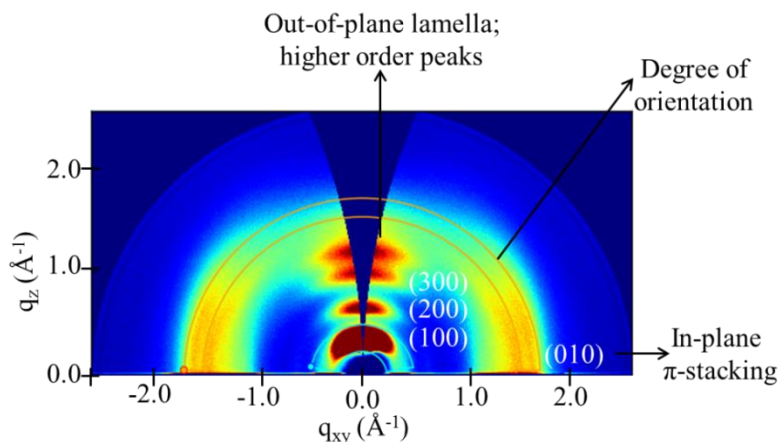


Figure 2-18. Typical GIWAXS image revealing information about π -stacking distances between (010) planes and lamellar packing between (100) planes. These planes can be in-plane or out-of-plane versus the substrate; hence, they will be diffracted along the q_{xy} and q_z axis respectively. The degree of orientation measures how diffuse the scattering intensity is over the ϕ range for a given q value.

In this thesis, distances between crystal planes were estimated from integration yielding line traces along q_{xy} and q_z (Figure 2-19). Gaussian fits to the line trace lead to visualization of crystalline and amorphous peaks as a function of the Gaussian's full width half maximum (FWHM) – arbitrarily, peaks with a FWHM below 0.3\AA^{-1} were considered crystalline and attributed to the relevant crystal plane. The distance between

planes was calculated from the peak position using equation 2-14 (recalled here), and the crystal size L was calculated from the FWHM using the Scherrer equation 2-18:

$$|q_B| = \frac{2\pi}{d_{hkl}} \quad (2-14)$$

$$FWHM(2\theta) = \frac{K\lambda}{L \cos(\theta)} \quad (2-18)$$

where K is the Scherrer constant, λ is the wavelength of the X-ray radiation and θ is half of the diffraction angle.

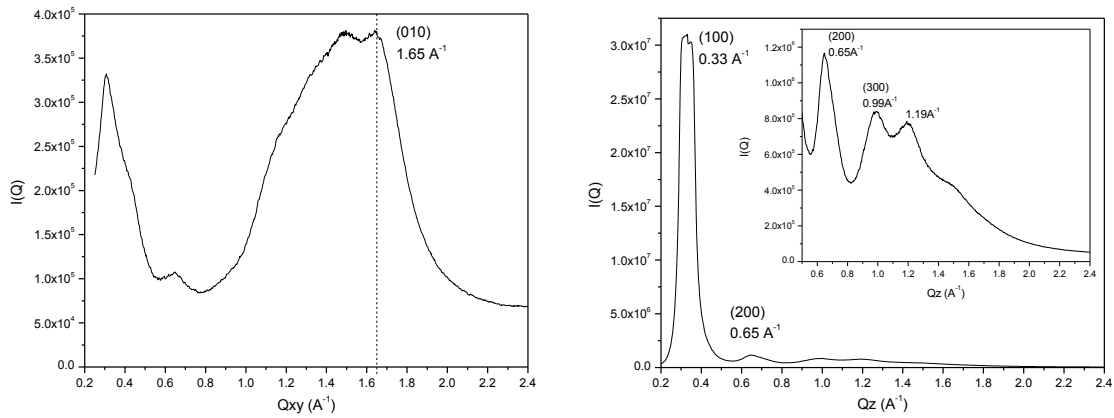


Figure 2-19. Integration along q_{xy} and q_z axes highlighting scattering peaks.

Integration of the scattering pattern over a quarter of the detector (due to a symmetrical scattering pattern) gives information over the degree of crystallinity of the film (Figure 2-20). After integration, the line trace can be fitted with Gaussians and the ratio of the area of crystalline peaks over the total area gives the degree of crystallinity.

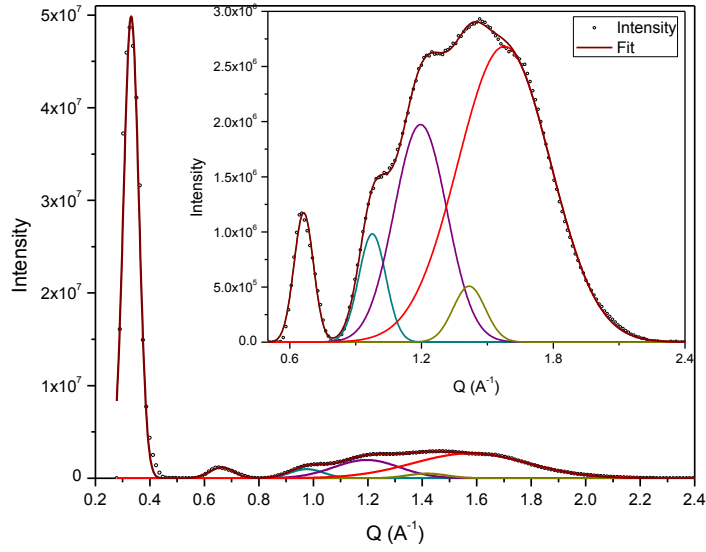


Figure 2-20. Gaussian fits to scattering integrated over a 0° to 90° χ range. Inset shows details in 0.5-2.4 Å⁻¹ range.

Finally, the Hermann orientation factor (HOF) can be calculated by integrating over ϕ for the relevant q value (Figure 2-21). The HOF quantifies the extent of orientation of the lamella relative to the substrate, with edge-on lamella (lamellar peaks along q_z) leading to HOF of 1, and face-on lamella (lamellar peaks along q_{xy}) leading to HOF of -0.5, while randomly oriented crystals lead to a HOF of zero. The formula is given by equation 2-19

$$HOF = \frac{3\langle \cos^2 \chi \rangle - 1}{2} \quad (2-19)$$

where $\langle \cos^2 \chi \rangle$ is the average cosine squared value for the (100) diffraction ring, which can be calculated via equation 2-20:

$$\langle \cos^2 \chi \rangle = \frac{\sum_{i=0}^{90} I_i \cos^2 \chi_i \sin \chi_i}{\sum_{i=0}^{90} I_i \sin \chi_i} \quad (2-20)$$

where I_i and χ_i are the intensity and angle at the i^{th} position (taken every 0.25° step) along the diffraction ring.

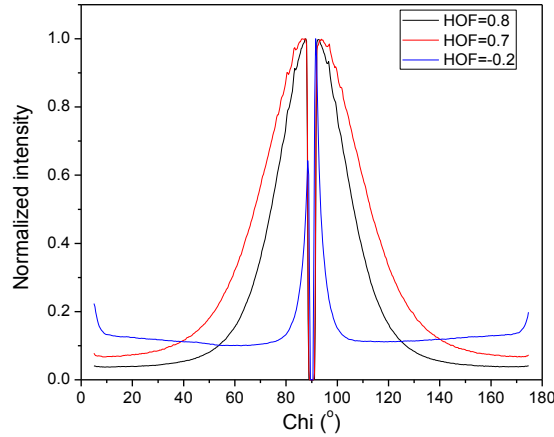


Figure 2-21. Orientation of (100) peaks along χ , and the corresponding Herman orientation factors.

2.8.4.2. X-Ray Photoelectron Spectroscopy

X-Ray photoelectron spectroscopy (XPS) is a surface sensitive technique (1-10 nm depth) revealing elemental composition of a surface in the parts per thousand range. The X-ray photoelectron is an electron ejected from an inner shell (core electrons) when an X-ray is absorbed by an atom, schematically represented in Figure 2-22.

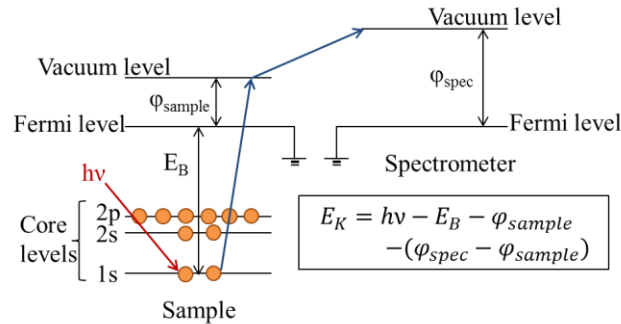


Figure 2-22. Emission process of core electrons in XPS with the kinetic energy of the photoelectron detected by the spectrophotometer.

In XPS, the kinetic energy of the ejected electron E_K is measured by an electron detector and can be used to calculate the binding energy of the atom's photoelectron E_B based on:

$$E_B = h\nu - E_k - \varphi \quad (2-21)$$

where ϕ is the parameter representing the energy required for an electron to escape from a material's surface (depends on both the material of the sample and the spectrometer), h is Planck's constant and ν is the frequency of the incident X-ray. The binding energy of core electrons is characteristic to a given orbital for a given element. For instance, a carbon element would emit electrons from the 1s, 2s, and 2p atomic orbitals, each with a different binding energy.

XPS measurements were conducted on the active layer of OPV devices, and the analysis was performed at Georgia Tech by Rayford Bulloch on a Thermo Scientific K-Alpha XPS system with a monochromatic aluminum source and a 180° double focusing hemispherical electron energy analyzer. The sample was angled relative to the detector entrance (around 45°), resulting in a probing depth of 2-4 nm based on the attenuation lengths for organic materials. Data was collected in 0.1 eV increments with a collection time of 50 ms at each increment. Atomic ratios were calculated using the Vision Manager software and related back to film composition as discussed by Dr. Ken Graham.¹³⁰

2.8.4.3. Neutron Reflectivity

Neutron reflectivity is a neutron diffraction technique measuring the structure of thin films normal to the interface (Figure 2-23) leading to compositional depth profiles. It involves shining highly collimated beams of neutrons at a total reflection angle at, or below, a critical angle (to form an evanescent wave) onto a flat surface and measuring the intensity of the reflected radiation (or reflectivity R) as a function of the scattering vector q_z , which describes the change in momentum Q after reflecting from the material. In SANS, it is assumed that a neutron is only scattered once while passing through the sample (Born approximation); however, in the case of reflection close to the critical

angle, this approximation is no longer verified. Instead, classical optics can be used to model the behavior of neutrons in these conditions. The data is expressed as reflectivity versus momentum transfer, and gives information about the composition, thickness and roughness of each layer.

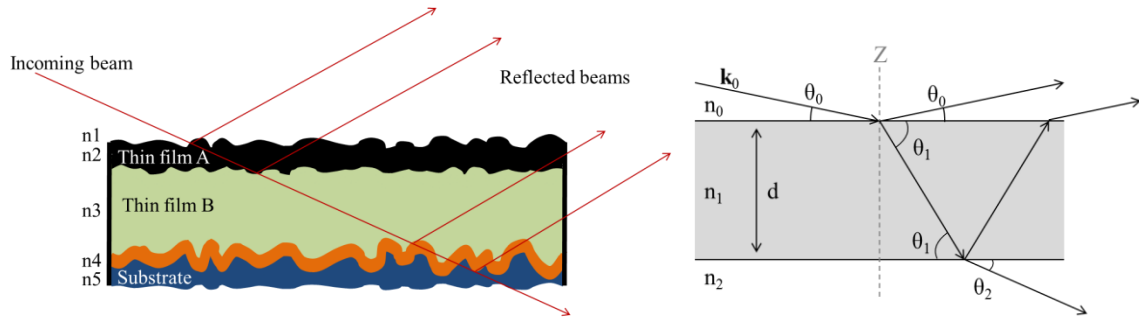


Figure 2-23. Scheme of specular reflection of neutron beams and how the different layers normal to the surface are probed.

Specular reflection, or reflectivity, is defined as reflection where the angle of reflection is equal to the angle of incidence. The critical angle θ_c below which total reflection occurs is given by Snell's law as a function of the refractive index of the two media n_0 and n_1 :

$$\cos \theta_c = \frac{n_1}{n_0} \quad (2-22)$$

The refractive index for neutrons is given by (when ρ smaller than 10^{-6} \AA^{-2}):

$$n_i = 1 - \frac{\lambda^2 \rho_i}{2\pi} \quad (2-23)$$

where ρ_i is the nuclear scattering length density of the i layer, as was described in paragraph 2.5.2, and λ the incident neutron beam wavelength.

In neutron reflectivity, the reflectivity is measured and is defined by the ratio of the number of neutron reflected at a certain q_z over the number of incident neutrons. It is linked to the reflectance r by:

$$R = \frac{\# \text{ neutrons reflected at } q_z}{\# \text{ incident neutrons}} = r \cdot r^* \quad (2-24)$$

Thus, the reflectivity from an interface is given by Fresnel's law:

$$R = \left| \frac{n_0 \sin \theta_0 - n_1 \sin \theta_1}{n_0 \sin \theta_0 + n_1 \sin \theta_1} \right|^2 \quad (2-25)$$

For a single thin film at an interface, this can be expressed by:

$$R = \left| \frac{r_{01} + r_{12} e^{-2i\beta_1}}{1 + r_{01} r_{12} e^{-2i\beta_1}} \right|^2 \quad (2-26)$$

with $r_{ij} = \frac{n_i \sin \theta_i - n_j \sin \theta_j}{n_i \sin \theta_i + n_j \sin \theta_j}$ and $\beta_i = \frac{2\pi}{\lambda} n_i \sin(\theta_i) d_i$, where d_i is the thickness of layer i .

Surface roughness, expressed by the root-mean-square roughness σ , causes diffuse scattering, which modifies the reflectivity for a simple interface to:

$$R = R_0 e^{-q_0 q_1 \sigma^2} \quad (2-27)$$

with the scattering vector $q_i = \frac{4\pi}{\lambda} \sin \theta_i$.

This can be extended to reflection from multiple layers either through the Born and Wolf matrix formulism or the Abeles method. In cases where the Born approximation is applicable, the reflectivity R is simplified to:

$$R(\mathbf{q}_z) = \frac{16\pi^2}{q_z^2} |\hat{\rho}(q_z)|^2 \quad (2-28)$$

where \mathbf{q}_z is the scattering vector projected along the Z axis and $\hat{\rho}(q_z)$ is the one-dimensional Fourier transform of the scattering length density profile normal to the interface.

Practically, the reflectivity R versus momentum transfer q_z $R(q_z)$ is fitted using Parratt iteration to obtain a model for the reflectivity of multiple layers yielding information on the SLD ρ as a function of depth z , $\rho(z)$. The RasCAL software was used to fit the reflectivity data leading to a composition profile.²⁹⁴ The parameters used in the fit for

each layer are: thickness, SLD and roughness. The dependence of $R(q)$ on film thickness, interface roughness, and SLD is described in Figure 2-24. One issue with multilayer systems is that different combinations of $\rho(z)$ (SLD, roughness, and thicknesses) lead to the same $R(q_z)$, hence complementary techniques such as TEM or XPS should be used to verify the accuracy of the $\rho(z)$ fit.

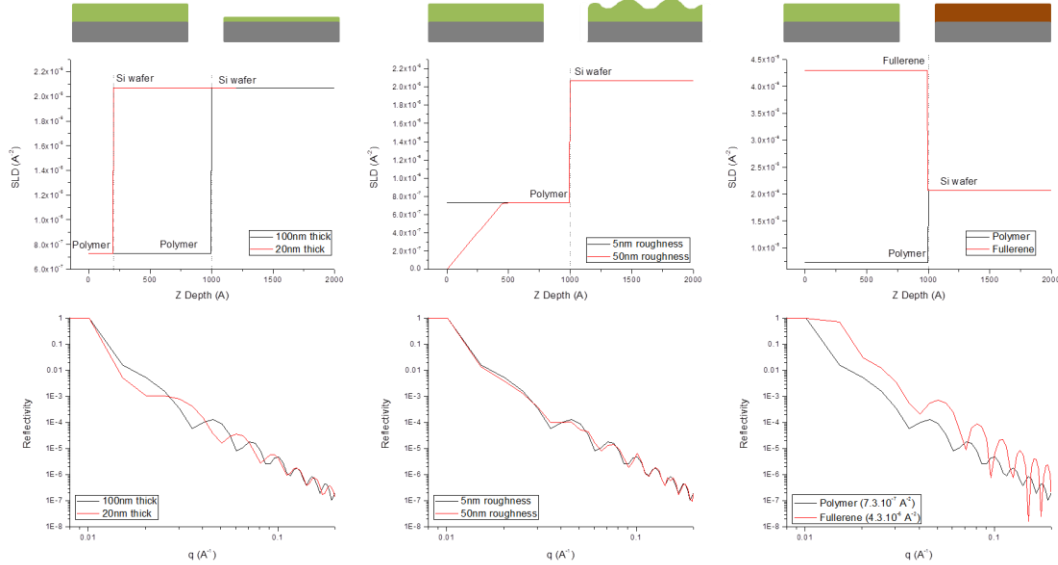


Figure 2-24. Influence of thin-film parameters (thickness, roughness and material/SLD) on composition depth profile and on the reflectivity measurement. Model systems were input into the RasCAL software and the corresponding reflectivity curves were plotted in order to give the reader an idea of the link between reflectivity curve and SLD profile.

CHAPTER 3. ISOINDIGO IN N- AND P-TYPE POLYMERS FOR ORGANIC PHOTOVOLTAICS

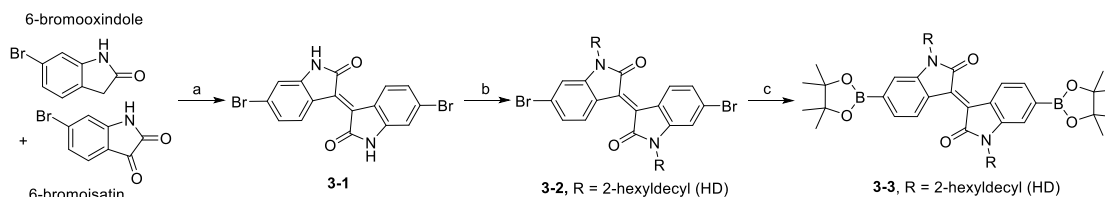
3.1. All-Acceptor Isoindigo-Based Conjugated Polymers

As discussed in the introduction, isoindigo (iI) is an electron-deficient dye, which can be incorporated into materials for organic electronics much like the diketopyrrolopyrrole (DPP) unit.¹³⁴ The low-lying energy levels of model compounds and broad light absorption in iI systems motivated the design of conjugated polymers containing iI as n-type materials to replace fullerene derivatives with limited absorption in bulk heterojunction (BHJ) solar cells. In order to investigate the effect of strong electron withdrawing units and of steric hindrance, four iI-based conjugated polymers were designed: the homopolymer of isoindigo P(iI) along with copolymers with 2,1,3-benzothiadiazole (BTD) P(iI-BTD), thienopyrrolodione (TPD) P(iI-TPD), and diketopyrrolopyrrole (DPP) P(iI-DPP), ranging from more electron-deficient to less electron-deficient co-monomers.

3.1.1. Polymer Synthesis of P(iI), P(iI-BTD), P(iI-TPD), and P(iI-T-DPP-T)

In order to synthesize this family of polymers containing electron-deficient units, Suzuki or direct arylation were chosen as the polymerization methods. The iI monomers used were synthesized as described in Scheme 3-1. The two brominated precursors to form 6,6'-dibromoisindigo (compound 3-1), 6-bromoisatin and 6-bromooxindole, are commercially available, and an aldol condensation under acidic conditions using a catalytic amount of concentrated hydrochloric acid in acetic acid as the solvent yielded compound 3-1 as a brown powder. Precursor 3-1 was further purified by filtration, and washed with water, ethanol and ethyl acetate. After alkylation under basic conditions,

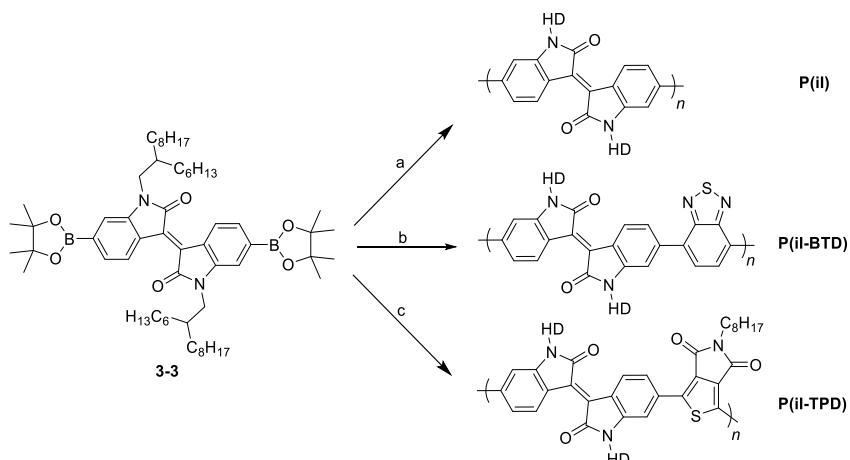
6,6'-dibromoisindigo 3-2 was borylated under Miyaura conditions using the pinacol ester of diboron in anhydrous 1,4-dioxane in the presence of potassium acetate and catalytic amounts of $\text{PdCl}_2(\text{dppf})$. This affords the diboron monomer 3-3 in good yields after precipitation in cold methanol and further washing of the filtered solids with methanol.²⁹⁵



Scheme 3-1. Synthesis of the dibromo- and diboron-isindigo monomers. a) HCl conc., AcOH, 90 °C, 95%. b) 1-iodo-2-hexyldecane, K_2CO_3 , DMF, 95 °C, 71%. c) Pinacolester diboron, $\text{PdCl}_2(\text{dppf})$, KOAc, 1,4-dioxane, 80 °C, 56%.

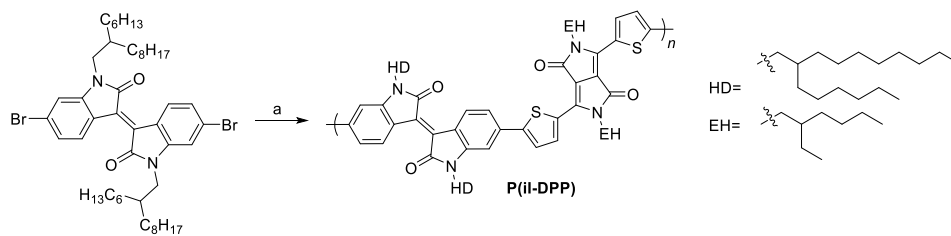
Subsequently, monomer 3-3 was reacted with the dibromo-functionalized iI 3-2, BTD, and TPD via Suzuki polycondensation to yield the homopolymer P(iI), and the alternating copolymers P(iI-BTD) and P(iI-TPD) as shown in Scheme 3-2. Synthesis and optoelectronic characterization of P(iI) and P(iI-BTD) were carried out by Dr. Romain Stalder in the Reynolds group. Suzuki polycondensation reactions were carried out in degassed toluene at 85 °C using $\text{Pd}_2(\text{dba})_3$ and tri(*ortho*-tolyl)phosphine as the catalytic system, and a solution of degassed 1 M tetraethylammonium hydroxide in water as the boron-activating base. After reaction for 72 h, the reaction mixture was precipitated in methanol, followed by dissolution of the precipitate in chloroform with diethylammonium diethyldithiocarbamate as a palladium scavenger for a couple hours at room temperature. The solution was then concentrated and precipitated in methanol before Soxhlet extraction with methanol then hexanes in order to remove low molecular weight products. Chloroform was then used to extract higher molecular weight

compounds, and the solution was precipitated in methanol and filtered to yield the desired polymers.



Scheme 3-2. Synthesis of three all-acceptor polymers based on iI. a) $\text{Pd}_2(\text{dba})_3$, $\text{P}(o\text{-tyl})_3$, Et_4NOH , toluene, 85°C , 74%. b) $\text{Pd}_2(\text{dba})_3$, $\text{P}(o\text{-tyl})_3$, Et_4NOH , toluene, 85°C , 95%. c) $\text{Pd}_2(\text{dba})_3$, $\text{P}(o\text{-tyl})_3$, Et_4NOH , toluene, 85°C , 40%.

$\text{P}(\text{iI-TPD})$ can also be obtained by direct arylation as shown by Grenier *et al.*,²⁵⁹ and this procedure was followed by Kin Lo in the Reynolds group to yield $\text{P}(\text{iI-DPP})$ as described in Scheme 3-3. Direct arylation has the benefit of decreased reaction steps to synthesize the monomers, however, the regioselectivity to the 2-position on thiophene rings can be difficult to control. One strategy to prevent reaction at the 3,4-positions is to append methyl groups on the thiophene ring, although torsion along the polymer backbone will likely be affected by the use of 3,4-dimethylthiophene compared to unsubstituted thiophene.²⁹⁶



Scheme 3-3. Direct arylation polymerization yielding $\text{P}(\text{iI-DPP})$. a) 3,6-Bis(5-bromo-2-thienyl)-2,5-dihydro-2,5-di(2'-ethylhexyl)-pyrrolo[3,4c]pyrrolo-1,4-dione, Hermann's catalyst, tris(*o*-methoxyphenyl)phosphine, Cs_2CO_3 , THF, 120°C , 80%.

The number average molecular weight (M_n) of the chloroform soluble fraction of P(iI) is 28.7 kDa with a polydispersity index (PDI) of 2.4 after Soxhlet extraction as measured by gel permeation chromatography in THF against polystyrene standards. By comparison, P(iI-BTD), P(iI-TPD) and P(iI-DPP) exhibit a M_n (PDI) of 16.3 kDa (3.5), 25.9 kDa (2.9), and 24.6 kDa (3.9) respectively, which can be converted in degrees of polymerization of 20 (40 iI repeat units), 19, 26, and 20 for P(iI), P(iI-BTD), P(iI-TPD) and P(iI-DPP) respectively.

3.1.2. Optical Properties and Electrochemistry of P(iI), P(iI-BTD), P(iI-TPD) and P(iI-DPP)

The UV-vis-NIR absorption spectra of P(iI), P(iI-BTD), P(iI-TPD), and P(iI-DPP) were recorded in the solid-state (Figure 3-1), showing absorption past 600 nm for all polymers. In particular, P(iI-DPP) exhibits complementary absorption to P3HT into the NIR.

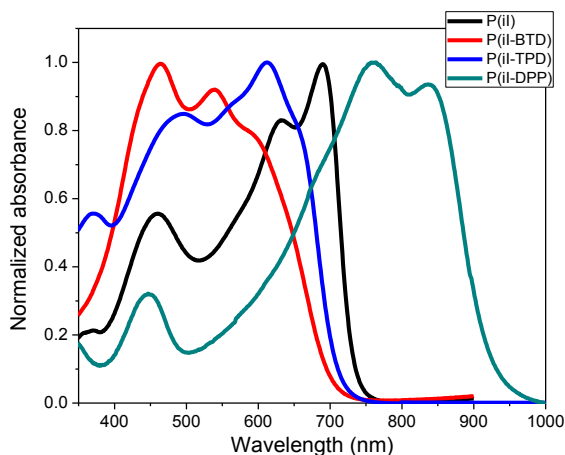


Figure 3-1. Normalized UV-Vis absorption spectra of P(iI), P(iI-BTD), P(iI-TPD), and P(iI-DPP) in thin films.

In the solid state, P(iI) has an onset of absorption at 731 nm (or 1.70 eV) and a maximum absorption peak at 690 nm. Compared to the homopolymer, P(iI-BTD) and

P(iI-TPD) have a blue-shifted absorption, with an onset at 700 nm (1.77 eV) and 721 nm (1.72 eV) respectively, and absorption maxima at 464 nm and 616 nm respectively. P(iI-DPP) has the lowest energy absorption onset of the four polymers, most likely due to the electron-rich thiophene linkers between the iI and DPP units. If the polymer backbones were planar, trends in frontier molecular orbitals (FMOs) would follow the electronic nature of the monomers with incorporation of TPD along the backbone leading to a decreased energy gap and a red-shifted onset of absorption compared to BTd, which is on par with the observations from the UV-vis-NIR spectra.

In order to pin-point the origin of these variations in absorption, electrochemical measurements were conducted on polymer thin films drop cast onto platinum button electrodes. These films were electrochemically oxidized and reduced in a 0.1 M TBAPF₆ solution in dry acetonitrile under inert atmosphere, and the potentials reported here are calibrated against an internal standard, the ferrocene/ferrocenium couple (Fc/Fc⁺) set at -5.1 eV versus vacuum as was discussed in Chapter 2. Figure 3-2 shows the tenth CV cycles of oxidation and reduction as well as the reductive DPV for the four polymers, and oxidative DPV in the case of P(iI-TPD). The reductive CV show one reversible redox process, and no or non-reversible oxidation reactions. The onset of reductive DPV is used to estimate the electron affinity (EA) of the polymers.

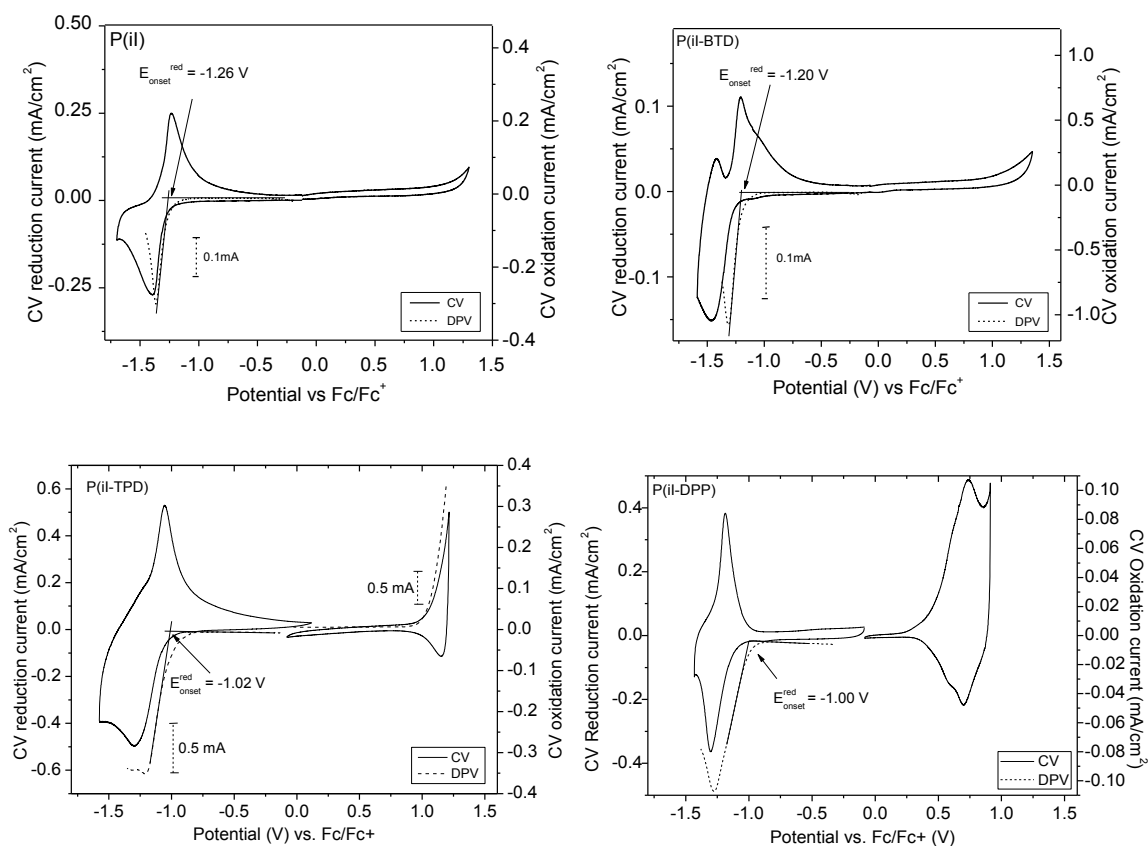


Figure 3-2. CV and DPV of (a) P(iI), (b) P(iI-BTD), (c) P(iI-TPD), and (d) P(iI-DPP) recorded on thin-films of polymer drop-cast on a Pt-button electrode in 0.1 M TBAPF₆/acetonitrile electrolyte versus the Fc/Fc⁺ redox standard.

The onset of reduction is found at -1.26 V, -1.20 V, -1.02 V and -1.00 V vs. Fc/Fc⁺ for P(iI), P(iI-BTD), P(iI-TPD) and P(iI-DPP) respectively, which correspond to estimated electron affinities of 3.84 eV, 3.90 eV, 4.08 eV and 4.10 eV. Because the unstable oxidation of the polymers prevents an electrochemical determination of the ionization potential (IP), it was calculated from the optical energy gap of the thin films. In these case of P(iI-TPD) for example, the optical gap of 1.72 eV leads to an estimated IP of 5.80 eV. In all cases, the polymers display high enough EA to promote electron transfer from P3HT, and high IP to be stable to oxidation in air.

3.1.3. Polymer Modeling by DFT

A change in optoelectronic properties can arise either from a change in the electron-donating or accepting strength of the co-monomer and/or a change in the extent of delocalization affected by the dihedral angle between the two monomeric units. Density functional theory (DFT) calculations at the B3LYP/6-31G* level were performed on P(iI) and P(iI-BTD) by Dr. Leandro Estrada and on P(iI-TPD) in order to explain the trends seen in the absorption spectra. As shown in Figure 3-3, DFT model compounds show that steric hindrance between hydrogens on phenyl-phenyl linkages along the backbone, either between two isoindigo units or between isoindigo and BTD, leads to higher dihedral angles (35°) compared to phenyl-thienyl linkages between isoindigo and TPD (15°). These theoretical results are in agreement with crystal structures obtained on small molecule model systems that crystallize with dihedral angles of 39° and 6° between phenyl rings and iI and thienyl rings and iI respectively.¹⁵¹

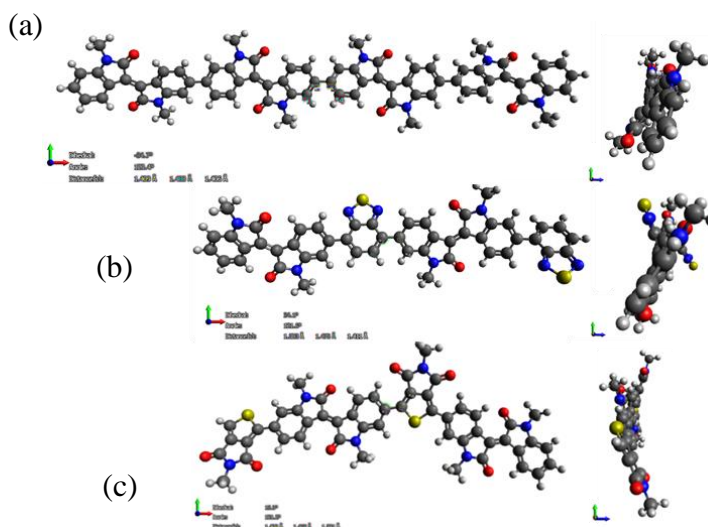


Figure 3-3. Lowest energy geometry (a) P(iI), (b) P(iI-BTD), and (c) P(iI-TPD) model tetramers as calculated by DFT.

Model oligomers of iI, going from one iI unit to the tetramer, show a destabilization of the HOMO and a stabilization of the LUMO as the number of units is increased as is

expected for the homopolymer. On the other hand, there is little change in the FMO energy levels of oligomers of iI-BTD past the dimer, which explains the more red-shifted absorption of P(iI) compared to P(iI-BTD).¹⁵¹ In the case of P(iI-TPD), the HOMO energy levels is calculated at -5.51 eV vs. vacuum and the LUMO at -3.20 eV vs. vacuum in model iI-TPD-iI-TPD. Extending the iI-TPD oligomers shows the LUMO staying at -3.20 eV past the iI-TPD-iI trimer, with the HOMO around -5.51 eV. The trends in energy gap and energy levels follows what was observed from UV-vis-NIR and electrochemistry with P(iI-TPD) having a similar energy gap to P(iI) but with higher estimated ionization potential and electron affinity as shown in Figure 3-4.

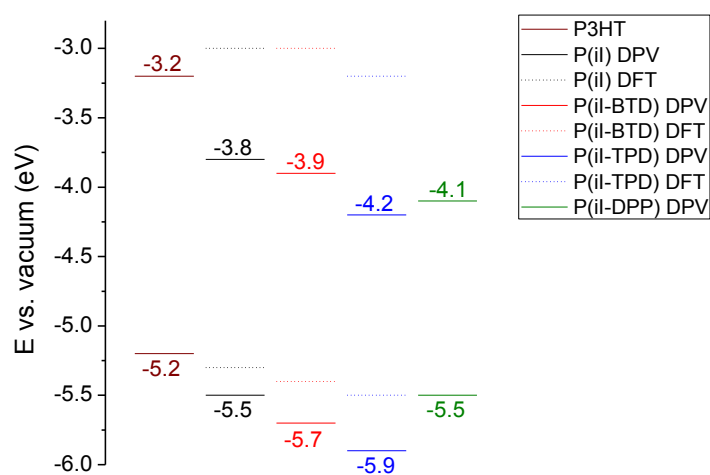


Figure 3-4. Summary of electron affinities and ionization potentials for the four polymers, and their comparison to the energy levels in P3HT measured under the same conditions.(adapted from²⁹⁷)

3.1.4. All-polymer Active Blend Solar Cells

3.1.4.1. Device Characteristics

Due to their suitable electron affinities for exciton dissociation from P3HT and their complementary absorption properties to P3HT, P(iI) and P(iI-BTD) were used in all-polymer blends for conventional architecture BHJ photovoltaic devices. These devices

were fabricated by spin-coating mixtures of P3HT and P(iI) or P(iI-BTD) in chlorobenzene (CB) at a total solid concentration of 12 mg/mL onto PEDOT:PSS covered ITO slides, followed by sequential evaporation of calcium (10 nm) and aluminum (100 nm) as the cathode.

P3HT:P(iI) active layers were obtained by spin coating at 2000 rpm for 55 s with a three second ramp up and annealing at 150 °C for 10 min prior to cathode deposition. By changing the weight ratio of P(iI) to P3HT, the light absorption as well as the phase separation between the two polymers can be tuned, leading to varying current-density – voltage (J-V) curves obtained on these devices as seen in Figure 3-5.

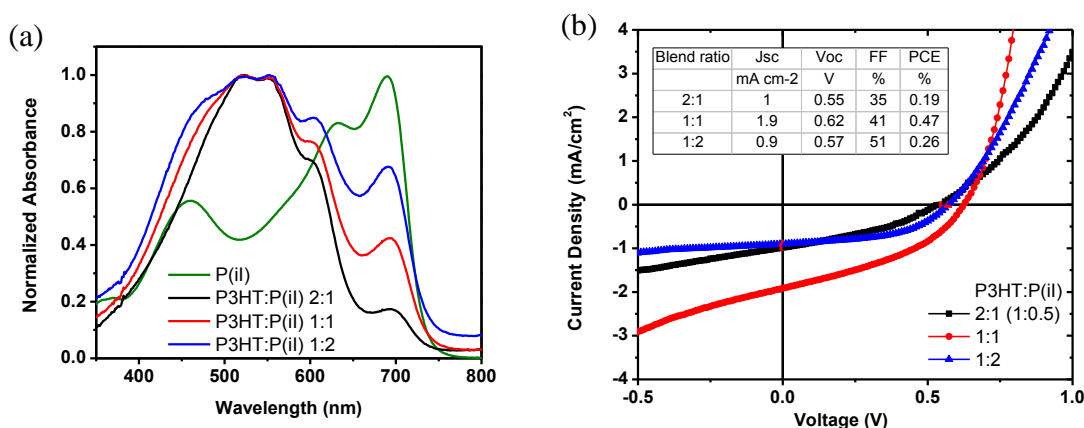
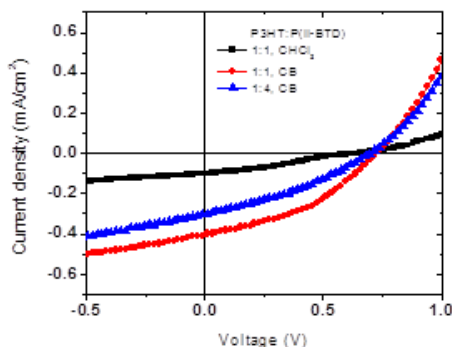


Figure 3-5. (a) Normalized thin-film absorbance of P(iI) and of P3HT:P(iI) active layers at different blend ratios (2:1, 1:1, and 1:2), and (b) J-V curves obtained at different P3HT:P(iI) blend ratios under AM1.5 illumination.

The resulting films have a thickness around 110 nm and show broad absorption from 400 nm to 750 nm, and at a 1:2 P3HT:P(iI) ratio the contribution from P(iI) at its maximum 688 nm scales to 68% of the maximum absorption of P3HT. By comparison, in P3HT:PC₆₀BM cells, the absorption of the active layer spans to 670 nm,¹⁰³ which limits the contribution of photons with energies lower than 1.85 eV to current generation. The OPV device parameters are summarized in the inset of Figure 3-5b, and highlight that

there is no significant gain in open-circuit voltage (V_{oc}) in P3HT:P(iI) blends compared to P3HT:PC₆₁BM devices (~ 0.6 V). The efficiencies of 0.5% are obtained in 1:1 blends, with short-circuit currents (J_{sc}) of 1.9 mA cm^{-2} and fill factors (FF) around 0.41.

Devices fabricated using P3HT:P(iI-BTD) in a 1:1 ratio as the active layer demonstrated higher performance when spun-cast from CB compared to chloroform, as shown in Figure 3-6. When CB is used as the solvent, an increase in the J_{sc} is observed compared devices fabricated with chloroform; however, increasing the amount of P(iI-BTD) to 80% of the active layer yields a slight decrease in the short-circuit currents. In P3HT:P(iI-BTD) devices efficiencies of 0.1% are obtained in 1:1 blends, which exhibit the highest FF of the studied P3HT:P(iI-BTD) devices. Interestingly, the V_{oc} of these blends is 0.1 V higher than in P3HT:P(iI) blends.



Blend ratio, solvent	J_{sc} (mA cm^{-2})	V_{oc} (V)	FF (%)	PCE (%)
1:1, CHCl ₃	0.1	0.66	29	0.02
1:1, CB	0.4	0.73	40	0.12
1:4, CB	0.3	0.70	34	0.07

Figure 3-6. J-V curves of P3HT:P(iI-BTD) conventional devices under AM1.5 illumination fabricated from chloroform or chlorobenzene (CB) at varying blend ratios.

The device parameters measured for these active layers are to be compared to the best performing all-polymer solar cells currently, where the open circuit voltage and fill factor are on par with other reported all-polymer blends but short circuit currents are increased to 7 mA cm^{-2} in the best performing devices.^{244,246,247,298} In order to understand the factors causing this difference in short-circuit current, the active layer morphology and transport properties in P3HT:P(iI) and P3HT:P(iI-BTD) blends were studied.

3.1.4.2. Morphology of All-Polymer Blends

Phase separation between the two polymers was imaged using tapping mode atomic force microscopy (AFM). As discussed in Chapter 1, the large entropic barrier to polymer mixing typically leads to large phase separation and domain sizes in polymer blends. Indeed, this is what is observed in the case of P3HT:P(iI) AFM images in Figure 3-7a, with domain sizes on the order of 100 nm rather than 10-20 nm, which are deemed optimal for OPV devices. However, recent reports of all-polymer blends with similar domain sizes, yet power conversion efficiencies of 3.3% point to other limiting factors in blends with isoindigo polymers.²⁴⁷

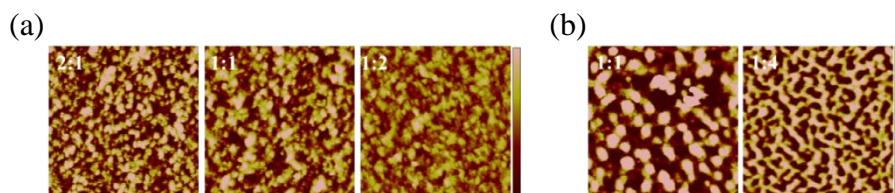


Figure 3-7. AFM height images of (a) P3HT:P(iI) blends and (b) P3HT:P(iI-BTD) blends spun-cast from chlorobenzene at varying ratios ($5 \times 5 \mu\text{m}^2$ scan, 20 nm height scale).

Similar AFM topology images are recorded on P3HT:P(iI-BTD) blends as seen in Figure 3-7b, with even larger feature sizes observed in the 1:1 blend ratio active layer compared to P3HT:P(iI) films. This can explain the drop in J_{sc} from 1.9 mA cm^{-2} to 0.4 mA cm^{-2} in P3HT:P(iI) and P3HT:P(iI-BTD) 1:1 blends respectively.

3.1.4.3. Transport properties via SCLC Devices

In addition to phase separation recent work has highlighted the importance of balanced charge transport in all-polymer active layers to increase short circuit currents,²⁹⁹ hence electron mobilities in P(iI), P(iI-BTD), P(iI-TPD) and P(iI-DPP) were measured using space charge limited devices as described in Chapter 2. In this section, films of P(iI) or P(iI-BTD) were spun-cast at 1000 rpm for 55 s from a 12 mg/mL solution in

chlorobenzene onto an aluminum covered ITO slide, and annealed at 150 °C before deposition of 1 nm lithium fluoride (LiF) followed by 100 nm of aluminum as the top contact. Figure 3-8 shows the field dependent fits to the current density versus effective voltage curves in the SCLC region, where the slope of the log-log plot is close to 2. From the SCLC fits electron mobilities were calculated to be $3.7 \times 10^{-7} \text{ cm}^2 \text{ V}^{-1} \text{ s}^{-1}$ and $1.4 \times 10^{-6} \text{ cm}^2 \text{ V}^{-1} \text{ s}^{-1}$ in P(iI) and P(iI-BTD) thin films respectively, and are to put in perspective to hole mobilities of $3.3 \times 10^{-4} \text{ cm}^2 \text{ V}^{-1} \text{ s}^{-1}$ in P3HT films.²⁰³ SCLC electron only devices were also fabricated for P(iI-TPD) and P(iI-DPP), but no SCLC region was observed for these polymers.

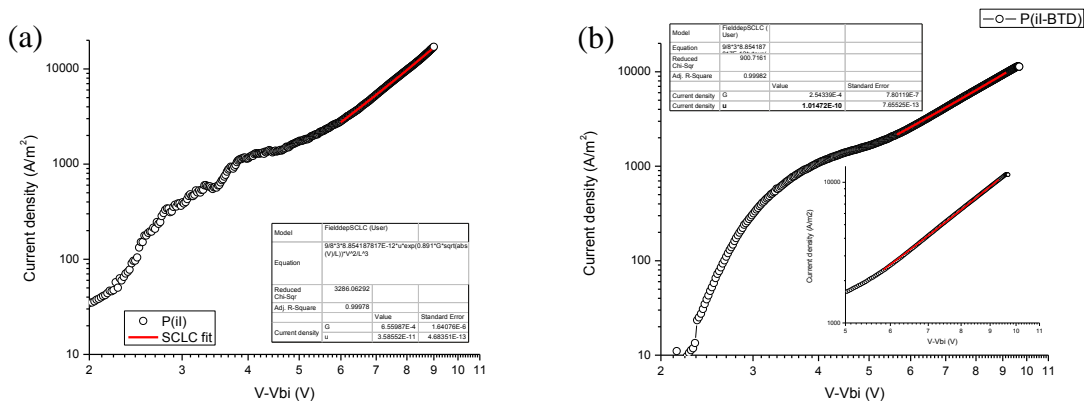


Figure 3-8. SCLC region in electron-only (a) P(iI) and (b) P(iI-BTD) devices. The electron mobility is extracted from the region with a slope of 2 in the log-log curve.

Structure-property relationships were attempted to be outlined as shown in Table 3-1, however, little correlation was found between polymer structure and charge transport in these systems due to the lack of transport characteristics for P(iI-TPD) and P(iI-DPP). The electron mobilities around 10^{-7} and $10^{-6} \text{ cm}^2 \text{ V}^{-1} \text{ s}^{-1}$ found for P(iI) and P(iI-BTD) are two to three orders of magnitude below the targeted electron mobility of $10^{-4} \text{ cm}^2 \text{ V}^{-1} \text{ s}^{-1}$ for balanced hole and electron mobilities, and are expected to be one of the limiting factors in these P3HT:isoindigo-based polymer blends.

In conclusion, this study shows that n-type polymers based on isoindigo lead to PCEs of 0.5% in blends with P3HT. The low electron transport properties in P(iI) and P(iI-BTD), as well as large phase separation in these all-polymer blends are detrimental to OPV device performance. It is hypothesized that the steric hindrance from the phenyl rings along the backbone limits charge mobility in these polymers, and further n-type polymer designs could rely on thienyl-phenyl linkages to improve charge mobility, and morphology could also be optimized by using solvent blends to form smaller domains in the active layer.^{190,300}

Table 3-1. Summary of optoelectronic properties of P(iI), P(iI-BTD), P(iI-TPD) and P(iI-DPP), including SCLC electron mobilities.

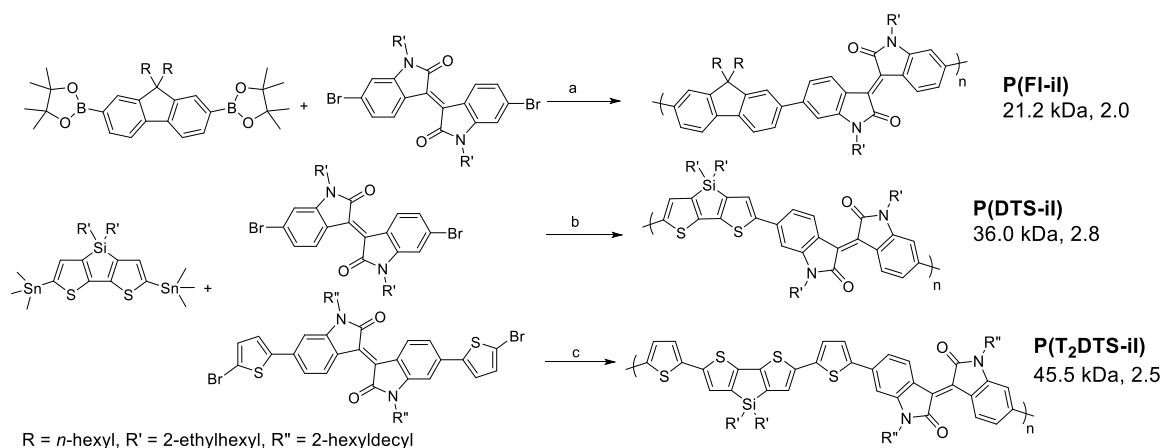
			UV-vis-NIR		DPV		DFT	SCLC
	M_n (kDa)	PDI	λ_{\max} (nm)	$E_{\text{gap}}^{\text{opt.}}$ (eV)	$E_{\text{on}}^{\text{ox}}$ (V)/ IP (eV)	$E_{\text{on}}^{\text{red}}$ (V)/ EA (eV)	Dihedral angle	μ_e ($\text{cm}^2 \text{V}^{-1} \text{s}^{-1}$)
P(iI)	28.7	2.4	690	1.70	NA/5.54	-1.26/3.84	34.5	3.7×10^{-7}
P(iI-BTD)	16.3	3.5	464	1.77	NA/5.67	-1.20/3.90	35.0	1.4×10^{-6}
P(iI-TPD)	25.9	2.9	616	1.72	NA/5.80	-1.02/4.08	15.0	
P(iI-DPP)	24.6	3.9	760	1.34	NA/5.46	-1.00/4.10		

3.2. Donor-Acceptor Polymers for Blends with Fullerenes

3.2.1. Polymer Synthesis of P(FI-iI), P(DTS-iI), and P(T₂DTS-iI)

In the previous section it was shown that using more electron-rich co-monomers such as thiophene-flanked DPP results in extended absorption to the near-IR. In order to investigate further the impact of interactions between electron donating and accepting moieties along the backbone for OPV materials, three polymers were synthesized: poly(fluorene-*alt*-isoindigo) P(FI-iI), poly(dithienosilole-*alt*-isoindigo) P(DTS-iI), and its derivative with thiophene bridges P(T₂DTS-iI) (Scheme 3-4). The use of bridged aromatic rings, like fluorene or dithieno[3,2-b:2',3'-d]silole, has been a widely used

handle to increase planarity in the donor unit, while providing the possibility of appending a solubilizing group without disturbing the structure's planarity as would be the case for bithiophene for instance.²⁹⁶ Polymerizations were carried out by Dr. Romain Stalder,⁴² using either Suzuki copolymerization conditions to synthesize the less electron-rich P(FI-iI) using borylated 9,9-dihexylfluorene and 6,6'-dibromo-N,N'-(2-ethylhexyl)-isoindigo as the monomers, and Stille coupling conditions for the more electron-rich 2,2'-bistrimethylstannyl-4,4'-bis-(2-ethylhexyl)-dithieno[3,2-b:2',3'-d]silole co-monomer to yield P(DTS-iI) and P(T₂DTS-iI).



Scheme 3-4. Synthesis of P(FI-iI) via Suzuki coupling, and P(DTS-iI) and P(T₂DTS-iI) via Stille coupling. a) Pd₂(dba)₃, P(*o*-tyl)₃, Et₄NOH (1 M), toluene, 85 °C, 93%. b) Pd₂(dba)₃, P(*o*-tyl)₃, toluene, 85 °C, 94%. c) Pd₂(dba)₃, P(*o*-tyl)₃, toluene, 85 °C, 90%.

2-Bromothiophene and 2-trimethyltin thiophene were added sequentially in the reaction medium to install thiophene rings as an end-group on the backbone. After purification by diethylammonium diethyldithiocarbamate to remove the palladium catalyst, a Soxhlet extractor was used to fractionate polymers by solubility, using methanol, and hexanes prior to extracting the higher molecular weight fraction with

chloroform. The molecular weights reported in Scheme 3-4 for the three polymers were obtained by gel permeation chromatography in THF against polystyrene standards.

3.2.2. Optical Properties and Electrochemistry

In order to gauge the range of light absorption in these three polymers, UV-vis-NIR spectroscopy was measured on the polymer thin-films (Figure 3-9). The broad absorption spectra of P(iI-Fl) from 400 nm to 650 nm makes it an ideal candidate for OPV devices, as well as the NIR absorption of P(iI-DTS) and P(iI-T₂DTS) with absorption onsets of 805 nm and 795 nm respectively in thin films.

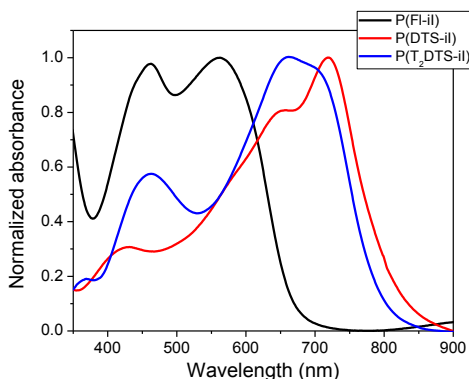


Figure 3-9. Thin film normalized UV-vis-NIR absorbance of P(Fl-iI), P(DTS-iI) and P(T₂DTS-iI).

The observed blue shift of P(iI-T₂DTS) compared to P(iI-DTS) is explained by the more electron donating thiophenes present along that backbone, which raise the HOMO energy level. This is supported by DPV results with the onset of oxidation against ferrocene being at 0.26 V for P(iI-T₂DTS) versus 0.45 V for P(iI-DTS), and is in agreement with other reports using thiophene spacers.³⁰¹ One interesting aspect of these two polymers is their LUMO energy offset with PC₆₁BM around 0.15 eV, while it is though that an energy difference of 0.2 - 0.3 eV is needed for exciton dissociation.¹⁰²

3.2.3. Polymer:Fullerene Active Blend Solar Cells

3.2.3.1. Device Optimization and Characteristics

In collaboration with Dr. Franky So's research group at the University of Florida, BHJ photovoltaic devices with conventional (ITO/PEDOT:PSS/polymer:PCBM/LiF/Al) and inverted (ITO/ZnO/polymer:PCBM/MoO₃/Ag) architectures were fabricated and characterized under AM1.5G illumination. The inverted architecture promotes the use of high work function, air-stable top electrodes, which are amenable to roll-to-roll device fabrication. The type of fullerene derivative, ratio of polymer to fullerene, solvent, solution concentration, spin-coating speed and annealing conditions were optimized for all three polymers. However, despite optimization, blends based on P(FI-iI) gave performance equal to or less than 0.01%. Figure 3-10 shows the variation in the J-V characteristics as a function of processing and device structure in P(DTS-iI) and P(T₂DTS-iI) blends with PC₇₁BM. In the case of P(DTS-iI), a donor/acceptor weight ratio of 1:4 in chlorobenzene (CB) at a concentration of 25 mg/mL spun cast at 1000 rpm and annealed at 150 °C before LiF/Al deposition gave the best efficiency, while optimal fabrication was found to be a donor/acceptor weight ratio of 1:4 in chlorobenzene (CB) at a concentration of 14 mg/mL spun cast at 1000 rpm and without thermal annealing in the case of P(T₂DTS-iI).

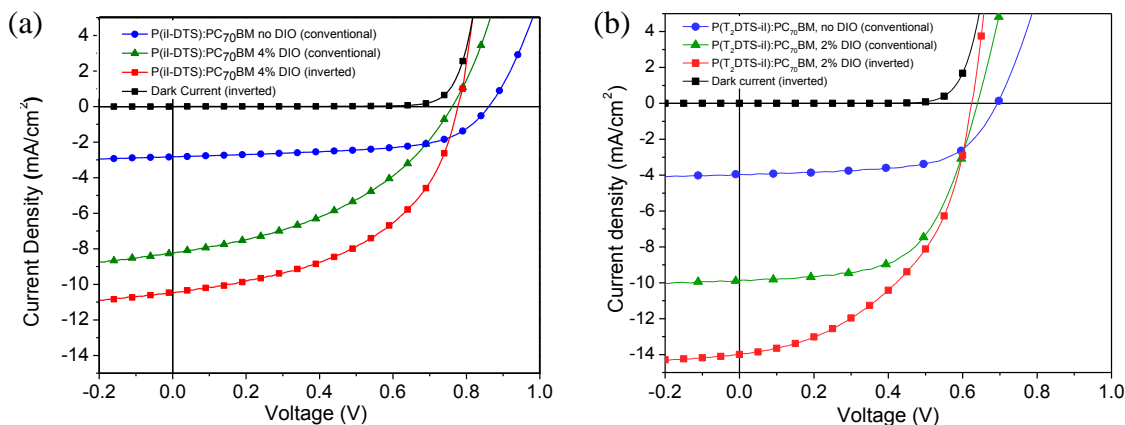


Figure 3-10. J-V characteristics of (a) P(DTS-iI):PC₇₁BM and (b) P(T₂DTS-iI):PC₇₁BM under illumination and in the dark as a function of processing and device architecture.

Despite the low energy offset between the polymer donor and fullerene acceptor P(iI-DTS) and P(iI-T₂DTS) show good PCE in blends with fullerenes of 2.6% and 3.5% respectively. The impact of structure and energy differences on exciton dissociation in devices is currently being studied by the So group, with the hypothesis that isoindigo polymers tend to have higher dielectric constants in the active layer compared to other p-type polymers.⁷⁴ An increased dielectric constant would decrease the exciton binding energy, allowing the use of blend materials with close LUMO levels.^{302,303} Furthermore, using P(T₂DTS-iI) leads to an increase of the J_{sc} , which can be explained by optoelectronic or morphologic effects. In the following paragraphs, the reason for the poor device performance in P(iI-FI) devices is first investigated, and the variations in P(DTS-iI) and P(T₂DTS-iI) device characteristics are subsequently studied.

Moreover, solvent additives such as octanedithiol or 1,8-diiodooctane (DIO) have been shown to decrease phase separation in the active layer BHJ, possibly leading to an increase in short-circuit currents in OPV devices.^{231,304} Some interesting effects can be noted from the J-V curves in Figure 3-10. Firstly, using DIO as a solvent additive does indeed increase the devices' short circuit currents; however, the open-circuit voltage is

simultaneously decreased. One hypothesis that could explain these observations is a change in the blend morphology, as is tested in paragraph 3.2.3.3.

3.2.3.2. Rationalizing low OPV performance of P(Fl-iI) blends

Atomic force microscopy and SCLC devices were used to pin-point what structural aspects of P(Fl-iI) lead to lower performance compared to P(DTS-iI). Figure 3-11a shows the $1\ \mu\text{m}^2$ topology of a P(Fl-iI):PC₆₁BM blend at a 1:3 ratio spun-cast from a 15 mg/mL solution in chloroform after annealing at 100 °C. The AFM height image does not show extensive phase separation between the polymer and fullerene derivative. By contrast, Figure 3-11b shows large domain sizes in P(DTS-iI):PC₇₁BM blends, which still give short circuit currents of $3\ \text{mA cm}^{-2}$.

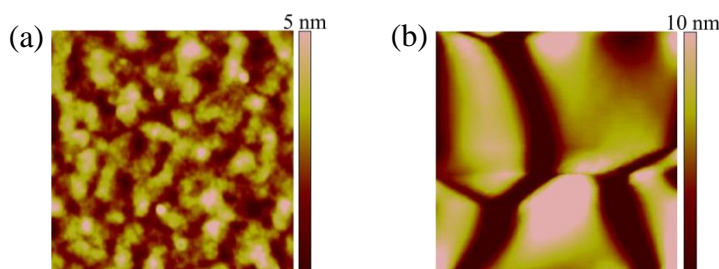


Figure 3-11. AFM height image of (a) P(Fl-iI):PC₆₁BM (1:2 ratio in CHCl₃, annealed at 100 °C) blend and (b) P(DTS-iI):PC₇₁BM (1:4 in CB) blend ($1\times 1\ \mu\text{m}^2$ scan size).

From the previous paragraph, it seems unlikely that phase separation in P(Fl-iI) blends alone causes such low performing devices. In order to highlight structure-property relationships to understand the parameters leading to improved device parameters, the transport properties of the three polymers were measured in space-charge limited current (SCLC) devices using a ITO/PEDOT:PSS/active layer/Au architecture. Films of P(DTS-iI) and P(T₂DTS-iI) both exhibit hole mobilities of $1\times 10^{-5}\ \text{cm}^2\ \text{V}^{-1}\ \text{s}^{-1}$ through film thicknesses of 130 nm and 120 nm respectively, while the current extracted from P(Fl-iI) 80 nm thick devices could not be distinguished from instrument noise. This observation is

on par with the $10^{-9} \text{ cm}^2 \text{ V}^{-1} \text{ s}^{-1}$ hole mobility measured for poly(9,9-dioctylfluorene) in SCLC devices.¹²⁹ As such, poor hole transport is considered to be one parameter limiting current generation in P(Fl-iI) OPV devices.

3.2.3.3. Effect of DIO in P(DTS-iI) and P(T₂DTS-iI) devices

As highlighted previously, using 1,8-diiodooctane (DIO) as a processing additive in chlorobenzene leads to an increase in the J_{sc} in OPV devices. AFM and TEM were used to investigate morphological changes that could lead to increased current generation by increasing interfacial surface between the donor and acceptor phases (Figure 3-12). In blends with PC₇₁BM processed from chlorobenzene (CB) alone, large phase separation is observed for both polymers; however adding a small volume fraction of DIO in the initial processing solution leads to the formation of a fibrillar network, with fiber widths on the order of 20 nm. Similar changes in morphology were previously observed in other DTS polymers, where fullerene clusters were reduced in size in the presence of DIO.³⁰⁵

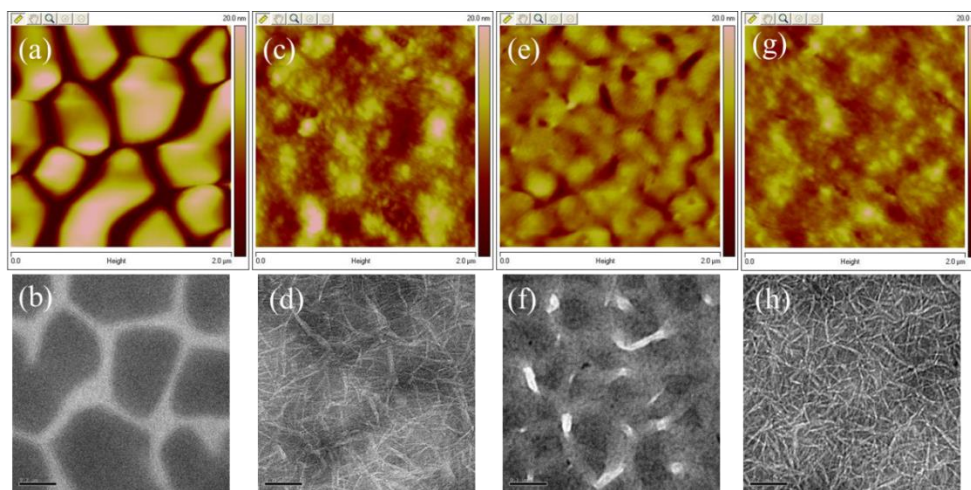


Figure 3-12. AFM and TEM images of thin films of P(DTS-iI):PC₇₁BM at a 1:4 ratio without (a,b) and with 4%v DIO (c,d), and of thin films of P(DTS-iI):PC₆₁BM at a 1:4 ratio without (e,f) and with 2.5%v DIO (g,h). AFM: top, $2 \times 2 \mu\text{m}^2$, 20 nm height. TEM: bottom, 200 nm scale bar.

The differences in terms of morphology between blends with PC₆₁BM or PC₇₁BM stem from their difference in shape and solubility, and have been previously observed with other donor-acceptor polymers.³⁰⁶ Kastner *et al.*³⁰⁷ emphasized the importance of the miscibility between the polymer and fullerene, crystallinity and solubility on the active layer phase separation. In this study, three bulk morphologies were described: (i) intimate mixing of the polymer and fullerene due to good miscibility between the two leading to little or no phase separation, (ii) less intimate mixing controlled by polymer and/or fullerene aggregation, and (iii) increased miscibility between the polymer and fullerene but *reduced fullerene solubility* in the common solvent leading to large fullerene domains in a polymer:fullerene matrix. Based on this description, blends of P(DTS-iI) fall under category (ii) when mixed with PC₆₁BM and (iii) when mixed with PC₇₁BM, but this explanation does not hold when comparing PC₆₁BM and PC₇₁BM, as PC₇₁BM is more soluble than PC₆₁BM in chlorobenzene (80 mg mL⁻¹ compared to 50 mg mL⁻¹, respectively).³⁰⁷ This difference in solubility between PC₆₁BM and PC₇₁BM can be explained by the molecular shapes and the polarizabilities of two fullerene cages as hypothesized by Nath *et al.*²²² regarding C₆₀ and C₇₀. The ellipsoidal shape of C₇₀ leads to a higher polarizability than the spherical C₆₀, and as the film dries, smaller C₆₀ aggregates crash out of solution whereas C₇₀ aggregates are maintained in solution and are allowed to grow in size, leading to greater domain sizes in the final film. Furthermore, Pearson *et al.*²²⁹ have demonstrated *in situ* that at 1:4 ratios of polymer:PC₇₁BM, PC₇₁BM aggregation precedes polymer organization. At these ratios, it is thought that fullerene solubility alone controls the morphology, i.e. the polymer chains remain mobile as the solvent evaporates rather than forming crystalline fibrils. In the case of P(DTS-

iI):fullerene blends, it is then hypothesized that early aggregation and precipitation PC₆₁BM followed by organization of P(DTS-iI) as the film dries leads to fine phase separation and formation of polymer fibrils, while PC₇₁BM aggregates remain in solution for longer times and are allowed to grow further as the solvent evaporates, leading to larger PC₇₁BM domains embedded in a polymer:PC₇₁BM matrix.

Moreover, solvent additives are thought to affect solubility of the polymer and/or fullerene, which leads to a modification of the phase separation in the dried film. As hypothesized by Schmidt *et al.*²³³ in the case of 1-chloronaphthalene (CN) and a diketopyrrolopyrrole (DPP) polymer, CN could lead to small crystallite formation in solution, which increases the nuclei density in the film as polymer fibers are forming, and in turn promote smaller domains than when a single solvent is used. Another hypothesis is that solvent additives, such as DIO, selectively solubilize fullerene clusters in the casting solution through electrostatic interactions between the iodine and the fullerene cage,²³⁴ and prevent PC₇₁BM aggregation into the large domains seen in Figure 3-13 by promoting mixing of smaller fullerene aggregates with the polymer-rich phases. Further work by Gao *et al.*²³⁵ has highlighted different pathways for morphology control when aliphatic and aromatic additives are used. Their study has shown that DIO leads to the formation of amorphous polymer aggregates in a chloroform solution while o-dichlorobenzene (oDCB) promotes formation of crystalline aggregates. Both mechanisms will be tested in a subsequent study. Similar results are seen in P(T₂DTS-iI):PCBM devices to varying extents depending on whether PC₆₁BM (1:2 ratio) or PC₇₁BM (1:4 ratio) are used (Figure 3-13), and where the morphology of the blend can also be tuned by DIO as a solvent additive.

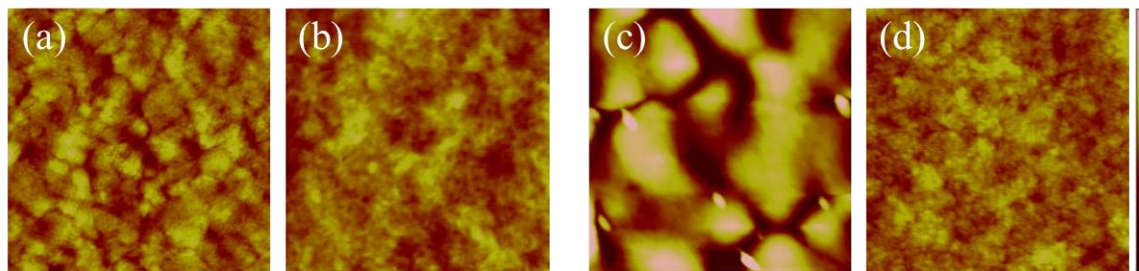


Figure 3-13. AFM topography of P(T₂DTS-iI):PC₆₁BM (1:2) without (a) and with 2% v DIO (b), and P(T₂DTS-iI):PC₇₁BM (1:4) without (c) and with 2% v DIO (d). All images are 1×1 μm², with a 10 nm height scale.

In conclusion, p-type polymers based on isoindigo were designed and show PCEs around 4% when DIO is used as a processing additive. Structure-property relationships highlighted in the first two sections of the chapter demonstrate that the electron affinity of isoindigo-based polymers tends to be around 3.9 eV, regardless of the co-monomer. Furthermore, the steric hindrance from phenyl-phenyl linkages along the backbone has proven to be detrimental to charge mobility in both P(iI), P(iI-BTD) and P(FI-iI), and future polymer designs for OPV materials should focus on other linkages.

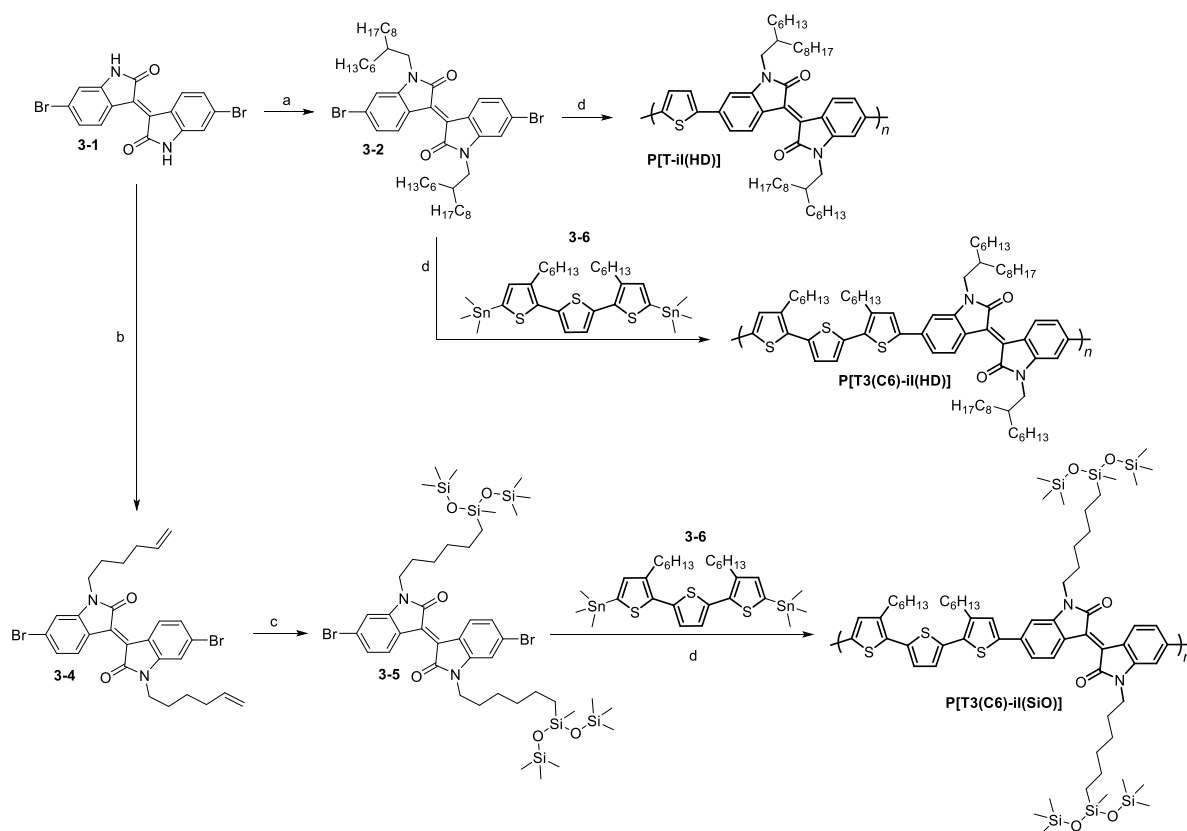
3.3. Principles Directing Transport and Charge Separation in Oligothiophene-Isoindigo Polymers

To further understand the effect of structure on morphology and on open-circuit voltage, a family of three poly(oligothiophene-*alt*-isoindigo) was synthesized. Using poly(thiophene-isoindigo) P[T-iI(HD)] and poly(terthiophene-isoindigo) with varying side chains P[T3(C6)-iI(HD)] and P[T3(C6)-iI(SiO)] shown in Scheme 3-5, the goal is to understand how variations in polymer packing and energy levels lead to changes in the short circuit current density (J_{sc}) and open circuit voltage (V_{oc}) in devices.

3.3.1. Polymer Synthesis and Characterization

Wang *et al.*¹⁵⁹ have previously reported the synthesis of a high performance (6% power conversion efficiency, PCE) terthiophene-*alt*-isoindigo polymer, followed by the synthesis and characterization of families of oligothiophene-*alt*-isoindigo by Ma *et al.*¹⁶⁰ and Ho *et al.*¹⁶¹ Furthermore, Mei *et al.*¹⁵⁷ described a two-step synthesis to yield a siloxane-functionalized isoindigo monomer, which moves the side-chain branching point away from the backbone and allows for closer backbone packing. In this work, the terthiophene-*alt*-isoindigo backbone is synthesized by Stille polycondensation of 5,5'-bis(trimethylstannyl)-3,3''-hexyl-2,2':5',2''-terthiophene 3-6 with functionalized 6,6'-dibromoisindigo 3-2 or 3-5 as shown in Scheme 3-5. The synthesis of 3-6 was conducted based on previously reported procedures for 3,3''-alkyl-2,2':5',2''-terthiophenes,^{308,309} starting with a Kumada coupling to yield the 3-hexylthiophene, followed by bromination by N-bromosuccinimide (NBS) and Stille coupling with 2,5-bis(trimethylstannyl)thiophene to yield 3,3''-dihexyl-2,2':5',2''-terthiophene. The bifunctional tin monomer 3-6 was obtained by lithiation using *n*-butyllithium followed by quenching with trimethyltin chloride.

After running the polymerization for 72h, 2-(tributylstannyl)thiophene followed by 2-bromothiophene were added to the reaction mixture and left to react as end-cappers for 12h. The polymers were then collected by precipitation in methanol followed by filtration and extraction by Soxhlet. The fractionation yields depended on the solubility of the polymers, with most of P[T-iI(HD)] being extracted with dichloromethane while the less soluble P[T3(C6)-iI(HD)] and P[T3(C6)-iI(SiO)] polymers were extracted using chloroform.



Scheme 3-5. Synthesis of P[T-iI(HD)], P[T3(C6)-iI(HD)] and P[T3(C6)-iI(SiO)]. a) 1-iodo-2-hexyldecane, K₂CO₃, DMF, 95 °C, 71%; b) 6-bromo-1-hexene, K₂CO₃, DMF, 95 °C, 85%; c) 1,1,3,3,5,5,5-heptamethyltrisiloxane, Karstedt's catalyst, toluene, 50 °C, 40%; d) Pd₂(dba)₃, P(*o*-tyl)₃, toluene, 90 °C. Yields: P[T-iI(HD)]: 80% (dichloromethane fraction); P[T3(C6)-iI(HD)]: 80% (chloroform fraction); P[T3(C6)-iI(SiO)]: 75% (chloroform fraction).

The molecular weight of the polymers were estimated by size-exclusion chromatography (SEC) in tetrahydrofuran (THF); however, due to limited solubility of P[T3(C6)-iI(HD)], aggregation peaks are present in the chromatograph. As such, SEC using *o*-dichlorobenzene (oDCB) as the eluent was also conducted. The number average molecular weight for P[T-iI(HD)], P[T3(C6)-iI(HD)] and P[T3(C6)-iI(SiO)] in THF are 26 kDa (PDI: 2.1), 18 kDa (PDI: 3.7) and 32 kDa (PDI: 2.2) respectively, corresponding to degrees of polymerization of 34, 16, and 25 (i.e. 102, 80, and 125 aromatic rings) respectively. In oDCB, the chromatograph of P[T3(C6)-iI(HD)] shows a single

population of chains and the molecular weight is measured to be 103 kDa (PDI: 1.6). Interestingly, the molecular weight of P[T3(C6)-iI(SiO)] is measured to be 49 kDa (PDI: 5.4) in oDCB, but for this polymer an aggregation shoulder is observed in the SEC run in oDCB and not in the SEC run in THF. The polymer purity was assessed by elemental analysis, with all elemental compositions being within 0.74%, 0.29%, 1.55% for P[T-iI(HD)], P[T3(C6)-iI(HD)] and P[T3(C6)-iI(SiO)] respectively.

3.3.2. Optoelectronic Characterization

Previous work on isoindigo molecules and polymers has highlighted that the electron density in the LUMO level is mostly localized on the isoindigo unit, leading to a LUMO energy level around -3.9 eV.^{151,152} In order to understand if the same observation can be made in the case of P[T-iI] and P[T3-iI] polymers, density functional theory (DFT) calculations were conducted and compared to electrochemically estimated ionization potential and electron affinity. Calculations were conducted on model structures (where side-chains have been replaced by methyl groups) at the B3LYP/6-31G(d) level, as Estrada *et al.*¹⁵¹ as well as Salvatori *et al.*²⁵⁰ both showed good correlation between DFT calculations at the B3LYP/6-31G(d) level and electrochemically estimated frontier orbital energy levels in isoindigo-based systems.

Figure 3-14 shows the trend in calculated frontier molecular orbital (FMO) energy levels as a function of T-iI and T3-iI oligomer size. As expected, the energy difference between the HOMO and LUMO level decreases as the conjugation length increases, and extrapolation to infinite chains estimates the energy gap to be 1.85 eV and 1.77 eV for P[T-iI] and P[T3-iI] respectively. The HOMO and LUMO energy levels are extrapolated to be at -4.97 eV and -3.12 eV for P[T-iI] and -4.72 eV and -2.95 eV for P[T3-iI].

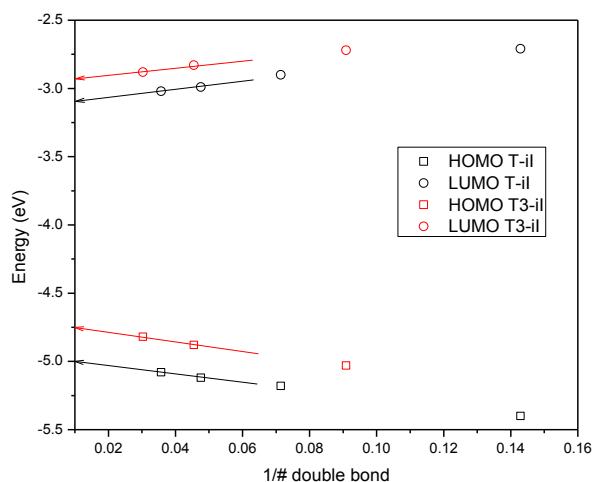


Figure 3-14. Frontier molecular orbital energies for the T-iI and T3-iI model compounds at the B3LYP/6-31G(d) level of theory as a function of oligomer size, and extrapolated HOMO/LUMO values for an infinite polymer chain.

The electronic density in the FMOs visualized in Figure 3-15 shows delocalization through 6 to 8 units in the HOMO level, but localization of the electronic density on the isoindigo core in the LUMO level, which is consistent with the relatively constant LUMO level regardless of the nature of the comonomer. It would appear that T-iI exhibits continuous orbital overlap between iI units, whereas there seems to be a break in conjugation on the thiophene units in the LUMO of T3-iI.

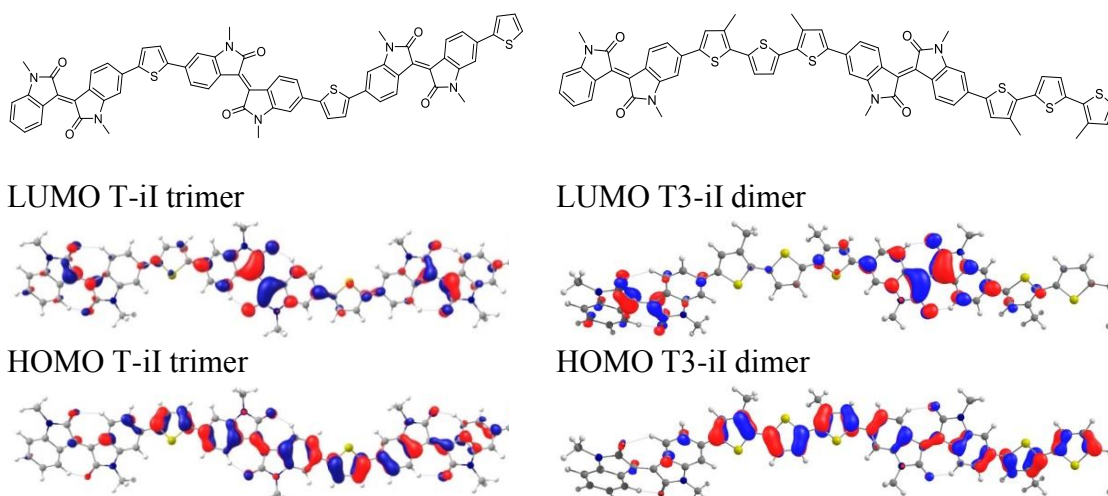


Figure 3-15. Model compounds and orbital localization in T-iI trimer and T3-iI dimer HOMO and LUMO levels.

Experimentally, the ionization potential and electron affinity were estimated electrochemically via differential pulse voltammetry (DPV). Cyclic voltammetry (CV) was conducted prior to DPV to determine the stability of the oxidation and reduction peak to repeated cycles. As shown in Figure 3-16, the three polymers show two quasi-reversible reduction peaks and at least one quasi-reversible oxidation peak. Unfortunately, the oxidation process was unstable under the selected electrochemical conditions, and the polymer films delaminated from the Pt electrode as the film was oxidized, leading to a decrease in current density. However, the reduction processes were stable and the first reduction peak dependence on scan rate is close to linear indicating that the electrochemical reduction is not diffusion limited and the current results from faradaic processes.

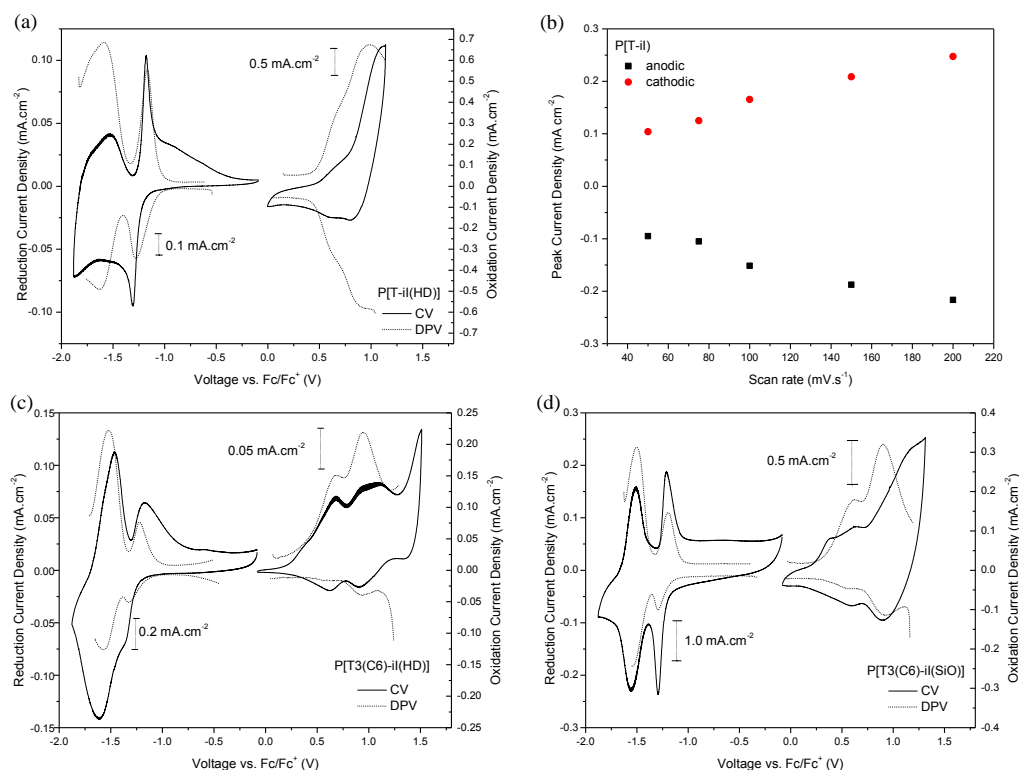


Figure 3-16. (a) CV and DPV of thin films of P[T-iI(HD)] and (b) its corresponding scan rate dependence of the first reduction peak, and CV and DPV of thin films of (c) P[T3(C6)-II(HD)] and (d) P[T3(C6)-iI(SiO)] on Pt-button electrode in 0.1 M TBAPF₆/acetonitrile solution.

Figure 3-17 summarizes the differential pulse voltammograms for the three polymers upon oxidation and reduction. As expected, the onsets of reduction are all around -1.17 V vs. Fc/Fc^+ , corresponding to an estimated electron affinity around 3.9 eV considering that the ionization potential for ferrocene is at 5.1 eV vs. vacuum, as discussed in Chapter 2. The DPV onsets of reduction and oxidation are summarized in Table 3-4.

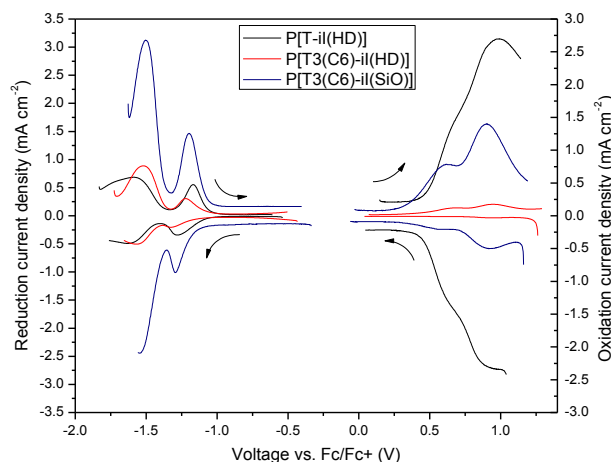


Figure 3-17. Differential pulse voltammograms of P[T-iI(HD)], P[T3(C6)-iI(HD)] and P[T3(C6)-iI(SiO)] on Pt-button in 0.1 M TBAPF₆ in acetonitrile, recorded with a step size of 2 mV and step time of 0.05 s with a amplitude of 96 mV. The arrows indicate the direction of the voltage scan.

As observed in Figure 3-18, the absorption spectra show a broad coverage of the visible region with absorption maxima around 700nm for P[T-iI(HD)] and 660 nm for P[T3(C6)-iI(HD)] and P[T3(C6)-iI(SiO)] in both chloroform solutions and thin films. Dual band absorption with local maxima at 400 nm and 660 nm corresponding to a π - π^* transition and a charge transfer transition respectively in P[T3(C6)-iI(HD)] leads to bluish-green solutions, while P[T-iI(HD)] solutions look blue. In transitioning from solution to thin films, a low energy aggregation shoulder is observed for the films of P[T3(C6)-iI(HD)] and P[T3(C6)-iI(SiO)], corresponding to increased interactions of the π -orbitals between the conjugated backbones. This shoulder is not observed in the case of

P[T-iI(HD)], suggesting less interactions between the polymer backbones in thin films of P[T-iI(HD)] compared to the T3-iI polymers. This different order in the solid state is hypothesized to be due to the higher density of branched alkyl chains along the backbone, thus preventing strong interchain interactions. The onset of absorption in thin films is used to calculate the optical energy gap for the three polymers, and the results are summarized in Table 3-4.

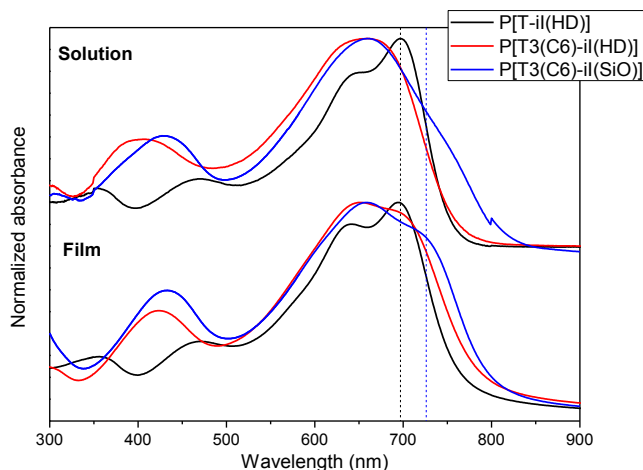


Figure 3-18. Normalized UV-vis spectra of P[T-iI(HD)] (black), P[T3(C6)-iI(HD)] (red), and P[T3(C6)-iI(SiO)] (blue) in chloroform solution (top) and thin film (bottom).

The UV-Vis-NIR data correlates with the trends obtained from electrochemistry, with P[T-iI(HD)] exhibiting the highest optical energy gap at 1.62 eV and P[T3(C6)-iI(SiO)] the lowest optical energy gap at 1.55 eV (Table 3-2). In the case of P[T3(C6)-iI(SiO)], the energy gap estimated via DPV is lower than the optical gap due to its surprising low ionization potential at 5.4 eV. Considering that the conjugated backbone of P[T3(C6)-iI(SiO)] is similar to P[T3(C6)-iI(HD)], the unstable oxidation process in these films possibly leads to deviations in the ionization potential determination.

Table 3-2. Size exclusion chromatography (SEC) results and optoelectronic properties of P[T-iI(HD)], P[T3(C6)-iI(HD)] and P[T3(C6)-iI(SiO)].

Polymer	SEC		UV-vis-NIR			Electrochemistry		
	Mn (kDa)	PDI	E_{\max}^b (eV) solution	E_{\max}^b (eV) film	$E_{\text{gap}}^{\text{opt}}$ (eV)	IP ^c (eV)	EA ^c (eV)	E_{gap} (eV)
P[T-iI(HD)]	26	2.1	1.79	1.79	1.62	5.59	3.90	1.69
P[T3(C6)-iI(HD)]	18	3.7	1.88	1.90	1.58	5.57	3.93	1.64
	103 ^a	1.6 ^a						
P[T3(C6)-iI(SiO)]	32	2.2	1.89	1.88	1.55	5.43	3.94	1.46
	49 ^a	5.4 ^a						

^aSEC performed in chlorinated solvents (all others in THF), ^bAbsorption maxima in chloroform solution and thin film, ^cionization potential and electron affinity estimated from DPV using $E_{\text{IP(EA)}} = 5.1 + E_{\text{onset}}^{\text{ox(red)}}$ vs. Fc^+/Fc .

3.3.3. Polymer Packing

Grazing incidence wide angle X-ray scattering (GIWAXS) was used to determine polymer packing in thin films, and the extent of interactions between the polymer backbones. The films were fabricated by spin coating a solution of polymer in oDCB onto a silicon wafer substrate. The GIWAXS data gives a measure of microstructural organization as shown in Figure 3-19, and the π -stacking (π - π) and chain-to-chain distances (d) are summarized in Table 3-3. In as-cast polymer films, the π -stacking distances calculated from the (010) peaks range from 3.7 Å for P[T3(C6)-iI(SiO)] to 3.8 Å for P[T-iI(HD)] and 4.1 Å for P[T3(C6)-iI(HD)]. The smallest π - π distance for P[T3(C6)-iI(SiO)] correlates well what is observed from thin film absorbance, with P[T3(C6)-iI(SiO)] showing the largest red shift in transitioning from solution to film among the three polymers. The larger π - π distance for P[T3(C6)-iI(HD)] can be explained by increased rotational freedom in the terthiophene unit containing alkyl chain, compared a single thiophene unit in P[T-iI(HD)]. The chain-to-chain distance d

determined from the position of the (100) peak is similar in films of P[T-iI(HD)] and P[T3(C6)-iI(HD)], around 18 Å, but increases to 25 Å in films of P[T3(C6)-iI(SiO)], possibly due to the longer Si-O-Si distance compared to C-C-C distance (3.1 Å vs. 2.5 Å leading to an overall side chain maximum length of around 11 Å and 13 Å in the case of 2-hexyldecyl and siloxane side chains respectively). The values for π -stacking and lamellar distances are similar to previous results reported on oligothiophene-isoidindigo polymers.^{157,160,161} In the pristine polymer films, a second order (200) peak for the lamellar packing is seen for P[T3(C6)-iI(HD)], and on the integrated line trace of P[T3(C6)-iI(SiO)]. In contrast, P[T-iI(HD)] does not exhibit higher order peaks suggesting less long range ordering in these films, which is coherent with the UV-vis-NIR observations.

The orientation of the polymer planes relative to the substrate can also be resolved by determining if the (010) scattering peak is along the Q_{xy} axis (the corresponding π - π scattering planes, i.e. polymer backbone, are then perpendicular to the substrate, with the scattering direction being parallel to the substrate – edge-on orientation) or along the Q_z axis (the corresponding π - π planes are then parallel to the substrate, with the scattering direction being perpendicular to the substrate – face-on orientation). P[T-iI(HD)] and P[T3(C6)-iI(SiO)] have similar scattering orientations, with their (100) peaks along the Q_z axis and their (010) peaks along the Q_{xy} axis, indicating that a majority of the chains are face-on with regards to the substrate. However, the halo of the (010) peaks indicates that these two samples are made up of a distribution of crystal orientations. In contrast, the thin film of P[T3(C6)-iI(HD)] has its (100) peak along the Q_z axis and its (010) peak oriented along the Q_{xy} axis, with a slight increase in peak intensity around $\sim 30^\circ$. This

indicates that the P[T3(C6)-iI(HD)] chains are mainly oriented edge-on with respect to the silicon substrate.

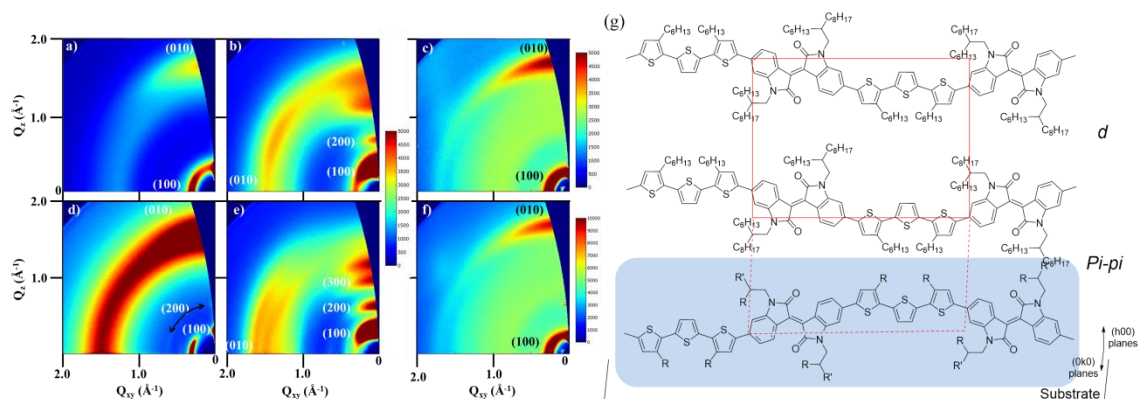


Figure 3-19. GIWAXS images of pristine (a-c) and thermally annealed at 200°C (d-f) P[T-iI(HD)](a,d), P[T3(C6)-iI(HD)](b,e) and P[T3(C6)-iI(SiO)] (c,f) thin films prepared from oDCB. (g) Possible chain conformation in a unit cell illustrating an edge-on backbone orientation. In (a-f) the intensity scales are different to visualize lower intensity peaks before annealing, without saturating the scattering intensity after annealing; in (g) a polymer backbone plane is in blue, with a plausible unit cell in red.

After thermal annealing at 200 °C for 10 min under a helium atmosphere, all three polymer films show an increase in their scattering intensities indicating an increase in the number of scattering sites. In particular, higher order (h00) peaks appear in the GIWAXS of P[T3(C6)-iI(HD)] and the orientation of the polymer chains is more defined after thermal annealing as indicated by the more localized (100) in Figure 3-19d. As summarized in Table 3-5, the characteristic distances are also influence by thermal treatment, but each polymer exhibits different trends in their d and π - π distances with thermal annealing. P[T-iI(HD)] and P[T3(C6)-iI(HD)] films exhibit increased d ; however, in P[T-iI(HD)] films π - π distance increases to 4.0 Å while it decreases to 3.7 Å in P[T3(C6)-iI(HD)] films. This indicates that polymer packing is metastable in the as-cast films; on the other hand, P[T3(C6)-iI(SiO)] does not exhibit any changes in its d and π - π distances indicating that a thermally stable structure is formed by spin coating.

Table 3-3. Thin film polymer microstructure determined by GIWAXS.

	As-cast		Post -annealing			
	(100) d (Å)	(010) π - π (Å)	(100) d (Å)	(010) π - π (Å)	(010) crystal size (Å)	(010) π -stack Orientation
P[T-iI(HD)]	19	3.8	20	4.0	80	Along Q_{xy} and Q_z , mixed face-/edge- on
P[T3(C6)-iI(HD)]	18	4.1	19	3.7	100	Along Q_{xy} , edge-on
P[T3(C6)-iI(SiO)]	25	3.7	25	3.7	92	Along Q_z , face-on

3.3.4. Transport Characteristics in Organic Field-Effect Transistors

Polymer packing has been shown to have a large impact on charge carrier mobility in organic field-effect transistors (OFETs). In order to determine the parameters impacting charge carrier mobility in these oligothiophene-isoindigo polymers, bottom-gate/bottom contact OFET devices were fabricated by drop casting each compound from a 2 mg/mL chloroform solution onto an HMDS modified SiO₂ substrate, with subsequent annealing at 150 °C for 1h. Although the processing conditions are different from those used to deposit thin films for GIWAXS, previous work has shown that the microstructure in the OFET semiconducting films is comparable to what was observed from films spun cast from oDCB.

P[T-iI(HD)] exhibits ambipolar charge transport, with a hole mobility μ_h of $4 \times 10^{-2} \text{ cm}^2 \text{ V}^{-1} \text{ s}^{-1}$ and an electron mobility of $1 \times 10^{-1} \text{ cm}^2 \text{ V}^{-1} \text{ s}^{-1}$. P[T3(C6)-iI(HD)] and P[T3(C6)-iI(SiO)] display only hole carrier transport, with the hole mobility of P[T3(C6)-iI(HD)] measured at $5 \times 10^{-2} \text{ cm}^2 \text{ V}^{-1} \text{ s}^{-1}$, on the same order of magnitude than P[T-iI(HD)]. The hole mobility of P[T3(C6)-iI(SiO)] is $4 \times 10^{-3} \text{ cm}^2 \text{ V}^{-1} \text{ s}^{-1}$, an order of magnitude lower than P[T3(C6)-iI(HD)]. The differences in ambipolar transport in P[T-

iI(HD)] versus hole carrier transport in P[T3-iI] polymers is hypothesized to arise from several factors. Electron transport could be affected by the difference in electron-accepting isoindigo density along the backbone, where P[T-iI(HD)] has a more delocalization of electron density in the LUMO than P[T3-iI] polymers. Another parameter is how solid-state interchain packing allows for electron carrier transport through hopping, where overlap of electron-deficient units would further enable electron transport. This effect was previously reported by Donley *et al.*³¹⁰ and Van Vooren *et al.*³¹¹ in poly(9,9-di-*n*-octylfluorene-*alt*-benzothiadiazole).

Another interesting observation is in the impact of microstructure on charge carrier transport. P[T-iI(HD)] and P[T3(C6)-iI(HD)] have similar orientation onto silicon wafers, with the polymer backbones being primarily face-on versus the substrate, however their transport characteristics show an order of magnitude difference in their hole carrier mobility. By comparison, P[T-iI(HD)] and P[T3(C6)-iI(HD)] exhibit drastically different polymer packing, in particular in terms of face-on and edge-on orientation, while retaining similar hole carrier mobility. The lack of correlation between backbone orientations relative to the substrate has been pointed out by Sirringhaus.⁷⁸

3.3.5. Photovoltaic Devices

3.3.5.1. Device Parameters

Conventional OPV devices with an ITO/PEDOT:PSS/active layer/LiF/Al architecture were fabricated by spin coating the polymer:PC₇₁BM (1:1.5) blend from an oDCB solution. The OPV device characteristics are summarized in Table 3-4, which already highlights large differences in the device characteristics of P[T3(C6)-iI(HD)] and P[T3(C6)-iI(SiO)]. Even though the two polymers have the same backbone and present

similar optoelectronic properties, they exhibit J_{sc} of 12.5 mA cm^{-2} and 1.6 mA cm^{-2} and FF around 0.56 and 0.37 for P[T3(C6)-iI(HD)] and P[T3(C6)-iI(SiO)] respectively. This difference in OPV device characteristics with changes to the side chain was previously reported by comparing P[T2-iI(HD)] and P[T2-iI(SiO)], but in this case the J_{sc} of P[T2-iI(SiO)]:PC₇₁BM devices was four-times that of P[T2-iI(HD)]:PC₇₁BM devices.³¹²

Table 3-4. Conventional OPV device characteristics.

Polymer:PC ₇₁ BM	J_{sc} (mA cm ⁻²)	V_{oc} (V)	FF (%)	PCE (%)
P[T-iI(HD)]	2.3±0.1	0.97±0.01	52±2	1.2±0.1
P[T-iI(HD)], 2.5% DIO	5.8±0.1	0.90±0.01	55±1	2.9±0.1
P[T3(C6)-iI(HD)]	12.5±0.5	0.72±0.01	56±1	5.0±0.2
P[T3(C6)-iI(HD)], 2.5% DIO	15.2±0.1	0.70±0.01	62±1	6.6±0.1
P[T3(C6)-iI(SiO)]	1.6±0.3	0.69±0.01	37±1	0.4±0.1
P[T3(C6)-iI(SiO)], 2.5% DIO	8.6±0.2	0.66±0.01	49±1	2.8±0.1

The active layer morphology was optimized by using 1,8-diiodooctane (DIO) as a high boiling point processing additive. Interestingly in the films processed from oDCB with DIO led to increases in PCE, with varying extents depending on the polymer structure. Furthermore, when the P[T3(C6)-iI(HD)]:PC₇₁BM sample is kept under vacuum right after spin-coating the active layer, followed by LiF/Al deposition, the devices showed a V_{oc} of 0.7 V, a J_{sc} of 14.2 mA cm^{-2} , and FF of 59%. The PCE was therefore calculated to be 6.0±0.1 %. However, after drying the active layer overnight at room temperature in a nitrogen atmosphere, the J_{sc} , FF, and PCE increased to 15.2 mA cm^{-2} , 62 %, and 6.6±0.1 %, respectively. It is hypothesized that the low vapor pressure of DIO allows it to remain in the active layer thin film for longer times than oDCB alone and allows the polymer and/or fullerene molecules to remain mobile for longer times

leading to further polymer and/or reorganization to occur, yielding higher J_{sc} and FF. This is particularly interesting since little change in the phase separation is observed at the micrometer scale when DIO is added to the coating solution, as seen in the following section. It is further hypothesized that DIO is removed from the film when the devices are set under high vacuum (10^{-7} mbar) for thermal evaporation of the top contacts.

3.3.5.2. Morphology of Blends of P[T-iI(HD)], P[T3(C6)-iI(HD)] or P[T3(C6)-iI(SiO)] with PC₇₁BM

As shown previously in blends of P(DTS-iI):PC₇₁BM, DIO typically leads to a reduction of domain sizes as seen via AFM. This is observed again in the case of P[T-iI(HD)]:PC₇₁BM blends as shown in Figure 3-20a and b, where presumably large PC₇₁BM-rich domains are observed in films cast from oDCB but finer phase separation is produced when DIO is present. The effect of DIO is less visible in the AFM images of P[T3(C6)-iI(HD)]:PC₇₁BM and P[T3(C6)-iI(SiO)] :PC₇₁BM. The two-fold increase in J_{sc} in P[T-iI(HD)] processed with 2.5%v DIO compared to without DIO can thus be partially explained by a reduced phase separation. The five-fold increase in J_{sc} with addition of DIO is particularly interesting due to the similar phase separation observed via AFM on blends processed without and with DIO.

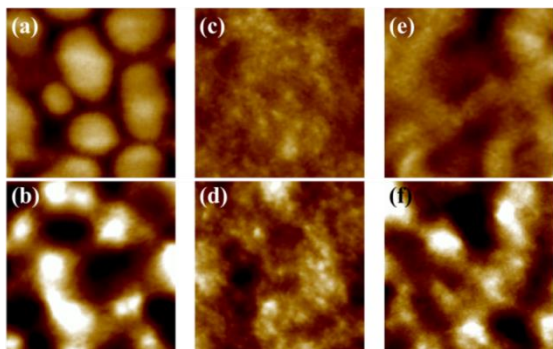


Figure 3-20. AFM images of blends of PC₇₁BM with (a,b) P[T-iI(HD)], (c,d) P[T3(C6)-iI(HD)], and (e,f) P[T3(C6)-iI(SiO)] without (top) and with 2.5%v DIO (bottom). All images are $1 \times 1 \mu\text{m}^2$ with 30 nm height scales.

To further understand the effect of DIO on phase separation, neutron reflectivity (NR) on the active layer was conducted as described in Chapter 2 and highlights several difference in the vertical composition profile of the P[T3(C6)-iI(HD)]:PC₇₁BM depending on processing (Figure 3-21). First of all, the fits indicate that the thickness of the active layer beneath the aluminum (Al) electrode is around 125 nm and 100 nm for the blends processed without and with DIO respectively. Profilometry on the active layer of OPV devices measures an active layer thickness of 130±3 nm and 120±3 nm for the films processed without and with DIO respectively, which highlights good correlation of the NR fits to the experimentally determined active layer thickness. Overall, it appears that P[T3(C6)-iI(HD)]:PC₇₁BM blends have what is thought as the optimal vertical phase separation for conventional devices, with fullerene-rich domains towards the Al cathode and polymer-rich domains towards the ITO anode. When DIO is used to process the same blend, the polymer-rich phase towards the PEDOT:PSS layer becomes even more polymer-rich but also becomes thinner. Based on these NR fits, it is shown that DIO not only has an impact on lateral phase separation but also on vertical composition, which is consistent with other reports.³¹³

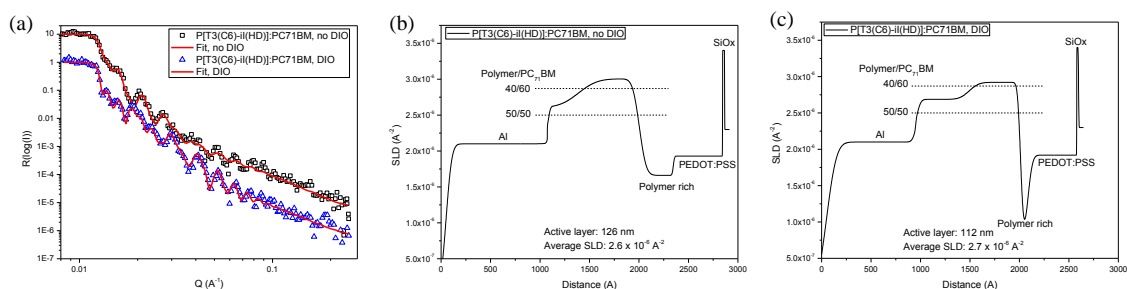


Figure 3-21. Neutron reflectivity data and fits (a) leading to scattering length density profiles of P[T3(C6)-iI(HD)] devices spun cast from oDCB without (b) and with 2.5% DIO (c).

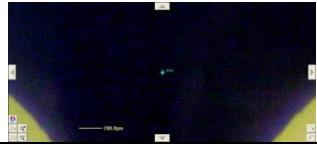

In order to verify the composition profile obtained from the NR fits, X-ray photoemission spectroscopy (XPS) was used to quantify the surface elemental composition and compare it to the composition obtained from NR. The results from XPS are summarized in Table 3-5. Some discrepancies between the NR fits and the XPS data can be observed. Indeed, XPS indicates that the first couple nanometers of the active layer are polymer-rich in both cases but NR fits indicate that the active layer is PC₇₁BM-rich in the first 50 nm.

Table 3-5. XPS data showing elemental composition and calculated material concentrations at the film surface as a function of processing conditions.

P[T3(C6)-iI(HD)] :PC ₇₁ BM	C (%)	N (%)	O (%)	S (%)	Polymer (%)	PC ₇₁ BM (%)
No DIO	92.0	2.3	2.8	2.8	83±12	16±10
2.5% DIO	92.5	1.5	3.0	3.0	69±13	30±10

To understand these discrepancies, XPS data was collected as a function of device location, as illustrated in Table 3-6. As the XPS measurement is taken closer to the active area defined by the Al top electrode the polymer content at the surface decreases from 83% to 71%. It is hypothesized that the difference in the size of the area analyzed by each technique (4 cm² in the case of NR, and less than 0.5 mm² in the case of XPS) accounts for variations between NR and XPS results.

Table 3-6. XPS analysis as a function of device area probed in P[T3(C6)-iI(HD)]:PC₇₁BM (1:1.5) blends spun cast from oDCB without DIO.

P[T3(C6)-iI(HD)]:PC ₇₁ BM	C (%)	N (%)	O (%)	S (%)	Polymer (%)	PC ₇₁ BM (%)	Position of XPS measurement
Between Al contacts	92.0	2.3	2.8	2.8	83±12	16±3	
Near Al contact	87.2	1.8	8.3	2.6	71±2	26±5	

In summary, NR is a powerful tool for non-destructive characterization of the elemental composition through the active layer underneath the top electrode; however, the challenges associated with fitting for multiple layers highlight the need for complimentary techniques to characterize vertical phase separation. The observed effect of DIO on vertical phase separation could explain, in part, the increase in J_{sc} and FF in P[T3(C6)-iI(HD)]:PC₇₁BM processed with DIO compared to oDCB alone.

3.3.5.3. Photovoltage losses by CMEAS

In OPV devices, V_{oc} of 0.9V and 0.7V are measured in P[T-iI(HD)]:PC₇₁BM and P[T3(C6)-iI(HD)]:PC₇₁BM respectively, in agreement with previous reports.³¹⁴ The limited correlation between the onset of oxidation and the V_{oc} in these blends is further supported by ultraviolet photoelectron spectroscopy (UPS), where the IP is measured to be around 5.2 eV and 5.3 eV in films of P[T-iI(HD)] and P[T3(C6)-iI(HD)] respectively. This 0.1 eV difference measured by UPS does not account for the 0.2 V difference in the V_{oc} of the blends. The correlation between effective energy gap or charge transfer states (rather than IP alone) and V_{oc} can be uncovered using charge modulated electro-

absorption spectroscopy (CMEAS) to probe sub-energy gap charge transfer states (Figure 3-22), as discussed in Chapter 2.

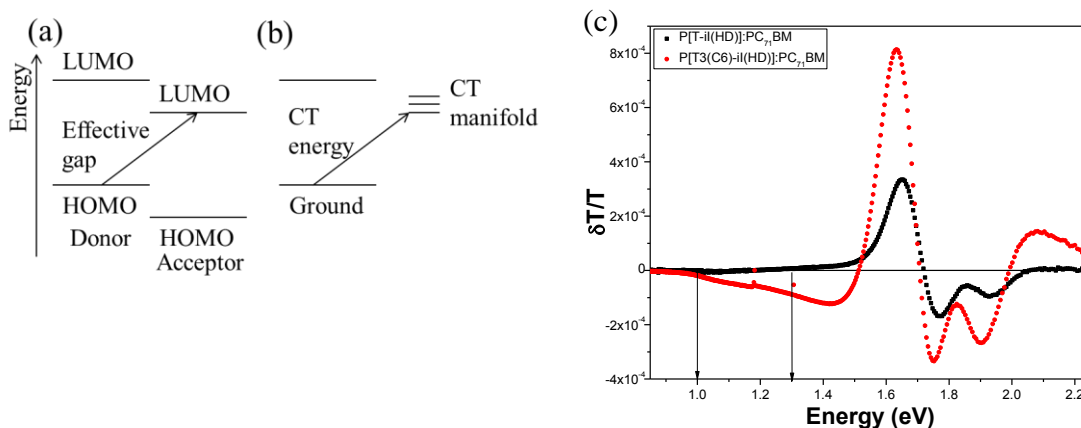


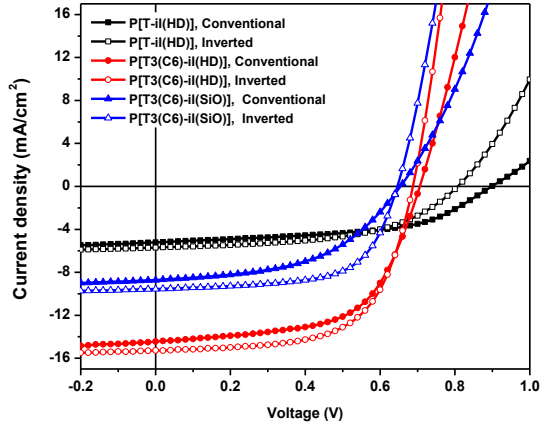
Figure 3-22. Correlation between effective energy gap (molecular orbital picture, a) and CT states energy (electronic state view, b), and CMEAS results showing sub-energy gap absorption of P[T-iI(HD)] and P[T3(C6)-iI(HD)] blends with PC₇₁BM (c).

Through this measurement, the energy of the CT state is estimated to be 1.3 eV and 1.0 eV in blends of PC₇₁BM with P[T-iI(HD)] and P[T3(C6)-iI(HD)] respectively, matching the voltage difference seen in devices. The CMEAS results indicate that while polymers may have similar onsets of oxidation, the CT states formed at the donor/acceptor interface can have different energy levels. The difference between CT state energy and V_{oc} is further explained by energy losses to reach charge separated states.

3.3.5.4. Inverted Devices and Roll-to-roll Processing

The effect of device architecture on device properties was further investigated in inverted devices, using an ITO glass/ZnO–PVP nanocomposites/isoindigo-based polymer:PC₇₁BM/MoOx/Ag architecture more amenable to roll-to-roll fabrication. The inverted devices were fabricated using the same conditions for the active layer deposition as for conventional devices, and the results are summarized in Table 3-7.

Table 3-7. Conventional and inverted device characteristics based on P[T-iI(HD)], P[T3(C6)-iI(HD)], and P[T3(C6)-iI(SiO)] polymer:PC71BM blends processed with DIO.



	J_{sc} (mA cm ⁻²)	V_{oc} (V)	FF (%)	PCE (%)
P[T-iI(HD)] conv.	5.8±0.1	0.90±0.01	55±1	2.9±0.1
P[T-iI(HD)] inv.	5.6±0.1	0.81±0.01	52±1	2.4±0.1
P[T3(C6)-iI(HD)] conv.	15.2±0.1	0.70±0.01	62±1	6.6±0.1
P[T3(C6)-iI(HD)] inv.	15.2±0.3	0.68±0.01	63±1	6.5±0.2
P[T3(C6)-iI(SiO)] conv.	8.6±0.2	0.66±0.01	49±1	2.8±0.1
P[T3(C6)-iI(SiO)] inv.	9.5±0.1	0.64±0.01	63±1	3.8±0.1

In the case of P[T-iI(HD)] and P[T3(C6)-iI(HD)], conventional devices and inverted devices showed similar device performances. On the other hand, inverted devices based on P[T3(C6)-iI(SiO)] showed higher device performance such as higher J_{sc} and FF in spite of lower V_{oc} compared to conventional devices based on P[T3(C6)-iI(SiO)]. The increase in device efficiency in P[T3(C6)-iI(SiO)]:PC₇₁BM inverted OPV devices could not only result from a difference in electrode work function but also from variations in the blend morphology and carrier recombination dynamics.³¹⁵ Based on previous results, it is hypothesized that UV-treated ZnO-PVP decreases carrier recombination at the ZnO-PVP/active layer interface and increases carrier lifetime leading to increased currents and fill factor in the case of P[T3(C6)-iI(SiO)].³¹⁶

To further demonstrate the scalability and efficiency of active layers based on P[T3(C6)-iI(HD)], solar devices were fabricated at Risø DTU, Denmark using this inverted architecture to evaluate the device characteristics of P[T3(C6)-iI(HD)]:PC₇₁BM OPV devices, where the active layer is printed by slot-die coating (Figure 3-23). The devices exhibit a 1.4% PCE on an active area of 0.046 cm², stressing the need to

understand possible morphological changes in transitioning from spun-cast cells to roll-to-roll processes.

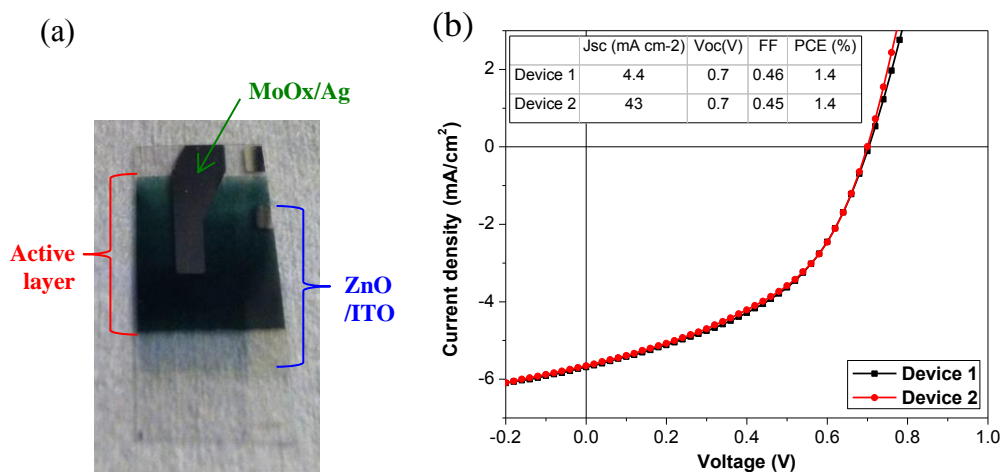


Figure 3-23. (a) Roll-to-roll processed P[T3(C6)-iI(HD)] cell based on PET/ITO/ZnO / P[T3(C6)-iI(HD)]:PC₇₁BM (1:1.5) + 2.5%v DIO in CB/MoO_x /Ag, and (b) J-V curves of slot-die coated cells with device parameters in inserted table.

In conclusion, the density of electron-rich thiophene units along the polymer backbone does not significantly impact the IP of the polymer but does lead to changes in the CT state energy in blends with PC₇₁BM. The morphology of the blends is drastically different depending on the density of branched side-chains along the polymer chain, with P[T-iI(HD)]:PC₇₁BM exhibiting large, round domains while P[T3-iI]:PC₇₁BM blends show more of a fibrillar topology. The use of DIO as a processing additive has a more visible impact on the lateral microscale phase separation of P[T-iI(HD)]:PC₇₁BM but also leads to a five-fold increase in the J_{sc} of P[T3(C6)-iI(SiO)]:PC₇₁BM blends. Overall, the straightforward synthesis of P[T3(C6)-iI(HD)] leading to blends with PCEs over 6% makes this polymer an ideal candidate for further fundamental studies.

3.4. Synthetic Details

6,6'-dibromoisindigo (3-1).^{148,149} To a suspension of 6-bromooxindole (500 mg, 2.36 mmol) and 6-bromoisatin (533 mg, 2.36 mmol) in acetic acid (15 mL), a concentrated

HCl solution (0.1 mL) was added and heated under reflux for 24 h. The mixture was allowed to cool and filtered. The solid material was washed with DI water, ethanol and ethyl acetate. After drying under vacuum, 6,6'-dibromoisindigo was yielded as a brown powder (951 mg, 95% yield). ¹H NMR (300 Hz, (CD₃)₂NOD, DMF, ppm): δ 10.7 (d, 2H), 9.14 (d, 2H), 7.19 (m, 4H).

6,6'-dibromo-N,N'-bis(2-hexyldecyl)-isoindigo (3-2).²⁹⁷ In dry 100mL round bottom flask, 6,6'-dibromoisindigo (1.89 g, 4.5 mmol) and K₂CO₃ (3.73 g, 27 mmol, 6 equiv) powders were dried under vacuum for 30 min. 40 mL dry DMF was added via cannula and 2-hexyldecyliodine (4.86 g, 13.5 mmol, 3 equiv) was injected through the septum into the reaction mixture. The reaction was heated to 95°C for 10h, then cooled to RT and quenched with 500 mL of water. Extraction with ethyl acetate followed by a silica gel column using 4:1 hexane:DCM yielded desired product (2.77 g, 71% yield). ¹H NMR (300 Hz, CDCl₃, ppm): δ 9.08 (d, 2H), 7.15 (dd, 2H), 6.92 (d, 2H), 3.61 (t, 4H), 1.88 (m, 2H), 1.24 (m, 48H), 0.86 (m, 12H).

6,6'-(N,N'-2-hexyldecyl)-pinacoldiboronisoindigo (3-3).²⁹⁷ 3-2 (4.35 g, 5.0 mmol), pinacol ester of diboron (3.05 g, 12.0 mmol, 2.4 equiv), PdCl₂(dppf) (220 mg), and potassium acetate (2.95 g, 30 mmol) were mixed at room temperature under an argon atmosphere. Anhydrous 1,4-dioxane (2 mL) was injected with a syringe through a septum. The solution was heated at 80 °C for 30 h and then cooled to room temperature. The reaction mixture was filtered by passing through a short pad of silica gel, and washed by a mixture of methylene chloride and hexane (1:1). The collected filtration was concentrated and precipitated into cold methanol (100 mL). The precipitate was filtered and dried to give a dark red shiny powder (3.6 g, 75%). ¹H NMR (300 Hz, CDCl₃, ppm) δ

9.15 (d, 2H), 7.48 (d, 2H), 7.15 (d, 2H), 3.69 (d, 2H), 1.95 (bs, 2H), 1.59-1.19 (m, 72H), 0.85 (t, 6H).

General procedure for Suzuki polymerization for P(iI-TPD). In a dry schlenk tube with a stir bar, a mixture of 1,3-dibromo-5-octyl-4H-thieno[3,4-c]pyrrole-4,6(5H)-dione (106 mg, 0.25 mmol), 3-3 (248 mg, 0.25 mmol), Pd₂dba₃ (26.6 mg, 12% equiv), and P(*o*-tol)₃ (21.9 mg, 28% equiv) was deoxygenated three times and refilled with argon, and then toluene dried over MS (6 mL) and freeze-pump-thawed for five cycles was added. A solution of Et₄NOH (5 mL, 1 M in H₂O) was added to the reaction mixture. The reaction mixture was set in an oil bath at 95°C overnight under argon. After cooling to room temperature, a spatula tip of diethyldithiocarbamic acid diethylammonium salt was added to the mixture and stirred for 3 hours. The mixture was precipitated into methanol (300 mL). The precipitate was filtered through a filtration apparatus, set in a cellulose thimble, and purified via Soxhlet extraction for 12 hours with methanol, acetone, and hexanes sequentially. The polymer was extracted with chloroform, concentrated by evaporation, and then precipitated into methanol. The collected polymer was a shiny brown solid (140 mg, 58%).

6,6'-dibromo-N,N'-bis(hex-5-en-1-yl)-isoindigo (3-4).¹⁵⁷ In dry 100mL round bottom flask, 6,6'-dibromoisoidigo (1.47 g, 3.5 mmol) and K₂CO₃ (1.93 g, 14 mmol, 4 equiv) powders were dried under vacuum for 30 min. 30 mL dry DMF was added via cannula and 6-bromo-1-hexene (1.37 g, 8.4 mmol, 2.4 equiv) was injected through the septum into the reaction mixture. The reaction was heated to 100 °C for 10 h, then cooled to RT and quenched with 200 mL of water. Extraction with DCM followed by a silica gel column using 1:1 DCM:hexane yielded desired product (1.74 g, 85% yield). ¹H NMR

(300 Hz, CDCl₃, ppm): δ 9.08 (d, 2H), 7.15 (dd, 2H), 6.92 (d, 2H), 5.79 (m, 2H), 5.05 (m, 4H), 3.74 (t, 4H), 2.11 (m, 4H), 1.70 (m, 4H), 1.51 (m, 4H).

6,6'-dibromo-N,N'-bis(6-(1,1,1,3,5,5,5-heptamethyltrisiloxan-3-yl)hexyl)-isoindigo

(3-5).¹⁵⁷ Compound 3-4 (1.17 g, 2 mmol) was dissolved in 15 mL anhydrous toluene under argon atmosphere. 1,1,3,3,5,5,5-heptamethyltrisiloxane (1.06 g, 4.8 mmol, 2.4 equiv.) was injected through a septum, followed by the addition of 40 μ L of Karstedt's catalyst (platinum divinyltetramethyl-siloxane complex in xylene, 3 wt%). The reaction mixture was stirred at 50°C under argon until consumption of 6,6'-dibromoisoidigo as monitored by TLC. The solution was directly subjected to silica gel chromatography using 2:3 DCM:hexane as the eluent, yielding a dark red oily solid (900 mg, 43% yield). ¹H NMR (300 Hz, CDCl₃, ppm): δ 9.09 (d, 2H), 7.15 (dd, 2H), 6.92 (d, 2H), 3.72 (t, 4H), 1.67 (m, 4H), 1.35 (m, 12H), 0.47 (t, 4H), 0.08 (m, 36H), 0.01 (s, 6H).

3-hexylthiophene (3-7). The reagent 1-bromohexane (66.6 g, 403.6 mmol) was added dropwise to a solution of ground magnesium turnings (8 g, 333.3 mmol) with a tip of iodine in 100 mL dry ethyl ether in an air-free 3-neck flask fitted with a condenser. Once the addition was over, the reaction mixture was heated to 45°C for two hours. The reaction mixture was then transferred to a 3-neck flask containing 3-bromothiophene (47.3 g, 290.2 mmol) and Ni(dppp)Cl₂ (2.09 g, 3.9 mmol, 0.013 equiv) in 200 mL dried ethyl ether. After addition, the brown solution was refluxed at 45 °C overnight. Upon cooling to room temperature, 150 mL of H₂O, 50 mL 0.1 M HCl was added to the reaction, and the resulting mixture was filtered over coarse filter paper. The filtrate was extracted three times with 200 mL of diethyl ether. The combined organic layer was washed once with NaHCO₃, thrice with 200 mL of H₂O, once with 100 mL of brine, and

the organic layer was dried over MgSO_4 . After filtration, the solvent was removed by rotary evaporation to afford a brown oil that was purified by distillation. A colorless oil was obtained as pure product (20.24 g, 30% yield). ^1H NMR (300 Hz, CDCl_3 , ppm): δ 7.28 (dd, 1H), 7.00 (d, 2H), 2.70 (t, 2H), 1.70 (m, 2H), 1.36 (m, 6H), 0.98 (t, 3H).

2-bromo-3-hexylthiophene (3-8). N-bromosuccinimide (NBS) (10.68 g, 60 mmol) was added in three portions over 45 min to a solution of 3-7 (10.10 g, 60 mmol) in 200 mL of dried DMF at 0°C kept in the dark. The mixture was stirred overnight at room temperature and poured into 1 L of water. The organic material was extracted with hexane (3×250 mL). The combined organic extracts were washed with water (200 mL) and brine (200 mL) and dried over anhydrous MgSO_4 . After filtration and removal of the solvent, the remaining organic material was passed through a silica plug using hexanes to give 6.21 g of compound 3-8, yield 41%. ^1H NMR (300 Hz, CDCl_3 , ppm): 7.20 (d, 1H), 6.80 (d, 1H), 2.55 (t, 2H), 1.59 (m, 2H), 1.28 (m, 6H), 0.91 (t, 3H).

3,3''-dihexyl- 2,2':5',2''-terthiophene (3-9). In a dry schlenk flask with a stir bar, a mixture of 2,5-bis(trimethylstannyl)thiophene (1.85 g, 4.54 mmol), 3-8 (2.80 g, 11.34 mmol), Pd_2dba_3 (207.0 mg, 0.23 mmol, 4.8% equiv), and $\text{P}(o\text{-tyl})_3$ (151.0 mg, 0.50 mmol, 10.9% equiv) was deaerated three times with argon, and then toluene dried over MS (40 mL) and freeze-pump-thawed for three cycles was added. The reaction mixture was set in an oil bath at 95°C overnight under argon. After cooling, the solvent was evaporated, and hexanes added to flask to precipitate out tin salts which were filtered out. After the solvent had been removed, the residue was purified by column chromatography with hexanes on silica gel to afford 3-9 as a light yellow liquid with a yield of 70% (1.33 g,

3.19 mmol). ^1H NMR (300 Hz, CDCl_3 , ppm): δ 7.18 (d, 2H), 7.08 (s, 2H), 6.95 (d, 2H), 2.81 (t, 4H), 1.67 (m, 4H), 1.33 (m, 12H), 0.98 (m, 6H).

5,5''-Bis(trimethylstannyl)-3,3''-hexyl-2,2':5',2''-terthiophene (3-6). n-butyllithium (1.6 M in hexanes, 4.37 mL, 7.02 mmol) was added to a solution of compound **3-9** (1.33 g, 3.19 mmol) in 30 mL of dry diethyl ether at -78°C . The mixture was maintained at this temperature for 30 min, warmed to room temperature for another 30 min, and then cooled back to -78°C . Trimethyltin chloride (1 M in THF, 7.02 mL, 7.02 mmol) was added at once. The mixture was stirred overnight at room temperature and poured into water for extraction with diethyl ether (3×50 mL). The combined organic layers were washed with brine (2×100 mL) and dried over MgSO_4 . After the solvent had been removed under reduced pressure, purification by HPLC (60:40 ACN:acetone) yields 0.98g of 3-6 (41% yield). ^1H NMR (300 Hz, CDCl_3 , ppm): δ 7.06 (s, 2H), 7.02 (t, 2H), 2.81 (t, 4H), 1.68 (m, 4H), 1.33 (m, 12H), 0.88 (t, 6H), 0.39 (m, 18H).

General procedure for Stille polymerization for P[T-iI(HD)], P[T3(C6)-iI(HD)] and P[T3(C6)-iI(SiO)]: The dibrominated monomer (0.5 mmol, 1 equiv.), $\text{Pd}_2(\text{dba})_3$ (15 mg) and $\text{P}(o\text{-tyl})_3$ (10 mg) were added to a flame-dried Schlenk flask which was then evacuated and backfilled with argon three times to dry the powders. The bis(trimethylstannyl) comonomer (0.5 mmol, 1 equiv) was dissolved in a dried separate vial in 5 mL of toluene, subsequently degassed with argon for one hour. The solution was then added to the Schlenk flask and the reaction mixture was stirred at 90°C for 60 hours under argon, after which appropriate end-cappers (0.2 mmol) were added and allowed to react for another 3 hours. The reaction mixture was then cooled down to room temperature, and a spatula tip of diethylammonium diethyldithiocarbamate was added to

act as a palladium scavenger. The reaction mixture was left stirring with the scavenger at room temperature for 3 hours, and then the mixture was precipitated in 100 mL of methanol and filtered through a 0.45 μ m nylon filter. The dark solids were purified using a Soxhlet apparatus with methanol until the extracts appeared colorless. The polymers were then fractionated in the Soxhlet apparatus using acetone, hexanes, dichloromethane and chloroform fractions, which contained varying amounts of oligomers and polymer after complete extraction depending on the nature of the comonomer used. Concentration and reprecipitation in methanol allowed filtering the solids through a 0.45 μ m nylon filter to afford the targeted polymer after complete drying in vacuo.

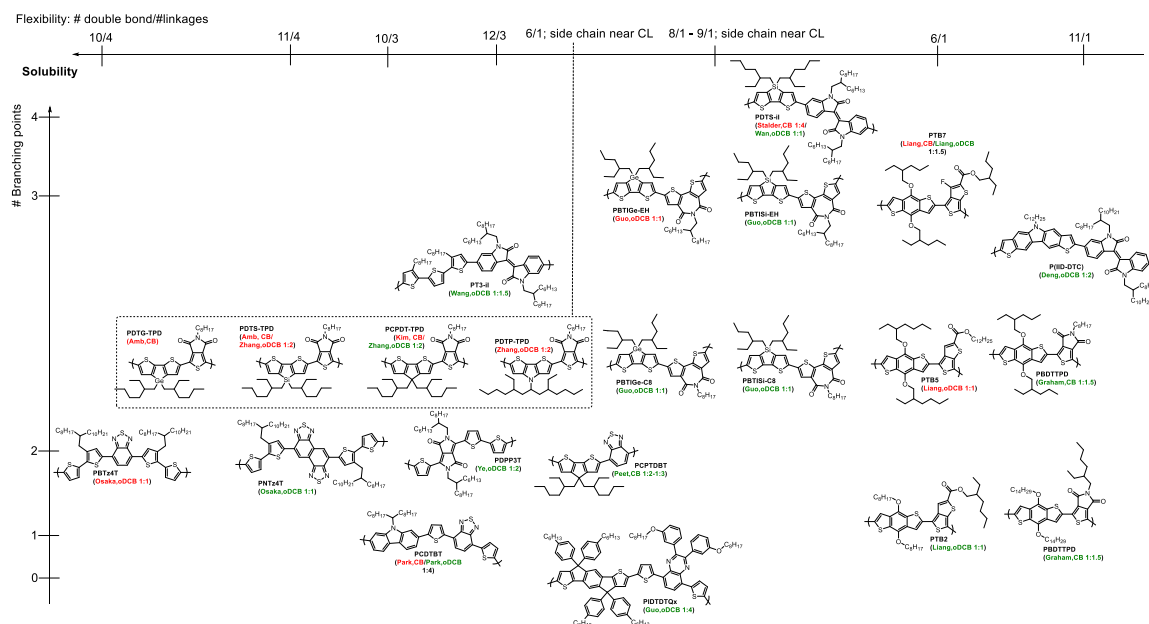
Poly(2,5-thiophene-*alt*-N,N'-bis(2-hexyldecyl)-6,6'-isoindigo) P[T-iI(HD)]: Brown solid (344 mg, 86% CH₂Cl₂ fraction). M_n : 26.4 kDa, PDI: 2.1 (THF). Anal. Calcd for C₅₂H₇₄N₂O₂S C: 78.94, H: 9.43, N: 3.54, S: 4.05. Found C: 78.20, H: 9.48, N: 3.50, S: 3.98.

Poly(5,5''-3,3''-hexyl-2,2':5',2''-terthiophene-*alt*-N,N'-bis(2-hexyldecyl)-6,6'-isoindigo) P[T3(C6)-iI(HD)]: Brown solid (457 mg, 90% chloroform fraction). M_n : 17.7 kDa, PDI: 3.7 (THF). Anal. Calcd for C₇₂H₁₀₂N₂O₂S₃ C: 76.95, H: 9.15, N: 2.49, S: 8.56. Found C: 76.66, H: 9.02, N: 2.52, S: 8.75.

Poly(5,5''-3,3''-hexyl-2,2':5',2''-terthiophene-*alt*-N,N'-bis(6-(1,1,1,3,5,5,5-heptamethyltrisiloxan-3-yl)hexyl)-6,6'-isoindigo) P[T3(C6)-iI(SiO)]: Brown solid (385 mg, 60% chloroform fraction). M_n : 31.7 kDa, PDI: 2.2 (THF). Anal. Calcd for C₆₆H₁₀₂N₂O₆S₃Si₆ C: 61.73, H: 8.01, N: 2.18, S: 7.49. Found C: 60.18, H: 7.96, N: 1.99, S: 7.05.

CHAPTER 4. POLYMER PACKING TO CONTROL THIN-FILM MORPHOLOGY

Recently, polymer solubility has emerged as a determining factor in blends with fullerenes, impacting polymer fibril width in the solid state.¹⁹⁴ In the Introduction, the solvent choice, along with the polymer design, has been described as having an impact on phase separation in polymer:fullerene blends. Scheme 4-1 gives an overview of donor polymer structures for fullerene-based OPVs along with their processing solvent and the qualitative phase separation achieved in thin films (red: phase separation ≥ 50 nm, green: phase separation < 50 nm). The solubility of the polymers is qualitatively determined based on the rigidity of the backbone, including the flexibility in the side-chain ordering via the bridging atom in these structures, and on the number of branching points on the side-chains.



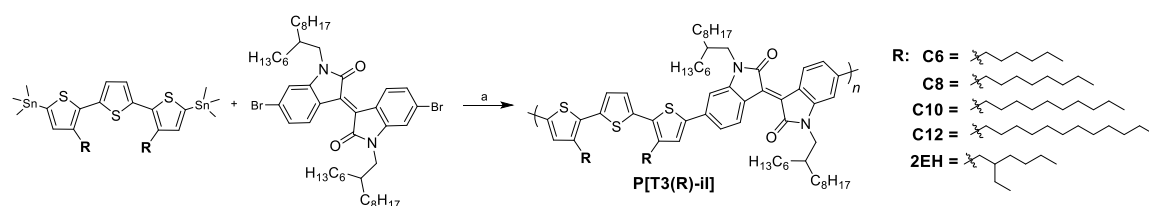
Scheme 4-1. Polymer structures reported in the literature and their processing conditions in blends with PC₇₁BM for OPVs. Conditions leading to small phase separation with fullerenes are written in green and those leading to large phase separation are in red.

As expected, the use of *o*-dichlorobenzene (oDCB) rather than chlorobenzene (CB) promotes longer drying times and smaller phase separation; however some blends still exhibit large phase separation when cast from oDCB. Furthermore, the qualitative determination of polymer solubility does not explain the trends in phase separation as observed by atomic force microscopy in most cases. In order to fundamentally understand the structural parameters influencing polymer packing and phase separation in bulk heterojunction cells with fullerene derivatives, poly(terthiophene-*alt*-isoindigo) described in the previous chapter was chosen as the base structure, which can be modified by selecting various side chains. In this work, it was originally thought that polymer packing would be controlled mainly via the 2-hexyldecyl side-chains on the isoindigo units, and as such the side chains on the terthiophene units were modified to increase polymer solubility. After quantification of polymer solubility, the polymer packing and phase separation with PC₇₁BM were investigated to highlight structure-property relationships and processes leading to film formation.

4.1. Synthesis of P[T3(R)-iI] Polymers

A family of five different polymer structures was synthesized, keeping the same alternating units of terthiophene and isoindigo but modifying the solubilizing chain on the terthiophene unit. The choice of having the side chains on the 3,3''-positions was made to reduce possible steric hindrance with the neighboring phenyl ring.¹⁵⁹ The synthesis of the terthiophene monomers was conducted by Kumada coupling to install the alkyl chains at the 3-position of the thiophene ring, followed by bromination with N-bromosuccinimide (NBS) at the 2-position, Stille coupling with 2,5-bis(trimethylstannyl)thiophene, and finally lithiation with *n*-butyllithium followed by quenching with trimethyltin chloride.

The polycondensation reactions were then carried out under Stille coupling conditions using Pd₂dba₃ and tri(*o*-tolyl)phosphine (P(*o*-tol)₃) as the catalyst and ligand system, and left to react under inert atmosphere for 72 h. Finally, 2-(tributylstannyl)thiophene and 2-bromothiophene were added to the reaction mixture to install thiophene end-groups on the polymer chains. Due to the similar structure of the end-groups compared to the polymer backbone, the presence of the end-cappers on the polymer structure could not be confirmed and as such are not shown in the polymer structures.



Scheme 4-2. Synthesis of a family of terthiophene and isoindigo alternating polymers with varying side chains. a) Pd₂dba₃, P(*o*-tol)₃, toluene, 95 °C.

In order to remove Pd from the reaction mixture, a palladium scavenger was added prior to precipitation of the mixture in methanol. The polymer was isolated by filtration and then purified by Soxhlet extraction. Based on their solubility, C6, C8, C10, and C12 were collected from the chloroform fraction; however, some lower molecular weight C12 was collected from the dichloromethane fraction and due to its higher solubility, 2EH was collected in the hexanes fraction. It is important to note that the synthesis of P[T3(C6)-ii(HD)] was conducted on two 1 gram scales. One batch was used for this study, and the second batch was used for the study described in Chapter 5. The purity of the polymers was determined by elemental analysis and their molecular weight was estimated against polystyrene standards using size exclusion chromatography at the Max Planck Institute (MPI) in 1,2,4-trichlorobenzene at 85 °C as the eluent. The results are summarized in Table 4-1.

The change in the side chain is thought to have an influence on the thermal properties of the polymer. Thermogravimetric analysis (TGA) under a nitrogen flow was used to evaluate the thermal stability of the polymers, which demonstrated decomposition temperatures (defined as 5 % mass loss) above 390 °C. Figure 4-1 demonstrates that differential scanning calorimetry on C6 at a rate of 10 °C/min shows no thermal transition between -60 °C and 250 °C for C6. In contrast, 2EH exhibits a melting peak at 180 °C and crystallization peaks at 144 °C (shoulder) and 150 °C (peak) (Figure 4-1b). Previous studies have shown a melting transition for C8 at 289 °C.¹⁶⁰ In order to see the melting peak of C6, the temperature range was increased to 375 °C with a scan rate increased to 20 °C/min in order to increase the sensitivity of the instrument to the glass transition of the polymer. Figure 4-1c shows the presence of a T_g around 60 °C and two melting points for C6 at 270 °C (shoulder) and 287 °C (peak). However, no crystallization peak is observed upon cooling, and the magnitude of the melting peaks is decreased in the subsequent cycle. The presence of the two crystallization peaks in 2EH and the two melting peaks in the C6 sample indicates the formation of two different polymorphs in these structures.

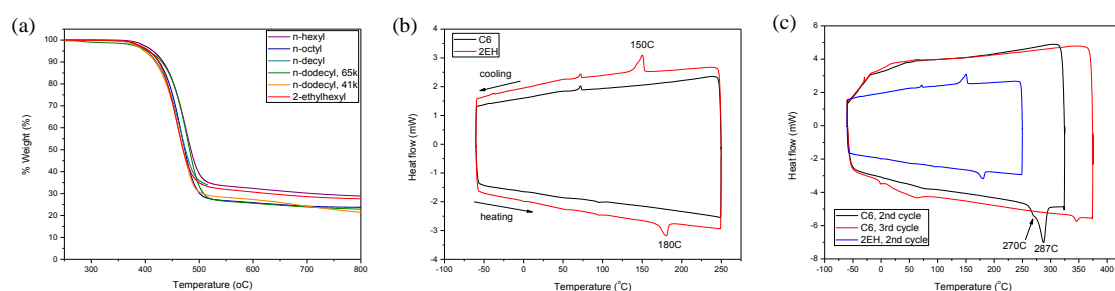


Figure 4-1. (a) TGA trace of the six polymers. (b) DSC analysis of C6 and 2EH at 10 °C/min (third DSC scan showed), and (c) DSC analysis of the second and third cycle of C6 at 20 °C/min (2EH is recalled from (b) as a reference).

4.2. Polymer Behavior in Solution - Quantification of Solubility

To quantify the impact of the polymer structure on solubility, the amount of polymer soluble in oDCB was measured at room temperature by saturating an oDCB solution and removing insoluble material via a centrifuge. The absorption of the supernatant was compared to a calibration UV-vis-NIR curve in order to determine the amount of solubilized polymer. The calibration curves for C6 and 2EH are reported in Figure 4-2. The results are summarized in Table 4-1 and show that solubility can be tuned by varying the length and branching of the side-chain, as well as by changing the molecular weight. The family of six polymers spans solubilities in oDCB ranging from 2 mg/mL to 27 mg/mL at room temperature.

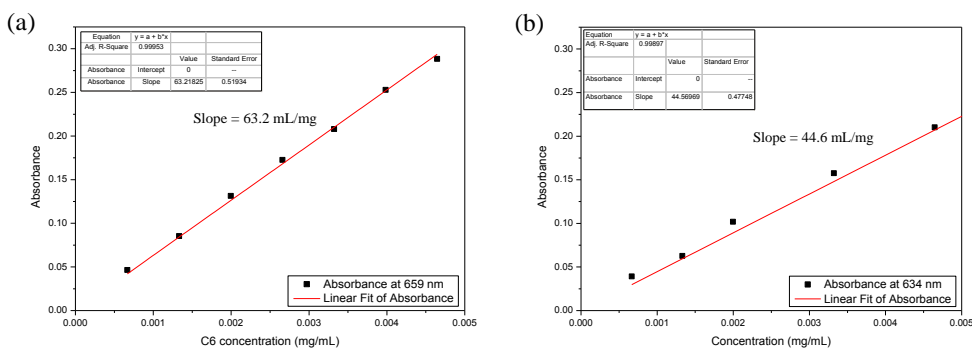


Figure 4-2. Calibration curves of absorbance at 659 nm versus the concentration of C6 (a) and at 634 nm versus the concentration of 2EH (b) in oDCB.

4.3. Optoelectronic Properties of the P[T3(R)-iI(HD)] Family

It is expected that variations in the side-chains will have minimal impact on the absorption properties of P[T3(R)-iI], except in the case of 2EH, where previous work has shown that torsion along the backbone caused by steric hindrance from alkyl chains leads to an increased energy gap and increased ionization potential (IP).²⁹⁶ Here, UV-vis-NIR spectroscopy in Figure 4-3 shows overlap in the oDCB solution absorption of P[T3(R)-iI] with linear side-chains, and a blue shifted absorption maximum for 2EH. This indicates

that the conjugation length in solution is lower in 2EH compared to the other P[T3-iI] polymers. One hypothesis for this is the reduced orbital overlap due to increased torsion induced by the steric influence of the 2-ethylhexyl side chains.

Considering the film absorption in Figure 4-3, 2EH exhibits a slight red shift in the solid state compared to solution (18 nm or 54 meV), indicating planarization of the polymer backbone. Indeed, the absorption maximum is 635 nm in solution and 653 nm in thin film. The other P[T3-iI] polymers do not exhibit significant planarization of their backbone when they transition from solution to the solid state (4 nm blue shift in the case of C6); however, the thin film absorption for these structures does show the appearance of a new aggregation peak around 700 nm. The blue shifted onset of absorption for 2EH compared to the other polymers remains in the solid state, indicating an increase in the optical energy gap as was previously reported in thiophene-based polymers. Furthermore, an increase in scattering (arrow in Figure 4-3b) can be observed going from 2EH to C6 most likely due to an increase in film roughness with decreasing solubility.

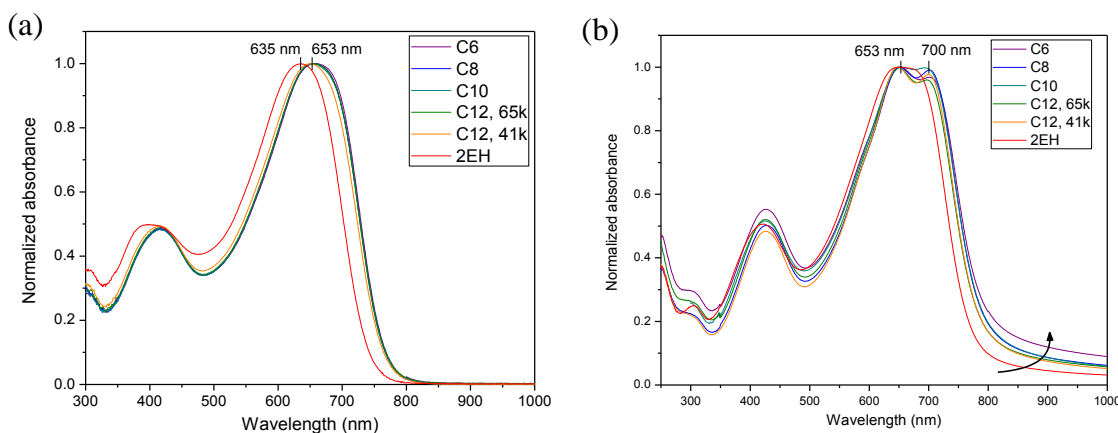


Figure 4-3. (a) Solution absorption spectra in oDCB, and (b) film absorption spectra of P[T3(R)-iI] polymers.

These trends in the absorption spectra are further supported by the measurement of the polymers' electrochemical potentials by differential pulse voltammetry (DPV)

(Figure 4-4). The measurements were conducted on polymer thin films deposited on Pt electrodes in a 0.1 M TBAPF₆ in acetonitrile electrolyte. Onsets of oxidation and reduction were determined relative to Fc/Fc⁺, and the estimates of ionization potential (IP) and electron affinity (EA) were calculated using 5.1 eV below vacuum as the potential of Fc/Fc⁺ (assuming that the reorganization of the chains upon oxidation/reduction is similarly affected by the electrolyte solution for all polymers). As with other isoindigo-based polymers, the onset for reduction is determined to be around -1.20 V against Fc/Fc⁺ with two reduction peaks being observed. This leads to an estimated EA of around 3.90 eV across this polymer series, on par with other reported isoindigo-based polymers.¹⁵¹ Little change is observed for polymers with linear chains with IP around 5.6 eV; however, the IP of 2EH is increased by 0.2 eV compared to the polymers with linear chains to 5.8 eV. This increase in IP with branched side-chains is expected to increase the open-circuit voltage in organic photovoltaic (OPV) devices.

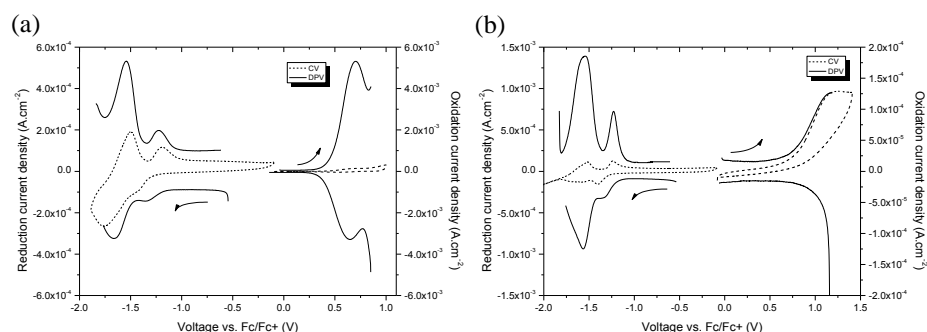


Figure 4-4. CV and DPV versus Fc/Fc⁺ of (a) C6 and (b) 2EH on a Pt button electrode in 0.1M TBAPF₆ in acetonitrile.

The structural characterizations along with optoelectronic properties are summarized in Table 4-1. The polymers exhibit around 0.1 eV difference in their fundamental versus optical energy gap, except in the case of C10, where the fundamental and optical gap are similar, and in the case of 2EH, where the difference is 0.22 eV. This difference between

fundamental and optical gap stems from the exciton binding energy, thus pointing to the fact that excitons formed on 2EH are more tightly bound than in the polymers with linear chains.

Table 4-1. Purity, Molecular Weight, Solubility, Electrochemical, and Optical Properties of P[T3(R)-iI] polymers.

R group	EA ^a	Mn/Mw (kDa), PDI ^b	Solubility ^c (mg/mL)	E_{ox}^{onset} (V)/ IP ^d (eV)	E_{red}^{onset} (V)/ EA ^e (eV)	E_{gap}^f (eV)	$E_{gap}^{abs}^g$ (eV)
C6	0.3%	80/207, 2.6	2 ± 1	0.48/5.58	-1.17/3.93	1.65	1.57
C8	0.3%	70/146, 2.1	10 ± 2	0.48/5.58	-1.20/3.90	1.68	1.57
C10	0.2%	61/126, 2.1	12 ± 2	0.50/5.60	-1.04/4.06	1.54	1.55
C12							
65k	0.9%	65/125, 1.9	12 ± 2	0.45/5.55	-1.26/3.84	1.71	1.58
41k	0.6%	41/103, 2.5	21 ± 5	0.45/5.55	-1.21/3.89	1.66	1.58
2EH	0.4%	53/126, 2.4	27 ± 5	0.71/5.81	-1.17/3.93	1.88	1.60

^acarbon elemental analysis % error ^bmolecular weight distribution estimated by GPC in 1,2,4-trichlorobenzene (TCB) at 135 °C, ^csolubility in oDCB, ^destimate of ionization potential and ^eestimate of electron affinity measured by DPV vs. Fc/Fc⁺, ^fenergy gap estimated from oxidation and reduction onsets in DPV trace, ^goptical energy gap calculated from absorption onset of polymer films.

4.4. Molecular Interactions by GIWAXS

Grazing-incidence wide-angle X-ray scattering was used to measure the differences in polymer packing in the solid state. The polymers films were spun cast from a filtered oDCB solution onto a silicon wafer, and measured at the Stanford Synchrotron Radiation Lightsource (SSRL) as described in Chapter 2. After integration over a quadrant of the detector, line shape analysis was conducted using Gaussian functions to fit the scattering peaks – the peak positions are attributed to the (hkl) scattering planes and the full widths at half maximum (FWHM) give indications on the crystallinity of the scattering peak. The peaks which could be attributed to scattering planes of the polymer were considered crystalline (typically FWHM below 0.3 Å⁻¹), and peaks with FWHM above 0.3 Å⁻¹ were considered amorphous. The relative degree of crystallinity of each film was calculated by

the ratio of the total area of crystalline peaks over the total scattering area. Information about the size of crystallites is contained within the width of the diffraction peaks, and the coherence length was calculated using the Scherrer equation. However, this is an approximation in the case of polymers, where disorder also impacts the width of the diffraction peak and is difficult to de-correlate from finite crystal sizes.¹⁷⁶ Finally, the orientation of the crystallites versus the substrate was calculated through the Hermann orientation factor. All these methods were described in Chapter 2.

Figure 4-5 summarizes the data obtained on the as-cast films. A first observation is the mixed organization of the polymer chains relative to the substrate. Films of P[T3(R)-iI] with C8 and C12 reveal features in the pattern characteristic of face-on and edge-on arrangement, as discussed in Chapter 3. The edge-on orientation is indicated by out-of-plane (h00) reflections related to the layer structure, while a broad wide-angle scattering intensity also located out-of-plane of the pattern suggests a face-on population. A coexistence of both organization fractions is not untypical and has been reported for several high performance polymers, and can be explained by the different interactions at the polymer:silicon interface, in the bulk and at the polymer:air interface. P[T3(C6)-iI] exposes even a 3rd population with a (010) peak tilted at a 30° angle, although the orientation of the (100) peak is mainly around the q_z axis, with little distribution of its orientation. Furthermore P[T3(C10)-iI] assembles mainly in edge-on layers with some face-on population, similarly to the other polymer films. However, the order within the polymer lamellae is low as only an isotropic amorphous halo in the π -stacking region is found.

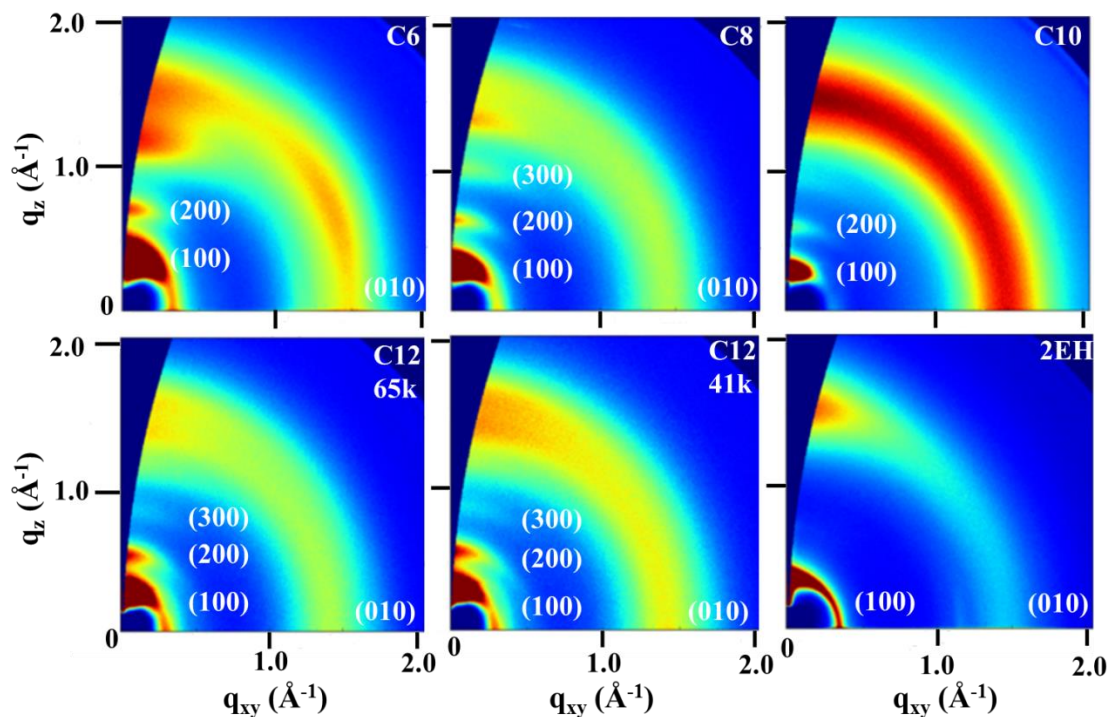


Figure 4-5. GIWAXS images in as-cast films of P[T3(R)-iI] from oDCB.

P[T3(2EH)-iI] exhibits a striking difference in terms of out-of-plane ($h00$) reflections, and it is thought that there is a higher population of chains in a face-on orientation for this polymer compared to the polymers with linear chains. Chen *et al.*^{196,317} and Zhang *et al.*⁹³ have hypothesized that (100) alkyl-terminated planes will interact more favorably with the low energy SiO₂ surface on the silicon wafer than the π -terminated (010) planes, leading to edge-on orientation being more thermodynamically stable. This hypothesis is consistent with the observation that thermal annealing leads to a drastic change in polymer backbone orientation from mainly face-on to mainly edge-on after reorganization from the melt.²¹⁶ As such, one explanation for the face-on orientation in thin films of 2EH is the increase in bulky side-chains leading to increased solubility and hindering π -stacking, which slows down ordering and yields increased dispersion interactions between the substrate and the π -system as observed in other systems with a

high density of branched alkyl side-chains.⁹³ Moreover, polymers with linear alkyl chains show increased order in as-cast thin films, with higher order (h00) diffraction peaks at higher q_z values. By comparison, 2EH films containing more twisted backbones due to the bulkier 2EH side-chain show less ordered packing structures, which in turn can explain the lack of aggregation peaks in the solid-state UV-visible spectrum of 2EH.

SSRL offers the capability of in-situ annealing under a helium atmosphere, and Figure 4-6 summarizes the GIWAXS data obtained on the same films after *in situ* annealing at 200 °C for 10 min. A first observation is the increase in polymer ordering with higher order (h00) peaks being observed in all systems. In particular 2EH was annealed past its melting temperature of 180 °C, and exhibits very crystalline peaks.

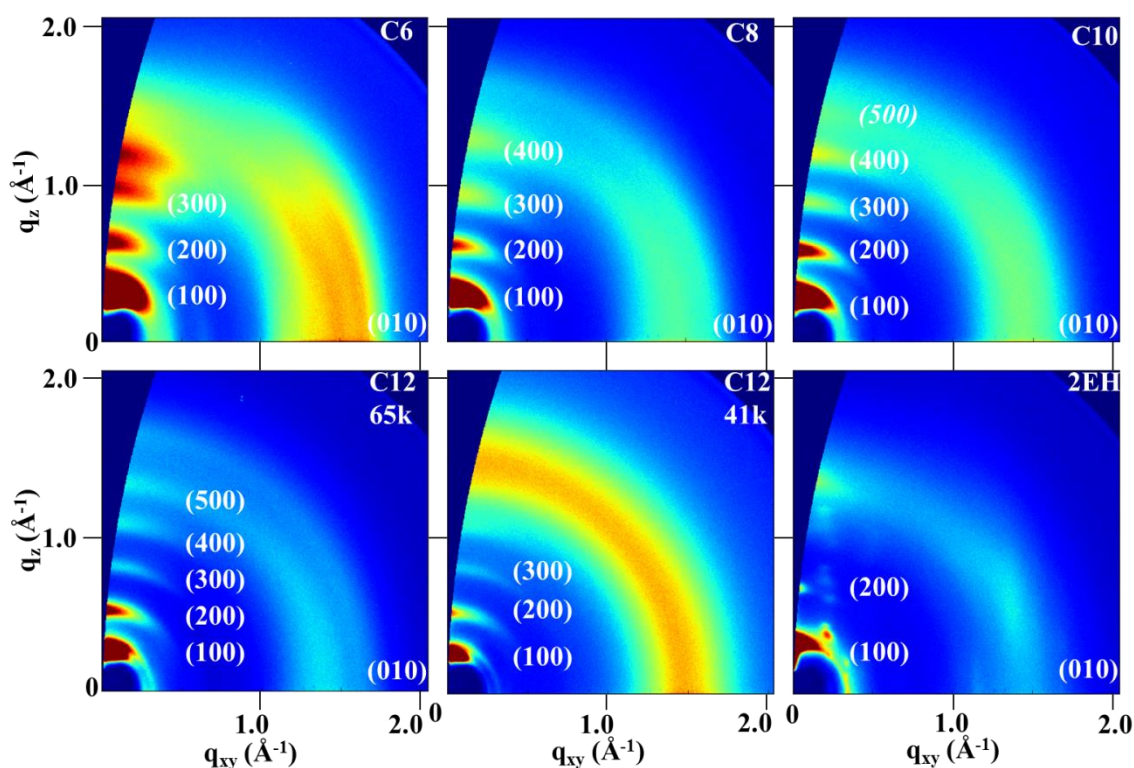


Figure 4-6. GIWAXS of P[T3(R)-il] polymers annealed at 200 °C, and cooled to room temperature.

Peak assignments were based on the observed transitions as the sample was heated to 200 °C and cooled to 40 °C. An example is given in Figure 4-7 of the changes in scattering of a C6 thin film with thermal annealing. As the temperature is increased, the peak intensities decrease, indicating loss of ordering in the film and the possibility for the chains to reorganize to a more thermodynamically favored packing structure. Based on the DSC data, it is expected that these polymers can achieve different ordered structures. The fact that these polymers are polymorph i.e. with two possible crystalline structures can explain the presence of peaks that cannot be assigned to (hkl) planes in a straightforward manner.

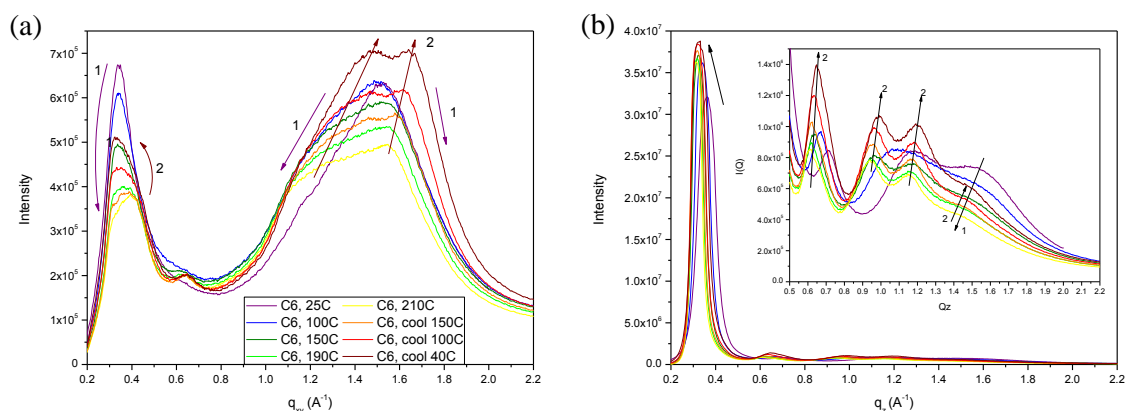


Figure 4-7. (a) q_{xy} and (b) q_z line integrations as a function of sample temperature. The inset in (b) focuses on higher q_z peaks. The arrows labeled (1) indicate transitions as the films are heated, and (2) as they are cooled.

In these polymer thin films, thermal annealing leads to an increase in the more thermodynamically favored edge-on population.²¹⁶ The orientation of the polymer chain-to-chain direction is quantified by the Herman orientation factor (HOF) for the (100) peak and is reported in Table 4-2. The HOF quantifies the extent of orientation of the polymer chains relative to the substrate, (h00) peaks strictly along q_z leading to a HOF of 1, and (h00) peaks along q_{xy} leading to a HOF of -0.5, while randomly oriented crystals

lead to a HOF of zero. A HOF of 0.5 as is the case here points to a majority of the population having chain-to-chain packing out-of-plane (i.e. π -stacking edge-on) with some chains having chain-to-chain packing in plane (i.e. π -stacking face-one). Beyond having an impact on crystallite orientation, thermal annealing also impacts coherence length, L_c , and crystallinity in the thin films. Generally, thermal annealing yields longer chain-to-chain d distances and shorter π - π distances, suggesting that the alkyl side-chains are extending away from the polymer backbones and that the backbones are in closer contact after annealing. The size of the crystals in the chain-to-chain direction also increases with thermal annealing, with crystallites being extended by two to three polymer chains on average. The percent crystallinity of the thin films is also increased with thermal annealing, but to different extents with different polymer structures.

Table 4-2. Backbone-to-backbone π and chain-to-chain d distances determined from polymer thin film GIWAXS and their corresponding coherence length, along with film crystallinity and HOF for the (100) peak.

Derivative	GIWAXS As-cast				GIWAXS Annealed					
	π (Å)	d (Å)	L_c, d (Å)	Crystallinity (%)	π (Å)	L_c, π (Å)	d (Å)	L_c, d (Å)	HOF	Crystallinity (%)
C6	4.1	18	105	60	3.7	57	19	129	0.5	64
C8	4.2	19	122	48	3.7	61	20	158	0.5	58
C10	4.2	20	125	19	3.8	42	20	167	0.5	54
C12, 65k	4.3	21	113	45	3.7	55	22	205	0.5	56
C12, 41k	4.3	21	116	40	/	/	22	207	0.5	42
2EH	4.1	17	152	42	4.2	/	18	202	0.6	61

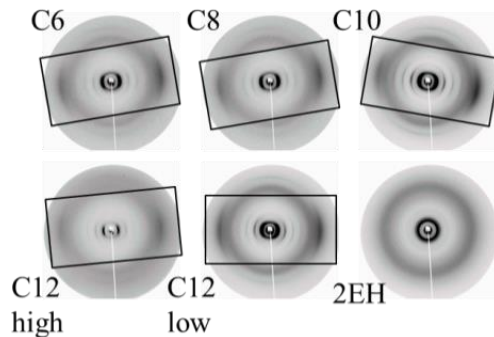
Interestingly, the higher molecular weight C12, 65k polymer leads to apparently more crystalline and ordered films than C12, 41k. This can be explained both by an increased number of chain ends in C12, 41k films compared to C12, 65k films, which can act as defects and interrupt the formation of polymer crystallites, and an increased PDI in the case of the C12, 41k polymer (2.5 versus 1.9 in the case of C12, 65k). The impact of

thermal annealing on polymer packing in thin films is also expected to influence charge carrier mobilities in OFET devices.

To verify our assumptions for peak assignment in the GIWAXS data, 2DWAXS was obtained on extruded polymer fibers annealed at 200 °C. 2DWAXS analysis investigates bulk structural organization and highlights the fact that P[T3(R)-iI] polymers assemble in chain-to-chain structures oriented in the extrusion direction as shown by scattering in the equatorial direction with both chain-to-chain and π -stacks oriented perpendicular to the extrusion direction. Similarly to the GIWAXS data, the 2EH is melted at 200 °C and as such exhibits diffuse rings compared to the other polymers. The characteristic distances were determined from line integration along the equatorial direction, and the data is summarized in Table 4-3. In general, after annealing at 200 °C, the packing distances in the bulk are slightly lower than what is observed in thin films annealed at the same temperature, and could be due to the strain of the extrusion process or to the lack of influence of a substrate on polymer packing.

Table 4-3. π -stacking π and chain-to-chain d distances (left) estimated from line integration of equatorial peaks in the 2DWAXS data (right).

	2DWAXS		2DWAXS annealed	
	π (Å)	d (Å)	π (Å)	d (Å)
C6	3.9	19	3.7	19
C8	4.0	20	3.8	21
C10	4.0	22	3.8	22
C12	3.9	24	3.9	24
65k				
C12	4.0	24	3.8	24
41k				
2EH	4.2	19	4.2	19



Interestingly, both the GIWAXS and 2DWAXS data show a doubling of the (100) peak at low q after annealing as illustrated in Figure 4-8. The presence of the two peaks is

challenging to understand as no further peak splitting is observed for the higher order peaks. However, similar splitting of the (100) diffraction peaks was observed by Rogers *et al.*³¹⁸ in PCDTBT films and was attributed to two different crystal structures. Overall, from this structural data, it is concluded that polymers with linear chains on the terthiophene unit exhibit increased ordering in thin films compared to 2EH.

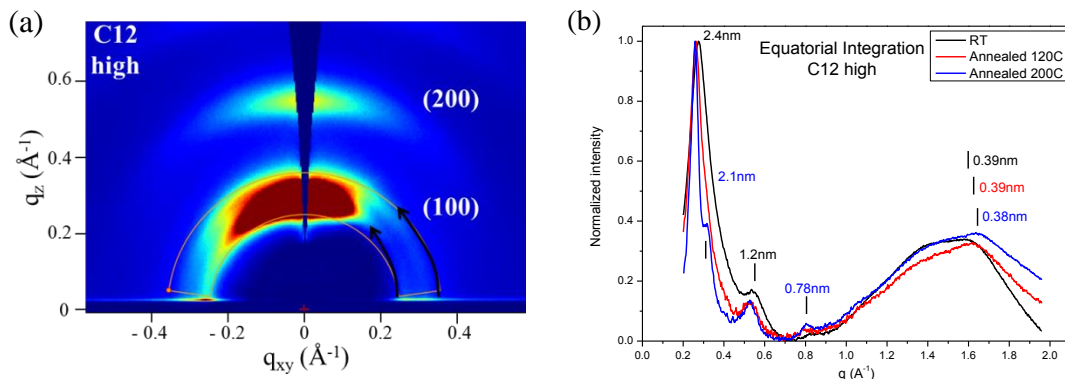


Figure 4-8. (a) GIWAXS plot of C12 65k film focusing on (100) and (b) 2DWAXS equatorial integration plot of C12 high extruded fibers at RT and annealed at 120 °C and 200 °C.

4.5. Charge Transport in OFET devices

In order to probe the effect of side-chains on packing and charge transport, bottom-gate/bottom-contact OFET devices were fabricated on heavily p-doped silicon wafers covered with hexamethyldisilazane- (HMDS) modified SiO₂. Gold electrodes were patterned to form 10 μm long and 700 μm wide channels. The polymer layers were drop-cast from a solution at 4.4 mg/mL in oDCB at 120 °C onto the substrate maintained at 120 °C, and subsequently annealed at 120 °C for 1 h. It is important to note the difference in processing between the films used to obtain GIWAXS data and the active films in OFET devices. Table 4-4 summarizes the OFET performance obtained across the polymer series, where the mobilities were determined from the OFET saturation regime.

Table 4-4. Hole μ_h and electron μ_e OFET mobility, and OFET threshold voltage V_T after annealing at 120 °C.

Sample	$\mu_h [\text{cm}^2 \cdot \text{V}^{-1} \text{s}^{-1}]$ $\times 10^{-3}$	$V_T [\text{V}]$	$\mu_e [\text{cm}^2 \cdot \text{V}^{-1} \text{s}^{-1}]$ $\times 10^{-3}$	$V_T [\text{V}]$
C6	26.0	-20	4.0	49
C8	7.0	-25	-	-
C10	23.0	-20	4.0	43
C12, 65k	28.0	-23	0.1	34
C12, 41k	2.0	-25	0.1	44
2EH	4.0	-19	1.4	60

A first observation is that all polymers exhibit ambipolar transport, except for C8. In general, electron mobility is one to two orders of magnitude lower than hole mobility, except in the case of 2EH where the hole and electron mobility are 4.0×10^{-3} and $1.4 \times 10^{-3} \text{ cm}^2 \text{ V}^{-1} \text{ s}^{-1}$ respectively. In the case of C8, only hole carrier mobility is observed, which is different from a previous report on the same polymer structure where C8 is measured to exhibit hole and electron carrier mobilities of 3.0×10^{-2} and $5.0 \times 10^{-3} \text{ cm}^2 \text{ V}^{-1} \text{ s}^{-1}$ respectively in thin films spun-cast from chloroform and annealed at 170 °C.¹⁶⁰

For C6, C8, C10, and C12 high polymers, hole mobility is measured to be between 2.3×10^{-2} and $2.8 \times 10^{-2} \text{ cm}^2 \text{ V}^{-1} \text{ s}^{-1}$, showing little influence of the length of the side-chain on the hole mobility. However, comparison of the two fractions of P[T3(C12)-iI] highlights an increase by an order of magnitude when the higher molecular weight fraction is used in devices, with hole mobilities of $2 \times 10^{-3} \text{ cm}^2 \text{ V}^{-1} \text{ s}^{-1}$ for the lower molecular weight polymer. This increase in hole mobility with increasing molecular weight has been observed previously,²⁰⁷ and this work reinforces the importance of molecular weight in OFET devices. The hole mobility also drops to $4 \times 10^{-3} \text{ cm}^2 \text{ V}^{-1} \text{ s}^{-1}$ in devices fabricated with 2EH. Finally, thermal annealing plays a crucial role in optimizing OFET device performance. The highest charge carrier mobilities are achieved

after thermal annealing at 120 °C, which is consistent with the increased order within the lamellar stacks with thermal annealing as depicted in the GIWAXS images.

4.6. Photovoltaic Devices

The photovoltaic properties of the six polymers were examined in BHJ devices with (6,6)-phenyl-C₇₁-butyric acid methyl ester (PC₇₁BM) as the electron acceptor. All solar cell devices were fabricated and tested under inert atmosphere and photocurrent was measured under simulated AM 1.5G solar illumination at an irradiation intensity of 100mW cm⁻². Blends of polymer:PC₇₁BM at a 1:1.5 ratio were spun-cast from oDCB solutions (without any solvent additives such as DIO) at 80 °C onto PEDOT:PSS (30 nm) coated ITO glass, and layers of calcium (10 nm) and aluminum (80 nm) were sequentially deposited on top of the active layer to form the cathode. The devices were not optimized but rather fabricated in the same fashion, tuning film thickness to achieve comparable light absorption for direct comparison of the effect of the side-chain and molecular weight on BHJ device parameters.

Devices fabricated from C6 and C8 reach average power conversion efficiencies (PCE) of 5.1% and 5.2% respectively (Table 4-5), in agreement with previously reported OPV devices prepared without additives.¹⁵⁹ Compared to other P[T3(R)-iI] polymers, the increased short-circuit current (J_{sc}) and fill factor (FF) leads to these higher efficiencies in C6 and C8. In particular, the FF decreases with increasing length of the alkyl chain, which can be partly explained by the need of thicker films to achieve the same light absorption.

Table 4-5. OPV performance of P[T3(R)-iI] derivatives with PC₇₁BM spun-cast from oDCB.

Polymer: PC ₇₁ BM	Solubility (mg/mL)	Integrated J _{sc} (mA.cm ⁻²)	J _{sc} (mA.cm ⁻²)	V _{oc} (V)	FF (%)	PCE (%)	Thickness (nm)
C6	2	11.2	12.3 ± 0.4	0.69 ± 0.01	58 ± 1	5.1 ± 0.1	94 ± 5
C8	10	11.3	12.7 ± 0.3	0.70 ± 0.02	57 ± 5	5.2 ± 0.4	105 ± 6
C10	12	10.6	11.6 ± 0.4	0.63 ± 0.01	54 ± 1	4.1 ± 0.1	113 ± 12
C12 65k	12	10.6	11.3 ± 0.4	0.66 ± 0.00	52 ± 1	4.0 ± 0.1	113 ± 5
C12 41k	21	9.8	11.0 ± 0.4	0.69 ± 0.01	51 ± 1	4.0 ± 0.1	120 ± 2
2EH	27	0.7	0.8 ± 0.1	0.88 ± 0.01	58 ± 3	0.3 ± 0.0	99 ± 12

Statistical data for each polymer was obtained from 12 cells over two separate devices.

As shown in the device current density vs. voltage (J-V) curves and incident photon-to-current efficiency (IPCE) (Figure 4-9), the most drastic change is obtained when the polymer backbone is fully functionalized with branched side-chains, leading to increased open-circuit voltage (V_{oc}), but an order of magnitude lower J_{sc}. The change in V_{oc} is probably related to the higher ionization potential of 2EH compared to the *n*-alkyl derivatives.²⁹⁶ A first hypothesis for the low J_{sc} could be the low hole mobility measured in OFET devices; however low molecular weight C12 polymer has a hole mobility of the same order of magnitude but one order of magnitude higher J_{sc}. In order to understand the origin of the low J_{sc} in 2EH:PC₇₁BM devices, differences in phase separation were investigated.

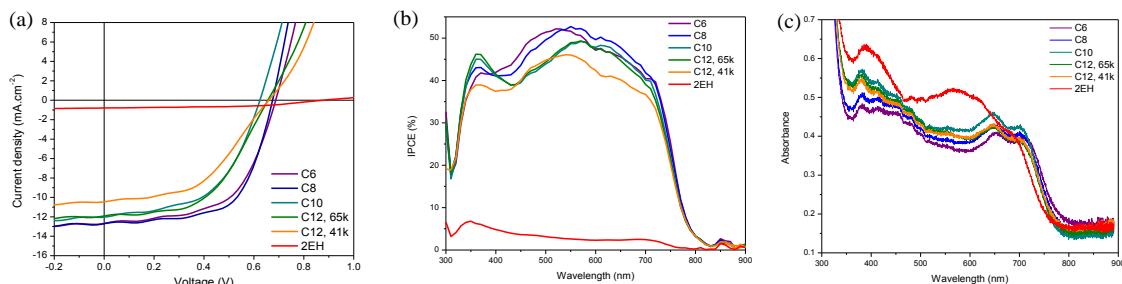


Figure 4-9. (a) J-V curves of P[T3(R)-iI]:PC₇₁BM blends spun cast from oDCB, (b) the corresponding IPCE curves, and (c) device absorption spectra.

4.7. Morphology Control via Polymer Structure

Atomic force microscopy (AFM) was employed to image the surface of the active layer to determine the active layer topology in polymer:PC₇₁BM thin films. It is expected that varying the side-chain length will influence polymer solubility with fullerene derivatives and phase separation. As seen in Figure 4-10, all films based on polymers with linear side-chains on the terthiophene unit exhibit features on the order of 20 nm in width. In these films, the root-mean-square (rms) roughness is determined to be between 2.5 nm and 4.7 nm with little correlation between polymer structure and roughness.

In the case of 2EH:PC₇₁BM blends large domains protruding from the surface are formed, leading to an increased rms roughness of 7.0 nm. It is hypothesized that the 2EH AFM image shows islands of PC₇₁BM that are encapsulated by a polymer layer as was seen in MDMO-PPV blends³¹⁹ and in blends of other highly soluble polymers with PC₇₁BM.^{305,320} The striking difference in phase separation between 2EH and the other five polymers supports the decrease in photocurrent of the 2EH:PC₇₁BM solar cells. Interestingly, the solubility of the polymers, whether influenced by the length of the side-chains or the molecular weight does not seem to have a drastic impact on the surface topology. Moreover, the torsion induced by the branched 2-ethylhexyl side-chain has a greater influence than polymer solubility alone.

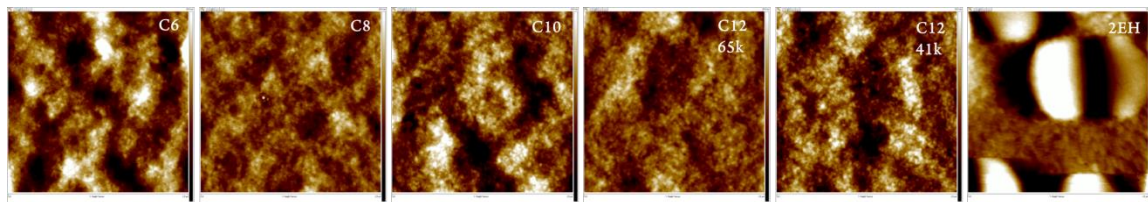


Figure 4-10. AFM height images of polymer:PC₇₁BM 1:1.5 blends spun cast from oDCB. (scan size: 2×2 μm², height scale: 20 nm)

At the nanometer scale, GIWAXS on the polymer:fullerene thin films deposited on PEDOT:PSS shows similar packing, as presented in Figure 4-11. The PC₇₁BM scattering ring can be seen at q values around $1.3\text{--}1.4\text{ \AA}^{-1}$, in addition to the scattering peaks from polymer crystallites. A higher order (200) peak can be seen in all GIWAXS images, except that of 2EH:PC₇₁BM blends, which is what was observed in Figure 4-5 in as-cast polymer thin films. Overall, scattering from polymer:PC₇₁BM blends is similar to what is observed in as-cast polymer films, with the PC₇₁BM scattering ring drowning out scattering peaks with q values above 1.2 \AA^{-1} .

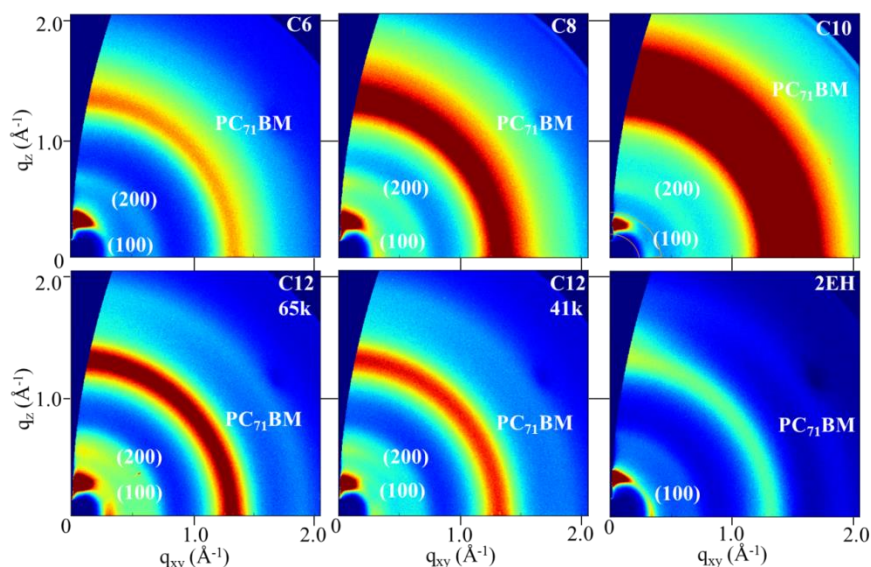


Figure 4-11. GIWAXS of P[T3(R)-iI]:PC₇₁BM blends spun cast from oDCB onto PEDOT:PSS-covered silicon wafers.

The chain-to-chain distances d of polymer crystallites in blends with PC₇₁BM is comparable to the lamellar distances in the pure polymer films, showing little disruption of the crystalline regions of the polymer domains by PC₇₁BM (Table 4-6). Quantitatively, the coherence length of the (100) peak along the q_z axis ($L_{c,d}$) is only slightly increased upon addition of PC₇₁BM. As such, the OPV device characteristics are predominantly influenced by the phase separation as observed on the micrometer scale via AFM.

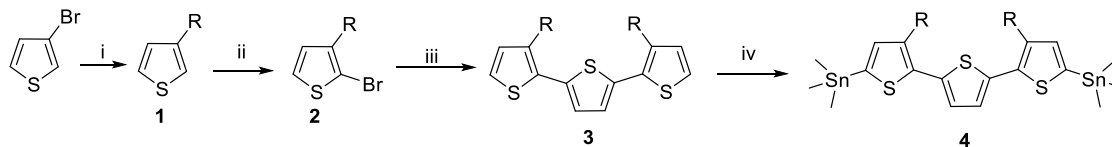
Table 4-6. Chain-to-chain distances d and their corresponding coherence length determined from pristine polymer films and polymer:PC₇₁BM blends GIWAXS.

	GIWAXS Polymer			GIWAXS Blends		
	d (Å)	$L_{c,d}$ (Å)	# chains in lamella	d (Å)	$L_{c,d}$ (Å)	# chains in lamella
C6	18	105	6	18	113	6
C8	19	122	6	18	125	7
C10	20	125	6	20	130	7
C12, 65k	21	113	5	21	121	6
C12, 41k	21	116	6	21	121	6
2EH	17	152	9	17	175	10

4.8. Parameters Influencing Polymer:Fullerene Phase Separation

The low impact of PC₇₁BM on the polymer packing observed via GIWAXS in polymer fullerene blends seems to indicate that polymer ordering is not disturbed during film formation in the blends. The fact that small features are observed under AFM in the case of the polymers with linear chains, regardless of their solubility, but not in the case of 2EH points to backbone twisting as the main parameter leading to the formation of larger PC₇₁BM domains. Mechanistically, it is hypothesized that when π -interactions between polymer chains are possible, fibrillar networks can be formed and drive phase separation. In the case of a twisted polymer backbone like P[T3(2EH)-iI], these interchain interactions are limited. Two processes can then occur to explain the large phase separation based on the relative solubilities of 2EH (27 mg/mL) and PC₇₁BM (70 mg/mL) in oDCB: i) both the polymer and fullerene remain in solution and lead to liquid-liquid demixing prior to any fibril formation, or ii) the polymer begins aggregating in solution, leading to poorly ordered domains, further growth of the fullerene aggregates, and thus yielding large phase separation in the active layer and low J_{sc} in OPV devices.

4.9. Synthetic Details



R = *n*-hexyl, *n*-octyl, *n*-decyl, *n*-dodecyl, 2-ethylhexyl

i. 1) Mg, I₂, C₆H₁₃Br, Et₂O, heat; 2) 1, Ni(dppp)Cl₂, Et₂O, heat; ii. NBS, DMF, 0°C to RT; iii. 2,5-dithiophene, Pd₂dba₃, P(*o*-tol)₃, toluene, heat; iv. 1) *n*-BuLi, Et₂O, -78°C; 2) Me₃SnCl in THF.

Scheme 4-3. Synthesis of stannylated terthiophene monomers.

Representative procedures for the synthesis of monomer 4. To note, for structure with chains longer than *n*-octyl, the compounds were purified by column chromatography using as hexanes the eluent, as opposed to distillation.

3-hexylthiophene (1-C6): The reagent 1-bromohexane (66.6 g, 403.6 mmol) was added dropwise to a solution of ground magnesium turnings (8 g, 333.3 mmol) with a spatula tip of iodine in 100 mL dry ethyl ether in an air-free 3-neck flask fitted with a condenser. Once the addition was over, the reaction mixture was heated to 45°C for two hours. The reaction mixture was then transferred to a 3-neck flask containing 3-bromothiophene (47.3 g, 290.2 mmol) and Ni(dppp)Cl₂ (2.09 g, 3.9 mmol, 0.013 equiv) in 200 mL dried ethyl ether. After addition, the brown solution was refluxed at 45 °C overnight. Upon cooling to room temperature, 150 mL of H₂O and 50 mL 0.1 M HCl were added to the reaction and the resulting mixture was filtered over coarse filter paper. The filtrate was extracted three times with 200 mL of diethyl ether. The combined organic layer was washed once with NaHCO₃, thrice with 200 mL of H₂O, once with 100 mL of brine, and the organic layer was dried over MgSO₄. After filtration, the solvent was removed by rotary evaporation to afford a brown oil that was purified by distillation. A colorless oil was obtained as pure product (20.24 g, 30% yield). ¹H NMR (300 MHz, CDCl₃, ppm): δ 7.28 (dd, 1H), 7.00 (d, 2H), 2.70 (t, 2H), 1.70 (m, 2H), 1.36 (m, 6H), 0.98 (t, 3H).

Other 3-alkylthiophenes were obtained, and their corresponding NMR data is reported below:

3-octylthiophene (1-C8): 37% yield. ¹H NMR: 7.25 (dd, 1H), 6.95 (m, 2H), 2.65 (t, 2H), 1.62 (m, 2H), 1.30 (m, 10H), 0.91 (t, 3H).

3-decylthiophene (1-C10): 40% yield. ¹H NMR: 7.25 (dd, 1H), 6.95 (m, 2H), 2.65 (t, 2H), 1.62 (m, 2H), 1.30 (m, 14H), 0.91 (t, 3H).

3-dodecylthiophene (1-C12): 41% yield. ¹H NMR: 7.25 (dd, 1H), 6.97 (m, 2H), 2.66 (t, 2H), 1.63 (m, 2H), 1.31 (m, 18H), 0.93 (t, 3H).

3-(2-ethylhexyl)thiophene (1-2EH): 71% yield. ¹H NMR: 7.26 (dd, 1H), 7.00 (m, 2H), 2.64 (d, 2H), 1.62 (m, 1H), 1.36 (m, 8H), 0.99 (m, 6H).

2-Bromo-3-hexylthiophenes (2-C6): N-bromosuccinimide (NBS) (10.68 g, 60 mmol) was added in three portions over 45 min to a solution of **1** (10.10 g, 60 mmol) in 200 mL of dried DMF at 0 °C kept in the dark. The mixture was stirred overnight at room temperature and poured into 1 L of water. The organic material was extracted with hexane (3 × 250 mL). The combined organic extracts were washed with DI water (200 mL) and brine (200 mL) and dried over anhydrous MgSO₄. After filtration and removal of the solvent, the remaining organic material was passed through a silica plug using hexanes to give 6.21 g of compound **2** (41% yield). ¹H NMR (300 MHz, CDCl₃, ppm): 7.20 (d, 1H), 6.80 (d, 1H), 2.55 (t, 2H), 1.59 (m, 2H), 1.28 (m, 6H), 0.91 (t, 3H).

2-bromo-3-octylthiophene (2-C8): 78% yield. ¹H NMR: 7.18 (d, 1H), 6.80 (d, 1H), 2.57 (t, 2H), 1.58 (m, 2H), 1.31 (m, 10H), 0.90 (t, 3H).

2-bromo-3-decylthiophene (2-C10): N-bromosuccinimide (NBS) (6.4 g, 35.6 mmol) was added in three portions over 45 min to a solution of **1** (8 g, 35.6 mmol) in 15 mL of dried CHCl₃ and 15 ml of glacial acetic acid at 0 °C kept in the dark. The mixture was stirred overnight at room temperature and poured into 1 L of water. The organic material was extracted with DCM (3 × 150 mL). The combined organic extracts were washed with DI water (200 mL) and brine (200 mL), and dried over anhydrous MgSO₄. After filtration and removal of the solvent, the remaining organic material was passed through a silica plug using hexanes to give compound **2** (56% yield). ¹H NMR (300 MHz, CDCl₃, ppm): 7.20 (d, 1H), 6.81 (d, 1H), 2.60 (t, 2H), 1.59 (m, 2H), 1.34 (m, 14H), 0.93 (t, 3H).

2-bromo-3-dodecylthiophene (2-C12): 50% yield. ¹H NMR: 7.20 (d, 1H), 6.81 (d, 1H), 2.60 (t, 2H), 1.59 (m, 2H), 1.34 (m, 18H), 0.93 (t, 3H).

2-bromo-3-(2-ethylhexyl)thiophene (2-2EH) : 38% yield. ¹H NMR: 7.18 (d, 1H), 6.78 (d, 1H), 2.52 (d, 2H), 1.62 (m, 1H), 1.31 (m, 8H), 0.90 (t, 6H)

3,3''-dihexyl- 2,2':5',2''-terthiophene (3-C6). In a dry schlenk flask with a stir bar, a mixture of 2,5-bis(trimethylstannyl)thiophene (1.85 g, 4.54 mmol), **2** (2.80 g, 11.34 mmol, 2.5 equiv), Pd₂dba₃ (207.0 mg, 0.23 mmol, 4.8% equiv), and P(*o*-tol)₃ (151.0 mg, 0.50 mmol, 10.9% equiv) was deaerated three times with argon, and then toluene (40 mL), dried over MS and freeze-pump-thawed for three cycles, was added. The reaction mixture was set in an oil bath at 95 °C overnight under argon. After cooling, the solvent was evaporated, and hexanes added to flask to precipitate out tin salts which were filtered out. After the solvent had been removed, the residue was purified by column chromatography with hexanes on silica gel to afford **3** as a light yellow liquid with a yield

of 70% (1.33 g, 3.19 mmol). ¹H NMR: 7.18 (d, 2H), 7.08 (s, 2H), 6.95 (d, 2H), 2.81 (t, 4H), 1.67 (m, 4H), 1.33 (m, 12H), 0.98 (m, 6H).

3,3''-dioctyl-2,2':5',2''-terthiophene (3-C8): 80% yield. ¹H NMR: 7.18 (d, 2H), 7.08 (s, 2H), 6.95 (d, 2H), 2.81 (t, 4H), 1.67 (m, 4H), 1.30 (m, 20H), 0.91 (m, 6H).

3,3''-didecyl-2,2':5',2''-terthiophene (3-C10): 99% yield. ¹H NMR: 7.18 (d, 2H), 7.08 (s, 2H), 6.95 (d, 2H), 2.81 (t, 4H), 1.68 (m, 4H), 1.29 (m, 28H), 0.91 (m, 6H).

3,3''-didodecyl-2,2':5',2''-terthiophene (3-C12): 82% yield. ¹H NMR: 7.18 (d, 2H), 7.05 (s, 2H), 6.95 (d, 2H), 2.78 (t, 4H), 1.65 (m, 4H), 1.25 (m, 36H), 0.88 (m, 6H).

3,3''-di(2-ethylhexyl)-2,2':5',2''-terthiophene (3-2EH) : 66% yield. ¹H NMR: 7.19 (d, 2H), 7.05 (s, 2H), 6.92 (d, 2H), 2.76 (d, 4H), 1.67 (m, 2H), 1.33 (m, 16H), 0.87 (m, 12H).

5,5''-Bis(trimethylstannyl)-3,3''-hexyl-2,2':5',2''-terthiophene (4-C6). *n*-butyllithium (1.6 M in hexanes, 4.37 mL, 7.02 mmol) was added to a solution of **3** (1.33 g, 3.19 mmol) in 30 mL of dry diethyl ether at -78 °C. The mixture was maintained at this temperature for 30 min, warmed to room temperature for another 30 min, and then cooled back to -78 °C. Trimethyltin chloride (1 M in THF, 7.02 mL, 7.02 mmol) was added at once. The mixture was stirred overnight at room temperature and poured into water for extraction with diethyl ether (3 × 50 mL). The combined organic layers were washed with brine (2 × 100 mL) and dried over MgSO₄. After the solvent had been removed under reduced pressure, purification by HPLC (60:40 ACN:acetone) yields 0.98 g of **4** (41% yield). ¹H NMR: 7.04 (s, 2H), 7.00 (t, 2H), 2.79 (t, 4H), 1.66 (m, 4H), 1.33 (m, 12H), 0.89 (t, 6H), 0.37 (m, 18H).

5,5''-Bis(trimethylstannyl)-3,3''-octyl-2,2':5',2''-terthiophene (4-C8): 513 mg, 56% yield. ¹H NMR: 7.05 (s, 2H), 7.02 (t, 2H), 2.81 (t, 4H), 1.65 (m, 4H), 1.29 (m, 20H), 0.89 (t, 6H), 0.39 (m, 18H).

5,5''-Bis(trimethylstannyl)-3,3''-decyl-2,2':5',2''-terthiophene (4-C10) : 51% yield. ¹H NMR: 7.18 (s, 2H), 7.16 (t, 2H), 2.96 (t, 4H), 1.83 (m, 4H), 1.42 (m, 28H), 1.03 (t, 6H), 0.53 (m, 18H).

5,5''-Bis(trimethylstannyl)-3,3''-dodecyl-2,2':5',2''-terthiophene (4-C12): 969 mg, 53% yield. ¹H NMR: 7.03 (s, 2H), 6.95 (t, 2H), 2.78 (d, 4H), 1.65 (m, 4H), 1.25 (m, 32H), 0.87 (t, 6H), 0.37 (m, 18H).

5,5''-Bis(trimethylstannyl)-3,3''-(2-ethylhexyl)-2,2':5',2''-terthiophene (4-2EH) : 928 mg, 59% yield. ¹H NMR: 7.02 (s, 2H), 6.95 (t, 2H), 2.72 (d, 4H), 1.66 (m, 2H), 1.31 (m, 16H), 0.84 (m, 12H), 0.37 (m, 18H).

General Stille polycondensation procedure (C8): In a dry schlenk tube with a stir bar, a mixture of 5,5''-bis(trimethylstannyl)-3,3''-octyl-2,2':5',2''-terthiophene (406 mg, 0.5 mmol), 6,6'-dibromoisindigo (442 mg, 0.5 mmol), Pd₂dba₃ (18.0 mg, 4% equiv), and P(*o*-tol)₃ (10.0 mg, 6.6% equiv) was deoxygenated three times and refilled with argon, and then toluene dried over MS (5 mL) and freeze-pump-thawed for five cycles was added. The reaction mixture was set in an oil bath at 95°C overnight under argon. After cooling to room temperature, a spatula tip of diethyldithiocarbamic acid diethylammonium salt was added to the mixture and stirred for 3 hours. The mixture was precipitated into methanol (300 mL). The precipitate was filtered through a filtration apparatus, set in a cellulose thimble, and purified via Soxhlet extraction for 12 hours with methanol, acetone, hexanes and dichloromethane sequentially. The polymer was

extracted with chloroform, concentrated by evaporation, and then precipitated into methanol. The collected polymer was a shiny brown solid (578 mg, 96%).

C6: 978 mg, 87% yield (chloroform fraction).

C10: 800 mg, 67% yield (chloroform fraction), 88% yield overall (chloroform and dichloromethane fractions).

C12, 65k: 376 mg, 58% (chloroform fraction).

C12, 41k: 265 mg, 41% (dichloromethane fraction), 99% yield overall.

2EH: 584 mg, 99% yield (chloroform fraction).

CHAPTER 5. IMPACT OF POLYMER AND PROCESSING ADDITIVE STRUCTURES ON MORPHOLOGY IN POLYMER-BASED THIN- FILMS

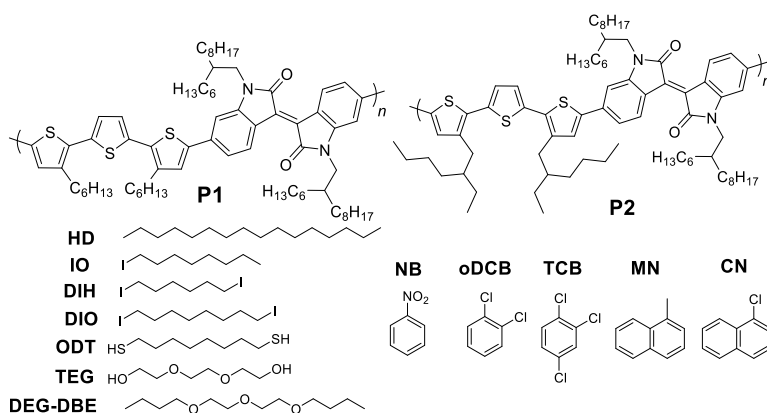
Chapter 4 has discussed the impact of polymer structure on polymer packing and phase separation in blends with PC₇₁BM. Besides choosing the appropriate side-chains for polymer solubility and morphology control, processing additives, or solvent additives, have been used to further tune the phase separation in bulk heterojunction devices with fullerene derivatives. Peet *et al.*²³¹ first discovered an increase in power conversion efficiency in PCDTBT:PC₇₁BM devices when 2% v 1,8-octanedithiol (ODT) was added to the coating solution. The authors further studied the impact of ODT on film morphology by measuring the film absorbance as it is drying using of UV-vis-NIR spectroscopy, and discussed the possibility for amorphous PCDTBT polymer chains to either planarize or form aggregates while remaining mobile as the film dries with ODT until a threshold viscosity is reached and locks in the phase separation.³²¹ In-situ X-ray scattering studies further demonstrated that ODT induced nucleation of polymer crystallite within 2 min of solution deposition, which was not seen when the blends were cast from chlorobenzene (CB) alone. Interestingly, the same crystallite formation could not be obtained in the PCDTBT:PC₇₁BM system by thermal annealing. It was hypothesized that ODT reduces the barrier for nucleation²³² and/or selectively solubilizes fullerene derivatives and extracts fullerenes from mixed domains to form more pure domains.³²² Building up on this initial research, other processing additives were uncovered for control of phase separation such as 1,8-diiodooctane (DIO), 1-chloronaphthalene (CN) or nitrobenzene (NB). Nitrobenzene is a typical plasticizer used

to reduce the glass transition temperature (T_g) of polyvinylchloride for example, and as such the effect of processing additives on liquid-solid polymer transitions can be hypothesized to be linked either to plasticization and vitrification or gelation of the polymer chains by modifying polymer-polymer interactions. Vitrification is associated to solidification of a polymer as it transitions to temperatures below its glass transition temperature; this has been discussed by Richter *et al.*¹⁷⁷ in the context of CN and ODT processing additives for OPVs. Using vitrification as the main mechanism for film formation, it is hypothesized that ODT and CN either act as plasticizers to the polymer chains to lower their T_g , facilitating ordering prior to solidification and/or removes the higher T_g fullerene derivatives from the amorphous domains of the polymer, again reducing the overall T_g and facilitating ordering. On the other hand, if polymer crystallites are formed in solution prior to deposition, the solidification process involving the polymer chains can be regarded as gelation through previously established physical crosslinks. This effect was discussed by Schmidt *et al.*²³³ in solutions of a diketopyrrolopyrrole-based polymer in chlorobenzene with and without CN. Indeed, the authors find that CN induces lamellar ordering within the polymer aggregates in solution, which can act as nucleating sites for polymer crystallite formation. In this chapter, the impact of both polymer and additive structure is discussed as it relates to the mechanisms for films formation in polymer:fullerene blends.

5.1. Choice of Polymers and Processing Additives

Aliphatic and aromatic additives with various functionalities (shown in Figure 5-1) were selected in order to study the impact of different interactions (van der Waals, dipolar, and hydrogen bonding interactions) on the solubility of the blend components,

and on their phase separation. The processing additives chosen for this study were based on commonly used processing additives such as DIO, ODT, NB and CN, and investigated changes in functionality and length of the aliphatic and aromatic structures. Non-functional HD and mono-functional IO were selected to investigate the impact of the iodine functionality, and DIH was chosen to study the impact of alkyl chain length compared to DIO. To investigate the impact of hydrogen bonding, TEG and DEG-DBE were selected and compared to ODT.



Scheme 5-1. Structures of P1 and P2, along with the investigated processing additives.

The use of Hansen solubility parameters (HSP) to predict solubility has been used in the context of small molecules,^{187,291,323} and can be extended to understand solubility of polymers in the processing additives (Table 5-1). Based on dispersive (δ_D), polar (δ_P) and hydrogen-bonding (δ_H) interactions, either obtained from the literature^{187,291,323} or calculated using group contributions,¹³⁰ the distance between two compounds in the Hansen solubility space (R_a) can be calculated following equation 5-1:

$$R_a = \sqrt{4(\delta_{D1} - \delta_{D2})^2 + (\delta_{P1} - \delta_{P2})^2 + (\delta_{H1} - \delta_{H2})^2} \quad (5-1)$$

where larger R_a values indicate that the compounds are further apart in the Hansen solubility space and that molecular interactions do not favor miscibility of the two

compounds. Literature reports on the solubility of polymers and fullerene derivatives in the various solvents are used to correlate R_a values to experimentally determined solubility values. The studied additives were selected based on their chemical structure compared to previously highlighted additives such as ODT, DIO and CN. ODT and DIO are both thought to selectively solubilize fullerene derivatives in polymer:fullerene blends, and NB is also shown to be a selective solvent for fullerenes.³²⁴ The aromatic structure of NB would be considered to lead to good solubility of the polymer in this solvent; however, the larger dipole induced by the nitro group possibly leads to a decrease solvent quality for the non-polar polymers. Aromatic additives, such as oDCB, TCB, MN and CN, which are good solvents for both the polymer and fullerene components,¹⁷⁷ were also investigated to study the impact of the chlorine functionality on phase separation. Table 5-1 highlights the strength of the HSP to predict solubility, with polymers being more soluble in solvents with $R_a < 5$ and PC₇₁BM being more soluble in solvents with $R_a < 6.5$. However, there are some limits to the HSP, as illustrated by IO and DIO. Indeed, the two molecules have similar HSP and R_a but lead to different PC₇₁BM solubility.

Beyond investigating the structural impact of processing additives, two polymer structures were chosen to investigate the mechanism for phase separation control in two cases: i) when the polymer demonstrates thermodynamic propensity to order, and ii) when ordering is thermodynamically prevented by steric hindrance. Polymer P[T3(2EH)-iI] (P2) from the previous chapter was used to illustrate the latter case, and a new batch of P[T3(C6)-iI] (P1) was synthesized to investigate the effect of processing additives on systems where long range order can be achieved in polymer crystallites. The new batch

of P[T3(C6)-iI] had the same polymer purity and optoelectronic properties than the previously reported batch.

Table 5-1. Boiling point (bp), Hansen solubility parameters (dispersive δ_D , polar δ_P , hydrogen bonding δ_H) and estimated component solubilities.

Solvent	bp (°C)	δ_D (MPa ^{1/2})	δ_P (MPa ^{1/2})	δ_H (MPa ^{1/2})	P1 R _a	P1 Solubility (mg/mL)	P2 R _a	P2 Solubility (mg/mL)	PC ₇₁ BM R _a	PC ₇₁ BM Solubility ¹ 87 (mg/mL)
CHCl ₃	61	17.8	3.1	5.7	4.7	2	4.3	27	5.4	61
HD	287	16.3	0	0	8.5	-	8.0	-	10.4	< 0.1
DEG-DBE	256	15.8	4.7	4.4	8.6	-	8.2	-	8.7	-
TEG	285	16.0	12.5	18.6	19.5	-	19.5	-	17.9	-
IO	225	17.0	4.4	6.1	6.6	-	6.3	-	6.6	-
NB	211	20.0	8.6	4.1	6.4	-	6.6	-	3.3	26
ODT	270	17.2	6.8	6.4	7.5	-	7.3	-	6.4	+
DIH	282	17.9	5.7	7.0	6.1	-	6.0	-	5.2	+
DIO	333	17.6	4.8	6.4	5.8	-	5.6	-	5.5	+
oDCB	180	19.2	6.3	3.3	4.4	2	4.4	27	2.4	203
TCB	214	20.2	3.2	2.3	2.1	+	2.2	+	3.1	+
MN	242	20.6	0.8	4.7	2.1	+	2.4	+	4.7	+
CN	260	19.9	4.9	2.5	3.1	+	3.2	+	2.1	> 400

Solubility estimates: based on literature observations. (-) solubilities are assigned if the solvent is estimated to be a poorer solvent than chloroform or oDCB; (+) solubilities are assigned if the solvent is estimated to be a similar or better solvent than chloroform or oDCB.

5.2. Solution Properties of P1 by UV-vis-NIR and SANS

In order to determine the impact of the processing additive on polymer solubility in the casting solution, UV-vis-NIR absorbance was obtained by diluting the casting solutions in chloroform (Table 5-2). In solutions based on P1, the absorption maxima at room temperature was maintained around 651 nm (1.90 eV) and slightly red shifted to 657 nm (1.89 eV) when NB is used as a processing additive. By comparing the same solutions as they are cooled from 50 °C to room temperature, all absorbance maxima are red shifted when the temperature of the solution was decreased to room temperature, indicating that the polymer chains adopt a more planar conformation at room temperature. The extent of planarization estimated from the shift in the maximum of absorption λ_{\max} is greatest when NB is present in solution, while all other solutions with

additives have similar behaviors to the control solution without additives in terms of shift in λ_{max} . In solutions based on P2, the absorption maxima are around 643 nm at room temperature, with blue shifted maxima to around 625 nm at 50 °C, again indicating a planarization of the backbones as the temperature is decreased. Solutions based on P2 do not exhibit any significant variations when additives are used compared to chloroform alone.

Table 5-2. Shift in absorption maxima in polymer:PC₇₁BM chloroform solutions as a function of additive and temperature.

				P1:PC₇₁BM in CHCl₃			P2:PC₇₁BM in CHCl₃		
Solvent additive	δ_D (MPa ^{1/2})	δ_P (MPa ^{1/2})	δ_H (MPa ^{1/2})	λ_{max} RT (nm)	λ_{max} 50°C (nm)	$\Delta\lambda$ (nm) [ΔE (meV)]	λ_{max} RT (nm)	λ_{max} 50°C (nm)	$\Delta\lambda$ (nm) [ΔE (meV)]
None (CHCl ₃)	17.8	3.1	5.7	651	638	13 (39)	643	625	18 (56)
DIH	17.9	5.7	7.0	651	641	10 (30)	/	/	/
DIO	17.6	4.8	6.4	651	640	11 (33)	642	623	19 (59)
NB	20.0	8.6	4.1	657	634	23 (68)	642	626	16 (49)
MN	20.6	0.8	4.7	651	640	10 (30)	644	625	19 (59)

To further study the impact of additives on the structure of polymer aggregates in solution, solution small-angle neutron scattering was measured at NIST Center for Neutron Research (NCNR). Small-angle neutron scattering was conducted on 0.54 %_w solutions (8 mg/mL) in CHCl₃, over a q range of 0.008 Å⁻¹ to 0.5 Å⁻¹, corresponding to length scales of 500 Å down to 15 Å, as shown in Figure 5-1. Four regions can be highlighted in the SANS plot: (A) at low q values, information is gathered on aggregate size in solution, (B and C) at intermediate q values, the rigidity of polymer chains involved in the aggregates can be evaluated based on the slope of the intensity plot (with a slope of -2 indicating the presence of random coils,¹⁹² with less negative slopes arising

from expanded coil conformations,²¹⁵ and a slope of -1 indicating the presence of rigid rod-like structures), and (D) at higher q values, information about polymer ordering within aggregates can be gathered. In solutions of P1 in chloroform with no additives (Figure 5-1a), the aggregates are too large to be observed using SANS, as no plateau in intensity is observed at low q values. However, intensity drop off with a slope of -1 and -1.6 in regions (B) and (C), indicating that the aggregates adopt an expanded coil conformation in chloroform. At higher q values in region (D) the scattering intensity falls to the measurement baseline. Similar scattering behavior of P1 is observed when MN is present in solution. By comparison, when DIO or NB are present in solution, the scattering intensity at high q values (region D) is increased compared to the control solution. The increase in scattering occurs for length scales around 30 Å, which could be due to the presence of swollen lamella structures within the aggregates. This was previously observed by Schmidt *et al.*²³³ in solution SAXS of a diketopyrrolopyrrole-based polymer in the presence of CN. In this study, the SANS data indicates the presence of ordered aggregates in P1 solutions containing DIO or NB compared to chloroform alone or in the presence of MN.

By comparison, in Figure 5-1b, solutions of P2 in chloroform alone have a similar scattering plot to P1 solutions, however a plateau in the scattering intensity appears at low q values (A), indicating that P2 aggregates are smaller than P1 aggregates and are being detected in the SANS experiment. Using the Debye model to fit regions A and B yields a radius of gyration around 14±3 nm for P2 aggregates in all solutions. As in P1 solutions with DIO and NB, P2 solutions exhibit an increase in scattering intensity at high q values,

indicating the presence of ordering within the aggregates. However, by comparison to P1, MN also leads to ordered aggregates in P2 solutions.

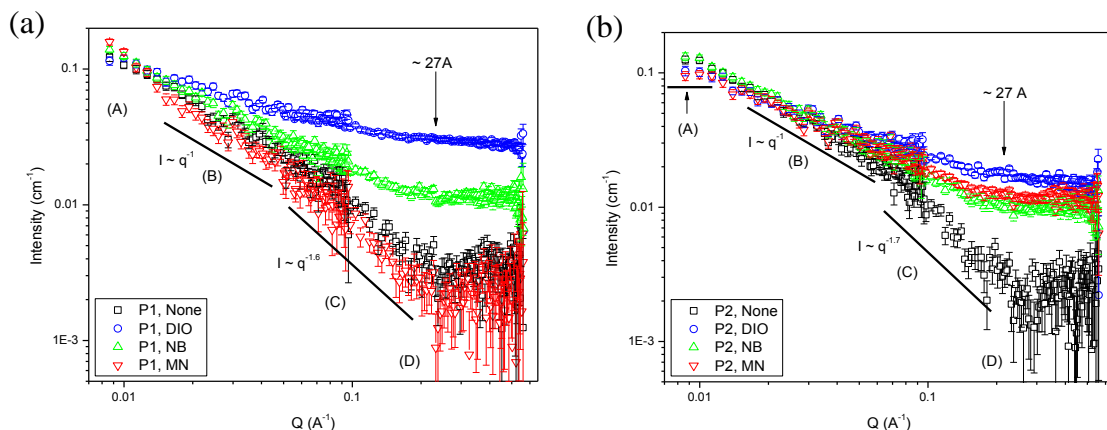


Figure 5-1. SANS of (a) P1 and (b) P2 in chloroform solutions without and with processing additives.

Overall the SANS data indicates that the polymer chains in chloroform tend to adopt an expanded coil conformation, regardless of the polymer structure. Furthermore, DIO and NB impact both P1 and P2 chains in chloroform solutions, and lead to more ordered aggregates. By comparison, MN does not lead to any changes in the solution behavior of P1 but does contribute to an increase in ordering within P2 aggregates. Several mechanisms can be at play with various additives: i) the additive does not modify the polymer behavior in solution, ii) the additive leads to collapsed polymer aggregates (slope more negative than -2) and increases π -interactions through lamellar formation, or iii) the additive leads to more expanded polymer chains, which in turn promotes interchain interactions and lamellar formation. Based on the SANS results, where no slope lower than -2 are observed, both DIO and NB lead to expanded coil conformations in P1 and P2 solutions (mechanism ii), whereas MN does not modify the solution behavior of P1 (mechanism i) but leads to expanded coil conformation of P2 in chloroform solutions.

The effects of DIO and NB can be rationalized by the fact that they are poorer solvents for the polymer relative to chloroform, and promote polymer/polymer interactions compared to polymer/solvent interactions. The differences in the impact of MN on the solution behavior of P2 compared to P1 can be explained by differences in solubility of the two polymers in chloroform. Indeed, at the concentrations studied, P1 is above its threshold for solubility and adding another good solvent does not impact its solution behavior. However, P2 is still well solubilized at the studied concentrations, and adding an aromatic solvent, which can promote interchain π -interactions,²¹¹ leads to more ordered P2 aggregates.

5.3. Implications for OPV Devices

5.3.1. OPV Device Characteristics

The impact of poor, selective and good solvents on OPV device parameters was investigated in P1:PC₇₁BM (1:2) blends cast from 8 mg/mL solutions in chloroform without and with 2%v processing additive, as shown in Figure 5-2. The blends cast from chloroform alone showed short-circuit current densities around 1.6 mA cm⁻², open-circuit voltages around 0.80 V and fill factors of 0.58, leading to PCEs around 0.7%. HD, TEG and DEG all gave very rough films, which led to decrease device performance, or shorting of the devices. IO gave comparable J_{sc} and FF to blends cast from chloroform alone, but led to a slight decrease in V_{oc} to 0.72 V. By comparison, a large increase in J_{sc} is obtained, regardless if the processing additive is selective to one component or a good solvent for both polymer and fullerene. These additives also tend to decrease the V_{oc} of the device from 0.80 V without additive to around 0.68 V. Based on Figure 5-2b, the relationship between additive structure and J_{sc} increase is still unclear from the J-V

curves alone, and physical properties of the additives, such as boiling point, do not clearly correlate to changes in J_{sc} .

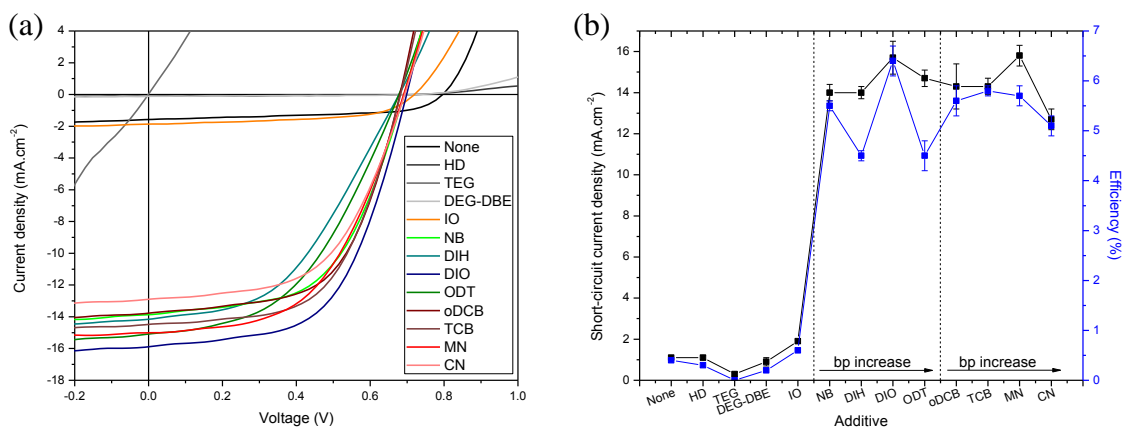


Figure 5-2. (a) Current density-voltage (J-V) curves of P1:PC₇₁BM (1:2) devices, and (b) the impact of processing additives on J_{sc} and PCE.

As shown in Figure 5-3, in the case of blends of P2:PC₇₁BM (1:1) cast from 8 mg/mL solutions in chloroform, processing additives seem to lead to a larger difference in J_{sc} based on their solubility factors, with oDCB and TCB and furthermore MN and CN leading only to a slight increase of the J_{sc} , while selective solvents lead to a three- to five-fold increase in the J_{sc} . In these blends, there is a more visible impact of the choice of additive on the V_{oc} of the device, which decreases from 0.88 V in blends cast with no additives to 0.69 V when DIH is added. Interestingly, in the case of good solvents, the V_{oc} seems to decrease with increasing boiling point of the additive, although the statistical relevance of this effect is in question, whereas no correlation of boiling point and V_{oc} is observed in selective solvents.

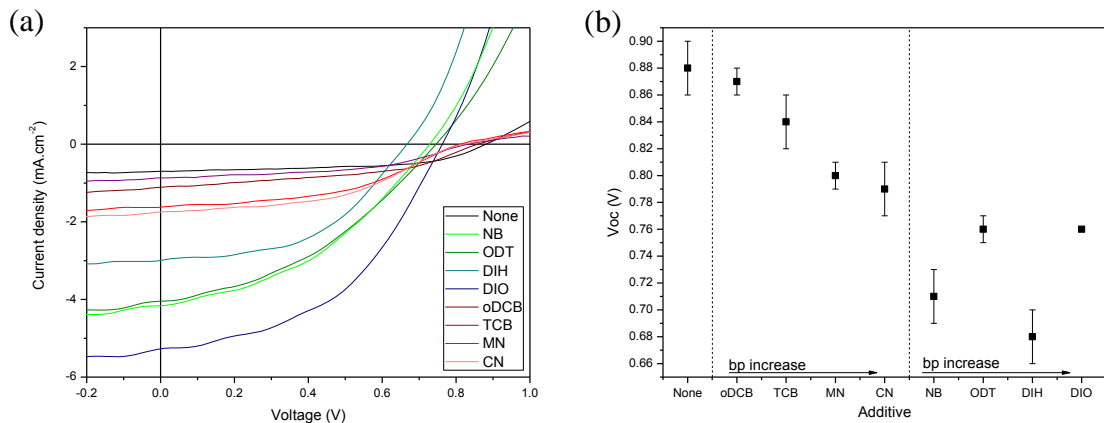


Figure 5-3. (a) Current density-voltage (J-V) curves of P2:PC₇₁BM (1:1) devices, and (b) the impact of processing additives on V_{oc}.

5.3.2. Charge Mobility in SCLC Devices

In some devices, the FF seems to be affected by the processing additive, in particular in devices using DIH, possibly linked to variations in charge carrier mobility. To determine the impact of additive on charge carrier mobility, hole-only SCLC devices were fabricated using the same conditions as OPV devices (Figure 5-4), and the results are summarized in Table 5-3.

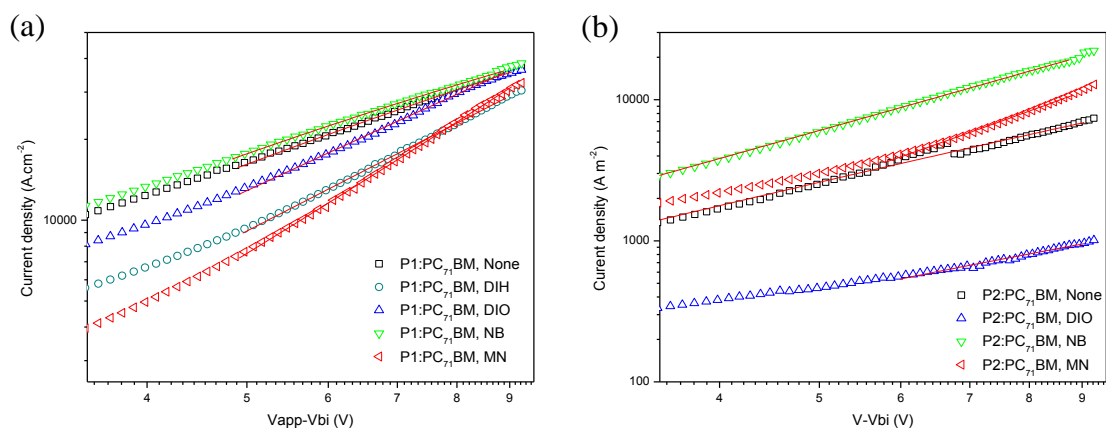


Figure 5-4. SCLC devices based on (a) P1:PC₇₁BM and (b) P2:PC₇₁BM with field-dependent fits.

Based on the SCLC field-dependent fits, blends based on P1 exhibit hole carrier mobility around $5 \times 10^{-4} \text{ cm}^2 \text{ V}^{-1} \text{ s}^{-1}$ when cast from chloroform alone, with little change

when NB is added to the casting solution. The hole carrier mobility drops to $1 \times 10^{-4} \text{ cm}^2 \text{ V}^{-1} \text{ s}^{-1}$ in blends processed with DIH and DIO and is further decreased to around $4 \times 10^{-5} \text{ cm}^2 \text{ V}^{-1} \text{ s}^{-1}$ when MN is added. In contrast, the hole carrier mobility in P2:PC₇₁BM blends cast from chloroform is around $1 \times 10^{-4} \text{ cm}^2 \text{ V}^{-1} \text{ s}^{-1}$, also similar to what is estimated in blends cast with NB. P2:PC₇₁BM blends cast with MN again exhibit the lowest hole carrier mobility. The main difference in blends based on P2 compared to P1 is the effect of DIO, where the hole carrier mobility in P2:PC₇₁BM blends cast with DIO is $3 \times 10^{-5} \text{ cm}^2 \text{ V}^{-1} \text{ s}^{-1}$, which is lower than in blends cast with NB contrary to what was observed in P1:PC₇₁BM blends. These hole carrier mobilities give some insight on the impact of additives on carrier transport; however, no correlation can be made between FF in OPV devices and mobilities estimated from SCLC devices.

Table 5-3. Estimated SCLC hole mobility in the active layer blends, and corresponding film thickness.

Additive	P1:PC ₇₁ BM (cm ² V ⁻¹ s ⁻¹)	Thickness (nm)	P2:PC ₇₁ BM (cm ² V ⁻¹ s ⁻¹)	Thickness (nm)
None	5.3×10^{-4}	92 ± 8	1.4×10^{-4}	131 ± 8
DIH	1.2×10^{-4}	99 ± 4	/	/
DIO	1.5×10^{-4}	83 ± 7	3.1×10^{-5}	129 ± 26
NB	5.2×10^{-4}	84 ± 11	1.5×10^{-4}	125 ± 8
MN	3.7×10^{-5}	91 ± 5	2.2×10^{-5}	122 ± 2

5.4. Thin Film Characterizations

5.4.1. Effect on Phase Separation with PC₇₁BM

Atomic force microscopy (AFM) was used to determine the microscopic phase separation in these blends, and Figure 5-5 gives an overview of the morphology achieved using the different processing additives in P1:PC₇₁BM blends. P1:PC₇₁BM active layers cast from chloroform alone exhibit protruding features on the order of 250 to 500 nm,

which are thought to be fullerene-rich domains.³²⁵ The use of non-solvents leads to large protruding features, similar to what is observed when the blend was cast from chloroform alone but with higher roughness. By comparing the AFM images to the HSP parameters in Table 5-1, some limitations of HSP for predicting solubility can be highlighted. For instance, IO has similar HSP to DIO, and as such similar phase separation would have been predicted. However Figure 5-5 shows drastic differences in the phase separation when IO and DIO are used. It is hypothesized based on the observed AFM image that IO is not a good solvent for fullerene derivatives (contrary to DIO). Based on the hypothesis formulated by Lou *et al.*²³⁴ that the iodine atoms on DIO electrostatically interact with the fullerene cage, leading to increased solubility of the fullerenes within DIO, it is hypothesized here that IO acts as a surfactant around PC₇₁BM aggregates, with the iodine-functionalized chain ends interacting with the fullerene cages. TEG in particular leads to interesting phase separation, where polymer fibrils seem to be visible. By comparison, the use of selective or good solvents induced smaller phase separation as seen via AFM, independently of the component solubility in the additive or of the additive structure and functionality.

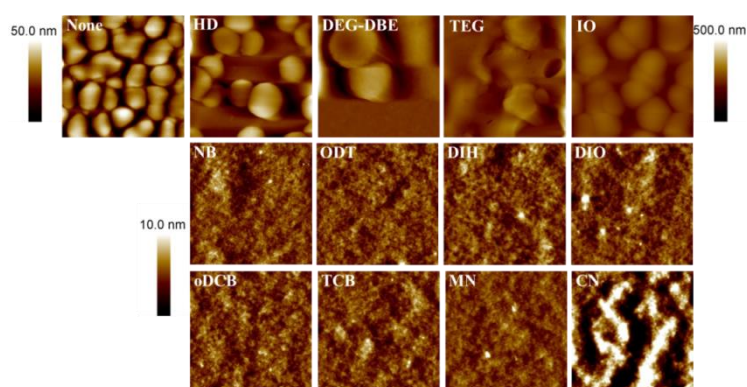


Figure 5-5. AFM height images of P1:P₇₁BM (1:2) devices spun-cast from CHCl₃ as the main solvent without and with 2%v processing additive. AFM images are 2 × 2 μm², with a 50 nm height scale for NB, a 500 nm scale for HD, DEG-DBE, TEG and IO, and a 10 nm scale for all other AFMs.

AFM of P2:PC₇₁BM blends cast from chloroform alone exhibited similar features to P1:PC₇₁BM blends and further addition of good solvents such as oDCB and TCB gave comparable features to chloroform alone (Figure 5-6). Interestingly, the phase separation obtained with oDCB as an additive is different to that obtained with oDCB as the main solvent as seen in Chapter 4, possibly linked to differences in evaporation time for the different processes. Furthermore, the fullerene-rich features' diameter and height slightly decreased when MN or CN were used, which explains the slight increase in J_{sc} observed in OPV devices. By comparison, all the selective solvents give finer features in the resulting films, although to different extents depending on their structure.

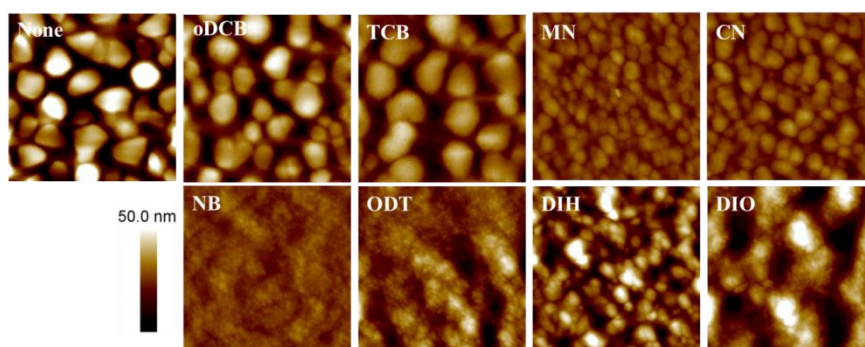


Figure 5-6. AFM height images of P2:P₇₁BM (1:1) devices spun-cast from CHCl₃ as the main solvent without and with 2% v processing additive. AFM images are $2 \times 2 \mu\text{m}^2$, with 50 nm height scale for all AFMs.

5.4.2. Effect of Additives on Polymer Packing

UV-vis-NIR absorption spectra of P1:PC₇₁BM devices were measured to investigate short-range order by monitoring the intensity of the aggregation peak around 705 nm, as shown in Figure 5-7. The use of processing additive that solubilize at least one blend component seem to always lead to an increase in the polymer aggregation peak compared to chloroform alone. Further separating the processing additives by structure (aliphatic vs. aromatic) and solubility properties (poor solvent for polymer in blue and NB in green,

and good solvent in red) in Figure 5-7a, there is little influence of the additive structure on the overall absorbance. By focusing on the aggregation peak (Figure 5-7b), the impact of poor solvents for the polymer (NB, ODT, DIH and DIO) is the same; however the intensity of the aggregation peak seems to increase with solvent boiling point in the case of good solvents for the polymer (oDCB, TCB, MN and CN). This observation points to a lack of influence of kinetic effects on short-range aggregation in the case of poor solvents for the polymer and the need to take into account evaporation time for increased short-range aggregation in the case of good solvents.

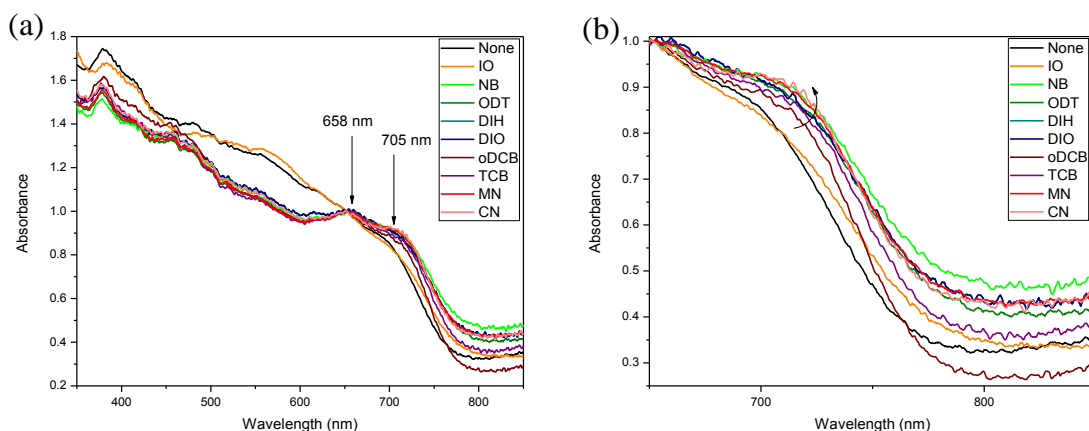


Figure 5-7. (a) Device absorbance through glass/ITO/PEDOT:PSS/P1:PC₇₁BM, and (b) focus on the 650 to 580 nm region looking at the aggregation peak.

To study longer range order, grazing incidence wide-angle X-ray scattering (GIWAXS) on P1 and P1:PC₇₁BM films spun-cast from chloroform, with and without different categories of processing additive is shown in Figure 5-8. Addition of processing additives in solutions of the polymer alone did not significantly impact P1 polymer packing in thin films, with the biggest difference being the increase in (100) peak intensity when MN is used as a processing additive. In blends with PC₇₁BM (with the fullerene scattering peak around 1.4 \AA^{-1}), a similar increase in scattering intensity with MN is also observed, as is the case with IO. Given that the film thickness is around 85

nm to 90 nm for all blends, the increase in scattering intensity is thought to arise from an increase in the number of scattering sites. Comparing the pristine polymer films to the blends, higher order (200) peaks become visible in all P1:PC₇₁BM films.

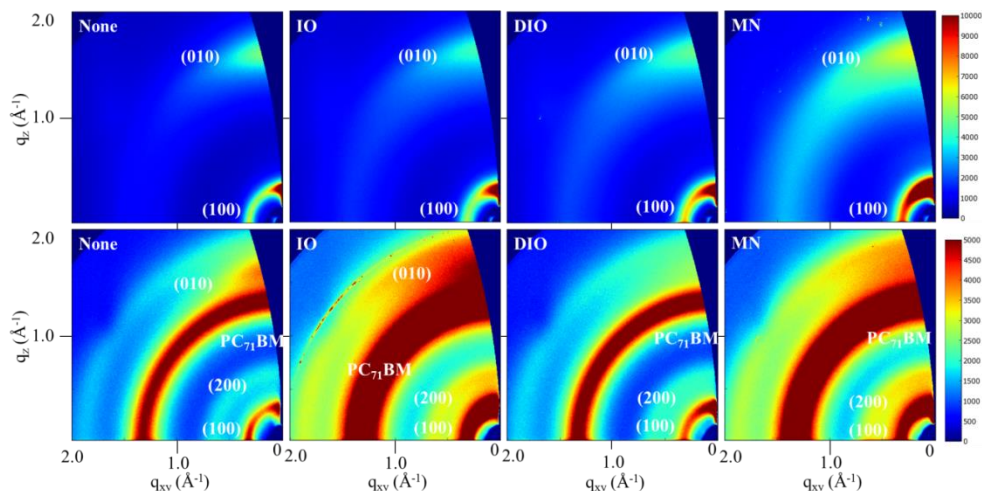


Figure 5-8. GIWAXS images of P1 (top) and P1:PC₇₁BM (bottom) cast from chloroform without and with 2%v processing additive. The intensity scale bars are different to take into account the different exposure times (500 s for pristine P1 films, 250 s for P1:PC₇₁BM films).

Line integration along the q_z axis, along with integration of the (100) peak along χ are shown in Figure 5-9. In the pristine polymer films (Figure 5-9a), chain-to-chain (100) and π -stacking (010) peaks are seen at 0.33 \AA^{-1} and 1.6 \AA^{-1} respectively, with addition of IO and DIO resulting in similar scattering intensities to P1 cast from chloroform alone but MN resulting in an overall increase in scattering intensity. Figure 5-9c shows that all (100) peaks show similar orientation, with scattering mostly out-of-plane (around 90°) in films cast without additive, which slightly broadens when IO, DIO or MN are used. This broadening is indicative of a slightly more random polymer crystallite orientation when additives are used, and has been attributed to crystallite formation within the bulk relative to more oriented crystallites when nucleation occurs at an interface.²³³ In blends with PC₇₁BM (Figure 5-9b), the fullerene scattering is visible between 1.3 \AA^{-1} and 1.4 \AA^{-1} ,

with the polymer (100) scattering remaining around 0.35 \AA^{-1} and a higher order (200) appearing in all blends. However the (010) peak at 1.6 \AA^{-1} is only visible in blends cast from chloroform without additive. Furthermore, in P1:PC₇₁BM blends, the films exhibit a drastic change in polymer crystallite orientation as seen in Figure 5-9d. Films cast from chloroform alone show polymer (100) orientation both in-plane (around 10° and 170°) and out-of-plane. However, blends cast with DIO or MN have a strong preference for chain-to-chain orientation out-of-plane with (100) scattering intensity maxima around 90° . Interestingly, addition of DIO or MN to blends leads to narrower distributions of the (100) peak, contrary to what was observed in blends based on P3HT.¹⁷⁷

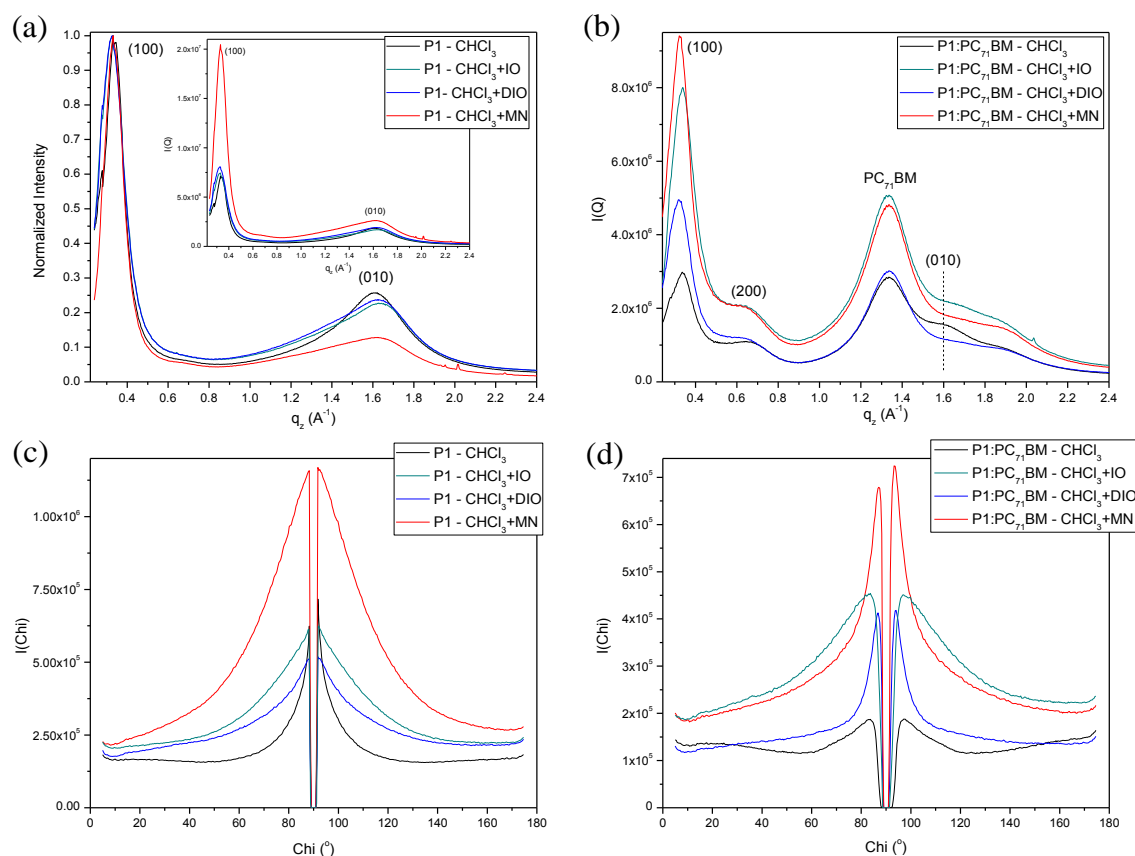


Figure 5-9. Line integration along the q_z axis of (a) P1 films and (b) P1:PC₇₁BM films, and integration along χ of the (100) scattering peak in (c) P1 films and (d) P1:PC₇₁BM films.

In summary, processing additives increase local order in P1:PC₇₁BM blends as seen via UV-vis-NIR. GIWAXS data also points to similar scattering plots in pristine P1 films cast from chloroform without and with DIO, and an increase in intensity when MN is used indicating an increase in the number of scattering sites. This increase in scattering intensity with MN is also seen in blends with PC₇₁BM.

Turning to P2:PC₇₁BM blends, UV-vis-NIR absorbance of the OPV device demonstrates the varying impact of the solvent quality for the polymer chains on polymer aggregation in the active layer. Indeed, compared to chloroform alone, good solvent for the polymer (oDCB, TCB, MN and CN) do not lead to a significant increase aggregation peak intensity, with a slight increase seen when MN or CN are used, whereas poor solvents for the polymer (NB, ODT, DIH DIO) lead to films with increase absorbance around 690 nm, indicating the presence of short range order within polymer aggregates in these films. Interestingly, this increase in the intensity of the aggregation peak with NB, ODT, DIH and DIO corresponds to lower V_{oc} observed in OPV devices. These observations point to an increase in polymer crystallization, leading to a decreased ionization potential and decreased V_{oc} .

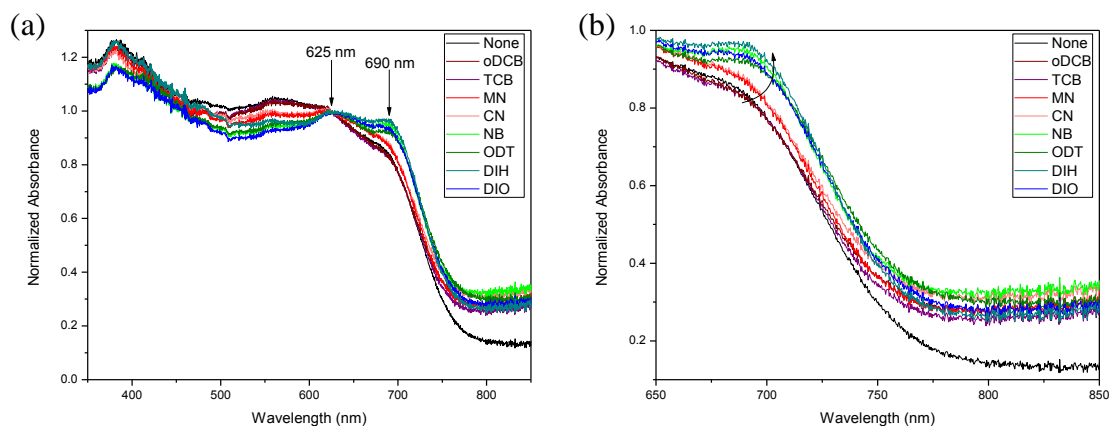


Figure 5-10. (a) Device absorbance through glass/ITO/PEDOT:PSS/P2:PC₇₁BM, and (b) focus on the 650 to 580 nm region looking at the aggregation peak.

In the GIWAXS images shown in Figure 5-11, P2 exhibits different behavior when cast from chloroform with and without DIO or MN. In pristine P2 films cast from chloroform, the (100) peak is visible both along the q_{xy} axis (in-plane) and the q_z axis (out-of-plane), whereas the (100) peak is mostly out-of-plane in films cast with MN. In films cast with DIO, the (100) peak doesn't seem to indicate a preferred chain-to-chain orientation, and is accompanied by an increase in the (010) peak intensity compared to films without additive. Similarly to P1:PC₇₁BM, P2:PC₇₁BM blends exhibit a higher order (200) peak and the (010) peak is only visible in blends cast from chloroform alone.

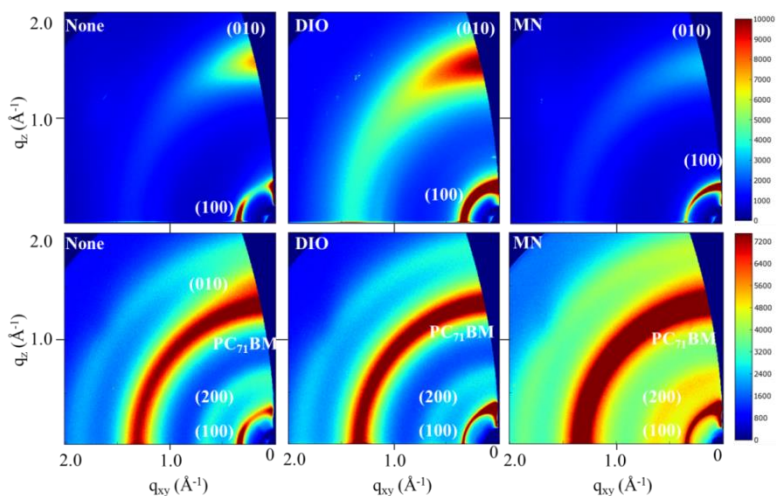


Figure 5-11. GIWAXS images of P2 (top) and P2:PC₇₁BM (bottom) cast from chloroform without and with 2%v processing additive. The intensity scale bars are different to take into account the different exposure times (500 s for pristine P1 films, 250 s for P1:PC₇₁BM films).

Line integration along the q_z axis of P2 and P2:PC₇₁BM GIWAXS images, along with integration of the (100) peak along χ are shown in Figure 5-12. Pristine P2 films exhibit a (100) and a (010) peak at 0.35 \AA^{-1} and around 1.51 \AA^{-1} respectively. The (100) peak intensity is increased with both DIO and MN; however the (010) peak intensity decreases with MN and increases with DIO compared to films cast without additive. Interestingly, a change in P2 crystallite orientation is also visible in Figure 5-12c, with (100) scattering

intensities increased at scattering angles of 0° and 180° in films cast from chloroform (chain-to-chain orientation in-plane), 40° and 140° in films cast with DIO and around 90° in films cast with MN (chain-to-chain orientation out-of-plane). Some reports have highlighted polymer ordering in solution as a driver for crystallite orientation in films, with pre-ordered polymers leading to lamellar peaks out-of-plane and more amorphous polymer chains leading to lamellar scattering in-plane based on surface energy matching.⁹³ Here, SANS showed the presence of amorphous P2 aggregates in chloroform, with more order induced in the aggregates with DIO and MN, which could explain the drastic change in orientation in pristine polymer films. Similarly to P1:PC₇₁BM, P2:PC₇₁BM blends exhibit a higher order (200) peak in Figure 5-12c, with the (010) peak appearing as a shoulder to the PC₇₁BM scattering peak. A difference in the polymer crystallite orientation in P2-based blends is also seen in Figure 5-12d, where P2 chain-to-chain crystallites are oriented both in-plane and out-of-plane when blends are cast from chloroform alone, whereas DIO and MN induce a preferred orientation of the chain-to-chain crystallites out-of-plane.

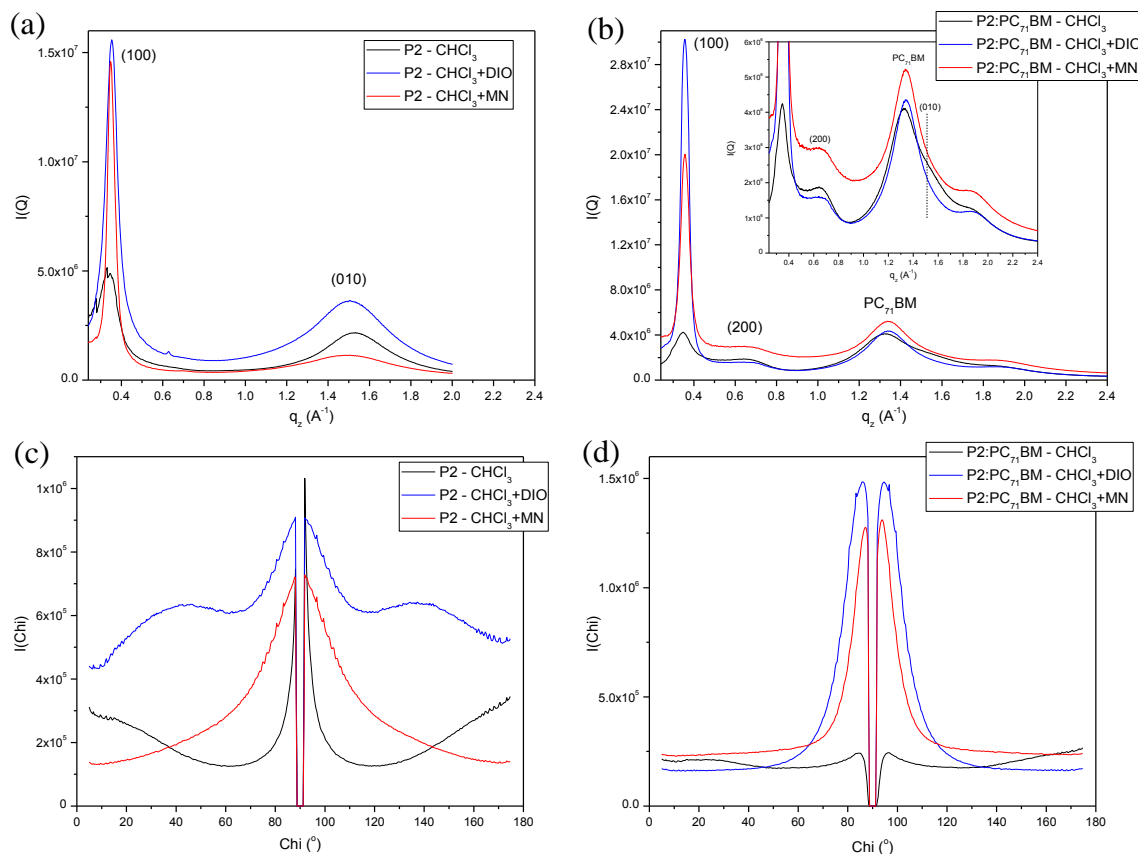


Figure 5-12. Line integration along the q_z axis of (a) P2 films and (b) P2:PC₇₁BM films, and integration along χ of the (100) scattering peak in (c) P2 films and (d) P2:PC₇₁BM films.

Interestingly, in both P1:PC₇₁BM and P2:PC₇₁BM blends, the use of DIO or MN as additives leads to preferred lamellar orientation out-of-plane. Table 5-4 summarizes the characteristic lengths calculated from the GIWAXS measurements, and demonstrates that for these polymers and blends, the additives have little impact on the π - and lamellar-stacking distances or on the number of polymer chains involved in the formation of these crystallites.

Table 5-4. π - π and lamellar (d) distances and coherence length of (100) peak ($L_{c,d}$) estimated from GIWAXS integration.

	P1			P1:PC₇₁BM			P2			P2:PC₇₁BM		
	π - π (Å)	d (Å)	$L_{c,d}$ (Å)	π - π (Å)	d (Å)	$L_{c,d}$ (Å)	π - π (Å)	d (Å)	$L_{c,d}$ (Å)	π - π (Å)	d (Å)	$L_{c,d}$ (Å)
None	3.9	19	90	3.9	19	98	4.1	18	101	4.2	18	98
IO	3.8	19	68	/	20	73						
DIO	3.8	20	70	/	19	78	4.1	18	135	/	18	209
MN	3.8	19	87	/	20	99	4.2	18	202	3.9	18	173

Based on the absorbance of the blends and on the GIWAXS data, the processing additives all have an impact on short range interactions, and in all cases MN increases the number of scattering sites. By comparison, DIO leads to a 1.5 time increase in the scattering intensity compared to P1 blends without additive but leads to an order of magnitude increase in the (100) intensity in P2 blends. These observations highlight different mechanisms followed in each case.

5.5. Mechanism of Action for Morphology Control using Additives

There are three main (simplified) pathways for phase separation: i) liquid-liquid demixing of the polymer and fullerene phase, ii) polymer solidification and growth followed by fullerene solidification; iii) fullerene aggregation and growth followed by polymer ordering.³²⁶ In the case of P1:PC₇₁BM and P2:PC₇₁BM blends cast from chloroform, liquid-liquid demixing (i) occurs due to the short drying times of the film. When high boiling point additives are used, the film drying time is increased and film formation can now also follow pathway ii) or iii), in addition to liquid-liquid demixing.

Based on the solution absorption and SANS results, the presence of ordered P1 aggregates in solution with DIO and NB prior to deposition, along with longer drying times, lead to promotion of polymer gelation through the polymer interactions formed

within the casting solution. The lack of dependence of the intensity of the aggregation peak in the UV-vis-NIR spectra with the boiling point of NB<ODT<DIH<DIO also supports that polymer ordering is not time-dependent in the case of selective additives. On the other hand, the lack of ordering within polymer aggregates in solutions with MN along with the increase in the intensity of the aggregation peak in the UV-vis-NIR absorption spectrum of the active layer with boiling point of oDCB<TCB<MN<CN indicate that polymer crystallite formation is time dependent when good solvents are used. The similar feature sizes in AFM images either with DIO or MN along with the similar GIWAXS images of P1:PC₇₁BM blends cast with either additives indicate that polymer ordering and solidification precede fullerene solidification, following pathway (ii). Both mechanisms (polymer crystallite formation prior or during film formation) of film formation when either selective or good additives are used promote finer domain sizes, and enhancement of J_{sc} leading to an order of magnitude increase in the PCEs from 0.5% to around 5%.

In P2:PC₇₁BM blends, using processing additives does lead to variations in the phase separation, with different effects when good solvents are used compared to selective solvents. However, the varying effects of the processing additives are not seen in solution, where all additives lead to formation of ordered aggregates prior to film deposition, but the additives seem to have different effects on the polymer ordering during film formation. As was the case in P1:PC₇₁BM blends, there is an increase in the intensity of the aggregation peak in the UV-vis-NIR absorption spectrum of the active layer following oDCB~TCB<MN~CN, which points to an impact of the additive structure (number of aromatic rings) relative to the additive's boiling point. Based on

these observations and on the AFM images, it is hypothesized that further polymer solidification from the pre-ordered aggregates in solution is hindered by growth of the fullerene aggregates. The presence of good solvents for P2 allows the polymer domains to remain mobile and form further crystallites (i.e. additives act as plasticizer, swell polymer domains), but also lead to further growth of the fullerene domains. When selective additives are present, the additive/polymer interactions are limited, and the polymer crystallites are allowed to grow as indicated by the increased scattering intensity in the GIWAXS data, while PC₇₁BM remains solubilized by the additive.

In conclusion, the mechanism for film formation depends on the polymer structure (polymer ordering allowing or hindering fullerene aggregate growth) and on the solubilizing effect of the additive, regardless of the additive structure as shown by DIO and NB. In the case where polymer ordering is thermodynamically favored (P1), either selective or good solvents lead to finer phase separation compared to blends cast from chloroform without additive and enhanced efficiencies. In the case where polymer ordering is limited (P2), only selective solvents (i.e. poor solvents for the polymer, good solvents for the fullerene derivative) lead to significant variations in the phase separation and increase the device efficiency.

CHAPTER 6. CONCLUSIONS AND PERSPECTIVES

Material Design for All-Polymer OPVs

The introductory remarks as well as the conclusions reached in Chapter 3 point to the need for polymers with balanced charge carrier mobilities for all-polymer OPVs. Once balanced charge transport is achieved, several strategies can be used to control polymer:polymer phase separation, such as selective polymer-solvent interactions or thermal annealing. The similarities between naphthalenediimide and isoindigo could be used to design all-isoindigo-based blends, as was the case with diketopyrrolopyrrole polymers.²⁴⁴ For example, P(Se-NDI) was shown to work well as an acceptor in blends with a donor-acceptor polymer donor, and P(T-iI) has been shown to have ambipolar transport with electron mobilities being one order of magnitude greater than hole carrier mobilities in OFETs. As such, P(Se-iI) could be synthesized and its optoelectronic properties compared to P(T-iI) as shown in Figure 6-2. Furthermore, blends of P3HT:P(T-iI), P(T3-iI):P(T-iI) and other polymer donors could be studied with regard to the influence of the semicrystallinity of the donor polymer and the chemical similarities between the two polymers.

Interestingly, as this work was being written, the importance of backbones accommodating side-chain disorder for high carrier mobility polymers, i.e. little distortion induced by the presence of the side-chains, was stressed by Venkateshvaran *et al.*³²⁷ One design to reduce energetic disorder is hypothesized to be long side-chain substitution on both sides of one of the conjugated units, which is common to the isoindigo, diketopyrrolopyrrole, and naphthalenediimide units. Beyond mobility however, is the limited charge transfer (CT) at polymer:polymer interfaces due to the more localized CT state in polymers compared to fullerene aggregates. As such, one design which could enable the improvement of both electron carrier mobility and CT is the use of a more rigid polymer backbone, with a minimal number of torsion-susceptible

linkages along the polymer backbone. Naphthalenediimides and isoindigo again appear as monomer units that could have a large impact on electron charge transport through the film thickness in SCLC devices.

One hypothesis for efficient charge dissociation in polymer:fullerene blends is also the presence of a three-phase system, which is not necessarily created through the use of new molecular acceptors.³²⁸ This could be one limit to 1D polymer acceptor structures, along with limited electron transport through the bulk and limited CT exciton delocalization over several polymer backbones. As such, molecular acceptors with multiple dimensions installed in their structures could be designed.

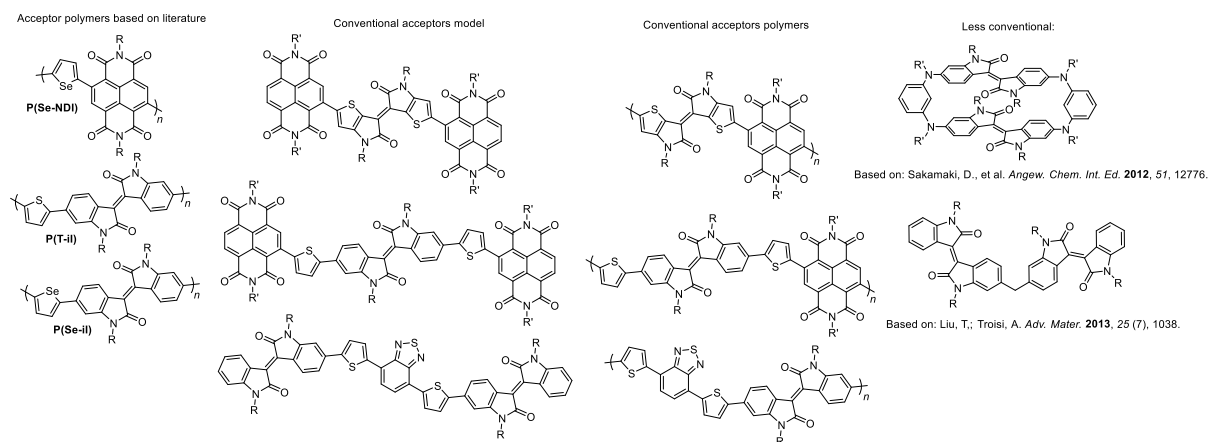


Figure 6-1. Suggested polymer and small molecule structures as novel acceptors for BHJ.

Material Design for Polymer:Fullerene OPVs

Chapter 3 highlighted the importance of energetic disorder on OPV parameters in polymer:fullerene bulk heterojunctions (BHJ), and the fact that the dielectric constant of the polymer:fullerene blends may have an impact on voltages loss. Although molecular structure can be used to infer information about dipoles at the molecular level, correlating structure and dipoles to dielectric constant (which is also dependent on frequency and orientation) is far from straightforward. In order to understand the influence of interfacial dipoles on OPV device processes, side-chain functionality can be designed to understand the effect of dipoles at the donor:acceptor interface,^{329,330} Although these principles have

been demonstrated using P3HT, combining the high dielectric constant found in isoindigo-based polymer:fullerene blends to enhanced dipoles at the polymer:fullerene interface could provide interesting observations in bilayer devices (Figure 6-3).

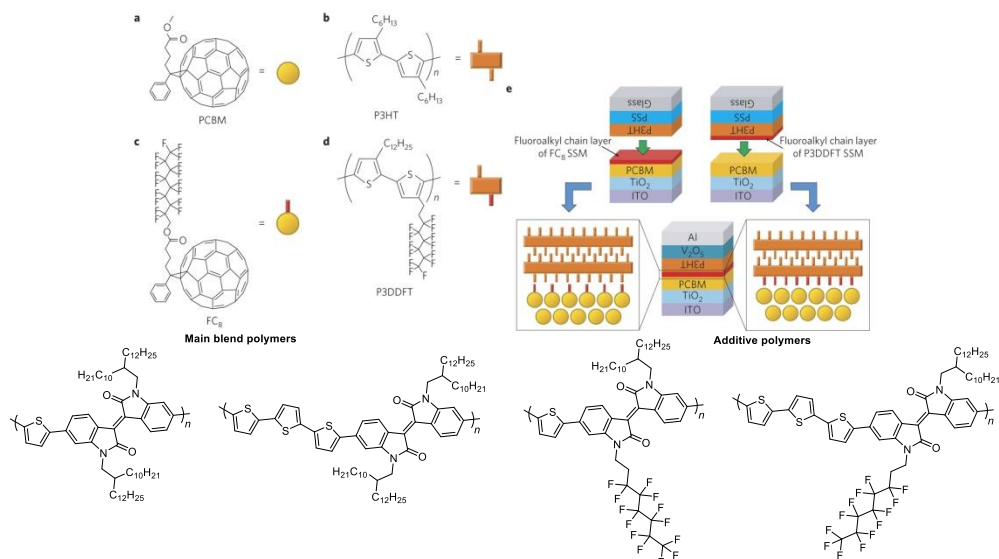


Figure 6-2. Illustration of previous work installing dipoles at the polymer:fullerene interface (adapted from ³²⁹), and proposed isoindigo-based polymer to study the impact of dielectric constant in the bulk versus dipoles at the interfaces.

Morphology Control in Polymer:Fullerene OPVs

The polymer's propensity to aggregate and order was shown to drive phase separation over polymer solubility in Chapter 4. Chapter 5 concluded to differences in the mechanism of film formation when aromatic versus aliphatic processing additives (or tailing solvents) are used. However, all these conclusions are based on spun-cast solution relying on chlorinated solvents, which would be a financial and health and safety challenge to implement on a large manufacturing scale. The development of non-halogenated solvent mixtures has been reported in the literature,²¹⁵ and since these organic thin films are typically thought of as coatings, some insight can be gained by monitoring advances in the coating industry. In particular, emulsions as they are found in paints could be formulated using conjugated polymers. The structure of the polymer could be modified to increase solubility in non-chlorinated solvents, by appending

triglyme chains along with alkyl chains to maintain the polymer glass transition temperature while increasing processability in polar solvents³³¹ or by functionalizing the polymer with polystyrene or other "commodity" structures which could help reduce gelation of the casting solution.³³² Fundamentally, side-chain functionality can be designed to understand the impact of the polymer vs. fullerene orientation at the donor:acceptor interface.

Futhermore, the optimal phase separation in BHJ layers is not thermodynamically stable, and thermal and photochemical stabilities should be achieved for increased device lifetime. One approach to stable morphologies is through reactive side-chains cross-linking,¹⁸⁵ which can also enable the solution-based fabrication of multiple layers without the need for orthogonal solvents. Other strategies to drive and stabilize optimal phase separation have been the use of conjugated block-copolymers or hydrogen-bonding,³³³ which could be of particular interest for future research in the Reynolds group considering the hydrogen-bond accepting and donating ability of isoindigo.

Although not discussed here, the functionality of the polymer end groups has been shown to have a great impact on polymer packing,³³⁴ and can be used to induce preferred orientation of the polymer backbone perpendicular to the substrate, through the bulk of the layer, as demonstrated by fluorinated end-groups on P3HT.³³⁵ There are two main challenges in working on end-group functionalization: one is the difficulty of characterization of polymer end-groups, especially in reconciling results obtained through various methods, and the second challenge is in installing asymmetric end-groups. To tackle the second issue, chain-growth-type polymerizations need to be developed for donor-acceptor polymers as demonstrated by Senkovskyy *et al.*³³⁶

APPENDIX A. BEAMTIME PROPOSAL

PI: Dr. John Reynolds / Spokesperson: Caroline Grand

Date: August 31th, 2013

Impact of Polymer Solubility and Processing on the Microstructure and Crystallinity of Isoindigo Polymers and their Blends with Fullerenes for Organic Photovoltaics

Background and Significance

Pi-conjugated polymer solid-state based organic photovoltaics (OPVs) have seen continual enhancements in performance which can be attributed to researchers developing a deeper understanding of the active layer p- and n-type materials and their blends in thin films.¹⁻³ The phase separation in donor-acceptor bulk heterojunction (BHJ) OPVs can be controlled through the solution formulation with processing additives, thermal annealing, or by varying the processing technique. Our group has previously demonstrated that processing additives can drastically change the blend morphology on the microscopic scale.^{4,5}

We are currently studying a p-type isoindigo polymer to understand how solubility and branching point along the solubilizing group impact crystallinity and phase separation in blends.^{6,7} Absorption measurements in thin films showed an increase in the vibration band intensity, which was hypothesized to derive from an increase in π - π interactions. These observations were demonstrated through preliminary GIWAXS results which showed that modifying the polymer's side chains induces dramatic changes in both the packing with a π -stacking distance difference of 0.5Å, and also in the orientation of the polymer backbones (Figure 1).

In OPV devices with P(T3-iI)-HD:PCBM BHJs (see Figure 1) 7% efficiency has been achieved. However, the use of different processing conditions, like the use of thermal annealing and processing additives, either does not change the maximum

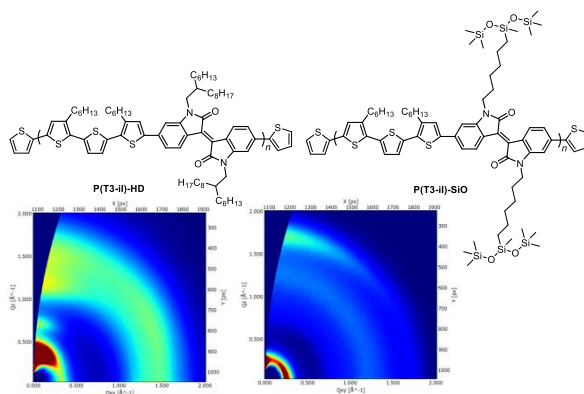


Figure 1. The structures of the two isoindigo polymers and their respective GIWAXS patterns.

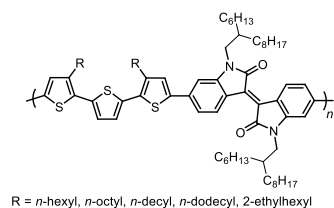
efficiency nor has a detrimental effect. The preliminary GIWAXS results have demonstrated that solvent additives alone did not affect the microstructure of the blends. This observation shows that there needs to be a more fundamental understanding of the interaction between processing additives and the polymer and fullerene compounds.

Specific Aims

This work aims to test the hypothesis that by tuning the polymer solubility through its structure (and without sacrificing π - π interactions) controlled aggregation can shed light on how processing additives impact the microstructure of polymer thin-films. The second hypothesis to be tested is that orientation cannot only be manipulated through chemical structure but also by processing conditions. Specifically we will explore the differences in processing associated with spin coating, doctor blading and slot die coating, and thermal annealing. To understand the effect on structures grazing incident wide-angle X-ray scattering (GIWAXS) with *in situ* thermal annealing capabilities will be exploited. The family of materials to be studied is based on isoindigo conjugated polymers. Specific topics to be studied in this work are:

1. The effect of polymer solubility through side chain modification and molecular weight control on the crystal growth in thin films;
2. The effect of processing additives on the crystal growth in polymer thin films and in blends with a fullerene acceptor;
3. The effect of thermal annealing on crystal growth and reorganization;
4. The effect of the processing technique on the crystal orientation, and crystal size.

Planned experiments



Scheme 1. Polymer structures to be investigated in thin-films by GIWAXS.

A family of poly(terthiophene-*co*-isoindigo) with varying side chains (Scheme 1) have been synthesized and are currently being characterized. Solubility measurements are being conducted, which together with UV-vis spectroscopy are being used to probe aggregation in solution and in thin-films. Thermal properties and crystallinity in the bulk will be studied by differential scanning calorimetry, which will in turn provide a framework for *in situ* thermal annealing experiments. OPV devices will be evaluated to look at the effect

of processing (solvent choice, solution formulation, drying time, thermal annealing) on the device performance. These observations will then be correlated by GIWAXS results with the microstructure. A first set of experiments will look at thin-films of the materials processed using similar conditions in OPV devices in order to look at the degree of order in these polymers. A second set of experiments will investigate blends of the polymers with a fullerene n-type material in order to probe changes in packing when the electron accepting material is added to the thin films. A third set will probe the influence of 1,8-diiodooctane (DIO) on the microstructure of the polymer films alone, and in the blends. Finally, a fourth set will study the impact of processing on the film properties for a selected polymer structure – in this case, changing the processing method from spin-coating, to doctor blading, to slot-die coating without and with thermal annealing simulating the process used for device fabrication will provide insight on how processing affects microstructure and orientation in thin-films of semiconducting materials.

Planned Interpretation Methods

The raw images will be processed using available software (eg. WxDiff 1.11 Compiled developed by Stefan C.B. Mannsfeld, Stanford Synchrotron Radiation Lightsource) for converting pixels into momentum transfer, q . Relative degree of crystallinity, crystal domain size, and degree of crystal orientation will be obtained from the line profiles a constant q .

Needs for Synchrotron Radiation

GIWAXS with synchrotron radiation is necessary for this work due to the intrinsically low contrast (in terms of the X-ray scattering length density) in the organic thin films. Beamline 8ID-E will be optimal for this work as has already been evidenced through the previous results on similar systems carried out by other groups.^{9,10} The variable temperature cells and vacuum environment will allow us to conduct annealing related measurements on device structures complete with electrode cappings. Based on the proposed experiments, the following time estimates are based on 10 minutes per sample for sample change and exposure time. Over the course of this study we plan the following:

1. Thirty samples of polymer thin films with varying solubility tuned through side chains and molecular weight – 5 hours

2. Sixty samples of polymer and fullerene blends with 1:1.5 and 1:4 ratios – 10 hours
3. Sixty samples of polymer-only with 1%v, 2.5%v, 5%v of processing additives- 10 hours
4. Sixty samples of polymer:PCBM thin films with 1%v, 2.5%v, 5%v of processing additives – 10 hours
5. Sixty samples of polymer-only and blends processed by blade coating and slot-die coating – 10 hours
6. Four time points per sample, twenty samples for annealing study – 8 hours depending on heating time

For reproducibility reasons, these experiments will be repeated twice on different samples. As such, it is estimated that seven 8-hour shifts will be needed over one scheduling period then another six 8-hour shifts over a subsequent scheduling period on beamline 11-3 are required for this set of experiments.

References

- (1) Henson, Z. B.; Müllen, K.; Bazan, G. C. *Nature Chem.* **2012**, *4*, 699.
- (2) Mei, J.; Diao, Y.; Appleton, A. L.; Fang, L.; Bao, Z. *J. Am. Chem. Soc.* **2013**, *135*, 6724.
- (3) Walker, B.; Kim, C.; Nguyen, T.-Q. *Chem. Mater.* **2010**, *23*, 470.
- (4) Stalder, R.; Grand, C.; Subbiah, J.; So, F.; Reynolds, J. R. *Polymer Chemistry* **2012**, *3*, 89.
- (5) Amb, C. M.; Chen, S.; Graham, K. R.; Subbiah, J.; Small, C. E.; So, F.; Reynolds, J. R. *J. Am. Chem. Soc.* **2011**, *133*, 10062.
- (6) Mei, J.; Kim do, H.; Ayzner, A. L.; Toney, M. F.; Bao, Z. *J. Am. Chem. Soc.* **2011**, *133*, 20130.
- (7) Kim, D. H.; Ayzner, A. L.; Appleton, A. L.; Schmidt, K.; Mei, J.; Toney, M. F.; Bao, Z. *Chem. Mater.* **2012**, *25*, 431.
- (8) Noriega, R.; Rivnay, J.; Vandewal, K.; Koch, F. P. V.; Stingelin, N.; Smith, P.; Toney, M. F.; Salleo, A. *Nature Mater.* **2013**, advance online publication.

REFERENCES

- (1) Muspratt, J. S.; Hofmann, A. W. *Mem. Proc. Chem. Soc.* **1843**, 2, 249.
- (2) Letheby, H. *J. Chem. Soc.* **1862**, 15, 161.
- (3) Dall'Olio, A.; Dascola, G.; Vacara, V.; Bocchi, V. *C. R. Acad. Sci. Paris* **1968**, 267, 433.
- (4) McNeill, R.; Siudak, R.; Wardlaw, J.; Weiss, D. *Aust. J. Chem.* **1963**, 16 (6), 1056.
- (5) Bolto, B.; Weiss, D. *Aust. J. Chem.* **1963**, 16 (6), 1076.
- (6) Bolto, B.; McNeill, R.; Weiss, D. *Aust. J. Chem.* **1963**, 16 (6), 1090.
- (7) De Surville, R.; Jozefowicz, M.; Yu, L. T.; Pepichon, J.; Buvet, R. *Electrochim. Acta* **1968**, 13 (6), 1451.
- (8) Jozefowicz, M.; Yu, L. T.; Perichon, J.; Buvet, R. *J. Polym. Sci. C, Polym. Symp.* **1969**, 22 (2), 1187.
- (9) Job, A.; Champetier, G. *C. R. Acad. Sci. Paris* **1929**, 189, 1089.
- (10) Shirakawa, H. *Angew. Chem. Int. Ed.* **2001**, 40 (14), 2574.
- (11) Berets, D. J.; Smith, D. S. *Trans. Faraday Soc.* **1968**, 64, 823.
- (12) Ito, T.; Shirakawa, H.; Ikeda, S. *J. Polym. Sci. Polym. Chem. Ed.* **1974**, 12 (1), 11.
- (13) Chiang, C. K.; Fincher, C. R.; Park, Y. W.; Heeger, A. J.; Shirakawa, H.; Louis, E. J.; Gau, S. C.; MacDiarmid, A. G. *Phys. Rev. Lett.* **1977**, 39 (17), 1098.
- (14) Chiang, C. K.; Druy, M. A.; Gau, S. C.; Heeger, A. J.; Louis, E. J.; MacDiarmid, A. G.; Park, Y. W.; Shirakawa, H. *J. Am. Chem. Soc.* **1978**, 100 (3), 1013.
- (15) Suzuki, A. *Angew. Chem. Int. Ed.* **2011**, 50 (30), 6722.
- (16) Rogers, J. A.; Someya, T.; Huang, Y. *Science* **2010**, 327 (5973), 1603.
- (17) Sekitani, T.; Someya, T. *Adv. Mater.* **2010**, 22 (20), 2228.
- (18) Arias, A. C.; MacKenzie, J. D.; McCulloch, I.; Rivnay, J.; Salleo, A. *Chem. Rev.* **2010**, 110 (1), 3.
- (19) Tsumura, A.; Koezuka, H.; Ando, T. *Appl. Phys. Lett.* **1986**, 49 (18), 1210.
- (20) Horowitz, G.; Fichou, D.; Peng, X.; Xu, Z.; Garnier, F. *Solid State Commun.* **1989**, 72 (4), 381.
- (21) Minemawari, H.; Yamada, T.; Matsui, H.; Tsutsumi, J. y.; Haas, S.; Chiba, R.; Kumai, R.; Hasegawa, T. *Nature* **2011**, 475 (7356), 364.
- (22) Ando, S.; Murakami, R.; Nishida, J.-I.; Tada, H.; Inoue, Y.; Tokito, S.; Yamashita, Y. *J. Am. Chem. Soc.* **2005**, 127 (43), 14996.
- (23) Li, J.; Zhao, Y.; Tan, H. S.; Guo, Y.; Di, C. A.; Yu, G.; Liu, Y.; Lin, M.; Lim, S. H.; Zhou, Y.; Su, H.; Ong, B. S. *Sci Rep* **2012**, 2, 754.
- (24) Dyer, A. L.; Thompson, E. J.; Reynolds, J. R. *ACS Appl. Mater. Interfaces* **2011**, 3 (6), 1787.
- (25) Burroughes, J. H.; Bradley, D. D. C.; Brown, A. R.; Marks, R. N.; Mackay, K.; Friend, R. H.; Burns, P. L.; Holmes, A. B. *Nature* **1990**, 347 (6293), 539.
- (26) Thejo Kalyani, N.; Dhoble, S. J. *Renew. Sust. Energ. Rev.* **2012**, 16 (5), 2696.
- (27) McQuade, D. T.; Hegedus, A. H.; Swager, T. M. *J. Am. Chem. Soc.* **2000**, 122 (49), 12389.

- (28) Sariciftci, N. S.; Smilowitz, L.; Heeger, A. J.; Wudl, F. *Science* **1992**, 258 (5087), 1474.
- (29) Liang, Y.; Yu, L. *Acc. Chem. Res.* **2010**, 43 (9), 1227.
- (30) You, J.; Dou, L.; Yoshimura, K.; Kato, T.; Ohya, K.; Moriarty, T.; Emery, K.; Chen, C.-C.; Gao, J.; Li, G.; Yang, Y. *Nature Commun.* **2013**, 4, 1446.
- (31) Günes, S.; Neugebauer, H.; Sariciftci, N. S. *Chem. Rev.* **2007**, 107 (4), 1324.
- (32) Beaujuge, P. M.; Amb, C. M.; Reynolds, J. R. *Acc. Chem. Res.* **2010**, 43 (11), 1396.
- (33) Beaujuge, P. M.; Fréchet, J. M. J. *J. Am. Chem. Soc.* **2011**, 133 (50), 20009.
- (34) Zhou, H.; Yang, L.; You, W. *Macromolecules* **2012**, 45 (2), 607.
- (35) Hoth, C. N.; Schilinsky, P.; Choulis, S. A.; Balasubramanian, S.; Brabec, C. J. In *Applications of Organic and Printed Electronics: A Technology-Enabled Revolution*; Cantatore, E., Ed.; Springer: **2013**, p 27.
- (36) Yuan, Y.; Giri, G.; Ayzner, A. L.; Zoombelt, A. P.; Mannsfeld, S. C.; Chen, J.; Nordlund, D.; Toney, M. F.; Huang, J.; Bao, Z. *Nature Commun.* **2014**, 5, 3005.
- (37) Giri, G.; Verploegen, E.; Mannsfeld, S. C. B.; Atahan-Evrenk, S.; Kim, D. H.; Lee, S. Y.; Becerril, H. A.; Aspuru-Guzik, A.; Toney, M. F.; Bao, Z. *Nature* **2011**, 480 (7378), 504.
- (38) Lim, S.-L.; Chen, E.-C.; Chen, C.-Y.; Ong, K.-H.; Chen, Z.-K.; Meng, H.-F. *Sol. Energ. Mater. Sol. Cells* **2012**, 107 (0), 292.
- (39) Søndergaard, R.; Manceau, M.; Jørgensen, M.; Krebs, F. C. *Adv. Energy Mater.* **2012**, 2 (4), 415.
- (40) Teichler, A.; Eckardt, R.; Hoeppener, S.; Friebe, C.; Perelaer, J.; Senes, A.; Morana, M.; Brabec, C. J.; Schubert, U. S. *Adv. Energy Mater.* **2011**, 1 (1), 105.
- (41) Na, S.-I.; Yu, B.-K.; Kim, S.-S.; Vak, D.; Kim, T.-S.; Yeo, J.-S.; Kim, D.-Y. *Sol. Energ. Mater. Sol. Cells* **2010**, 94 (8), 1333.
- (42) Stalder, R., University of Florida, **2011**.
- (43) Wudl, F.; Kobayashi, M.; Heeger, A. J. *J. Org. Chem.* **1984**, 49 (18), 3382.
- (44) Brédas, J. L.; Heeger, A. J.; Wudl, F. *J. Chem. Phys.* **1986**, 85 (8), 4673.
- (45) Bredas, J. L.; Street, G. B. *Acc. Chem. Res.* **1985**, 18 (10), 309.
- (46) Kaneto, K.; Yoshino, K.; Inuishi, Y. *Jpn. J. Appl. Phys.* **1982**, 21 (9A), L567.
- (47) Hunter, C. A.; Sanders, J. K. M. *J. Am. Chem. Soc.* **1990**, 112 (14), 5525.
- (48) Martinez, C. R.; Iverson, B. L. *Chem. Sci.* **2012**, 3 (7), 2191.
- (49) Sato, M.-A.; Tanaka, S.; Kaeriyama, K. *J. Chem. Soc., Chem. Commun.* **1986** (11), 873.
- (50) Elsenbaumer, R. L.; Jen, K. Y.; Oboodi, R. *Synth. Met.* **1986**, 15 (2–3), 169.
- (51) Jen, K.-Y.; Miller, G. G.; Elsenbaumer, R. L. *J. Chem. Soc., Chem. Commun.* **1986** (17), 1346.
- (52) Elsenbaumer, R. L.; Jen, K. Y.; Miller, G. G.; Shacklette, L. W. *Synth. Met.* **1987**, 18 (1–3), 277.
- (53) Yoshino, K.; Nakajima, S.; Gu, H. B.; Sugimoto, R.-i. *Jpn. J. Appl. Phys.* **1987**, 26 (8A), L1371.
- (54) Yokoyama, A.; Miyakoshi, R.; Yokozawa, T. *Macromolecules* **2004**, 37 (4), 1169.
- (55) Loewe, R. S.; Ewbank, P. C.; Liu, J.; Zhai, L.; McCullough, R. D. *Macromolecules* **2001**, 34 (13), 4324.

- (56) Sheina, E. E.; Liu, J.; Iovu, M. C.; Laird, D. W.; McCullough, R. D. *Macromolecules* **2004**, *37* (10), 3526.
- (57) Iovu, M. C.; Sheina, E. E.; Gil, R. R.; McCullough, R. D. *Macromolecules* **2005**, *38* (21), 8649.
- (58) Nguyen, T.-Q.; Doan, V.; Schwartz, B. J. *J. Chem. Phys.* **1999**, *110* (8), 4068.
- (59) Nguyen, T.-Q.; Yee, R. Y.; Schwartz, B. J. *J. Photochem. Photobiol. A, Chem.* **2001**, *144* (1), 21.
- (60) Henson, Z. B.; Müllen, K.; Bazan, G. C. *Nature Chem.* **2012**, *4* (9), 699.
- (61) Brédas, J. L.; Calbert, J. P.; da Silva Filho, D. A.; Cornil, J. *Proc. Natl. Acad. Sci. U.S.A.* **2002**, *99* (9), 5804.
- (62) Sherrill, C. D. *Acc. Chem. Res.* **2012**, *46* (4), 1020.
- (63) Cornil, J.; Beljonne, D.; Calbert, J. P.; Brédas, J. L. *Adv. Mater.* **2001**, *13* (14), 1053.
- (64) Brédas, J.-L.; Beljonne, D.; Coropceanu, V.; Cornil, J. *Chem. Rev.* **2004**, *104* (11), 4971.
- (65) Beljonne, D.; Cornil, J.; Coropceanu, V.; Filho, D. A. d. S.; Geskin, V.; Lazzaroni, R.; Leclère, P.; Brédas, J.-L. In *Handbook of Conjugated Polymers: Theory, Synthesis, Properties, and Characterization*; 3rd Edition ed.; Skotheim, T. A., Reynolds, J. R., Eds.; CRC Press: Boca Raton, **2006**.
- (66) Surin, M.; Hennebicq, E.; Ego, C.; Marsitzky, D.; Grimsdale, A. C.; Müllen, K.; Brédas, J.-L.; Lazzaroni, R.; Leclère, P. *Chem. Mater.* **2004**, *16* (6), 994.
- (67) Kim, J.; Swager, T. M. *Nature* **2001**, *411* (6841), 1030.
- (68) Tessler, N.; Preezant, Y.; Rappaport, N.; Roichman, Y. *Adv. Mater.* **2009**, *21* (27), 2741.
- (69) Yoon, J.; Jo, S.; Chun, I. S.; Jung, I.; Kim, H.-S.; Meitl, M.; Menard, E.; Li, X.; Coleman, J. J.; Paik, U.; Rogers, J. A. *Nature* **2010**, *465* (7296), 329.
- (70) Powell, D. M.; Winkler, M. T.; Choi, H. J.; Simmons, C. B.; Needleman, D. B.; Buonassisi, T. *Energy Environ. Sci.* **2012**, *5* (3), 5874.
- (71) Mozer, A. J.; Sariciftci, N. S. In *Handbook of Conjugated Polymers: Processing and Applications*; 3rd Edition ed.; Skotheim, T. A., Reynolds, J. R., Eds.; CRC Press: Boca Raton, **2006**.
- (72) Hummel, R. E. *Electronic Properties of Materials*; Springer, **2011**.
- (73) Mihailetschi, V. D.; Koster, L. J. A.; Hummelen, J. C.; Blom, P. W. M. *Phys. Rev. Lett.* **2004**, *93* (21), 216601.
- (74) Chen, S.; Tsang, S.-W.; Lai, T.-H.; Reynolds, J. R.; So, F. *Adv. Mater.* **2014**, *26* (35), 6125.
- (75) Kippelen, B.; Bredas, J.-L. *Energy Environ. Sci.* **2009**, *2* (3), 251.
- (76) Pope, M.; Swenberg, C. E. *Electronic Processes in Organic Crystals and Polymers*; 2nd ed. ed.; Oxford University Press: New York, **1999**.
- (77) Scholes, G. D.; Rumbles, G. *Nature Mater.* **2006**, *5* (9), 683.
- (78) Sirringhaus, H. *Adv Mater* **2014**, *26* (9), 1319.
- (79) Wang, C.; Hwang, D.; Yu, Z.; Takei, K.; Park, J.; Chen, T.; Ma, B.; Javey, A. *Nature Mater.* **2013**, *12* (10), 899.
- (80) Khodagholy, D.; Rivnay, J.; Sessolo, M.; Gurfinkel, M.; Leleux, P.; Jimison, L. H.; Stavrinidou, E.; Herve, T.; Sanaur, S.; Owens, R. M.; Malliaras, G. G. *Nature Commun.* **2013**, *4*.

- (81) Newman, C. R.; Frisbie, C. D.; da Silva Filho, D. A.; Brédas, J.-L.; Ewbank, P. C.; Mann, K. R. *Chem. Mater.* **2004**, *16* (23), 4436.
- (82) Kim, G.; Kang, S.-J.; Dutta, G. K.; Han, Y.-K.; Shin, T. J.; Noh, Y.-Y.; Yang, C. *J. Am. Chem. Soc.* **2014**, *136* (26), 9477.
- (83) Kang, I.; Yun, H.-J.; Chung, D. S.; Kwon, S.-K.; Kim, Y.-H. *J. Am. Chem. Soc.* **2013**, *135* (40), 14896.
- (84) McCulloch, I.; Heeney, M.; Bailey, C.; Genevicius, K.; MacDonald, I.; Shkunov, M.; Sparrowe, D.; Tierney, S.; Wagner, R.; Zhang, W.; Chabiny, M. L.; Kline, R. J.; McGehee, M. D.; Toney, M. F. *Nature Mater.* **2006**, *5* (4), 328.
- (85) McCulloch, I.; Heeney, M.; Chabiny, M. L.; DeLongchamp, D.; Kline, R. J.; Cölle, M.; Duffy, W.; Fischer, D.; Gundlach, D.; Hamadani, B.; Hamilton, R.; Richter, L.; Salleo, A.; Shkunov, M.; Sparrowe, D.; Tierney, S.; Zhang, W. *Adv. Mater.* **2009**, *21* (10-11), 1091.
- (86) Yan, H.; Chen, Z.; Zheng, Y.; Newman, C.; Quinn, J. R.; Dotz, F.; Kastler, M.; Facchetti, A. *Nature* **2009**, *457* (7230), 679.
- (87) Leufgen, M.; Rost, O.; Gould, C.; Schmidt, G.; Geurts, J.; Molenkamp, L. W.; Oxtoby, N. S.; Mas-Torrent, M.; Crivillers, N.; Veciana, J.; Rovira, C. *Org. Electron.* **2008**, *9* (6), 1101.
- (88) Tsao, H. N.; Cho, D. M.; Park, I.; Hansen, M. R.; Mavrinskiy, A.; Yoon, D. Y.; Graf, R.; Pisula, W.; Spiess, H. W.; Müllen, K. *J. Am. Chem. Soc.* **2011**, *133* (8), 2605.
- (89) Lee, J.; Han, A. R.; Yu, H.; Shin, T. J.; Yang, C.; Oh, J. H. *J. Am. Chem. Soc.* **2013**, *135* (25), 9540.
- (90) Takahashi, Y.; Hasegawa, T.; Horiuchi, S.; Kumai, R.; Tokura, Y.; Saito, G. *Chem. Mater.* **2007**, *19* (26), 6382.
- (91) Zhang, X.; Bronstein, H.; Kronemeijer, A. J.; Smith, J.; Kim, Y.; Kline, R. J.; Richter, L. J.; Anthopoulos, T. D.; Sirringhaus, H.; Song, K.; Heeney, M.; Zhang, W.; McCulloch, I.; DeLongchamp, D. M. *Nature Commun.* **2013**, *4*.
- (92) Noriega, R.; Rivnay, J.; Vandewal, K.; Koch, F. P. V.; Stingelin, N.; Smith, P.; Toney, M. F.; Salleo, A. *Nature Mater.* **2013**, *12*, 1038.
- (93) Zhang, X.; Richter, L. J.; DeLongchamp, D. M.; Kline, R. J.; Hammond, M. R.; McCulloch, I.; Heeney, M.; Ashraf, R. S.; Smith, J. N.; Anthopoulos, T. D.; Schroeder, B.; Geerts, Y. H.; Fischer, D. A.; Toney, M. F. *J. Am. Chem. Soc.* **2011**, *133* (38), 15073.
- (94) Green, M. A.; Emery, K.; Hishikawa, Y.; Warta, W.; Dunlop, E. D. *Prog. Photovoltaics Res. App.* **2011**, *19* (5), 565.
- (95) Darling, S. B.; You, F. *RSC Advances* **2013**, *3* (39), 17633.
- (96) Tang, C. W. *Appl. Phys. Lett.* **1986**, *48* (2), 183.
- (97) Service, R. F. *Science* **2011**, *332* (6027), 293.
- (98) *Heliotech consolidates its technology leadership by establishing a new world record for organic solar technology with a cell efficiency of 12%*, http://www.heliotech.com/newscenter/latest_news/neuer-weltrekord-fur-organische-solarzellen-heliotech-behauptet-sich-mit-12-zelleffizienz-als-technologiefuhrer/?lang=en (accessed November 2013).
- (99) Thompson, B. C.; Fréchet, J. M. J. *Angew. Chem. Int. Ed.* **2008**, *47* (1), 58.

- (100) Kraabel, B.; Lee, C. H.; McBranch, D.; Moses, D.; Sariciftci, N. S.; Heeger, A. J. *Chem. Phys. Lett.* **1993**, *213* (3–4), 389.
- (101) Heeger, A. J. *Adv. Mater.* **2014**, *26* (1), 10.
- (102) Burke, T. M.; McGehee, M. D. *Adv. Mater.* **2014**, *26* (12), 1923.
- (103) Dang, M. T.; Hirsch, L.; Wantz, G.; Wuest, J. D. *Chem. Rev.* **2013**, *113* (5), 3734.
- (104) Varotto, A.; Treat, N. D.; Jo, J.; Shuttle, C. G.; Batara, N. A.; Brunetti, F. G.; Seo, J. H.; Chabini, M. L.; Hawker, C. J.; Heeger, A. J.; Wudl, F. *Angew. Chem. Int. Ed.* **2011**, *50* (22), 5166.
- (105) Liu, T.; Troisi, A. *Adv Mater* **2013**, *25* (7), 1038.
- (106) Bredas, J.-L. *Science* **2014**, *343* (6170), 492.
- (107) Vithanage, D. A.; Devižis, A.; Abramavičius, V.; Infahsaeng, Y.; Abramavičius, D.; MacKenzie, R. C. I.; Keivanidis, P. E.; Yartsev, A.; Hertel, D.; Nelson, J.; Sundström, V.; Gulbinas, V. *Nature Commun.* **2013**, *4*.
- (108) Askat, E. J.; Adam, P. W.; John, R. T.; Wai-Lun, C.; Na, S.; Raluca, G.; Loren, G. K.; Kenrick, J. W.; Kevin, L.; Peter, J. R.; Zhu, X. Y. *Nature Mater.* **2012**, *12* (1), 66.
- (109) Bakulin, A. A.; Rao, A.; Pavelyev, V. G.; van Loosdrecht, P. H. M.; Pshenichnikov, M. S.; Niedzialek, D.; Cornil, J.; Beljonne, D.; Friend, R. H. *Science* **2012**, *335* (6074), 1340.
- (110) Grancini, G.; Maiuri, M.; Fazzi, D.; Petrozza, A.; Egelhaaf, H. J.; Brida, D.; Cerullo, G.; Lanzani, G. *Nature Mater.* **2013**, *12* (1), 29.
- (111) Armin, A.; Zhang, Y.; Burn, P. L.; Meredith, P.; Pivrikas, A. *Nature Mater.* **2013**, *12* (7), 593.
- (112) Grancini, G.; Binda, M.; Criante, L.; Perissinotto, S.; Maiuri, M.; Fazzi, D.; Petrozza, A.; Egelhaaf, H. J.; Brida, D.; Cerullo, G.; Lanzani, G. *Nature Mater.* **2013**, *12* (7), 594.
- (113) Gélinas, S.; Rao, A.; Kumar, A.; Smith, S. L.; Chin, A. W.; Clark, J.; van der Poll, T. S.; Bazan, G. C.; Friend, R. H. *Science* **2014**, *343* (6170), 512.
- (114) Vandewal, K.; Albrecht, S.; Hoke, E. T.; Graham, K. R.; Widmer, J.; Douglas, J. D.; Schubert, M.; Mateker, W. R.; Bloking, J. T.; Burkhard, G. F.; Sellinger, A.; Fréchet, J. M. J.; Amassian, A.; Riede, M. K.; McGehee, M. D.; Neher, D.; Salbeck, J. *Nature Mater.* **2014**, *13* (1), 63.
- (115) Puodziukynaite, E.; Wang, H.-W.; Lawrence, J.; Wise, A. J.; Russell, T. P.; Barnes, M. D.; Emrick, T. *J. Am. Chem. Soc.* **2014**, *136* (31), 11043.
- (116) Page, Z. A.; Liu, Y.; Duzhko, V. V.; Russell, T. P.; Emrick, T. *Science* **2014**, *346* (6208), 441.
- (117) Dou, L.; You, J.; Hong, Z.; Xu, Z.; Li, G.; Street, R. A.; Yang, Y. *Adv. Mater.* **2013**, *25* (46), 6642.
- (118) Yu, G.; Gao, J.; Hummelen, J. C.; Wudl, F.; Heeger, A. J. *Science* **1995**, *270* (5243), 1789.
- (119) Halls, J. J. M.; Walsh, C. A.; Greenham, N. C.; Marseglia, E. A.; Friend, R. H.; Moratti, S. C.; Holmes, A. B. *Nature* **1995**, *376* (6540), 498.
- (120) Yu, G.; Heeger, A. J. *J. Appl. Phys.* **1995**, *78* (7), 4510.
- (121) Lyons, B. P.; Clarke, N.; Groves, C. *Energy Environ. Sci.* **2012**, *5* (6), 7657.
- (122) Street, R. A.; Davies, D.; Khlyabich, P. P.; Burkhart, B.; Thompson, B. C. *J. Am. Chem. Soc.* **2013**, *135* (3), 986.

- (123) Li, W.; Furlan, A.; Hendriks, K. H.; Wienk, M. M.; Janssen, R. A. J. *J. Am. Chem. Soc.* **2013**, *135* (15), 5529.
- (124) Hendriks, K. H.; Li, W.; Wienk, M. M.; Janssen, R. A. J. *J. Am. Chem. Soc.* **2014**, *136* (34), 12130.
- (125) Lampert, M. A. *Phys. Rev.* **1956**, *103* (6), 1648.
- (126) Bässler, H. In *Semiconducting Polymers - Chemistry, Physics and Engineering* Hadziioannou, G., Hutten, P. F. v., Eds.; Wiley-VCH: Weinheim, **2000**.
- (127) Murgatroyd, P. N. *J. Phys. D, Appl. Phys.* **1970**, *3* (2), 151.
- (128) Heston, N., University of Florida, **2009**.
- (129) Nicolai, H. T.; Wetzelaer, G. A. H.; Kuik, M.; Kronemeijer, A. J.; de Boer, B.; Blom, P. W. M. *Appl. Phys. Lett.* **2010**, *96* (17), 172107.
- (130) Graham, K. R., University of Florida, **2011**.
- (131) Beaujuge, P. M., University of Florida, **2009**.
- (132) Havinga, E. E.; ten Hoeve, W.; Wynberg, H. *Synth. Met.* **1993**, *55* (1), 299.
- (133) Parker, T. C.; Patel, D. G.; Moudgil, K.; Barlow, S.; Risko, C.; Bredas, J.-L.; Reynolds, J. R.; Marder, S. R. *Mater. Horiz.* **2015**, *2* (1), 22.
- (134) Robb, M. J.; Ku, S.-Y.; Brunetti, F. G.; Hawker, C. J. *J. Polym. Sci. A Polym. Chem.* **2013**, *51* (6), 1263.
- (135) Liu, Z.; Zhang, G.; Cai, Z.; Chen, X.; Luo, H.; Li, Y.; Wang, J.; Zhang, D. *Adv. Mater.* **2014**, *26* (40), 6965.
- (136) Guo, X.; Facchetti, A.; Marks, T. J. *Chem. Rev.* **2014**, *114* (18), 8943.
- (137) Zhou, H.; Yang, L.; Stuart, A. C.; Price, S. C.; Liu, S.; You, W. *Angew. Chem. Int. Ed.* **2011**, *50* (13), 2995.
- (138) Son, H. J.; Wang, W.; Xu, T.; Liang, Y.; Wu, Y.; Li, G.; Yu, L. *J. Am. Chem. Soc.* **2011**, *133* (6), 1885.
- (139) Scherf, U. In *Handbook of Conjugated Polymers*; 2nd Edition ed.; Skotheim, T. A., Elsenbaumer, R. L., Reynolds, J. R., Eds.; CRC Press: Boca Raton, **1998**.
- (140) Babel, A.; Jenekhe, S. A. *J. Am. Chem. Soc.* **2003**, *125* (45), 13656.
- (141) Steckler, T. T.; Zhang, X.; Hwang, J.; Honeyager, R.; Ohira, S.; Zhang, X.-H.; Grant, A.; Ellinger, S.; Odom, S. A.; Sweat, D.; Tanner, D. B.; Rinzler, A. G.; Barlow, S.; Brédas, J.-L.; Kippelen, B.; Marder, S. R.; Reynolds, J. R. *J. Am. Chem. Soc.* **2009**, *131* (8), 2824.
- (142) van Mullekom, H. A. M.; Vekemans, J. A. J. M.; Havinga, E. E.; Meijer, E. W. *Mater. Sci. Eng. R-Rep.* **2001**, *32* (1), 1.
- (143) Li, Y. *Acc. Chem. Res.* **2012**, *45* (5), 723.
- (144) Farnum, D. G.; Mehta, G.; Moore, G. G. I.; Siegal, F. P. *Tetrahedron Lett.* **1974**, *15* (29), 2549.
- (145) Grandidier, Y.; Riegler, A.; Ruf, K.; Schlatter, U.; Deno, T., *EP1411092 B1* (EP20030104957), **2011**.
- (146) Wienk, M. M.; Turbiez, M.; Gilot, J.; Janssen, R. A. J. *Adv. Mater.* **2008**, *20* (13), 2556.
- (147) Silva, J. F. M. d.; Garden, S. J.; Pinto, A. C. *J. Braz. Chem. Soc.* **2001**, *12*, 273.
- (148) Flores, J.-C.; Berens, U.; Bienewald, F.; Kirnerand, H. J.; Turbiez, M. G. R., *WO2009053291 A1* (PCT/EP2008/063919), **2009**.
- (149) Mei, J.; Graham, K. R.; Stalder, R.; Reynolds, J. R. *Org. Lett.* **2010**, *12* (4), 660.
- (150) Christie, R. M. *Biotech. Histochem.* **2007**, *82* (2), 51.

- (151) Estrada, L. A.; Stalder, R.; Abboud, K. A.; Risko, C.; Brédas, J.-L.; Reynolds, J. R. *Macromolecules* **2013**, *46* (22), 8832.
- (152) Stalder, R.; Mei, J.; Graham, K. R.; Estrada, L. A.; Reynolds, J. R. *Chem. Mater.* **2014**, *26* (1), 664.
- (153) Wang, E.; Mammo, W.; Andersson, M. R. *Adv. Mater.* **2014**, *26* (12), 1801.
- (154) Lei, T.; Wang, J.-Y.; Pei, J. *Acc. Chem. Res.* **2014**, *47* (4), 1117.
- (155) Deng, P.; Zhang, Q. *Polym. Chem.* **2014**, *5* (10), 3298.
- (156) Lei, T.; Dou, J.-H.; Pei, J. *Adv. Mater.* **2012**, *24* (48), 6457.
- (157) Mei, J.; Kim do, H.; Ayzner, A. L.; Toney, M. F.; Bao, Z. *J. Am. Chem. Soc.* **2011**, *133* (50), 20130.
- (158) Lei, T.; Dou, J.-H.; Ma, Z.-J.; Liu, C.-J.; Wang, J.-Y.; Pei, J. *Chem. Sci.* **2013**, *4* (6), 2447.
- (159) Wang, E.; Ma, Z.; Zhang, Z.; Vandewal, K.; Henriksson, P.; Inganas, O.; Zhang, F.; Andersson, M. R. *J. Am. Chem. Soc.* **2011**, *133* (36), 14244.
- (160) Ma, Z.; Sun, W.; Himmelberger, S.; Vandewal, K.; Tang, Z.; Bergqvist, J.; Salleo, A.; Andreasen, J. W.; Inganas, O.; Andersson, M. R.; Muller, C.; Zhang, F.; Wang, E. *Energy Environ. Sci.* **2014**, *7* (1), 361.
- (161) Ho, C.-C.; Chen, C.-A.; Chang, C.-Y.; Darling, S. B.; Su, W.-F. *J. Mater. Chem. A* **2014**, *2* (21), 8026.
- (162) Deng, Y.; Liu, J.; Wang, J.; Liu, L.; Li, W.; Tian, H.; Zhang, X.; Xie, Z.; Geng, Y.; Wang, F. *Adv. Mater.* **2014**, *26* (3), 471.
- (163) Dang, D.; Chen, W.; Yang, R.; Zhu, W.; Mammo, W.; Wang, E. *Chem. Commun.* **2013**, *49* (81), 9335.
- (164) Jung, J. W.; Liu, F.; Russell, T. P.; Jo, W. H. *Energy Environ. Sci.* **2013**, *6* (11), 3301.
- (165) Okubo, Y.; Hattori, T., *US20140319509 A1* (14/358,333), **2012**.
- (166) Dutta, G. K.; Han, A. R.; Lee, J.; Kim, Y.; Oh, J. H.; Yang, C. *Adv. Funct. Mater.* **2013**, *23* (42), 5317.
- (167) Van Pruissen, G. W. P.; Gholamrezaie, F.; Wienk, M. M.; Janssen, R. A. J. *J. Mater. Chem.* **2012**, *22* (38), 20387.
- (168) Lei, T.; Dou, J.-H.; Cao, X.-Y.; Wang, J.-Y.; Pei, J. *J. Am. Chem. Soc.* **2013**, *135* (33), 12168.
- (169) He, B.; Pun, A. B.; Zherebetsky, D.; Liu, Y.; Liu, F.; Klivansky, L. M.; McGough, A. M.; Zhang, B. A.; Lo, K.; Russell, T. P.; Wang, L.; Liu, Y. *J. Am. Chem. Soc.* **2014**, *136* (42), 15093.
- (170) Lipomi, D. J.; Tee, B. C. K.; Vosgueritchian, M.; Bao, Z. *Adv. Mater.* **2011**, *23* (15), 1771.
- (171) Vosgueritchian, M.; Lipomi, D. J.; Bao, Z. *Adv. Funct. Mater.* **2012**, *22* (2), 421.
- (172) Sokolov, A. N.; Cao, Y.; Johnson, O. B.; Bao, Z. *Adv. Funct. Mater.* **2012**, *22* (1), 175.
- (173) Salleo, A.; Wong, W. S. *Flexible Electronics*; Springer US, **2009**.
- (174) Siegfried, B. *Nature Mater.* **2013**, *12* (10), 871.
- (175) Reeves, B. D.; Unur, E.; Ananthakrishnan, N.; Reynolds, J. R. *Macromolecules* **2007**, *40* (15), 5344.
- (176) Rivnay, J.; Mannsfeld, S. C. B.; Miller, C. E.; Salleo, A.; Toney, M. F. *Chem. Rev.* **2012**, *112* (10), 5488.

- (177) Richter, L. J.; DeLongchamp, D. M.; Bokel, F. A.; Engmann, S.; Chou, K. W.; Amassian, A.; Schaible, E.; Hexemer, A. *Adv. Energy Mater.* **2014**, *Early View*.
- (178) Abdelsamie, M.; Zhao, K.; Niazi, M. R.; Chou, K. W.; Amassian, A. *J. Mater. Chem. C* **2014**, *2* (17), 3373.
- (179) Jensen, J.; Dam, H. F.; Reynolds, J. R.; Dyer, A. L.; Krebs, F. C. *J. Polym. Sci. B Polym. Phys.* **2012**, *50* (8), 536.
- (180) Jin, H.; Tao, C.; Velusamy, M.; Aljada, M.; Zhang, Y.; Hambsch, M.; Burn, P. L.; Meredith, P. *Adv. Mater.* **2012**.
- (181) Yao, Y.; Dong, H.; Hu, W. *Polym. Chem.* **2013**, *4* (20), 5197.
- (182) Shin, N.; Richter, L. J.; Herzing, A. A.; Kline, R. J.; DeLongchamp, D. M. *Adv. Energy Mater.* **2013**, *3* (7), 938.
- (183) Amb, C. M.; Craig, M. R.; Koldemir, U.; Subbiah, J.; Choudhury, K. R.; Gevorgyan, S. A.; Jørgensen, M.; Krebs, F. C.; So, F.; Reynolds, J. R. *ACS Appl. Mater. Interfaces* **2012**, *4* (3), 1847.
- (184) Abdellah, A.; Viridi, K. S.; Meier, R.; Döblinger, M.; Müller-Buschbaum, P.; Scheu, C.; Lugli, P.; Scarpa, G. *Adv. Funct. Mater.* **2012**, n/a.
- (185) Patel, D. G.; Graham, K. R.; Reynolds, J. R. *J. Mater. Chem.* **2012**, *22* (7), 3004.
- (186) Kouijzer, S.; Michels, J. J.; van den Berg, M.; Gevaerts, V. S.; Turbiez, M.; Wienk, M. M.; Janssen, R. A. J. *J. Am. Chem. Soc.* **2013**, *135* (32), 12057.
- (187) Duong, D. T.; Walker, B.; Lin, J.; Kim, C.; Love, J.; Purushothaman, B.; Anthony, J. E.; Nguyen, T.-Q. *J. Polym. Sci. B Polym. Phys.* **2012**, *50* (20), 1405.
- (188) Park, C.-D.; Fleetham, T. A.; Li, J.; Vogt, B. D. *Org. Electron.* **2011**, *12* (9), 1465.
- (189) Painter, P. C.; Coleman, M. M. *Essentials of Polymer Science and Engineering*; DEStech Publications, Inc.: Lancaster, **2009**.
- (190) Pavlopoulou, E.; Kim, C. S.; Lee, S. S.; Chen, Z.; Facchetti, A.; Toney, M. F.; Loo, Y.-L. *Chem. Mater.* **2014**, *26* (17), 5020.
- (191) Miller-Chou, B. A.; Koenig, J. L. *Prog. Polym. Sci.* **2003**, *28* (8), 1223.
- (192) McCulloch, B.; Ho, V.; Hoarfrost, M.; Stanley, C.; Do, C.; Heller, W. T.; Segalman, R. A. *Macromolecules* **2013**, *46* (5), 1899.
- (193) Virkar, A. A.; Mannsfeld, S.; Bao, Z.; Stingelin, N. *Adv. Mater.* **2010**, *22* (34), 3857.
- (194) Li, W.; Hendriks, K. H.; Furlan, A.; Roelofs, W. S. C.; Wienk, M. M.; Janssen, R. A. J. *J. Am. Chem. Soc.* **2013**, *135* (50), 18942.
- (195) Yiu, A. T.; Beaujuge, P. M.; Lee, O. P.; Woo, C. H.; Toney, M. F.; Frechet, J. M. *J. Am. Chem. Soc.* **2012**, *134* (4), 2180.
- (196) Chen, M. S.; Lee, O. P.; Niskala, J. R.; Yiu, A. T.; Tassone, C. J.; Schmidt, K.; Beaujuge, P. M.; Onishi, S. S.; Toney, M. F.; Zettl, A.; Fréchet, J. M. J. *J. Am. Chem. Soc.* **2013**.
- (197) Lin, H.-W.; Lee, W.-Y.; Chen, W.-C. *J. Mater. Chem.* **2012**, *22* (5), 2120.
- (198) Chang, J.-F.; Sun, B.; Breiby, D. W.; Nielsen, M. M.; Sölling, T. I.; Giles, M.; McCulloch, I.; Sirringhaus, H. *Chem. Mater.* **2004**, *16* (23), 4772.
- (199) Yang, H.; Shin, T. J.; Yang, L.; Cho, K.; Ryu, C. Y.; Bao, Z. *Adv. Funct. Mater.* **2005**, *15* (4), 671.
- (200) Schwartz, B. J. *Annu. Rev. Phys. Chem.* **2003**, *54* (1), 141.

- (201) Reid, O. G.; Malik, J. A. N.; Latini, G.; Dayal, S.; Kopidakis, N.; Silva, C.; Stingelin, N.; Rumbles, G. *J. Polym. Sci. B Polym. Phys.* **2012**, *50* (1), 27.
- (202) Kline, R. J. *Macromolecules* **2005**, *38*, 3312.
- (203) Goh, C.; Kline, R. J.; McGehee, M. D.; Kadnikova, E. N.; Fréchet, J. M. J. *Appl. Phys. Lett.* **2005**, *86* (12).
- (204) Kline, R. J.; McGehee, M. D. *J. Macromol. Sci. C, Polym. Rev.* **2006**, *46* (1), 27.
- (205) Lee, J.; Han, A. R.; Kim, J.; Kim, Y.; Oh, J. H.; Yang, C. *J. Am. Chem. Soc.* **2012**, *134* (51), 20713.
- (206) Lei, T.; Cao, Y.; Zhou, X.; Peng, Y.; Bian, J.; Pei, J. *Chem. Mater.* **2012**, *24* (10), 1762.
- (207) Beaujuge, P. M.; Tsao, H. N.; Hansen, M. R.; Amb, C. M.; Risko, C.; Subbiah, J.; Choudhury, K. R.; Mavrinskiy, A.; Pisula, W.; Brédas, J.-L.; So, F.; Müllen, K.; Reynolds, J. R. *J. Am. Chem. Soc.* **2012**, *134* (21), 8944.
- (208) Niedzialek, D.; Lemaire, V.; Dudenko, D.; Shu, J.; Hansen, M. R.; Andreasen, J. W.; Pisula, W.; Müllen, K.; Cornil, J.; Beljonne, D. *Adv. Mater.* **2013**, *25* (13), 1939.
- (209) Guilbert, A. A. Y.; Frost, J. M.; Agostinelli, T.; Pires, E.; Lilliu, S.; Macdonald, J. E.; Nelson, J. *Chem. Mater.* **2013**, *26* (2), 1226.
- (210) Li, Y.-C.; Chen, C.-Y.; Chang, Y.-X.; Chuang, P.-Y.; Chen, J.-H.; Chen, H.-L.; Hsu, C.-S.; Ivanov, V. A.; Khalatur, P. G.; Chen, S.-A. *Langmuir* **2009**, *25* (8), 4668.
- (211) Zuo, L.-J.; Hu, X.-L.; Ye, T.; Andersen, T. R.; Li, H.-Y.; Shi, M.-M.; Xu, M.; Ling, J.; Zheng, Q.; Xu, J.-T.; Bundgaard, E.; Krebs, F. C.; Chen, H.-Z. *J. Phys. Chem. C* **2012**, *116* (32), 16893.
- (212) Fakis, M.; Anastopoulos, D.; Giannetas, V.; Persephonis, P. *J. Phys. Chem. B* **2006**, *110* (49), 24897.
- (213) Himmelberger, S.; Dacuna, J.; Rivnay, J.; Jimison, L. H.; McCarthy-Ward, T.; Heeney, M.; McCulloch, I.; Toney, M. F.; Salleo, A. *Adv. Funct. Mater.* **2013**, *23* (16), 2091.
- (214) Kline, J. R.; McGehee, M. D.; Toney, M. F. *Nature Mater.* **2006**, *5* (3), 222.
- (215) Lee, W.-Y.; Giri, G.; Diao, Y.; Tassone, C. J.; Matthews, J. R.; Sorensen, M. L.; Mannsfeld, S. C. B.; Chen, W.-C.; Fong, H. H.; Tok, J. B. H.; Toney, M. F.; He, M.; Bao, Z. *Adv. Funct. Mater.* **2014**, *24* (23), 3524.
- (216) Rivnay, J.; Steyrleuthner, R.; Jimison, L. H.; Casadei, A.; Chen, Z.; Toney, M. F.; Facchetti, A.; Neher, D.; Salleo, A. *Macromolecules* **2011**, *44* (13), 5246.
- (217) Wang, S.; Kappl, M.; Liebewirth, I.; Müller, M.; Kirchhoff, K.; Pisula, W.; Müllen, K. *Adv. Mater.* **2012**, *24* (3), 417.
- (218) Perez, L. A.; Chou, K. W.; Love, J. A.; van der Poll, T. S.; Smilgies, D.-M.; Nguyen, T.-Q.; Kramer, E. J.; Amassian, A.; Bazan, G. C. *Adv. Mater.* **2013**, *25* (44), 6380.
- (219) Chou, K. W.; Yan, B.; Li, R.; Li, E. Q.; Zhao, K.; Anjum, D. H.; Alvarez, S.; Gassaway, R.; Biocca, A.; Thoroddsen, S. T.; Hexemer, A.; Amassian, A. *Adv. Mater.* **2013**, *25* (13), 1923.
- (220) Kronholm, D.; Hummelen, J. C. *Mater. Matters* **2007**, *2* (3), 16.

- (221) Troshin, P. A.; Hoppe, H.; Renz, J.; Egginger, M.; Mayorova, J. Y.; Goryachev, A. E.; Peregudov, A. S.; Lyubovskaya, R. N.; Gobsch, G.; Sariciftci, N. S.; Razumov, V. F. *Adv. Funct. Mater.* **2009**, *19* (5), 779.
- (222) Nath, S.; Pal, H.; Sapre, A. V. *Chem. Phys. Lett.* **2002**, *360* (5–6), 422.
- (223) Collins, B. A.; Li, Z.; McNeill, C. R.; Ade, H. *Macromolecules* **2011**, *44* (24), 9747.
- (224) Collins, B. A.; Gann, E.; Guignard, L.; He, X.; McNeill, C. R.; Ade, H. *J. Phys. Chem. Lett.* **2010**, *1* (21), 3160.
- (225) Miller, N. C.; Cho, E.; Gysel, R.; Risko, C.; Coropceanu, V.; Miller, C. E.; Sweetnam, S.; Sellinger, A.; Heeney, M.; McCulloch, I.; Brédas, J.-L.; Toney, M. F.; McGehee, M. D. *Adv. Energy Mater.* **2012**, *2* (10), 1208.
- (226) Schmidt-Hansberg, B.; Sanyal, M.; Klein, M. F. G.; Pfaff, M.; Schnabel, N.; Jaiser, S.; Vorobiev, A.; Müller, E.; Colsmann, A.; Scharfer, P.; Gerthsen, D.; Lemmer, U.; Barrena, E.; Schabel, W. *ACS Nano* **2011**, *5* (11), 8579.
- (227) Guo, X.; Zhou, N.; Lou, S. J.; Hennek, J. W.; Ponce Ortiz, R.; Butler, M. R.; Boudreault, P.-L. T.; Strzalka, J.; Morin, P.-O.; Leclerc, M.; López Navarrete, J. T.; Ratner, M. A.; Chen, L. X.; Chang, R. P. H.; Facchetti, A.; Marks, T. J. *J. Am. Chem. Soc.* **2012**, *134* (44), 18427.
- (228) Osaka, I.; Shimawaki, M.; Mori, H.; Doi, I.; Miyazaki, E.; Koganezawa, T.; Takimiya, K. *J. Am. Chem. Soc.* **2012**, *134* (7), 3498.
- (229) Pearson, A. J.; Wang, T.; Dunbar, A. D. F.; Yi, H.; Watters, D. C.; Coles, D. M.; Staniec, P. A.; Iraqi, A.; Jones, R. A. L.; Lidzey, D. G. *Adv. Funct. Mater.* **2014**, *24* (5), 659.
- (230) Dang, M. T.; Wuest, J. D. *Chem. Soc. Rev.* **2013**, *42* (23), 9105.
- (231) Peet, J.; Kim, J. Y.; Coates, N. E.; Ma, W. L.; Moses, D.; Heeger, A. J.; Bazan, G. C. *Nature Mater.* **2007**, *6* (7), 497.
- (232) Rogers, J. T.; Schmidt, K.; Toney, M. F.; Bazan, G. C.; Kramer, E. J. *J. Am. Chem. Soc.* **2012**, *134* (6), 2884.
- (233) Schmidt, K.; Tassone, C. J.; Niskala, J. R.; Yiu, A. T.; Lee, O. P.; Weiss, T. M.; Wang, C.; Fréchet, J. M. J.; Beaujuge, P. M.; Toney, M. F. *Adv. Mater.* **2014**, *26* (2), 300.
- (234) Lou, S. J.; Szarko, J. M.; Xu, T.; Yu, L.; Marks, T. J.; Chen, L. X. *J. Am. Chem. Soc.* **2011**, *133* (51), 20661.
- (235) Gao, J.; Chen, W.; Dou, L.; Chen, C.-C.; Chang, W.-H.; Liu, Y.; Li, G.; Yang, Y. *Adv. Mater.* **2014**, *26* (19), 3142.
- (236) Liu, F.; Wang, C.; Baral, J. K.; Zhang, L.; Watkins, J. J.; Briseno, A. L.; Russell, T. P. *J. Am. Chem. Soc.* **2013**, *135* (51), 19248.
- (237) Verploegen, E.; Mondal, R.; Bettinger, C. J.; Sok, S.; Toney, M. F.; Bao, Z. *Adv. Funct. Mater.* **2010**, *20* (20), 3519.
- (238) Agostinelli, T.; Lilliu, S.; Labram, J. G.; Campoy-Quiles, M.; Hampton, M.; Pires, E.; Rawle, J.; Bikondoa, O.; Bradley, D. D. C.; Anthopoulos, T. D.; Nelson, J.; Macdonald, J. E. *Adv. Funct. Mater.* **2011**, *21* (9), 1701.
- (239) Hu, S.; Dyck, O.; Chen, H.; Hsiao, Y.-c.; Hu, B.; Duscher, G.; Dadmun, M.; Khomami, B. *RSC Advances* **2014**, *4* (53), 27931.

- (240) Pho, T. V.; Toma, F. M.; Tremolet de Villers, B. J.; Wang, S.; Treat, N. D.; Eisenmenger, N. D.; Su, G. M.; Coffin, R. C.; Douglas, J. D.; Fréchet, J. M. J.; Bazan, G. C.; Wudl, F.; Chabiniyc, M. L. *Adv. Energy Mater.* **2014**, 4 (5).
- (241) McNeill, C. R. *Energy Environ. Sci.* **2012**, 5 (2), 5653.
- (242) Liu, X.; Huettner, S.; Rong, Z.; Sommer, M.; Friend, R. H. *Adv. Mater.* **2012**, 24 (5), 669.
- (243) Khlyabich, P. P.; Burkhart, B.; Thompson, B. C. *J. Am. Chem. Soc.* **2012**, 134 (22), 9074.
- (244) Li, W.; Roelofs, W. S. C.; Turbiez, M.; Wienk, M. M.; Janssen, R. A. J. *Adv. Mater.* **2014**, 26 (20), 3304.
- (245) Swaraj, S.; Wang, C.; Yan, H.; Watts, B.; Luning, J.; McNeill, C. R.; Ade, H. *Nano Lett.* **2010**, 10 (8), 2863.
- (246) Mori, D.; Benten, H.; Ohkita, H.; Ito, S.; Miyake, K. *ACS Appl. Mater. Interfaces* **2012**, 4 (7), 3325.
- (247) Earmme, T.; Hwang, Y.-J.; Murari, N. M.; Subramaniyan, S.; Jenekhe, S. A. *J. Am. Chem. Soc.* **2013**, 135 (40), 14960.
- (248) André, J.-M.; Delhalle, J.; Brédas, J.-L. *Quantum Chemistry Aided Design of Organic Polymers*; World Scientific: Singapore, **1991**.
- (249) Hehre, W. J. *A Guide to Molecular Mechanics and Quantum Chemical Calculations*; Wavefunction, Inc., **2003**.
- (250) Salvatori, P.; Mosconi, E.; Wang, E.; Andersson, M.; Muccini, M.; De Angelis, F. *J. Phys. Chem. C* **2013**, 117 (35), 17940.
- (251) Zhurko, G. A. *ChemCraft 1.6*, <http://www.chemcraftprog.com> (accessed September 2014).
- (252) Carsten, B.; He, F.; Son, H. J.; Xu, T.; Yu, L. *Chem. Rev.* **2011**, 111 (3), 1493.
- (253) Hendriks, K. H.; Li, W.; Heintges, G. H. L.; van Pruissen, G. W. P.; Wienk, M. M.; Janssen, R. A. J. *J. Am. Chem. Soc.* **2014**, 136 (31), 11128.
- (254) Schlüter, D. A.; Hawker, C. J.; Sakamoto, J. *Synthesis of Polymers: New Structures and Methods*; 7th ed. ed.; Wiley-VCH: Weinheim, **2012**.
- (255) Coffin, R. C.; Peet, J.; Rogers, J.; Bazan, G. C. *Nature Chem.* **2009**, 1 (8), 657.
- (256) Richard, C. A., Georgia Institute of Technology, **2014**.
- (257) Ackermann, L.; Vicente, R.; Kapdi, A. R. *Angew. Chem. Int. Ed.* **2009**, 48 (52), 9792.
- (258) Berrouard, P.; Najari, A.; Pron, A.; Gendron, D.; Morin, P.-O.; Pouliot, J.-R.; Veilleux, J.; Leclerc, M. *Angew. Chem. Int. Ed.* **2011**, 51 (9), 2068.
- (259) Grenier, F.; Berrouard, P.; Pouliot, J.-R.; Tseng, H.-R.; Heeger, A. J.; Leclerc, M. *Polym. Chem.* **2013**, 4 (6), 1836.
- (260) Mercier, L. G.; Aich, B. R.; Najari, A.; Beaupre, S.; Berrouard, P.; Pron, A.; Robitaille, A.; Tao, Y.; Leclerc, M. *Polym. Chem.* **2013**, 4 (20), 5252.
- (261) Pavlishchuk, V. V.; Addison, A. W. *Inorg. Chim. Acta.* **2000**, 298 (1), 97.
- (262) Trasatti, S. *Pure Appl. Chem.* **1986**, 58 (7), 955.
- (263) Hansen, W. N.; Hansen, G. J. *Phys. Rev. A* **1987**, 36 (3), 1396.
- (264) Bard, A. J.; Faulkner, L. R. *Electrochemical Methods: Fundamentals and Applications*; Wiley: New York, **2001**.
- (265) Thompson, B., University of Florida, **2005**.

- (266) Cardona, C. M.; Li, W.; Kaifer, A. E.; Stockdale, D.; Bazan, G. C. *Adv. Mater.* **2011**, 23 (20), 2367.
- (267) Graham, K. R.; Mei, J.; Stalder, R.; Shim, J. W.; Cheun, H.; Steffy, F.; So, F.; Kippelen, B.; Reynolds, J. R. *ACS Appl. Mater. Interfaces* **2011**, 3 (4), 1210.
- (268) Carr, J. A.; Nalwa, K. S.; Mahadevapuram, R.; Chen, Y.; Andereg, J.; Chaudhary, S. *ACS Appl. Mater. Interfaces* **2012**, 4 (6), 2831.
- (269) Armarego, W. L. F.; Chai, C. L. L. In *Purification of Laboratory Chemicals (Sixth Edition)*; Chai, W. L. F. A. L. L., Ed.; Butterworth-Heinemann: Oxford, **2009**, p 88.
- (270) Hummelen, J. C.; Knight, B. W.; LePeq, F.; Wudl, F.; Yao, J.; Wilkins, C. L. *J. Org. Chem.* **1995**, 60 (3), 532.
- (271) Cowan, S. R.; Leong, W. L.; Banerji, N.; Dennler, G.; Heeger, A. J. *Adv. Funct. Mater.* **2011**, 21 (16), 3083.
- (272) Zhou, H.; Zhang, Y.; Seifter, J.; Collins, S. D.; Luo, C.; Bazan, G. C.; Nguyen, T.-Q.; Heeger, A. J. *Adv. Mater.* **2013**, 25 (11), 1646.
- (273) Allard, S.; Forster, M.; Souharce, B.; Thiem, H.; Scherf, U. *Angew. Chem. Int. Ed.* **2008**, 47 (22), 4070.
- (274) Mihailetschi, V. D.; Blom, P. W. M.; Hummelen, J. C.; Rispen, M. T. *J. Appl. Phys.* **2003**, 94 (10), 6849.
- (275) *Solar Spectral Irradiance Air Mass 1.5* <http://rredc.nrel.gov/solar/spectra/am1.5/> (accessed September 2014).
- (276) Zimmermann, E.; Ehrenreich, P.; Pfadler, T.; Dorman, J. A.; Weickert, J.; Schmidt-Mende, L. *Nature Photon.* **2014**, 8 (9), 669.
- (277) Lubner, E. J.; Buriak, J. M. *ACS Nano* **2013**, 7 (6), 4708.
- (278) Bayless, D. J. *Statistical Rejection of "Bad" Data – Chauvenet's Criterion*, <http://www.ohio.edu/people/bayless/seniorlab/chauvenet.pdf> (accessed November 2014).
- (279) Tsang, S.-W.; Chen, S.; So, F. *Adv. Mater.* **2013**, 25 (17), 2434.
- (280) Brown, T. M.; Cacialli, F. In *Handbook of Conjugated Polymers: Theory, Synthesis, Properties, and Characterization*; 3rd Edition ed.; Skotheim, T. A., Reynolds, J. R., Eds.; CRC Press: Boca Raton, **2006**.
- (281) Chen, W.; Nikiforov, M. P.; Darling, S. B. *Energy Environ. Sci.* **2012**, 5 (8), 8045.
- (282) Schnablegger, H.; Singh, Y. *A Practical Guide to SAXS*; Anton Parr, **2006**.
- (283) Hammouda, B. *Probing Nanoscale Structures –The SANS Toolbox*, http://www.ncnr.nist.gov/staff/hammouda/the_SANS_toolbox.pdf (accessed October 2014).
- (284) Jimison, L. H., Stanford University, **2011**.
- (285) Leng, Y. *Materials Characterization - Introduction to Microscopic and Spectroscopic Methods*; John Wiley & Sons: Singapore, **2008**.
- (286) King, S. M. In *Modern Techniques for Polymer Characterisation*; Pethrick, R. A., Dawkins, J. V., Eds.; John Wiley & Sons: **1999**.
- (287) *Neutron Activation Calculator*, <http://www.ncnr.nist.gov/resources/activation/> (accessed October 2014).
- (288) *NIST Center for Neutron Research*, <http://www.ncnr.nist.gov/index.html> (accessed October 2014).

- (289) Chen, W.; Xu, T.; He, F.; Wang, W.; Wang, C.; Strzalka, J.; Liu, Y.; Wen, J.; Miller, D. J.; Chen, J.; Hong, K.; Yu, L.; Darling, S. B. *Nano Lett.* **2011**, *11* (9), 3707.
- (290) Briber, R. M. *SANS from Polymers*, http://www.ncnr.nist.gov/summerschool/ss02/SANS_Polymers_Briber.pdf (accessed October 2014).
- (291) Graham, K. R.; Wieruszewski, P. M.; Stalder, R.; Hartel, M. J.; Mei, J.; So, F.; Reynolds, J. R. *Adv. Funct. Mater.* **2012**, *22* (22), 4801.
- (292) Cho, E.; Risko, C.; Kim, D.; Gysel, R.; Cates Miller, N.; Breiby, D. W.; McGehee, M. D.; Toney, M. F.; Kline, R. J.; Bredas, J.-L. *J. Am. Chem. Soc.* **2012**, *134* (14), 6177.
- (293) Mannsfeld, S. <http://code.google.com/p/wxdiff/> (accessed May 2013).
- (294) Piergies, D.; Hughes, A. <http://rscl.sourceforge.net/> (accessed October 2014), 2012.
- (295) Stalder, R.; Mei, J.; Reynolds, J. R. *Macromolecules* **2010**, *43* (20), 8348.
- (296) Ko, S.; Hoke, E. T.; Pandey, L.; Hong, S.; Mondal, R.; Risko, C.; Yi, Y.; Noriega, R.; McGehee, M. D.; Brédas, J.-L.; Salleo, A.; Bao, Z. *J. Am. Chem. Soc.* **2012**, *134* (11), 5222.
- (297) Stalder, R.; Mei, J.; Subbiah, J.; Grand, C.; Estrada, L. A.; So, F.; Reynolds, J. R. *Macromolecules* **2011**, *44* (16), 6303.
- (298) Schubert, M.; Dolfen, D.; Frisch, J.; Roland, S.; Steyrlleuthner, R.; Stiller, B.; Chen, Z.; Scherf, U.; Koch, N.; Facchetti, A.; Neher, D. *Adv. Energy Mater.* **2012**, *2* (3), 369.
- (299) Vaynzof, Y.; Brenner, T. J. K.; Kabra, D.; Sirringhaus, H.; Friend, R. H. *Adv. Funct. Mater.* **2012**, *22* (11), 2418.
- (300) Zhou, E.; Cong, J.; Wei, Q.; Tajima, K.; Yang, C.; Hashimoto, K. *Angew. Chem. Int. Ed.* **2011**, *50* (12), 2799.
- (301) Ma, Z.; Dang, D.; Tang, Z.; Gedefaw, D.; Bergqvist, J.; Zhu, W.; Mammo, W.; Andersson, M. R.; Inganäs, O.; Zhang, F.; Wang, E. *Adv. Energy Mater.* **2014**, *4* (6).
- (302) Leblebici, S. Y.; Chen, T. L.; Olalde-Velasco, P.; Yang, W.; Ma, B. *ACS Appl. Mater. Interfaces* **2013**, *5* (20), 10105.
- (303) Carsten, B.; Szarko, J. M.; Son, H. J.; Wang, W.; Lu, L.; He, F.; Rolczynski, B. S.; Lou, S. J.; Chen, L. X.; Yu, L. *J. Am. Chem. Soc.* **2011**, *133* (50), 20468.
- (304) Hoven, C. V.; Dang, X. D.; Coffin, R. C.; Peet, J.; Nguyen, T. Q.; Bazan, G. C. *Adv. Mater.* **2010**, *22* (8), E63.
- (305) Amb, C. M.; Chen, S.; Graham, K. R.; Subbiah, J.; Small, C. E.; So, F.; Reynolds, J. R. *J. Am. Chem. Soc.* **2011**, *133* (26), 10062.
- (306) Lindgren, L. J.; Zhang, F.; Andersson, M.; Barrau, S.; Hellström, S.; Mammo, W.; Perzon, E.; Inganäs, O.; Andersson, M. R. *Chem. Mater.* **2009**, *21* (15), 3491.
- (307) Kastner, C.; Susarova, D. K.; Jadhav, R.; Ulbricht, C.; Egbe, D. A. M.; Rathgeber, S.; Troshin, P. A.; Hoppe, H. *J. Mater. Chem.* **2012**, *22* (31), 15987.
- (308) Sato, S.; Hashimoto, K.; Tajima, K. *Synth. Met.* **2011**, *161* (13–14), 1289.
- (309) Kim, K.-H.; Yu, H.; Kang, H.; Kang, D. J.; Cho, C.-H.; Cho, H.-H.; Oh, J. H.; Kim, B. J. *J. Mater. Chem. A* **2013**, *1* (46), 14538.

- (310) Donley, C. L.; Zaumseil, J.; Andreasen, J. W.; Nielsen, M. M.; Sirringhaus, H.; Friend, R. H.; Kim, J.-S. *J. Am. Chem. Soc.* **2005**, *127* (37), 12890.
- (311) Van Vooren, A.; Kim, J.-S.; Cornil, J. *ChemPhysChem* **2008**, *9* (7), 989.
- (312) Kim, D. H.; Ayzner, A. L.; Appleton, A. L.; Schmidt, K.; Mei, J.; Toney, M. F.; Bao, Z. *Chem. Mater.* **2013**, *25* (3), 431.
- (313) Shao, M.; Keum, J. K.; Kumar, R.; Chen, J.; Browning, J. F.; Das, S.; Chen, W.; Hou, J.; Do, C.; Littrell, K. C.; Rondinone, A.; Geohegan, D. B.; Sumpter, B. G.; Xiao, K. *Adv. Funct. Mater.* **2014**, *24* (42), 6647.
- (314) Vandewal, K.; Ma, Z.; Bergqvist, J.; Tang, Z.; Wang, E.; Henriksson, P.; Tvingstedt, K.; Andersson, M. R.; Zhang, F.; Inganäs, O. *Adv. Funct. Mater.* **2012**, *22* (16), 3480.
- (315) Lai, T.-H.; Tsang, S.-W.; Manders, J. R.; Chen, S.; So, F. *Mater. Today* **2013**, *16* (11), 424.
- (316) Small, C. E.; Chen, S.; Subbiah, J.; Amb, C. M.; Tsang, S.-W.; Lai, T.-H.; Reynolds, J. R.; So, F. *Nature Photon.* **2012**, *6* (2), 115.
- (317) Chen, M. S.; Niskala, J. R.; Unruh, D. A.; Chu, C. K.; Lee, O. P.; Fréchet, J. M. J. *Chem. Mater.* **2013**, *25* (20), 4088.
- (318) Rogers, J. T.; Schmidt, K.; Toney, M. F.; Kramer, E. J.; Bazan, G. C. *Adv. Mater.* **2011**, *23* (20), 2284.
- (319) Hoppe, H.; Sariciftci, N. S. *J. Mater. Chem.* **2006**, *16* (1), 45.
- (320) Stalder, R.; Grand, C.; Subbiah, J.; So, F.; Reynolds, J. R. *Polym. Chem.* **2012**, *3* (1), 89.
- (321) Peet, J.; Cho, N. S.; Lee, S. K.; Bazan, G. C. *Macromolecules* **2008**, *41* (22), 8655.
- (322) Moulé, A. J.; Meerholz, K. *Adv. Funct. Mater.* **2009**, *19* (19), 3028.
- (323) Walker, B.; Tamayo, A.; Duong, D. T.; Dang, X.-D.; Kim, C.; Granstrom, J.; Nguyen, T.-Q. *Adv. Energy Mater.* **2011**, *1* (2), 221.
- (324) Moulé, A. J.; Meerholz, K. *Adv. Mater.* **2008**, *20* (2), 240.
- (325) Hedley, G. J.; Ward, A. J.; Alekseev, A.; Howells, C. T.; Martins, E. R.; Serrano, L. A.; Cooke, G.; Ruseckas, A.; Samuel, I. D. W. *Nature Commun.* **2013**, *4*, 2867.
- (326) Treat, N. D.; Chabinyc, M. L. *Annu. Rev. Phys. Chem.* **2014**, *65* (1), 59.
- (327) Venkateshvaran, D.; Nikolka, M.; Sadhanala, A.; Lemaire, V.; Zelazny, M.; Kepa, M.; Hurhangee, M.; Kronemeijer, A. J.; Pecunia, V.; Nasrallah, I.; Romanov, I.; Broch, K.; McCulloch, I.; Emin, D.; Olivier, Y.; Cornil, J.; Beljonne, D.; Sirringhaus, H. *Nature* **2014**, *515* (7527), 384.
- (328) Bloking, J. T.; Giovenzana, T.; Higgs, A. T.; Ponc, A. J.; Hoke, E. T.; Vandewal, K.; Ko, S.; Bao, Z.; Sellinger, A.; McGehee, M. D. *Adv. Energy Mater.* **2014**, *4* (12).
- (329) Tada, A.; Geng, Y.; Wei, Q.; Hashimoto, K.; Tajima, K. *Nature Mater.* **2011**, *10* (6), 450.
- (330) Lobez, J. M.; Andrew, T. L.; Bulović, V.; Swager, T. M. *ACS Nano* **2012**, *6* (4), 3044.
- (331) Mei, J.; Bao, Z. *Chem. Mater.* **2014**, *26* (1), 604.
- (332) Fang, L.; Zhou, Y.; Yao, Y.-X.; Diao, Y.; Lee, W.-Y.; Appleton, A. L.; Allen, R.; Reinspach, J.; Mannsfeld, S. C. B.; Bao, Z. *Chem. Mater.* **2013**, *25* (24), 4874.

- (333) Li, F.; Yager, K. G.; Dawson, N. M.; Yang, J.; Malloy, K. J.; Qin, Y. *Macromolecules* **2013**, *46* (22), 9021.
- (334) Koldemir, U., University of Florida, **2012**.
- (335) Ma, J.; Hashimoto, K.; Koganezawa, T.; Tajima, K. *J. Am. Chem. Soc.* **2013**, *135* (26), 9644.
- (336) Senkovskyy, V.; Tkachov, R.; Komber, H.; Sommer, M.; Heuken, M.; Voit, B.; Huck, W. T. S.; Kataev, V.; Petr, A.; Kiriy, A. *J. Am. Chem. Soc.* **2011**, *133* (49), 19966.

VITA

Caroline Grand

Caroline Grand was born in Lyon, France and stayed in France for 10 years before her family moved to Gothenburg, Sweden in 1997 and to Singapore in 2000. In 2003, her family came back to France and Caroline attended high school at the Lycée Blaise Pascal in Clermont-Ferrand. After obtaining her baccalauréat in science, she stayed in Clermont-Ferrand to study advanced topics in Mathematics, Physics, and Chemistry, which enabled her to enroll in the Graduate School of Physics and Chemistry of Bordeaux (ENSCP) after passing the Concours aux Grandes Ecoles. During her two years at ENSCP, she learned the principles behind Chemical Engineering, had the opportunity to conduct a five-month internship with Michelin, learning about living anionic polymerizations yielding functional polymers, and obtained her Masters in 2010. After this experience in industrial R&D, Caroline enrolled in the Chemistry graduate program at the University of Florida, where she joined the group of Prof. John Reynolds and began studying polymers for organic photovoltaics by fabricating and characterizing devices. In 2012, the group moved to Georgia Institute of Technology in Atlanta and Caroline's research interests shifted to polymer synthesis and morphology characterization. She graduated in Spring 2015, and is looking forward to starting an industrial career with the Dow Chemical Company.